The Rheology and Structure of Thermotropic

Liquid Crystalline Polymers in Extensional Flow

by

Thomas Stephen Wilson

Dissertation submitted to the Faculty of the

Virginia Polytechnic Institute and State University

in partial fulfillment of the requirements for the degree of

Doctor of Philosophy

in

Chemical Engineering

APPROVED:

Donald G. Baird, Chairman

Richard Davis

Kenneth L. Reifsnider

Thomas C. Ward

Garth L. Wilkes

June 10, 1991

Blacksburg, Virginia

The Rheology and Structure of Thermotropic Liquid Crystalline Polymers in Extensional Flow

by

Thomas Stephen Wilson

Donald G. Baird, Chairman

Chemical Engineering

(ABSTRACT)

The transient shear and elongational flow behavior of HPC EF, G, and HBA/HNA (Vectra A900) have been measured in order to determine the behavior of liquid crystalline polymer systems and to establish whether this behavior is different from that for isotropic flexible-chain polymer melts and isotropic systems of rodlike polymers. In order to accomplish this a rotary clamp extensional rheometer was constructed which is capable of measuring the elongational flow behavior of polymer melts up to 320 °C and which can measure elongational viscosities as low as 1000 Pa*s. Tests were conducted on HPC EF at 190 and 210 °C, on HPC G at 200 and 240 °C, and on HBA/HNA at 301 and 320 °C. It was determined that the transient shear stress behavior of the LCP systems scales with strain or alternately, reduced time and that the reduced stress is independent of shear rate over the range of rates investigated. This behavior is different from that for isotropic melts of flexible-chain and rodlike polymers in that the reduced stress for these systems is dependent on deformation rate. The transient elongational viscosity behavior of the LCPs was determined and found to follow linear viscoelastic response at very low strains and then shows mild strain hardening with increasing strain, which is qualitatively similar to the behavior of certain linear polyolefins such as PS and HDPE. From the elongational viscosity behavior determined for both isotropic and anisotropic HPC melts it was found that differences in the melt state can result in qualitative differences in the measured behavior. However, the presence of residual crystallinity in the systems studied makes it uncertain whether the results determined here are general for all LCP systems.

The prediction of the Doi theory for both steady and transient shear and elongational flow were calculated in order to establish whether the theory can predict or model the flow

behavior of LCPs and to establish whether the elongational flow behavior of LCPs can be predicted from their shear flow behavior. The Doi theory was evaluated with the viscous drag or rod-solvent friction term retained in the equation for the stress tensor. It was found that the Doi theory cannot predict the shear or elongational flow behavior of LCPs with parameters determined only from molecular properties. At the same time, the Doi theory was found to be able to semi-quantitatively model the steady shear viscosity behavior of isotropic and anisotropic systems of rodlike polymers with retention of the viscous drag contribution to the stress tensor. Also, the Doi theory was able to qualitatively model the transient flow behavior of the same systems, though agreement for the anisotropic systems depended on the use of a multidomain average to represent the globally unoriented state of the material at equilibrium. However, the Doi theory was not able to predict the transient elongational flow behavior of either isotropic or anisotropic systems with parameters fit to shear flow data. Furthermore, the predictions of the Doi theory for elongational flow showed only marginal qualitative agreement with the experimentally determined behavior of both isotropic and anisotropic systems.

to Richa

Acknowledgements

The author would first like to thank his family and especially his parents, Ab and Lou Wilson, for instilling in him the desire to want to know more, and for providing encouragement and support through his lifetime. My sincerest gratitude is also given to my advisor, Dr. Donald Baird, for his support, encouragement, valuable suggestions, and patience. The author feels privileged to have had the opportunity to study under Dr. Baird. The author wishes to thank his advisory committee: Professors Richy Davis, Ken Reifsnider, Tom Ward, and Garth Wilkes for their interest and suggestions. The use of Dr. Wilkes laboratory facilities was sincerely appreciated. Thanks also to Professors David Cox and Rosario Bretas for sitting in on his defense. Special thanks goes to Mr. Wendell Brown for his excellent machining skills and patience in constructing the extensional rheometer.

The author owes thanks to countless people who have been friends, coworkers, and sometimes even both:

- Soon to be Dr. Greg Lavender for years of trying to conduct intelligent conversation with the author in his quest for intelligent life on this planet.
- Many thanks to Dr. Scott White, Dr. Ravi Ramanathan, Dr. Dinshong Done, Dr. Kent Blizard, Dr. Ray Glaser, and Dr. Tony Brennen for advice.

- The author would not have kept as much sanity as he did without the friendship, advice, and humor of Drs. Randy Moynihan, Ashish Sukhadia, and soon-to-be Dr. Jo Ellen Kelly (DePorter). Remember Toto, just click your heels together 3 times and say "I want to go home."
- Dr. Arindam Datta and wife Dr. Ritu for their friendship and introduction to the Indian community.
- Dr. Dimitris Collias for his advice and for setting a pace to shoot for in conducting work.
- All members of Dr. Baird's group, past and present, and in particular soon-to-be Dr. Carl Reed, Paulo (Mr. Tennis) DeSouza, Margarita, Dr. Sun, Alice Wilson, Beth, Limin, Todd, and Bafna.
- Drs. Sidhartha Sen, Bala Kumar, and (soon to be) Dr. David Rodrigues for providing challenging racquetball.
- Mike Annen for removing the author from the lab to go fishing when it was necessary.
- Soon-to-be Dr. Joan Mullerleile and Ester for the Saturday Trek breaks.
- All members of Dr. Wilke's lab, past and present.
- Professors Mark Davis and David Cox for Volleyball and Friday night classes at Pedros.
- All of the chemical engineering department personnel including Billy, Carol, Diane C., Diane P., Sandy, Sue, and Dr. Conger for their help.
- The Virginia Tech Juggling Club, and in particular Lance and Kristen.
- All others inadvertently left out, with apologies.

Most importantly, the author would like to express his profound appreciation to a certain Hawaiian Goddess for her divine intervention, without which the author *might* now be selling used cars in Pittsburgh.

Original Contributions

The author considers the following items original contributions to research in polymer science:

1. The construction of a dual rotary clamp rheometer capable of making measurements up to 320 ^{o}C, which is approximately 100 ^{o}C higher than the upper limit of preceding rotary clamp type rheometers.

2. The use of 2 mutually immiscible immersion oils in the extensional rheometer reservoir, such that one oil is more dense and one oil is less dense than the polymer melt. The polymer sample is thus situated at the oil-oil interface. This significantly improves thermal stability of the sample and reduces sample degradation.

3. The determination of the elongational viscosity growth behavior of thermotropic liquid crystalline polymers under isothermal and constant rate deformation up to 2 strain units and the finding that the behavior appears not to be fundamentally different from that for flexible-chain polymer melts.

4. The finding that the elongational viscosity growth behavior of a polymer possessing a rigid molecule is qualitatively different in the liquid crystalline state than in the isotropic melt state.

5. The finding that the retention of the so-called rod-solvent interaction term in the equation for the stress tensor in the Doi theory significantly improves the ability of the theory to model the shear viscosity behavior of liquid crystalline polymers.

Table of Contents

List of Illustrations

List of Tables

1.0 Introduction

Liquid crystalline polymers (LCPs) have been the focus of a great deal of industrial and academic research over the past two decades. Although the interest in these materials was mainly due to their use in the production of fibers with exceptionally high modulus and strength, these materials have other useful properties. These include excellent resistance to solvents, low thermal expansion [1], high use temperatures, low melt viscosity, and low permeability to many gases [2]. Consequently, much of the current research on LCPs is concerned with their use in injection molded parts, blow molded parts, and extruded and blown films. Also, there is growing interest in the use of LCPs in blends with engineering thermoplastics and commodity resins as reinforcing agents [3].

While LCPs show a great deal of promise for future use, at the present time their rheological properties and corresponding morphology development are not well understood. In turn, optimizing the processing conditions for realizing the full potential of these materials is dependent on a fundamental knowledge of their behavior. The first two chapters of this dissertation serve to introduce liquid crystalline polymers, review present knowledge about their behavior, and establish areas where there is a need for further study, thereby justifying the research objectives of this work.

This first chapter is an introduction to liquid crystalline materials. In the first two sections (1.1 and 1.2), the nature and structure of liquid crystals and liquid crystal forming materials are reviewed. Next (section 1.3), the importance and current important industrial applications are briefly described, as well as some problems which prevent their use. In the following section (1.4) some key aspects to the processing of LCPs are discussed, with particular emphasis being placed on how the flow field affects orientation and structure. Some comments about LCP rheology are included in this section, including a brief discussion of constitutive theories available for these systems. From this introduction, some areas which need further investigation are broadly defined. The final section of the chapter (1.5) identifies these areas and defines the overall research objectives of this dissertation. A more detailed review of the literature is given in Chapter 2.

1.1 Nature of Liquid Crystals

In this section the liquid crystalline state is defined and compared to that of isotropic liquids and crystalline solids. The term liquid crystal itself is somewhat ambiguous, with the terms liquid and crystal being contradictory. Therefore, liquid crystals have been more accurately described as anisotropic fluids or "mesophases," meaning "of intermediate form" [4]. These terms will be used interchangeably throughout this dissertation.

The liquid crystal state is intermediate between that of a crystalline solid and an isotropic liquid. To help define liquid crystals more clearly, a comparison is made between the liquid crystalline state and those of isotropic liquids and crystalline solids. In a crystalline solid, the molecules or units of the molecule are arranged periodically in a rigid lattice structure with three dimensional order, giving rise to definite maxima for Bragg scattering of x-rays. In contrast, the orientational and positional molecular order in liquid crystals is only one or

two dimensional and shorter in range [4]. Also, liquid crystals lack any rigid lattice structure, so they will flow under an applied stress like a fluid.

A comparison of liquid crystals with isotropic liquids can also be made. Isotropic liquids have physical properties which are the same in all directions. Because of the molecular ordering present in liquid crystals, properties such as viscosity are often direction dependent on a microscopic scale [5]. Whereas isotropic fluids usually exhibit birefringence only under flow conditions, liquid crystals are birefringent under both flow and quiescent conditions. Thus, liquid crystals differ from isotropic liquids due to the local molecular ordering present in these materials.

1.2 Structure and Types of Liquid Crystals

Liquid crystalline order was first observed in low molecular weight organic materials a century ago [6]. Only within the past 30 to 40 years has liquid crystalline order been observed in polymeric systems and the existence of LC order in synthetic polymer systems was reported even more recently [7]. Though it is believed that both low molecular weight and polymeric liquid crystals form similar structures, the discussion to follow is directed at polymeric liquid crystals. In this section, the conditions and molecular structures leading to mesophase formation are reviewed, as well as the different types of mesophase structures.

Polymers may exhibit liquid crystalline order either in solution, in which case they are called "lyotropes," or in the bulk, in which case they are called "thermotropes." In the case of lyotropes, mesophase formation is both a function of concentration and temperature. At very low concentrations, the polymer solution is isotropic. As the concentration is raised the viscosity increases and reaches a maximum at a critical concentration, c^*, at which point the solution becomes birefringent. This marks the onset of liquid crystallinity. In the case of polymers, a two phase region (containing both liquid crystal and isotropic phases) is typically

seen, due to polydispersity, impurities, or chain defects. As polymer concentration increases the percentage of the material in the anisotropic phase increases, until only the mesophase exists. At even higher concentrations bulk polymer will precipitate out.

For thermotropic polymers, the mesophase forms as the bulk polymer is heated and undergoes a first order transition from a solid to a liquid crystal [4]. Thus, mesophase formation for a specific polymer depends only on temperature and may be detected by thermal means, such as DSC. As the temperature of a thermotrope is further raised, transitions to different mesophase types may occur. At even higher temperatures, the material will become isotropic or degrade depending on its chemical structure.

A large number of different chemical structural units lead to the formation of mesophases, but they generally have two common characteristics. Such structural units, whether they are entire molecules or molecular subunits, are usually very stiff and have high aspect ratios [9]. Indeed, Flory [10] has shown that these two geometric conditions provide an adequate basis for the formation of a thermodynamically stable anisotropic fluid. The term "mesogenic units" has been applied to these structures [9].

A summary of the common molecular moities or structures making up liquid crystalline polymers is shown in Figure 1 and further information can be found in the reviews by Chung [1], Calundann and Jaffe [7], Ober [11], and Noel [12]. Liquid crystalline polymers typically fall into four groups, based on the molecular configuration and conformation. These groups include rigid rod-like molecules, molecules which take on a rigid helical conformation, and block-like molecules with both mesogenic units and flexible spacer units in the main chain or with mesogenic units in the side groups but with a flexible chain backbone. The difference between the structure of low molecular weight liquid crystals and polymeric liquid crystals is that the LMW LC's are typically mesogenic groups, whereas in polymeric LC's the mesogenic units may be only part of the molecule, in addition to the obvious molecular weight differences.

Each of these four groups tends to form a specific mesophase structure, of which three categories have been defined: nematic, cholesteric, and smectic. These distinctions in type

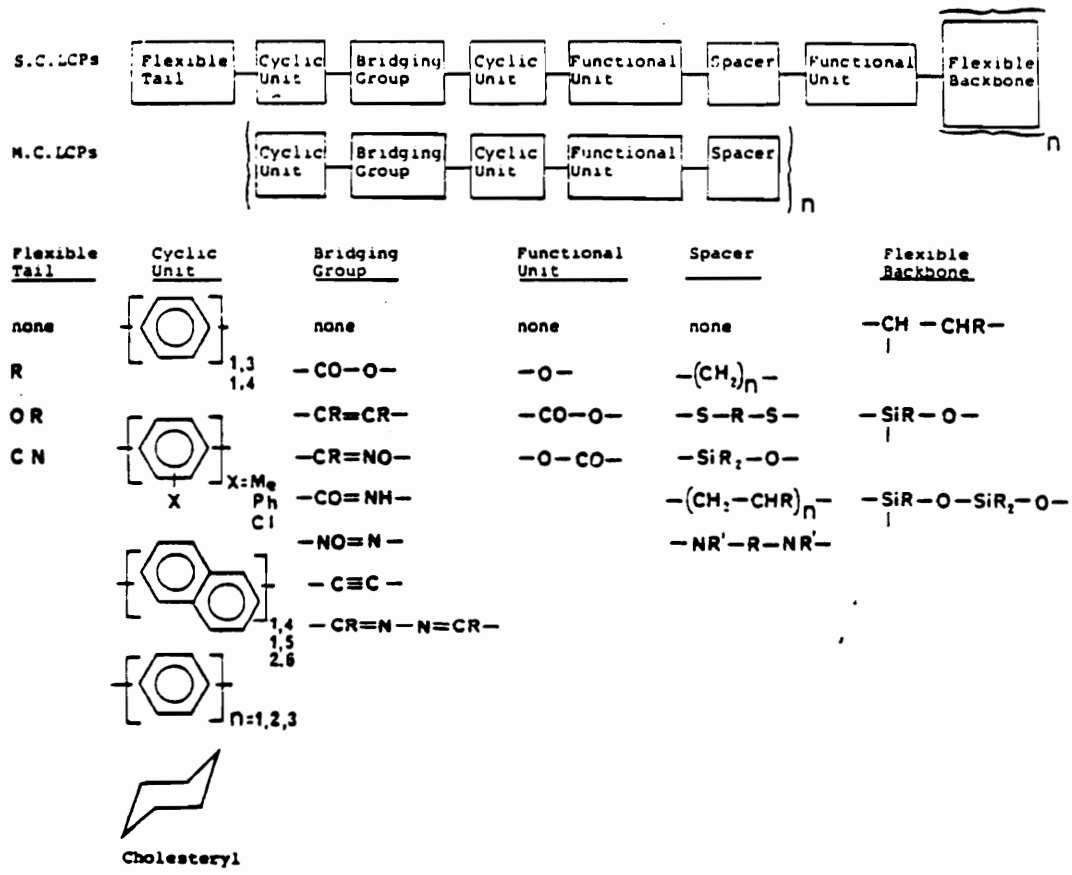

Figure 1. General chemical moities of main chain and side chain LCPs [1].

of structure are made in addition to the distinction between being lyotropic and thermotropic. The three different mesophase categories are defined on the basis of their orientational and positional order, a schematic of which is shown in Figure 2. In a nematic mesophase, the molecules are highly oriented about a certain direction **n**, called the director, but lack any positional correlation of their centers of gravity, resulting in one dimensional order. The molecules in a nematic mesophase possess a high degree of mobility, and are therefore greatly affected by external fields and forces [9]. Consequently, nematics are characterized by their low viscosities.

Cholesteric liquid crystals consist of planes of molecules within which nematic order exists. However, a certain angle of twist exists between the directors of adjacent planes and this results in a periodic helical structure with the axis of the helix perpendicular to the planes of molecular orientation. The distance between planes with the same orientation direction is about the wavelength of visible light. Bragg scattering of light by cholesterics results in brilliant colors. Also, the more highly ordered structure of the cholesteric mesophase results in a much higher viscosity relative to the nematic.

The smectic mesophase exhibits the highest degree of order of the three mesophase types. In a smectic mesophase the molecules are oriented parallel to one direction, while the centers of gravity of the molecules are arranged in distinct layers. The interlayer distance may be measured quantitatively by x-ray scattering [4]. Because of the two dimensional order present in a smectic mesophase molecular motion is greatly restricted, resulting in a viscosity much greater than that of a nematic. While a number of different smectic structures have been reported and even more shown to be possible, the focus of this work lies with the nematic type of LCPs. Hence, the reader is referred to DeGennes [4] and Luckhurst and Gray [9] for further information.

As previously stated, each type of mesogen conformation tends to lead to a specific mesophase structure. At this point it is instructive to review the types of structures formed by different mesogen conformations and the typical chemical groups which have these conformations. Rod-like and helical molecules will tend to form either nematic or cholesteric

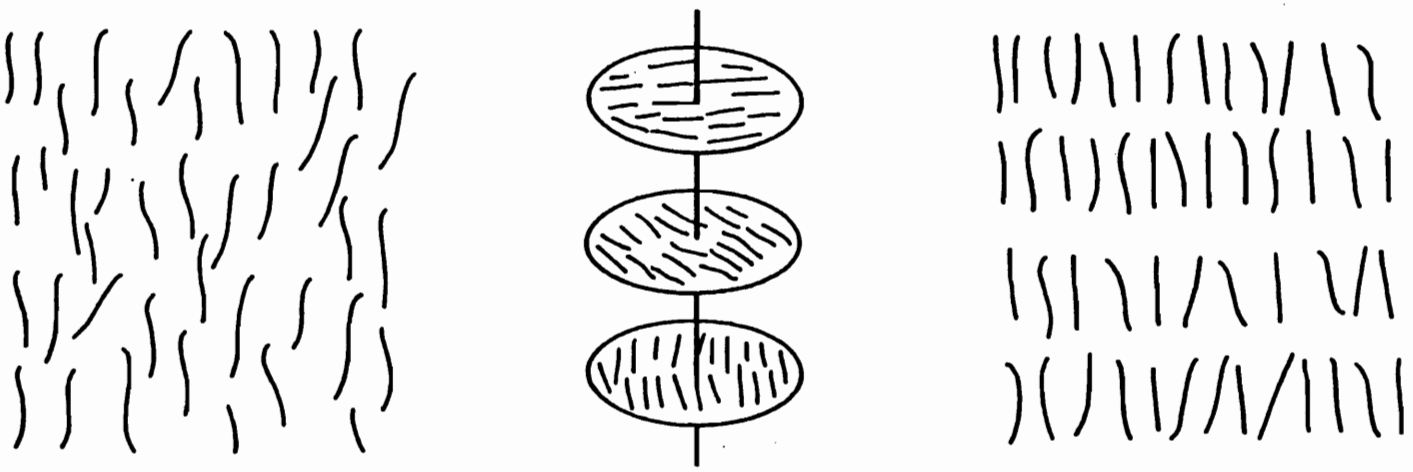

Figure 2. Types of liquid crystal mesophase structures: a) nematic, b) cholesteric, and c) smectic, after [1].

mesophases, either in solution or in the bulk. The type of mesophase formed will depend predominantly on the geometrical symmetry of the rod-like or helical coil [9]. Rigid molecules with uniaxial symmetry will tend to form nematic mesophases, while non racemic mixtures of rod-like molecules or helical coils tend to form cholesteric mesophases. For example, poly(γ-benzyl-L-glutamate) (PBLG) solutions form cholesteric mesophases while racemic mixtures of PBLG and poly(γ-benzyl-D-glutamate) (PBDG) are nematic [13].

Chemically, rod-like molecules typically consist of highly aromatic chains with the aromatic rings connected in the para conformation by rigid groups such as esters or amides, or by flexible spacers made up of aliphatic groups or ethers. Aromatic polyesters tend to form thermotropic liquid crystals while aromatic polyamides typically form lyotropes since they usually degrade before they melt. Helical molecules which form rigid helical coils in the bulk or in solvent include many biological molecules such as Tobacco Mosaic Virus (TMV) [14], ribonucleic acid (RNA), deoxiribonucleic acid (DNA), PBLG and PBDG [15].

The final type of molecules which display LCP structures is the block-like molecules, which can consist of alternating mesogenic units and flexible spacers or a flexible chain backbone with mesogenic units as side groups. Those molecules with mesogenic units as side groups tend to form smectic type mesophase structures, while those with the mesogenic units along the chain backbone can form all three types of mesophase structures, depending on the type and size of the blocks. For example, when the polymer has a chain backbone of rigid, optically inactive mesogenic units which alternate with flexible spacers, most often a nematic mesophase is seen. If the mesogenic units are optically active in the same type of alternating structure, a cholesteric structure is likely to be formed. Finally, when the polymer chain consists of large blocks of which are chemically incompatible, such as in a surfactant molecule with hydrophilic and hydrophobic units, there is a tendency to form a smectic mesophase.

One final point concerning mesophase structure must be brought up. In analogy to the polycrystalline nature of most crystalline solids, liquid crystalline polymers almost never consist of a homogeneous mesophase. Instead, the material consists of micro-sized regions within which a nematic, cholesteric, or smectic structure exists. These regions are called

"domains" and the overall structure is referred to as a polydomain structure or texture. Factors leading to the formation of this polydomain texture include the presence of impurities, low molecular weight chains, and amorphous chains.

The existence of the polydomain structure of liquid crystalline polymers greatly affects both their physical and mechanical properties. For example, the size of the domains is roughly that of the wavelength of visible light, giving rise to tremendous scattering and resulting in their being opaque. Also, the polydomain texture is thought to be responsible for the shear thinning behavior of LCPs at low shear rates [17,18]. A detailed discussion of the domain structure and how it relates to the properties of liquid crystalline polymers is given in the next chapter.

1.3 Importance of Liquid Crystalline Polymers

Liquid crystalline materials are important due to their presence in many biological systems and growing use in industry. In living systems liquid crystals appear to be involved in activities such as dynamic transformation, rhythmiticity, and communication in molecular domains [19]. As previously noted, both RNA and DNA form lyotropic cholesteric liquid crystals. Industrially, both low molecular weight and polymeric liquid crystals have useful applications. Low molecular weight liquid crystals are widely used in optical displays and as very sensitive thermal indicators [20]. Polymeric liquid crystals are used to make ultra-high strength fibers and in injection molded parts such as microwave cookware.

The most important industrial use of LCPs is in the production of extremely highly oriented fibers with ultra-high modulus and strength. Amazingly, the tensile moduli of fibers spun from both lyotropic aromatic polyamides [7,21] and thermotropic aromatic copolyesters [22] approach the theoretical limits for these materials, as calculated from bond bending energies and assuming extended chain conformations. Similar properties have only very recently been

obtained from flexible chain polymers [23], with the ultra-drawing of gelled polyethylene. Yet, it should be noted that properties obtained in the LCPs are for as spun and annealed fibers, whereas exotic methods must be used to obtain ultra high tensile properties from flexible chain polymers. Thus, the molecular order present in the mesophase allows a high degree of orientation to be obtained in spun fibers.

Though lyotropic LCPs are generally limited to use in one dimensional parts, the use of thermotropic LCPs for injection molded parts is growing. Although more expensive than conventional thermoplastic resins, the lower viscosity of LCPs and their higher solidification temperatures makes it possible to decrease cycle times and energy costs [24]. Mechanical properties of injection molded LCP parts are usually as good or better than those for highly reinforced conventional thermoplastics [25], and the lack of filler reduces equipment wear.

Finally, thermotropic LCPs have potential for use as reinforcing agents in blends and in objects or parts made by blow molding, thermoforming, film blowing, and flat film extrusion. However, before these processes can be fully utilized, certain problems associated with the processing of LCPs must be resolved. For example, in highly oriented parts the properties in the orientation direction are exceptional, but properties in the transverse directions can be correspondingly poor. Also, some processing methods require high melt strength, which thermotropic liquid crystalline polymers typically do not have above their melting temperatures. In the next section, the processing and rheology of liquid crystalline polymers is discussed.

1.4 Processing and Rheological Phenomena

In the last several years much research interest has shifted from lyotropic to thermotropic LCPs, since the thermotropes offer several processing advantages. For example, the processing of thermotropic LCPs involves no toxic or corrosive solvents. Although

lyotropic LCPs are limited to being used in spun fibers, thermotropic LCPs can be processed by other methods, such as injection molding, to produce complex parts. Therefore, the brief discussion to follow is directed at the thermotropic materials.

Liquid crystalline polymer mesophases were previously described to exist as ordered fluids which exhibit a domain microstructure at rest. When processed under certain conditions, a high degree of molecular orientation can be obtained and preserved in the solid, resulting in exceptional properties in the orientation direction. However, for objects whose geometries include important dimensions in two or three directions, e.g. films and molded parts, properties in the directions orthogonal to the orientation direction can be very poor [26]. Therefore, the processing variables which affect the orientation and microstructure of LCPs must be determined.

For example, Ide and Ophir [25,27] studied injection molded disks and extruded filaments of thermotropic copolyesters. In the case of the injection molded disks, a skin-core structure was observed. The skin was highly oriented, while the core showed little orientation as evidenced by birefringence. These results were explained as being due to the fountain flow effect at the advancing front, where an extensional flow exists. In the case of the extruded filaments, a low degree of orientation was seen in the as extruded samples, while a very high degree of orientation was obtained with moderate drawing. From these results and others to presented later in Chapter 2, it has been found that extensional flow is more effective than shear flow in producing high molecular orientation.

Viola [8,28] confirmed this hypothesis and also showed that shearing while cooling increased the amount of orientation retained in the solidified disk. Lewis and Fellers [29] have likewise shown that the modulus and strength of melt spun fibers, made from a 60 mole % hydroxybenzoic acid / poly(ethylene terephthalate) copolyester (hereafter referred to as 60HBA/PET), are higher for fibers spun under isothermal versus nonisothermal conditions. Although these two studies seem to contradict each other, it is apparent that thermal history affects the development or preservation of orientation in thermotropic LCPs.

The processing of LCPs involves other considerations besides orientation. For example, a polymer must have a minimum amount of melt strength to be used in processes such as film blowing and thermoforming. However, the viscosities of thermotropic LCPs above their melt temperatures are usually orders of magnitude too low to be successfully processed by means of these techniques. One way to overcome this difficulty is to process with the polymer in a supercooled state. Done and coworkers [18,30] have shown that some thermotropic LCPs will retain the same viscosity and storage modulus upon cooling well below their melting temperatures for several minutes before rising to equilibrium values. The polymer can be processed while its mechanical strength is increasing. Blizard and Baird [31,32] have successfully applied this to LCP film blowing, in which the polymer was extruded through a die kept 30 to 50°C lower than the melting temperature.

It has been shown that the final structure and properties of a thermotropic LCP depends on the structure developed in the melt during processing, which in turn is expected to be related to the rheological behavior of the materials. Numerous studies of the rheological behavior of LCPs have been made, reviews of which have been given by Baird [33,34] and Wissbrun [18]. Several interesting phenomena were reported and include an apparent yield stress, negative first normal stress differences, shear thinning at rates orders of magnitude lower than are seen for isotropic flexible chain melts, and multiple stress overshoot upon inception of steady shear flow.

In addition to the phenomena above, Onogi and coworkers [34] have studied the relationship between the molecular orientation and stress during the inception and cessation of steady shear flow for lyotropic solutions of hydroxypropylcellulose (HPC) and water. In particular, it was observed that the relaxations of stress and molecular orientation occurred on different time scales, with stress being roughly an order of magnitude faster. This behavior may be compared to that for flexible-chain polymer melts, where the stress and molecular orientation are usually directly related through the stress-optical law.

The exhibition of such complex rheological and physical behavior in LCPs raises the question of whether this behavior can be predicted. Any suitable constitutive model must be

able to separately predict both the stress response and the molecular orientation as a function of flow history. A number of continuum theories have been proposed for liquid crystals and include those of Ericksen and Leslie [35,36], Duffy [37], and Hand [38]. In these theories, the stress is assumed to be a function of the rate of deformation and a vector or tensor which describes the molecular structure and orientation. For example, in the theory of Ericksen and Leslie, all molecules are assumed to lie parallel to a common axis denoted by a vector **n**, the director. Although all of these theories suffer from some drawbacks, the theory of Ericksen and Leslie has been very successful in the modeling of low molecular weight nematics. Yet Viola [8] has shown that Ericksens theory could not predict the transient behavior of two thermotropic copolyesters and attributed this to the failure of the theory to account for the polydomain texture present in LCPs.

In addition to the continuum theories, Doi [39] has developed a constitutive equation for liquid crystals based on the molecular dynamics of rod-like molecules. The stress in the fluid is due to hydrodynamic drag effects and Brownian motion, which are both functions of the rate of deformation tensor and an order parameter tensor **S**, which describes molecular orientation. Although derivation of Doi's theory relies heavily on approximations and assumptions, it is appealing for two reasons. First, only two constants are needed, the dimensionless interaction potential U (in some papers C is used) and the rotational diffusion coefficient for concentrated isotropic solutions D_r. These constants can be calculated based on a knowledge of molecular properties or experimentally fitted using the steady shear viscosity and first normal stress difference. Second, the theory is based on molecular dynamics and thus it is possible to give physical meaning to the constants.

1.5 Research Objectives

In the previous sections of this chapter liquid crystalline materials were defined and many of the characteristics of LCPs were briefly described. The rheological behavior of LCPs in shear flow was described as being unusual when compared to that for isotropic flexible-chain polymer melts. At the present time it is not clear whether some of the behavioral features observed are general for all LCPs or are specific to certain polymer systems. The first objective of this work is to determine the dynamic and transient shear flow properties of several LCPs (the ones to be used for extensional testing) and establish whether the behavior observed is general for all LCPs or specific to those systems. A secondary part of this objective is then to determine the state of the polymers investigated, i.e. wholly liquid crystalline, biphasic (LC and isotropic, or LC with residual crystallinity), etc.. The fulfillment of this objective also provides necessary background for the main theme of this work, stated next.

It was shown in studies by Ide [25,27] and Viola [8,28] that extensional flow is more effective than shear flow in orienting LCPs. While this is generally true for all polymers and is expected from the flow kinematics, LCPs tend to be much easier to orient is extension than the materials which form isotropic melts. It is then somewhat surprising that very little effort has been made to determine the elongational viscosity of LCPs, and the studies which were performed are far from complete [42,45,114]. Therefore, the second objective of this work is to determine the uniaxial extensional flow behavior of a couple of thermotropic LCPs. This objective is carried out on a newly constructed extensional rheometer based on the designs of Meissner [40], Laun and Münstedt [41], Carter [120], and Ide and White [121]. Tests are run under isothermal conditions at constant extension rates, with several rates run for each material. Questions to be answered include whether LCPs have a steady state elongational viscosity, if they have a constant elongational viscosity is the Trouton ratio (ratio of steady state elongational viscosity to steady shear viscosity) 3 at low rates as is observed with flexi-

ble chain polymer melts, is the elongational flow behavior the same for a rodlike molecule is both isotropic and liquid crystal melt states, etc..

The existence of a polydomain structure in liquid crystalline polymers was also mentioned. Viola [8,28] has shown for the 60HBA/PET copolyester that the microstructure is a strong function of thermal and flow history. In particular, he showed that extensional flow could produce an elongated or fibrous microstructure. However, this study did not include the determination of how this structure develops during extensional flow. The third objective of this work is therefore to determine how the domain structure changes during extensional flow. First, the microstructure and orientation of extruded and drawn LCP films was determined in order demonstrate the degree molecular orientation and domain elongation that can be brought about by elongational flow. Also, the characterization of the film morphology provided information on the utility of the method of SALS for structure determination. Tests include wide angle x-ray scattering (WAXS), polarized optical microscopy (POM), scanning electron microscopy (SEM), and small angle light scattering (SALS). At the same time it was not possible to determine changes in LCP domain texture during isothermal constant rate elongation in this investigation.

The continuum theory of Ericksen and Leslie and the molecular theory of Doi were discussed in the previous section. While Ericksens theory adequately describes the steady shear behavior of low molecular weight liquid crystals, it has been shown to poorly describe the transient shear flow behavior of LCPs. At the same time, the Doi theory contains fewer adjustable constants and is based on molecular dynamics, giving physical meaning to those parameters. Additionally, the ability of the Doi theory to evaluate the transient shear and extensional flow behavior of LCPs has not been fully evaluated. Therefore, the fourth objective of this work is to establish whether the Doi theory, in its original or modified form, is able to model the transient shear and extensional flow behavior of LCPs. A primary part of this objective will be to establish whether the adjustable parameters fitted to shear data can predict the extensional flow behavior, thereby making the exceedingly difficult task of determining the extensional flow behavior of LCPs unnecessary.

The purpose of this chapter was to introduce the basic characteristics of liquid crystalline polymers, to relate their importance, and to briefly discuss the processing and rheology of LCPs so as to indicate research which is still needed in order to exploit the potential of these materials. Thereby, the motivation for this research was given and the overall objectives were stated. In the next chapter, the literature pertaining to the rheology and development of orientation and structure in LCPs is reviewed in detail.

2.0 Literature Review

In the first chapter liquid crystalline materials were defined. The molecular structure of these materials was then discussed and related to the three types of mesophases. Next, the importance of these materials was reviewed. However, the potential of these materials for use in many processes was shown to depend on a better understanding of their rheology, and the development of molecular orientation and structure during flow. Specifically, importance was placed on the measurement or prediction of extensional flow behavior and associated structural changes. The chapter concluded with a description of the research objectives of this work.

In this chapter, the ideas presented in chapter one will be reviewed in greater detail. In the preceding chapter the unusual rheological behavior of LCP's was referred to and it was noted that this behavior may be due to the development of molecular orientation or to the presence of a polydomain structure. In section 2.1 the rheological behavior of liquid crystalline polymers is discussed in more detail. A point is made to note features which distinguish LCP rheology from that for isotropic flexible chain polymer melts. In the next section (2.2) the development of molecular orientation and the polydomain texture of liquid crystalline polymers is reviewed. Emphasis is placed on the effect of flow and temperature history. In particular, a comparison is given of the effect of shear and extensional flow. Also, the tech-

nique of small angle light scattering is reviewed for the experimental study of the polydomain texture. In section 2.3 Doi's molecular based theory for the dynamics of rod-like molecules is developed and reviewed. Particular attention is paid to the predictions for steady and transient flows as well as modifications to the theory which could improve agreement with experiment.

In the final section of this chapter a brief summary is given of key points concerning the rheology and development of structure in liquid crystalline polymers. A point is made to stress certain areas where knowledge is incomplete or lacking. Thus, the motivation for the objectives stated in section 1.5 is reiterated. The details of the experimental and numerical methods used to fulfill these research objectives are described in Chapter Three.

2.1 Rheology of Liquid Crystalline Polymers

The rheological behavior of liquid crystalline polymers is reviewed in this section, yet a comprehensive review of all rheological studies is not the intention here. Rather, a point is made to distinguish the rheological behavior of liquid crystalline polymers from that of isotropic polymer melts or solutions. At the same time, a distinction will be made between behavior which is typical for the liquid crystalline state and that particular to certain systems. In this way the type of behavior that must be predicted by a constitutive theory for polymeric liquid crystals will be defined. The rheological behavior of low molecular weight liquid crystals, a review of which is given by Porter and Johnson [43], will only be discussed in relation to polymeric systems. Earlier reviews on the rheological behavior of polymeric liquid crystals are given in the articles by Baird [33,44] and Wissbrun [18], and in the dissertations of Viola [8], and Done [20]. Also, excellent reviews of the rheology of flexible-chain polymer melts and solutions are given by Bird [72] and Tanner [105].

The scope of this review is restricted to lyotropic or thermotropic polymer systems which display either a nematic or cholesteric mesophase. Particular attention is paid to hydroxypropylcellulose (HPC), a cellulose ether whose molecular conformation is helical, and to the thermotropic copolyesters of (1) para-hydroxybenzoic acid and poly(ethylene terephthalate) (HBA/PET) and (2) para-hydroxybenzoic acid and 2-hydroxy-6-naphthoic acid (HBA/HNA). The reason for this is not only that much of the rheological characterization work has been performed on these materials but also that they are used in the experimental portion of this work. First, the viscosity behavior of LCPs is reviewed. The occurrence of yield stresses, onset of shear thinning, and the magnitude of the plateau viscosity in relation to isotropic melts are examined. Next, the normal stress behavior of LCPs is discussed, followed by a comparison of steady and dynamic shear results. Thermal and shear history effects are then discussed, with some emphasis placed on transient testing, which provides the most rigorous test of a constitutive model. Finally, the extensional flow behavior of LCPs is reviewed.

2.1.1 Viscosity Behavior of LCPs in Steady Shear Flow

A large number of studies have been done on the viscosity behavior of liquid crystalline polymers, for both lyotropic and thermotropic systems [8, 15, 17, 20, 21, 24-26, 28, 29, 31, 33, 34, 42-44, 50-55, 58-63, 66-67, 69-71, 76, 81, 86-89, 93-99, 106-117]. While not all of these studies are reviewed here in detail, a point is made to use specific examples to demonstrate general behavior.

Onogi and Asada [17] first proposed a general flow curve for the viscosity behavior of liquid crystalline polymer systems. They proposed a three region flow curve, as is shown in Figure 3. Region I is a shear-thinning region, indicating the presence of a yield stress. Region II consists of a Newtonian plateau and is at moderate shear rates. Region III behavior, at still higher rates, is that of another shear thinning region. Onogi and Asada [17] have attributed

this three region behavior to the existence of a polydomain texture in the melt, with each region representing a different stage in the destruction of this polydomain texture to form a single nematic phase. The proposed mesophase morphology for each region is shown in Figure 4. The initial yield type behavior was attributed to the stress needed to align the molecules within the domains in the direction of shear. In the Region II range the domains break up into smaller domains and a mono-domain texture begins to form. A shear-thinning mono-domain texture is characteristic of Region III.

Both Wissbrun [18] and Viola [8] have examined the validity of the three region flow curve by comparison with experimental data. In Figure 5 is shown a plot of the viscosity behavior of several liquid crystalline polymers. It can be seen that only curves 1, 3, and 5 show three flow regions while curves 2, 4, and 7 show only one shear-thinning region and curve 6 shows only two regions. From the data of Figure 5 both Wissbrun [18] and Viola [8] conclude that the three region flow curve is not general for all liquid crystalline polymers. More recent investigations [54, 66, 70, 106-100, 112-113] also show behavior which conflicts with the three region flow curve and therefore the conclusions of Wissbrun and Viola are valid. At the same time, the three region flow curve has been widely used in the literature to describe the rheological behavior of LCPs and thus it was presented here.

2.1.1.1 Yield Stress

If the three region flow curve is a feature of nematic and cholesteric liquid crystalline materials, all such materials must exhibit yield stresses. In fact, many researchers have reported yield stresses in materials thought to be liquid crystalline. Yield stresses were reported in solutions of collagen in dilute HCl by Fukata and Date [47], in aqueous solutions of chitin by Marchessault and coworkers [48], and in aqueous solutions of wood and cotton cellulose by Hermans [49]. In all cases the yield stresses were thought to be due to liquid crystalline structure in the systems.

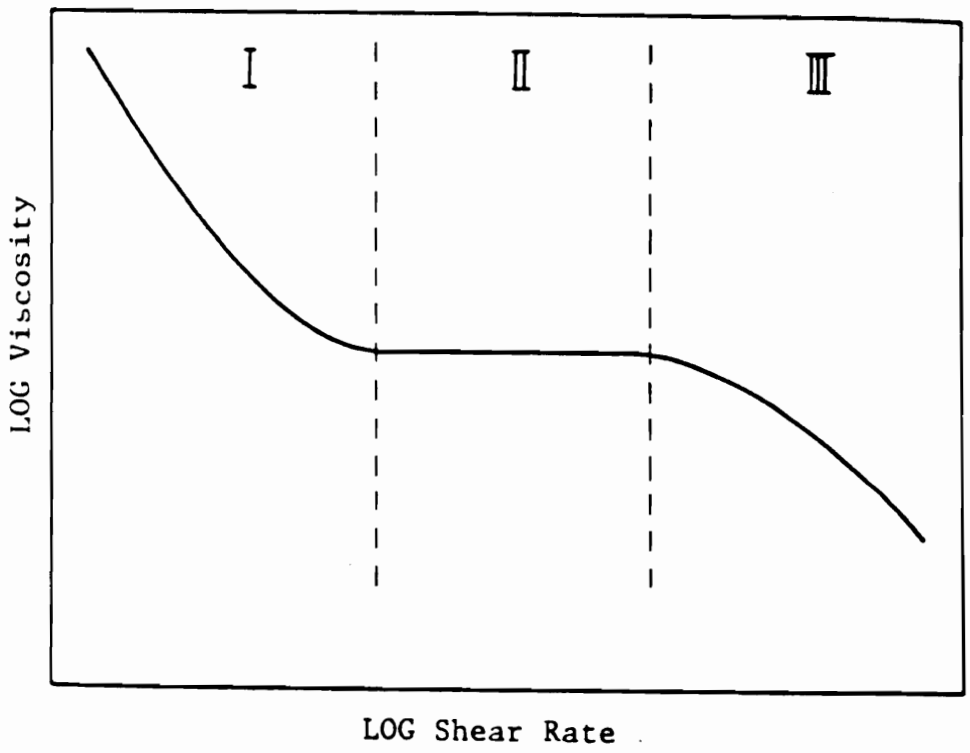

Figure 3. Three region flow curve proposed by Onogi and Asada [17].

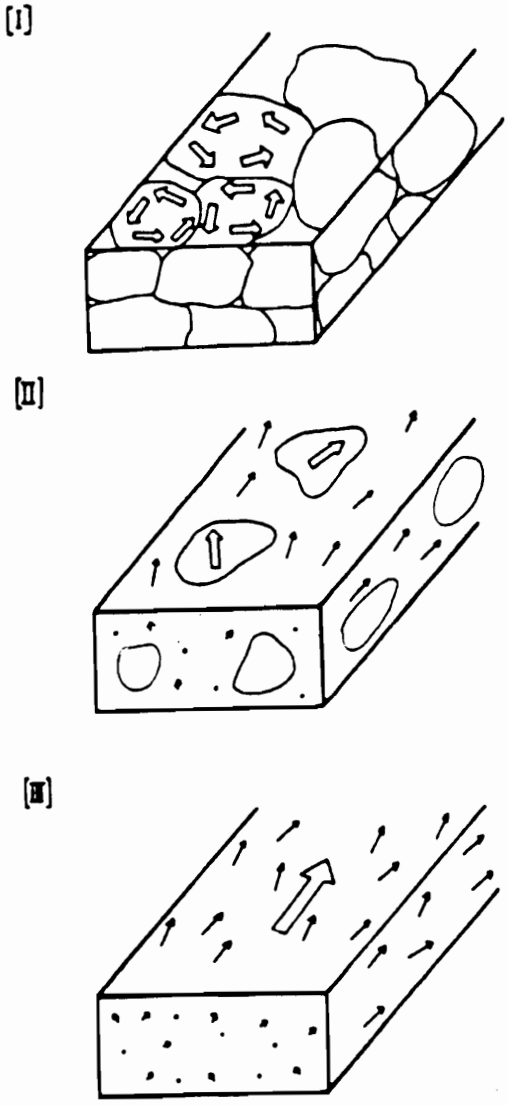

Figure 4. Structure of LCPs corresponding to the three flow regions of Fig. 3 [17].

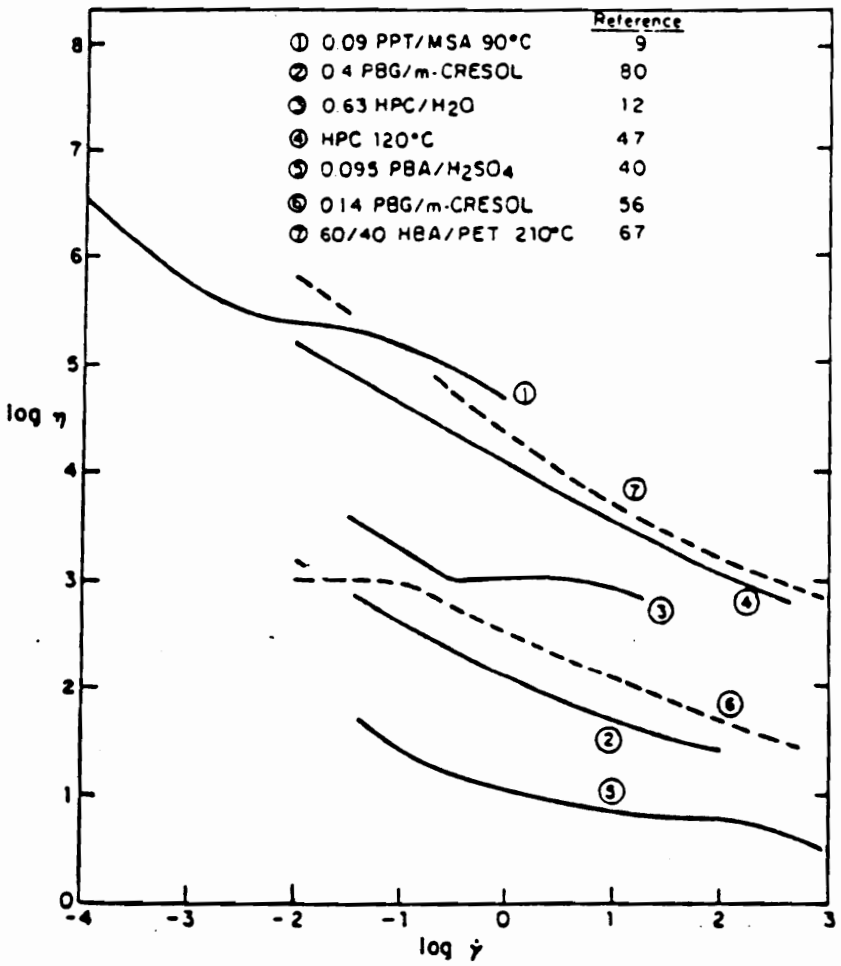

Figure 5. Viscosity behavior of several polymeric liquid crystals [18].

Aoki [15] and Baird [50,51] have investigated lyotropic solutions of poly(p-phenylene terephthalamide) (PPTA) in 100% sulfuric acid and Papkov [52] has investigated similar solutions of poly(p-benzamide) (PBA), both of which form a nematic mesophase. Aoki and Papkov have reported yield stress behavior, but Baird has shown that yield stresses are eliminated by preheating the material and by careful exclusion of moisture. Results for another lyotropic LCP, poly(γ-benzyl-glutamate) (PBG), are also conflicting. Kiss [53], Mewis [54,94,96], and Larson [111] report no yield stresses in both racemic and optically active solutions of PBG in m-cresol. At the same time, Yanase [55] reports shear thinning viscosity at rates as low as 0.01 s^{-1}.

In the case of thermotropic LCPs Elliot [56], Shimamura [57], and Suto [58] have noted the existence of yield stresses in liquid crystalline HPC. Wissbrun [18] and Sugiyama [59] have also reported yield stresses in the HBA/PET system at temperatures below 260 °C. However, in both cases there is some residual crystallinity in the materials at temperatures where the yield stresses were reported. Also, Sugiyama's extrapolation of data to obtain yield stress values at temperatures higher than 250 °C is questionable because of the limited shear rate range. Gotsis and Baird [60] report both steady state shear tests and stress relaxation after steady shearing for the HBA/PET copolyester at 260 and 275 °C. The observation of a zero shear viscosity and stress relaxation to zero stress indicate the absence of a yield stress. Additionally, in viscosity versus shear rate plots reported by other investigators on thermotropic copolyesters believed to be absent of residual crystallinity [70, 106,107,110] the viscosity levels off as shear rate decreases. Although yield stresses are seen to occur in some LCP systems, yield type behavior is not a general characteristic of the liquid crystalline state, but might be associated with unmelted crystallites. Therefore, liquid crystalline polymers do not in general show the behavior labelled as region I behavior by Onogi and Asada.

2.1.1.2 Plateau Viscosity

One of the most interesting phenomena in the rheology of liquid crystalline polymers is the observation that the viscosity of the liquid crystalline material can be lower than that of the corresponding isotropic state of the material [18]. In polymers which can exhibit lyotropic behavior, if one follows the "Newtonian" plateau viscosity as a function of concentration of polymer or as a function of temperature, a maximum is reached near the isotropic-anisotropic transition. Such behavior has been observed in solutions of PBA [19,49,61], PBG [53], and PPTA [62] and is regarded as a general trend for lyotropic liquid crystals [63]. In addition, Baird [62] and Kiss [53] have shown that the maximum in viscosity is shear rate dependent, shifting to lower concentrations as rate increases. This phenomenon was attributed to a shear induced decrease in the concentration at which the system becomes liquid crystalline. Bahar and Erman [64] have modified the lattice theory of Flory and Ronca [65] for solutions of rigid rods and have shown that the effect of a shear field is to lower the concentration for the isotropic to anisotropic transition, in agreement with the studies cited above.

An increase in viscosity in going through the liquid crsytal to isotropic transition has also been observed in some thermotropic liquid crystal systems. In low molecular weight nematics, it has been observed that as the temperature is raised and the polymer goes through the nematic to isotropic transition, the viscosity increases [43]. In the case of polymeric liquid crystals, the transition is much broader due to impurities and a distribution of molecular weights. Since both isotropic and nematic phases have viscosities which decrease with temperature, it is possible for the increase in viscosity due to the thermodynamic transition to be offset by the intrinsic decrease in viscosity with temperature, resulting in no maximum [66]. Both possibilities have been observed for thermotropic LCPs. Elliot [56] reported that the viscosity of HPC decreased as the temperature was raised from 190 to 200 °C, but increased as the temperature was raised higher. Similar results for HPC were obtained by Suto [58], Chen [114], Fujiyama [115], and Horio [116] and were shown to coincide with a liquid crystal to isotropic phase transitions. Fujiyama [115] also showed that the shape of the viscosity ver-

sus temperature curve is rate dependent, with a small shift in the transitions to higher temperatures as rate increases. Several researchers [66-70] have reported similar results for several thermotropic copolyesters. Kiss [66] investigated a copolymer of HBA, isophthalic acid (IA), and hydroxquinone (HQ). It was found that the increase in viscosity with temperature was shear rate dependent too. Similar results were reported by Blumstein [69], Tuttle [70], and Wunder [112]. While Bickel [71] observed no increase in viscosity with temperature at the nematic-isotropic transition of a thermotropic copolyester synthesized from the monomers HO-ϕ-$COOCH_2CH_2OH$ and ClOC-ϕ-COCl, a distinct plateau was seen in the temperature versus viscosity curve. It is probable that in this case the viscosity increase due to the nematic-isotropic phase transition was washed out by the decrease in viscosity of the individual phases.

In summary, rheological data for both lyotropic and thermotropic LCPs show that the nematic phase has a lower viscosity than the corresponding isotropic state, which can therefore be used as an indication that a transition has occurred. However, the accuracy of this method in determining such a transition may be adversely affected by polymer polydispersity, temperature dependence of the individual phases, and shear rate dependence.

2.1.1.3 Onset of Shear-Thinning

The point at which polymeric materials start to shear-thin is an important aspect of their viscosity behavior. The rate at which shear-thinning begins is related to a characteristic relaxation time of the polymer [72]. Therefore, the relaxation behavior of a material in its isotropic and liquid crystalline states can be compared by the viscosity behavior of those states. Also, a knowledge of this behavior is necessary for modelling.

In lyotropic systems a comparison of the viscosity behavior of the isotropic and anisotropic states is facilitated since the zero shear viscosity for the isotropic phase and the Region II viscosity for the anisotropic phase can be made equal [18]. Wissbrun [18] has

compiled the data of a number of separate studies on the PBLG system as shown in Table 1. Without going into detail, it is seen that there is no general agreement on which phase shear thins first. Other studies on PBLG in m-cresol and in dichloroacetic acid (DCA) were made by Yang [73,74]. The PBLG molecule exists as a helix in m-cresol and as a random coil in DCA. It was found that the m-cresol solutions shear-thinned at a rate of approximately 150 s^{-1}, while the DCA solutions were Newtonian over nearly the entire range of rates tested.

Comparisons of the isotropic and anisotropic viscosity behavior have also been performed on the PPTA/H_2SO_4 system. Baird [62] found that for anisotropic and isotropic solutions with the same zero shear viscosity at 60 °C, the anisotropic solutions shear-thinned at lower shear rates. Wong and Berry [75] also found the anisotropic solution began to shear thin at lower rates than the isotropic solution at lower rates for PPTA solutions. However, Aoki and coworkers [15] report no appreciable shear-thinning for an anisotropic solution of PPTA comparable to that reported by Baird [62], though a different range of rates is investigated in the two studies. Thus, no general conclusions can can be made.

Relatively little work has been done to compare the viscosity behavior of polymers in thermotropic and isotropic states, mainly because most thermotropic polymers degrade before the liquid crystal-isotropic transition. Wissbrun and Griffin [67] studied a copolyester which was modified with aliphatic spacing groups to lower the LC-isotropic transition. The viscosity of this copolyester was measured in the isotropic state at 240 °C and was found to be Newtonian up to the highest rate measured, which was 100 s^{-1}. In comparison, anistropic melts were tested at 210 °C and found to shear-thin at all rates measured. However, the observation of a yield stress at 210°C implies the presence of solids, possibly crystallinity, and these results are therefore inconclusive. Tuttle and coworkers [70] investigated the viscosity behavior of a copolyester based on terephthaloyl chloride, isophthaloyl chloride, and 1,10-bis(4-hydroxyphenyl)-decane. Their copolyester, designated as 0.75/0.25, had a crystal to nematic transition at just below 240 °C and the nematic to isotropic transition was complete at 270 °C. Shear thinning was observed in the nematic state whereas mainly Newtonian behavior was observed for the isotropic melt. Blumstein and coworkers [69] compared the

Table 1. Onset of Shear Rate Dependence of Viscosity of PBLG [18].

Solvent	Form[a]	Concentration (wt %)	Viscosity (poise)	$\dot{\gamma}_{1/2}$ (s^{-1})	Ref.
m-Cresol	I	6	25	100	Kiss and Porter[63]
	C	16	20	1000	
m-Cresol	I	6	4	>500	Aoki, White, and Fellers[64]
	C	10	25	>500	
	C	16	15	>500	
Dioxane	I	4	25	>200	Iizuka[62]
	I	7	150	100	
	C	13	30	100	
CH_2Br_2	I	7	16	>200	
	N + I	10	5	150	
	N	13	6	150	

[a] I → isotropic, C → cholesteric, N → nematic, N + I → biphasic.

viscosity behavior of the nematic and isotropic states for a copolyester composed of rigid mesogenic units, bridged by flexible spacers. Although both nematic and isotropic melts showed shear thinning behavior over the entire shear rate range (2 to 200 s^{-1}), the nematic melt was seen to be much more shear-thinning than the isotropic melt. The results given above indicate that thermotropic LCPs show shear-thinning at lower shear rates and to a larger extent in the liquid crystalline state than in the isotropic state.

Although a direct comparison between the isotropic and anistropic state is not possible for the HBA/PET system, this system has been extensively studied. In several separate studies [26,55,59,60,73] it has been reported that the HBA/PET copolymers exhibit lower values of viscosity and are more shear thinning than the PET homopolymer. Wissbrun [18] and Jackson [77] estimated the ratio of relaxation times of 60HBA/PET to those of similar intrinsic viscosity samples of PET through a comparison of the elastic compliance, J', of the respective polymers and found that the relaxation time of 60HBA/PET is about 1000 times greater than that of the PET homopolymer.

The factors which determine just how shear-thinning a particular LCP is are not well established, but would intuitively be related to the characteristics of the particular polymer system, such as molecular weight, molecular weight distribution, chain stiffness, etc. Blumstein [69] studied a well fractionated thermotropic polyester and found that polydisperse samples showed a higher degree of shear-thinning than the fractionated samples. No other results have been found for other LCPs, but similar results for suspensions of fibers in polymer melts are well known [78].

In summary, the viscosity behavior of liquid crystalline polymers has been extensively studied. The three region flow curve of Onogi and Asada does not describe the viscosity behavior of liquid crystalline polymers, yet has been widely used in the literature as a framework for the description of the viscosity behavior of LCPs and for comparisons with the behavior of the isotropic state. Although many liquid crystalline polymer systems exhibit yield stresses, that behavior is seen to be associated with the presence of solids, and therefore the pure liquid crystalline phase most likely does not exhibit a yield stress. As is observed for low

molecular weight nematic LCs, LCPs in the nematic state have a lower viscosity than the corresponding isotropic state. Finally, liquid crystalline systems appear to shear-thin at much lower rates than corresponding isotropic systems. However, there is some contrary evidence for lyotropic systems and limited evidence for thermotropic systems, possibly making this generalization premature.

2.1.2 Normal Stress Behavior

Another important rheological property is the normal stress difference behavior in steady shear flow. The first normal stress difference, N1, is often used as a measure of elasticity in a material and gives an indication of deviation from Newtonian behavior [72]. For example, the value of N1 has been correlated with die swell and elastic recoil [105]. In this section the normal stress difference behavior of LCPs is reviewed.

The first normal stress difference (N1) has also been measured by many of the investigators referenced above. For the PPTA and PBG systems N1 has been found to have the same concentration dependence as the viscosity; i.e., a maximum was seen when plotted versus concentration [15,53,62]. Baird [62] found that N1 was the same for anisotropic and isotropic solutions with the same viscosity. However, Aoki and coworkers [15] found that N1 was an order of magnitude greater for the anistropic solutions of PPTA than for the isotropic solutions. A possible explanation for this discrepancy is that the two studies covered different ranges of shear rate. Also, Aoki didn't take care to use 100 % H_2SO_4, which could result in the presence of a crystalline phase of the PPTA [79].

For the PBLG system, Kiss and Porter [53,80] reported negative values of N1 for steady state shear flow over well defined shear rate ranges for the anisotropic solutions. Mewis and Moldenaers [54] obtained similar results for PBLG and showed that the data could be normalized to compensate for the effect of temperature. Although no explanation was given for this behavior, Kiss and Porter ruled out the possibility of secondary flow effects. Iizuka [81]

also reported negative values of N1 at low shear rates, which was attributed to surface tension without further explanation.

Negative values of N1 have also been reported in some thermotropic systems. Wissbrun [86], Gotsis [87], and Baird and coworkers [88] have reported transient negative values of N1 for the 60HBA/PET copolyester. Steady negative values of N1 were also reported by Gotsis [89] for the 80HBA/PET copolyester at low shear rates and at temperatures below 328 °C. Guskey and Winter [214] also have reported steady negative values of N1 in HBA/HNA (Vectra A900) at 290 °C and at low shear rates. Explanations for the negative values of N1 include the existence of a suspension of crystalline material in the mesophase, texture development in the mesophase, boundary layer effects, and changes in density due to shear induced crystallization [89]. The 80HBA/PET copolyester is known to contain some HBA crystallinity up to 328 °C [89], which is the upper temperature limit where the steady negative values of N1 were observed. At the same time, it has been shown that the HBA/HNA copolyester can contain residual crystallinity up to about 320 °C [100]. The observation of steady negative values of N1 in thermotropic LCPs might then be related to the presence of residual crystallinity.

It should be noted that negative N1 values have been reported for material systems other than LCPs such as for block copolymers and concentrated suspensions. Transient negative values of N1 have been reported by Duke and Chapoy [82] for lecithin in dodecane, by Hutton for lubgrease [83], and by Hwang [84] for styrene-butadiene-styrene block copolymers. Also, Lem and Han [85] observed steady negative values of N1 for concentrated suspensions of high density polyethylene in a thermoset polyester resin.

There is some theoretical evidence for the existence of negative N1 values. Ogagawa, Cox, and Mason [90] showed that monodisperse suspensions of rigid spheroids at low concentrations in a Newtonian solvent could exhibit negative N1 values during steady shear flow. The theories of Leslie and Ericksen have been shown by Currie [91] to be capable of predicting negative values of N1 in shear flow for the case where $\alpha_3 < 0$ (i.e. the molecules orient in the flow direction) and for a range of orientation conditions at the fluid boundary. Chaffey and Porter [92] have proposed a mechanism by which negative values of N1 can exist and are the

result of the tendency for perfect molecular alignment due to the intermolecular potential, which creates a compressive force during steady flow.

Marrucci and Maffettone [119] have come up with an explanation similar to that of Porter and Chaffey using a 2 dimensional analog of the Doi theory. They have shown that negative values of N1 can be generated in a 2 dimensional system of rodlike molecules when the action of shear flow is to broaden the orientation distribution from the equilibrium value in the fluid at rest. This was shown to occur at low shear rates and when the intermolecular potential is large, resulting in a narrow distribution of orientations in the system at equilibrium. In this case the rotational nature of the shear flow causes tumbling of domains of rods. At higher shear rates viscous forces overcome the elastic forces due to spread in the orientation distribution and the value of N1 then becomes positive. It should be pointed out that rheo-optical results (presented in section 2.2) support the picture of a system of tumbling domains from the standpoint that a low degree of macroscopic molecular orientation is seen in LCP systems during shear flow at low rates [17]. Also, recently Larson [218] has extended the work of Marrucci and Maffettone to a 3 dimensional system and shown that similar results are obtained.

While there is seen to be a theoretical basis for the occurrence of negative values of N1, it should be pointed out that the basis from the Leslie-Ericksen theory as determined by Currie [91] and the basis from the Doi theory as determined by Marrucci and Grizzuti [119] and Larson [218] are conflicting. In the case of the Leslie-Ericksen theory the molecules take on a stable flow induced alignment, while the 2- and 3-dimensional analogs of the Doi theory predict that negative values of N1 occur only when there is large scale domain tumbling. While there is some rheo-optical evidence supporting the explanation due to the Doi theory, this is not conclusive.

In summary, the significance of the observation of negative first normal stress differences in LCPs is not clear and might be associated with residual crystallinity or the presence of a solid phase. At the same time, a theoretical basis exists for the observation of negative

values of N1 in nematic liquid crystals. It is clear that more work needs to be done in order to establish whether or not negative values of N1 are a general feature of LCPs.

2.1.3 Comparison of Steady State and Dynamic Behavior

Dynamic mechanical testing of polymers enables the rheological properties of a polymer to be measured at very small strain levels, minimizing effects due to orientation, disentanglement of molecules, or thixotropic breakdown. At the same time, angular frequencies higher than the corresponding shear rates used in steady shearing tests can often be obtained [56]. On the other hand, steady shearing subjects the material being tested to large total strains. Changes in the shear stress with time during steady shear tests gives information about structural changes in the material. Thus, comparison of steady and dynamic flow behavior gives insight into flow mechanisms and can also be used to test constitutive equations.

For the case of isotropic solutions or melts it has been found empirically that certain dynamic and steady flow quatities are simply related. The *Cox-Merz rule* has been suggested relating the dynamic and steady state shear viscosities [72] at corresponding values of frequency and shear rate, and is stated as:

$$\eta(\dot{\gamma}) = \eta^*(\omega) \quad \text{for } \dot{\gamma} = \omega \text{ and as } \dot{\gamma} \rightarrow 0$$

A relationship between the dynamic storage modulus, G′, and the steady first normal stress difference, N1, has also been observed and follows from constitutive equations for second order fluids [72]. This relationship is given as:

$$N1(\dot{\gamma})/2 = G(\text{ omega }) \%\%\%\%\% \text{ for } \%\% \gamma\alpha\mu\mu\alpha\ \delta o\tau = o\mu\varepsilon\gamma\alpha\ \%\% \wedge \text{as gamma} \rightarrow 0$$

Generally, it has been seen that these relationships hold for isotropic solutions and melts of flexible-chain polymers [72,105]. Likewise, Baird [50] and Wissbrun [67] have confirmed that

isotropic solutions of PPTA/H_2SO_4 and isotropic copolyester melts respectively also obey the Cox-Merz rule at low deformation rates.

The steady and dynamic behavior of several liquid crystalline polymers have been examined by several investigators. Some of these results are tabulated in Table 2.2. It is seen that $\eta(\dot{\gamma})$ and $\eta^*(\omega)$ are generally comparable. Suto [58] found for anisotropic melts of HPC that η and η^* were qualitatively similar, but η^* was greater in magnitude. The discrepancy between η and η^* was explained as being due to the presence of solids, creating a yield stress. Baird [44] reports good agreement between η and η^* at low rates for the HBA/PET copolyester at 275 °C, with $\eta < \eta^*$ at high rates. Yanase and Asada [55] report that η and η^* are nearly equal for an anisotropic solution of PBG, while Moldenaers [94] found that $\eta > \eta^*$ for the same system.

Examples of good agreement and poor agreement between N1 and 2G′, twice the storage modulus, can be found for liquid crystalline materials. Baird [62] found some agreement for anisotropic solutions of PPTA at 60 °C, while Aoki [15] found $N1 > > 2G'$ at the same temperature. However, at 25 °C Aoki did report seeing agreement between N1 and 2G′. For the PBLG system, Kiss and Porter [53] report $N1 > 2G'$ at all shear rates and this was confirmed by Mewis and Moldenaers [54]. In the case of the 60HBA/PET system, Wissbrun [18] found that N1 is greater than 2G′ by a factor of 5 to 100 at all temperatures tested. However Baird [44] and Viola [8] report for the same system that there is good agreement between N1 and 2G′ at 275 °C, which is above the highest crystalline melting point as determined by DSC.

In comparison to experimental results just presented, few theoretical predictions have been given for the dynamic shear flow behavior of LCP systems. Larson and Mead [209] have recently determined the predictions of the Doi theory for oscillatory small-strain shear flow. For the case of a monodomain system, the rheological quantities of interest (G′, G″, and η^*) depend on the director orientation and at certain director orientations there is no stress generated since the director oscillates in phase with the deformation. In this case there can be no general relation between the dynamic and steady flow results.

Table 2. Steady Shear versus Dynamic Properties [18].

				Ref.
PPT (60°C)		$\eta(\dot{\gamma}) \approx \eta^*(\omega)$	$N_1(\dot{\gamma}) \approx 2G'(\omega)$	Baird[65]
		$\eta \approx \eta^*$	$N_1 \gg 2G'$	Aoki et al.[64]
(25°C)		$\eta^* \gg \eta$	$N_1 \approx 2G'$	Aoki et al.[64]
PBLG		$\eta \approx \eta^*$	$N_1 > 2G'$	Kiss and Porter[56,63]
Thermotropic Polyesters	High temp.	$\eta \approx \eta^*$	$N_1 > 2G'$	Wissbrun[67]
	Low temp.	$\eta^* > \eta$	$N_1 > 2G'$	

Larson and Mead also used the same theory to make predictions for a polydomain system, using two different methods of averaging the contributions from the different domains and these are schematically represented in Figure 6. In the first case, a Voigt Average is used, so that all of the domains undergo a similar strain history. The resulting stress is then the sum of the contributions to stress from all possible director orientations. This gives the upper limit of stress response, with G′ proportional to ω^2 and G″ proportional to ω at low frequencies. However, experimental studies on 60HBA/PET by Gotsis and Baird [60,89] have shown that G′ is proportional to ω at low rates. Additionally, the Doi theory predicts that N1 is directly proportional to the shear rate at low rates [45].

The second averaging scheme used by Larson and Mead [209] is a Reuss Average, which specifies that each domain is subjected to the same shear stress. For this average the stress in the system is controlled by the lowest modulus layer. Since certain layers will be at orientations for which there is zero shear stress, this model predicts the shear modulus to be zero at all rates. The Doi theory therefore predicts the failure of the Cox-Merz rule for liquid crystalline systems.

In another recent study, Burghardt [210] used the Leslie-Ericksen theory to determine the dynamic shear flow behavior of a nematic material using the parallel plate geometry. Like Larson and Mead [209], he found that the behavior predicted by the model depended on the director orientation at the surface of the sample. While predictions were only calculated for the condition that the director was perpendicular to the plate surfaces, Burghardt notes that similar results are obtained at other orientations as well. For this case, the value of G′ was proportional to ω^2 and the value of G″ was proportional to ω at low frequencies. Additionally, the dynamic viscosity was found to equal the steady shear viscosity at low rates but deviates from the steady shear viscosity at moderate rates.

While experimental studies show qualitative agreement with the viscosity behavior predictions determined by Burghardt, there are still problems with the predictions of the theory. First, the agreement between the steady and dynamic viscosity determined by Burghardt is due to the absence of elastic effects at low rates, while disagreement at higher rates is the

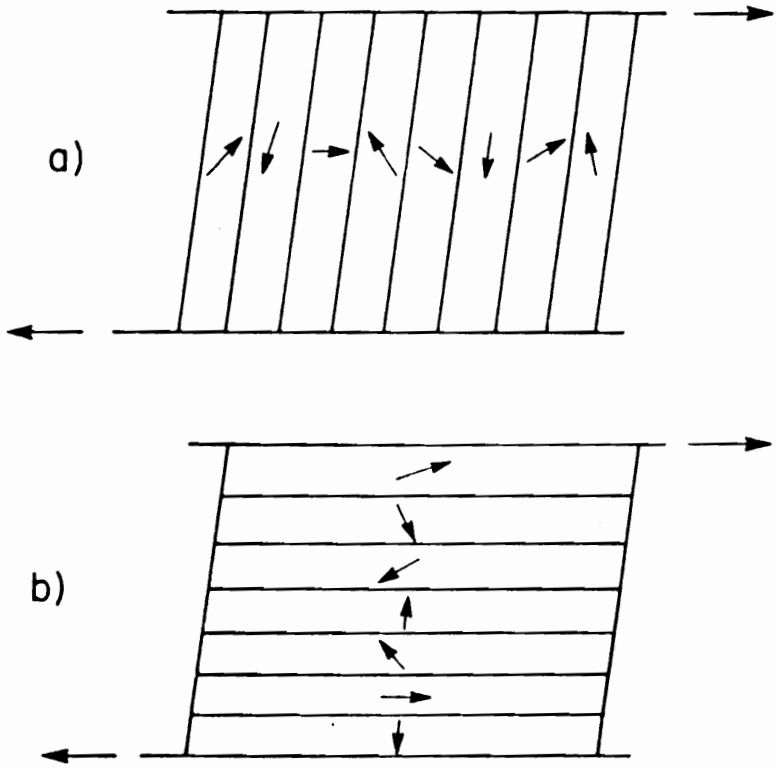

Figure 6. Arrangement of liquid crystalline domains with respect to shearing surfaces for a) Voigt and b) Reuss averaging [209].

result of elastic contributions to stress from the distortion of the director. However, elastic contributions to stress would more likely be significant at low rates, where viscous stress is relatively weak. Second, the dependence of G′ on ω disagrees with that seen experimentally in [60, 89]. Therefore, the Leslie-Ericksen theory can not predict the viscoelastic behavior of LCPs in the present form.

In summary, in liquid crystalline systems there is generally good agreement between η and η^* at low shear rates, with some exceptions seen. At the same time, no general agreement is seen between N1 an 2G′. In addition, negative values of N1 have been reported. Although crystallinity has been named as a possible cause of negative N1 values in thermotropic LCPs, no reasonable explanation has been given for the observations of Kiss on PBLG [53,80]. Therefore, the empirical relationships which relate dynamic and steady state shear flow properties of isotropic melts do not hold for LCP systems in general. Additionally, no analogous theoretical relationships have been derived which successfully describe the relationship between the steady and dynamic shear flow behavior of LCPs. It has been suggested that no such relationships are possible due to differences in the polymer structures present during the two types of flow [210].

2.1.4 History Dependence

A number of investigators have observed both shear and thermal history effects in liquid crystalline polymers. In the processing of polymers, the material often experiences quite complex thermal and deformation histories, which will be reflected in the morphology and properties of the solid material. Shear and thermal history effects are therefore reviewed here in some detail.

2.1.4.1 Shear History Effects

The shear history has been shown to influence the rheological behavior of both thermotropic and lyotropic liquid crystalline polymers by a number of investigators [44, 56, 67, 70, 93-96]. Many different phenomena have been observed including a decrease in viscosity upon prior shearing at a higher rate, hysteresis during frequency sweeps in dynamic tests, and secondary stress overshoot upon startup of flow. In this section these phenomena are examined and explanations for their occurrence are given when possible.

Cogswell [93] used a capillary rheometer, modified with a rotating cylindrical bob inside the barrel but before the die, to quantitatively measure the effect of preshear on the viscosity of a 20 weight % solution of PPTA in sulfuric acid at 85 °C and a thermotropic copolyester of chlorohydroquinone (50%), terephthalic acid (25%), and ethylene-4,4′-dioxybenzoic acid (25%). When the PPTA solution was left to stand for 16 hours, the solution became paste-like with a yield stress of the order 10^5 dyne/cm^2. When this paste-like solution was presheared at 200s^{-1}, it reformed a low viscosity state. For the thermotropic copolyester, a paste-like inextensible extrudate was obtained from extrusion below the melting temperature and with no preshearing. Upon preshearing the extrudate was observed to be uniform and highly oriented. The possibility of this being caused by viscous heating was investigated and it was found that without preshear the polymer had to be heated 20 °C higher for the same ease of extrusion and orientation to be obtained. Even so, the extrudate obtained without preshear was thought to be inhomogenous because of extrudate "wander". The paste-like textures described in both samples above was attributed to the formation of some crystallinity, which was then broken up by the shearing action.

In another study Wissbrun and Griffin [67] examined the rheological behavior of a thermotropic polyester which had a solid-nematic transition at 185 °C and a nematic-isotropic transition at 212 °C [97]. In testing of the nematic state at 210 °C they found that the viscosity $\eta^*(\omega)$ and storage modulus G′ were reduced by shearing of the sample prior to dynamic tests as shown in Figure 7. The viscosity is seen to be reduced more as the preshear rate in-

creases. In the same study, there was "hysteresis" in measurement of the complex viscosity, i.e. the measured values varied depending on whether the sweep direction was to a higher or lower frequency. In an earlier study, Wissbrun [78] reported the same type of hysteresis for a copolyester of 15 mole % bis (4-carboxyphenoxy)ethane, 15 % terephthalic acid, 40 % p-hydroxybenzoic acid, and 30 % methyl hydroquinone (BCPE/TA/HBA/MHQ). Neither the hysteresis nor the shear history effects were observed when the material was in the isotropic state. In a similar study, Tuttle [70] also reports a decrease in G^* due to preshearing. Wissbrun and Griffin [67] explain this behavior as being due to the change in the polydomain texture of the melt with shear and the relaxation of this texture. The DSC data of Griffin [97] indicate that no residual crystallinity is present in the nematic melt at the test temperature. At the same time, the presence of a yield stress has been previously associated with residual crystallinity in LCPs and it is known that DSC measurements are insensitive to small amounts of crystallinity [98].

In the case of lyotropic LCPs, Moldenaers and Mewis [94] observed that η^* decreases with time for solutions of PBLG after cessation of steady shearing. The time it took for η^* to reach a steady value was found to be 1 to 2 orders of magnitude greater than the time for stress relaxation upon cessation of steady flow and was independent of temperature, strain amplitude, or frequency. Moldenaers and Mewis concluded that this decrease in η^* with time is due to structural changes in the material and is general for liquid crystalline polymers, which is shown to be in error by the results given above for the thermotropic polymers. Furthermore, Wissbrun [67] notes that the reformation of the equilibrium polydomain structure should result in an increase in viscosity. However, no other explanation has been found for this behavior.

Studies of the transient behavior of the shear viscosity have also been made in order to follow the development of orientation and structure in liquid crystalline polymers. The most extensive study has been conducted by Viola and Baird [8,95] on the 60/40 and 80/20 HBA/PET copolyesters in stress growth and relaxation experiments. In the case of the 60HBA/PET copolyester tests were conducted at temperatures of 250, 260, and 275 °C. In the stress growth

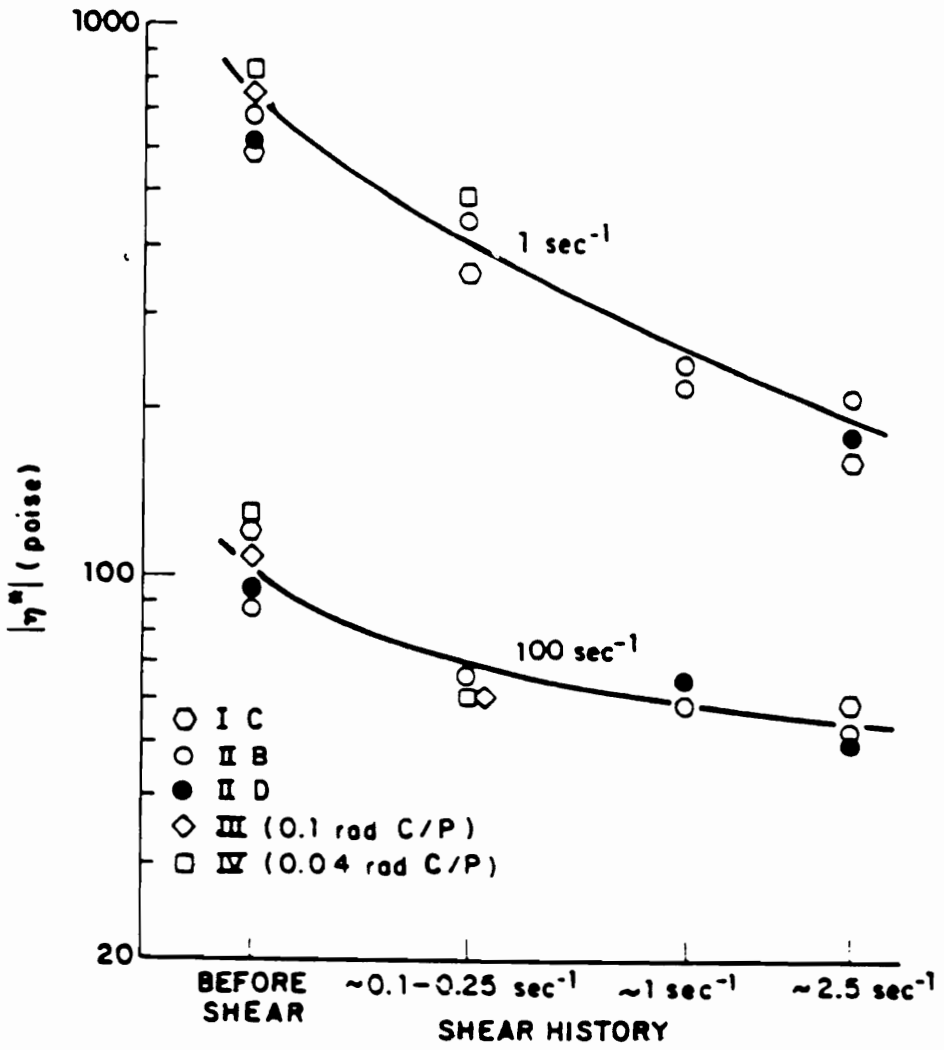

Figure 7. Effect of preshear on the complex viscosity of a thermotropic LCP [67] at 1 and 100 s^{-1} and at 210 °C: Different symbols represent runs on different samples. Also, (I and II) were run with PP geometry.

experiments overshoot was observed at all shear rates tested. Increasing the rate was found to increase the magnitude of the overshoot while peaks were found to occur at nearly the same total strain, regardless of rate. At temperatures above 250 °C, two overshoot peaks were observed, one at about 1-2 strain units and one at 50-60 strain units. Wissbrun [86] reported similar results for the (BCPE/TA/HBA/MHQ) copolyester, but the second peak was observed at strains of about 80 units. Baird [44] attributed the first peak as being due to the development of orientation of the domain structure, while the second peak was attributed to the two phase nature of this system. Relaxation of the structure was followed using interrupted stress growth tests and the results are shown in Figure 8. The first peak is not recovered even after 3 minutes, while the second peak is recovered after only about 6 seconds. Also, the first peak was absent upon reversal of the shear direction. Stress relaxation measurements upon cessation of steady shear showed the stress to relax to zero in just a few seconds. Therefore, the time scales for the relaxation of orientation and texture were shown to be much greater than those for stress. For the 80HBA/PET copolyester, the same transient behavior was seen, only at different temperatures.

Stress growth experiments have also been reported by Elliott [56] for HPC melts and Mewis and Moldenaers [96] for PBLG solutions. In his studies on HPC, Elliott reports a single overshoot peak for stress growth occurring at strains of 1-2 units for a range of shear rates and temperatures. The peak was attributed as being due to a thixotropic breakdown in structure, the structure being due to hydrogen bonding between molecules or the result of junction points between crystallites. However, it was not known at that time that HPC formed anisotropic melts and the reason could be due to a breakdown of the cholesteric structure of the HPC [56]. For PBLG solutions, Mewis and Moldenaers [96] found 3 overshoot peaks. Although no explanation was given for these peaks, it was noted that a theoretical basis exists for multiple peaks in systems which contain anisotropic particles if convective flow effects dominate Brownian motion.

Cogswell [93] studied the effect of preshear on the stress growth of a thermotropic copolyester. The melt was sheared at a rate of 0.04 s^{-1} until steady state was achieved and

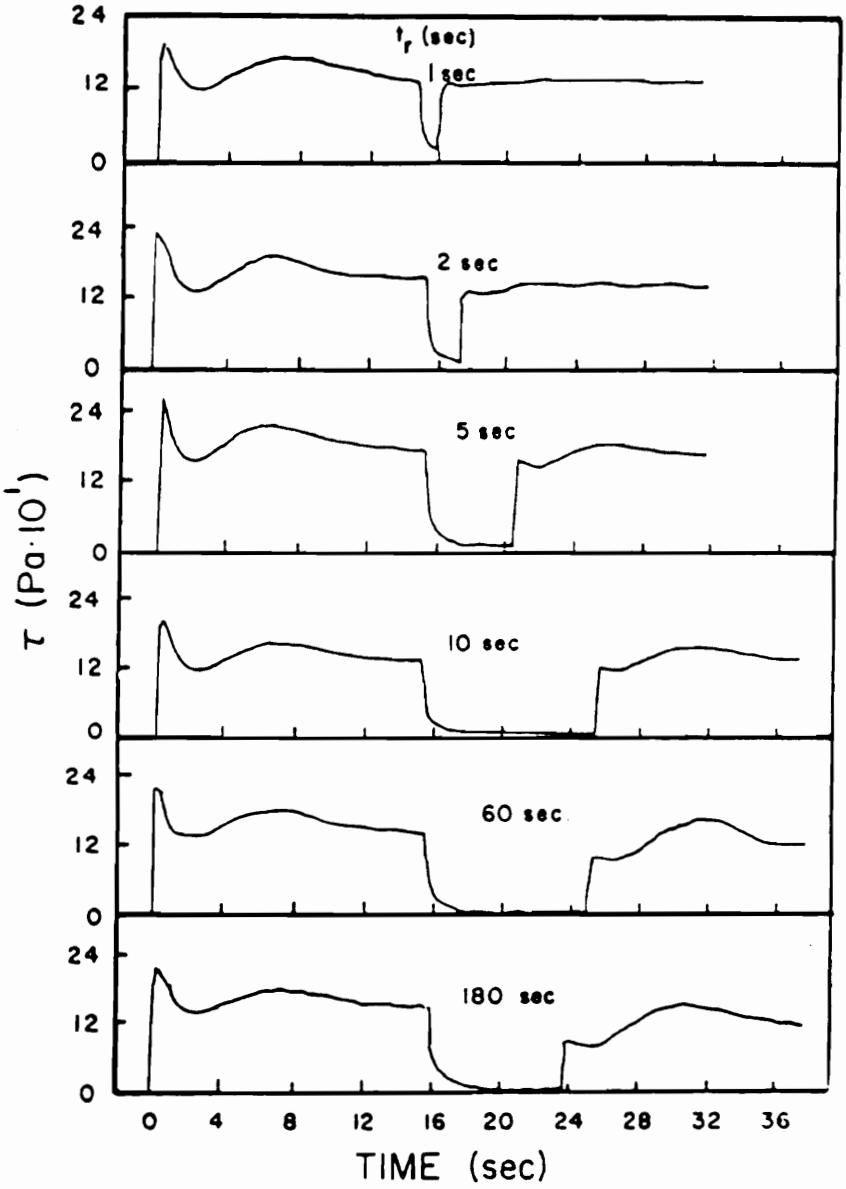

Figure 8. The effect of varying the relaxation time t_r for interrupted stress growth of 60HBA/PET at 275 °C and $\dot{\gamma} = 10\ s^{-1}$ [8].

the shearing was stopped. As soon as the stress fell below 200 dyne/cm^2 the shearing was started again at the same rate. Almost immediately the stress rose to its equilibrium value. However, when the sample was presheared at a rate of 1.14 s^{-1} and subjected to the same routine, the stress exhibited a large overshoot before coming to its equilibrium value. Cogswell attributed this behavior to the reorganization of texture. He proposed that a domain structure exists in the quiescent state and is broken up into smaller domains upon shearing, which become smaller as the shear rate increases. Also, at high rates, the domains are completely broken up. Cogswell explained that relaxation to an equilibrium domain structure was fast enough after shearing at the higher rate that this structure had to be broken up again upon startup, causing an overshoot peak. The transient shear tests of Baird [44] and Viola and Baird [95] confirm that relaxation is faster upon cessation of shear as the shear rate increases.

In summary, it is seen that unusual transient phenomema are observed for the liquid crystalline state in polymers which are not seen for isotropic materials. In general, preshearing is seen to reduce the viscosity of the material, the reduction increasing with rate of preshearing. In transient tests, multiple overshoot peaks have been observed, while in isotropic flexible-chain melts only one peak is observed. The size of these overshoot peaks depends on the shear history of the material. This transient behavior is usually explained in terms of a change in the orientation and structure of the polydomain texture of liquid crystalline polymers, though some of this complex behavior is certainly due to the presence of a small amount of crystallinity in the material. The effect of flow on the polydomain texture of LCPs is further reviewed in section 2.2.2.

2.1.4.2 Thermal History

In this section the effect of thermal history on the rheological behavior of liquid crystalline polymers is examined, specifically in regard to thermotropic LCPs. Wissbrun [86] studied the effect of preheating several thermotropic copolyesters, including the 60HBA/PET

copolyester, to temperatures higher than the measurement temperature prior to dynamic testing. Results for the 60HBA/PET copolyester are shown in Figure 9 for runs made at 210 °C, but preheated to 240 and 300 °C prior to testing. It can be seen that the viscosity is significantly lower for the cases where the material was preheated. Intrinsic viscosity measurements of the sample before and after rheological testing ruled out degradation as an explanation for this behavior. Both DSC and wide-angle x-ray scattering (WAXS) studies [86] indicated a small degree of HBA crystallinity in the copolyester for the case of no preheating, while a sample preheated and quenched showed no more than trace amounts of crystallinity. Wissbrun concluded that the presence of crystallinity in the sample could have accounted for the observed behavior. Cogswell [93] likewise observed that preheating of an LCP could change the behavior of the material from that of a paste-like solid to that of a viscoelastic liquid and suggested that a "supercooling" phenomenon was occurring.

In order to determine whether thermotropic copolyesters actually exhibit true supercooling behavior, Done [20] and Done and Baird [29] examined the effect of the thermal history on the 60HBA/PET and 80HBA/PET copolyesters as well as a copolyester consisting of HBA and 2-hydroxy-6-naphthoic acid (HNA). Dynamic properties were measured for preheating experiments similar to those of Wissbrun [86], temperature sweeps, and isothermal transient measurements following preheating. As in Wissbrun's preheating experiments, the testing temperatures were below the DSC measured crystalline melting points while samples were always preheated above the melting temperatures. Done found that the dynamic viscosity behavior of the 60 % HBA/PET copolyester measured at 240 °C after preheating at 275 °C for 3 minutes more closely resembled that measured isothermally at 275 °C than that measured at 240 °C with no preheating. Similar effects were seen for the 80 % HBA/PET copolyester, but to a lesser degree, while the HBA/HNA copolyester showed almost no effects due to preheating. In the transient experiments, the temperatures of the polymers were raised well above their respective DSC melting transitions and then the polymers were cooled at a rate on the order of 15 to 20 °C/minute while measurments were made of their dynamic moduli. These results are shown in Figure 10. The values of G′ do not rise from their high temperature

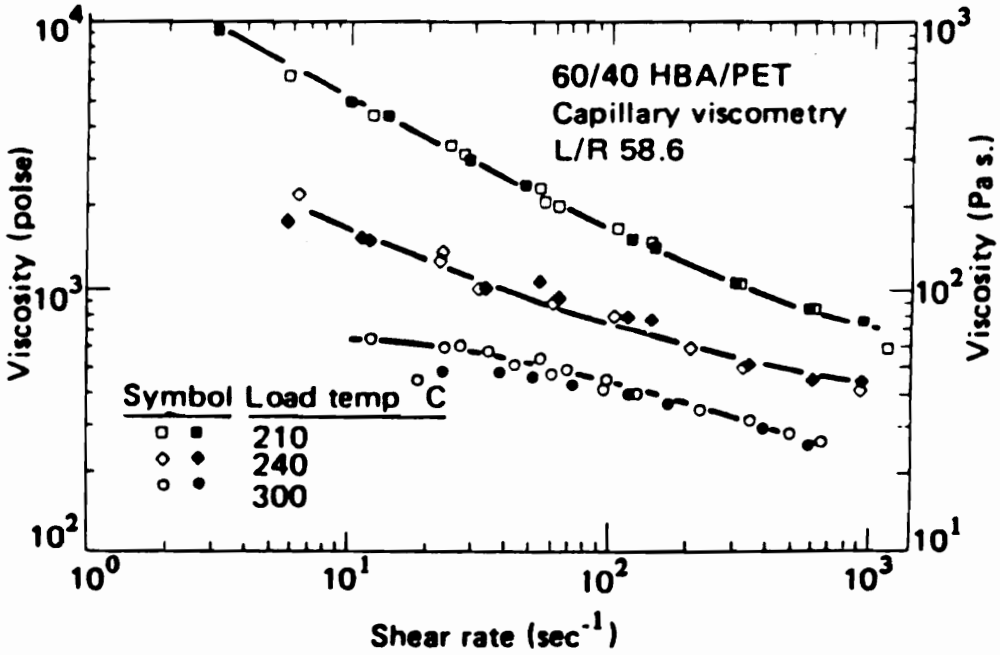

Figure 9. Effect of Preheating on the Viscosity of 60HBA/PET measured at 210 °C [86]. Double symbols indicate repeat runs.

values until all three copolyesters are well below their DSC melting temperatures with the largest degreee of supercooling observed in the 60HBA/PET copolyester. Finally, G′ was measured as a function of time for the copolyesters which had been preheated, then brought down to the testing temperature. The values of G′ for all three copolyesters rose to their equilibrium values within a time period of several minutes. At the same time, it is interesting to note that for the HBA/HNA copolyester, there was a finite time delay before G′ began to rise. Done and Baird [29] concluded that a supercooling of the nematic phase does indeed take place, at least for a finite time sufficient to deform the material. Additionally, it is the view of this author that the difference in the degree of supercooling observed for the different polymers is related to their potential degree of crystallinity, which in turn is expected to be related to their composition and monomer sequence distribution.

Other researchers have noted transient rheological behavior due to the formation of crystallinity in thermotropic copolyesters and the inherent thermal history effects associated with it. Elliott [56] studied the behavior of HPC melts at 190 °C and observed an increase in the value of G′ with time. Also, the value of tanδ was substantially lower after annealing at four hours as compared to annealing for one hour. Gochanour and Weinberg [99] examined the dynamic behavior of a copolymer of chlorohyrdroquinone, 4,4′-dihydroxy-diphenyl, terephthalic acid, and resorcinol with the mole ratio 30/5/50/15. Flow curves were measured for this polymer at 335 °C, 10 °C above the DSC melting point, after annealing at the test temperature for various times. The storage modulus was observed to increase with time and its frequency dependence was observed to show more solid-like behavior with increasing annealing time. Both further polymerization and degradation were ruled out as causes of this behavior as evidenced by intrinsic viscosity studies and thermogravimetric analysis (TGA). At the same time DSC studies of annealed samples showed the formation of high melting crystals after annealing at 335 °C. In another study, Lin and Winter [100] observed a similar increase in the dynamic modulus with time for a copolyester of HBA (73%) and HNA (27%) (Celanese Vectra A900), as shown in Figure 11. Lin and Winter showed by WAXS and DSC results that this behavior was due to the formation of HBA crystallinity. In addition, it was

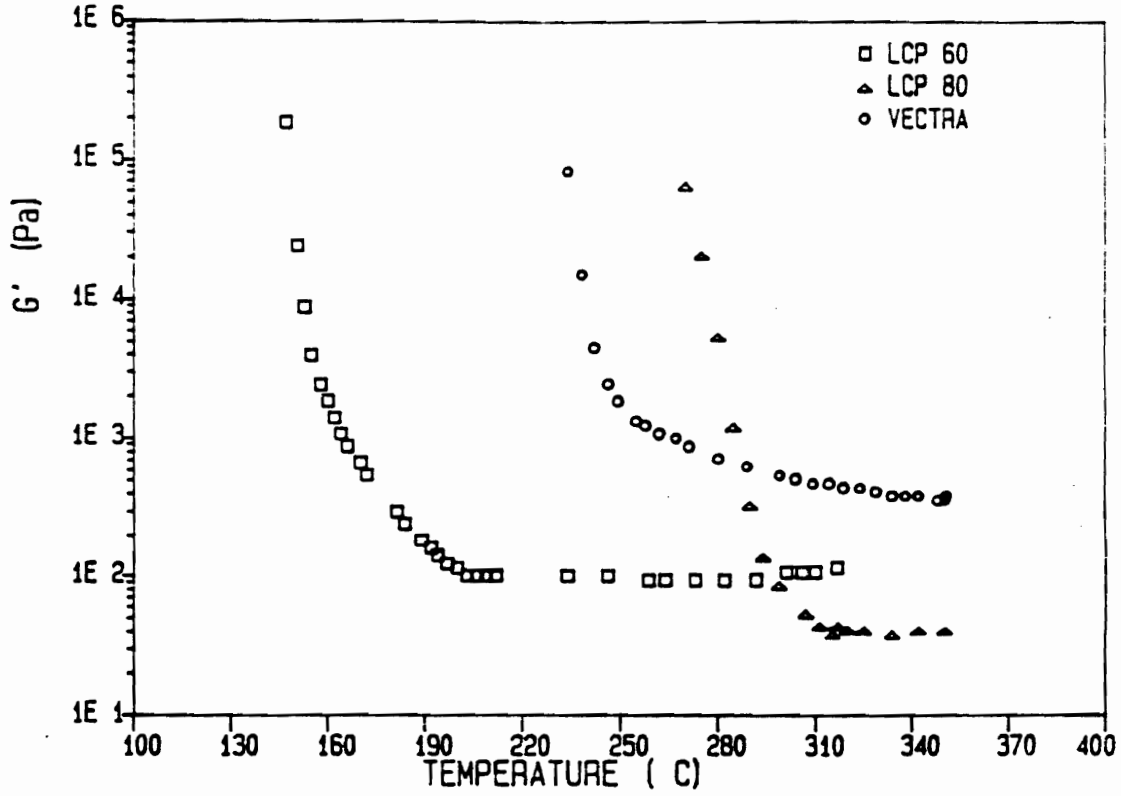

Figure 10. G′ versus temperature for three thermotropic copolyesters upon cooling from elevated temperatures [29].

shown that the increase in the value of G′ with time could be reversed by raising the temperature above the melting temperature of the high melting HBA crystals. Kalika [106] observed the same behavior for the 80HBA/PET copolyester and also showed that this was due to the formation of HBA crystallites. Wissbrun [67] similarly noted that bringing a thermotropic LCP above its isotropization temperature erased all previous shear history effects.

In Summary, thermal history has a great effect on the rheological behavior of thermotropic liquid crystalline polymers. By preheating the polymer above its melting transition, LCPs can then be deformed or processed below their melting or solidification temperatures due to a "supercooling" phenomenon. At the same time, the presence of residual crystallinity in the polymer can dramatically change its rheological behavior, making it time and deformation history dependent as well. Finally, preheating the polymer above the highest melting endotherm or to the isotropic state will erase the effects of previous shear or thermal histories of thermotropic LCPs.

2.1.5 Extensional Flow Behavior of LCPs

In view of the tremendous number of studies on the rheological behavior of LCPs in shear flow, it would appear somewhat surprising that there is almost a complete lack of results for shear-free or extensional flows. Prilutski [45] and Metzner and Prilutski [42] have reported on the uniaxial extensional flow behavior of a lyotropic solution consisting of 40 weight % hydroxypropylcellulose in acetic acid. Measurements were made using a gravity spinning type device and values of stress are plotted in Figure 12 versus the elongation rate at the same point in the spinline. The data covers elongation rates in the range of $10^{-2}\ s^{-1}$ to $10^{1}\ s^{-1}$. Within this range it is observed that the extensional viscosity is independent of elongation rate but that the Trouton ratio (the ratio of elongational to shear viscosity) was equal to 9. In contrast, a Trouton ratio of 3 is typically observed at low extension rates for flexible-chain isotropic polymer melts.

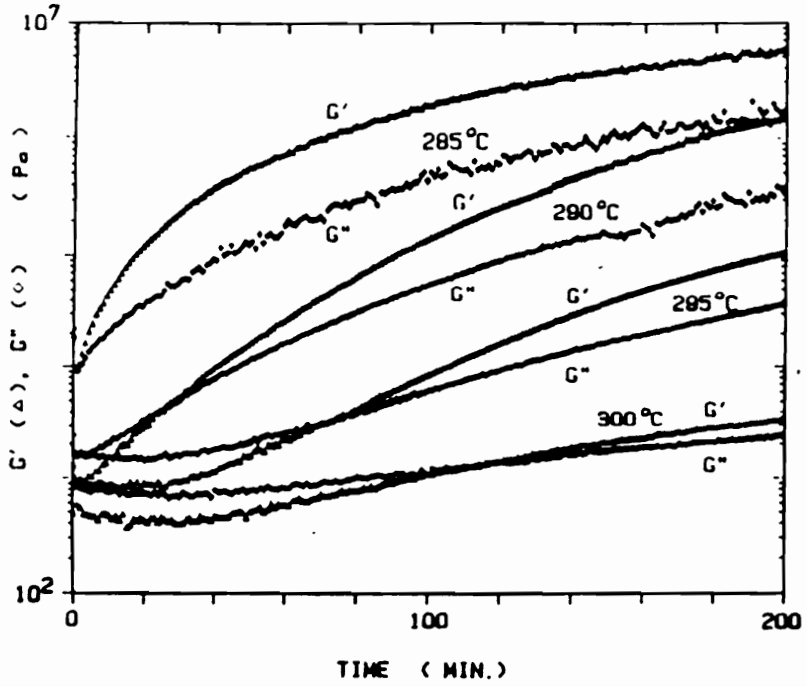

Figure 11. Time Dependence of G′ at Different Temperatures for Vectra A900 (HBA/HNA) [100].

While Prilutski reports excellent reproducibility in his results, it is the view of this author that there is considerable doubt as to the quantitative value of the results in terms of LCP behavior based on the test method used. In a gravity spinning device, the polymer comes out of a spinnerette after undergoing shear flow. Next, a fluid element experiences various deformation rates as it travels along the spinline. Thus, the material undergoes a complex deformation history with pre-shearing and is never truly at steady state during measurement. Since the viscosity values are calculated from the ratio of the stress to the deformation rate at specific points along the spun fiber, no steady state values are possible, even though they are reported that way. Without a knowledge of the strain dependence of the elongational stress at constant elongation rate, one cannot be sure of the quantitative significance of their results. Finally, transient elongational flow studies on flexible-chain polymer systems have shown that results obtained from the gravity spinning method generally do not agree quantitatively with tests involving isothermal and homogeneous flows [207]. In view of the relatively larger effects due to flow history in LCPs versus flexible-chain polymer melts, this discrepancy would be expected to be larger.

The only other elongational viscosity data known for LCPs was determined by Chen and coworkers [114] for a HPC melt at 180 °C and is shown in Figure 13 (lower curves). The device used here was a fixed end rotary clamp type rheometer which gives a fairly homogeneous flow and constant extension rate. The extensional viscosity of the HPC melt is seen to rise up monotonically to a constant value, level off, then decrease. The decrease at the end is presumably due to necking or fracture. Importantly, it is seen that the transient extensional viscosity initially is independent of rate, but at larger times shows a strain rate thinning effect, not previously observed in unfilled polymer systems to the knowledge of this author.

While the results of Chen and coworkers [114] are more acceptable than those of Prilutski from an experimental viewpoint, examination of the results show that the data only covers from 0.5 to 1.0 strain units and the maxima in the curves for the different rates occur at approximately 0.2 strain units. The polymer is not expected to have reached a steady state flow at such low strain values based on the results known for isotropic polymer systems (for

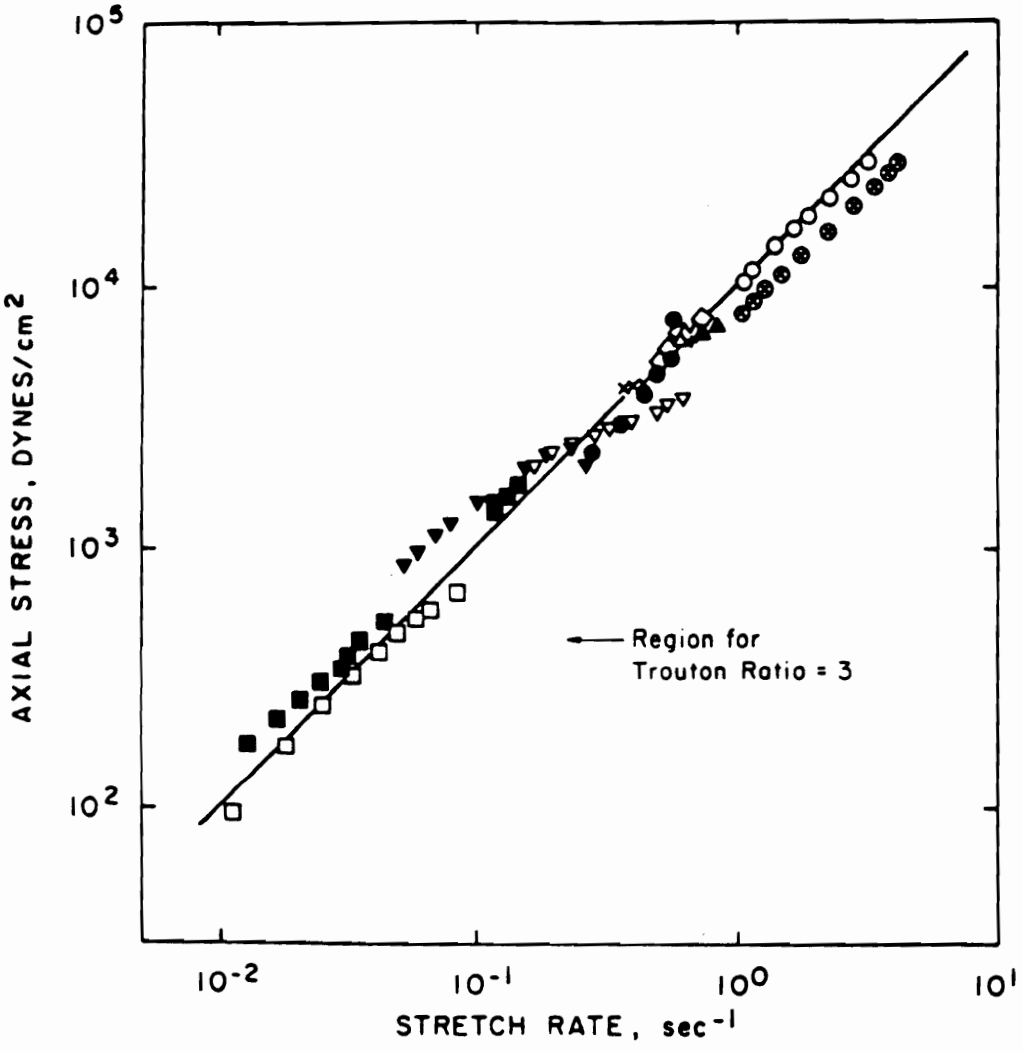

Figure 12. Elongational stress of a 40% HPC/acetic acid solution [42].

example [40,41,72,105,207,215]). Therefore, no determination of the Trouton ratio was possible for this system. Also, the observance of strain rate thinning extensional viscosity could be explained as due to a yield stress, known to be present in HPC at 180 °C [57-59].

In view of the similarity between the microstructure of LCPs and suspensions of fibers, it is worthwhile to establish whether there are similarities in their behavior. It should be noted that the observance of a Trouton ratio greater than 3 by Prilutski [45] is not unprecedented, but has been previously reported for suspensions of fibers in Newtonian solvents [78,101]. In the case of suspensions, the theory of Batchelor [102] for semi-concentrated solutions of suspended fibers agrees well with experimental results for these systems. The theory assumes that deformation in the system occurs due to shear flow of the solvent between fibers, thus predicting a rate independent elongational viscosity for a Newtonian solvent. However, when the theory is applied to LCP systems such as that investigated by Prilutski, the Trouton ratio is predicted to be from 2 to 3 orders of magnitude too large. Therefore, it appears that the extensional behavior of LCPs can not be accounted for by means of analogy to the behavior determined for fiber suspensions.

The only other known rheological results for extensional flows of LCPs is the work of Done [20], who measured the equibiaxial extensional flow properties of 60HBA/PET, 80HBA/PET, and HBA/HNA copolyesters. Representative data are shown in Figure 14. The results indicate that for equibiaxial extensional flow the biaxial extensional viscosity, η_B^+, is not equal to $6\eta^+$ (as expected for Newtonian or linearly viscoelastic fluids), decreases with increasing extension rate, and increases with increasing strain. Although the reproducibility of these results was reported to be good, they must be regarded with caution. The reason for this is that at the respective testing temperatures of 250, 300, and 330 °C these polymers are still thought to have some crystallinity [20]. Also, loss of lubricant between the sample and the plates in the instrument limits the range of strain for which the data is accurate, and this range is only approximately known.

In summary, very little data pertaining to the extensional flow behavior of liquid crystalline polymers has been reported. The steady state elongational viscosity of lyotropic HPC

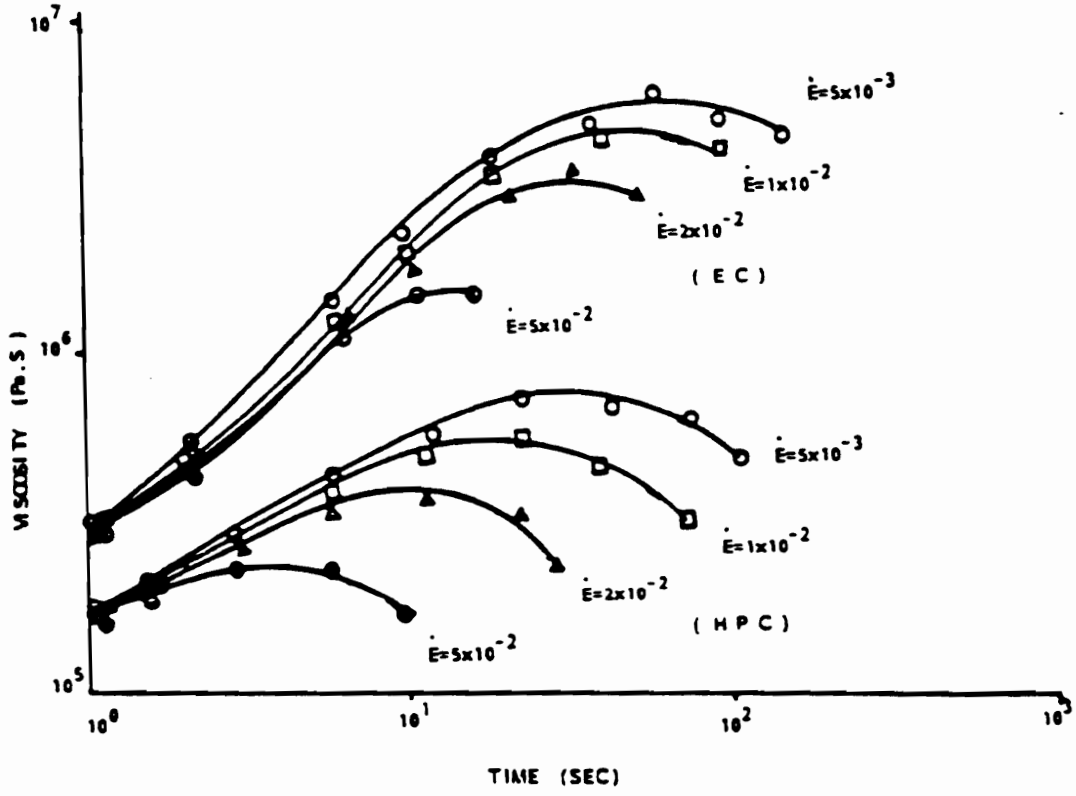

Figure 13. Transient elongational viscosity of HPC at 180 °C [114].

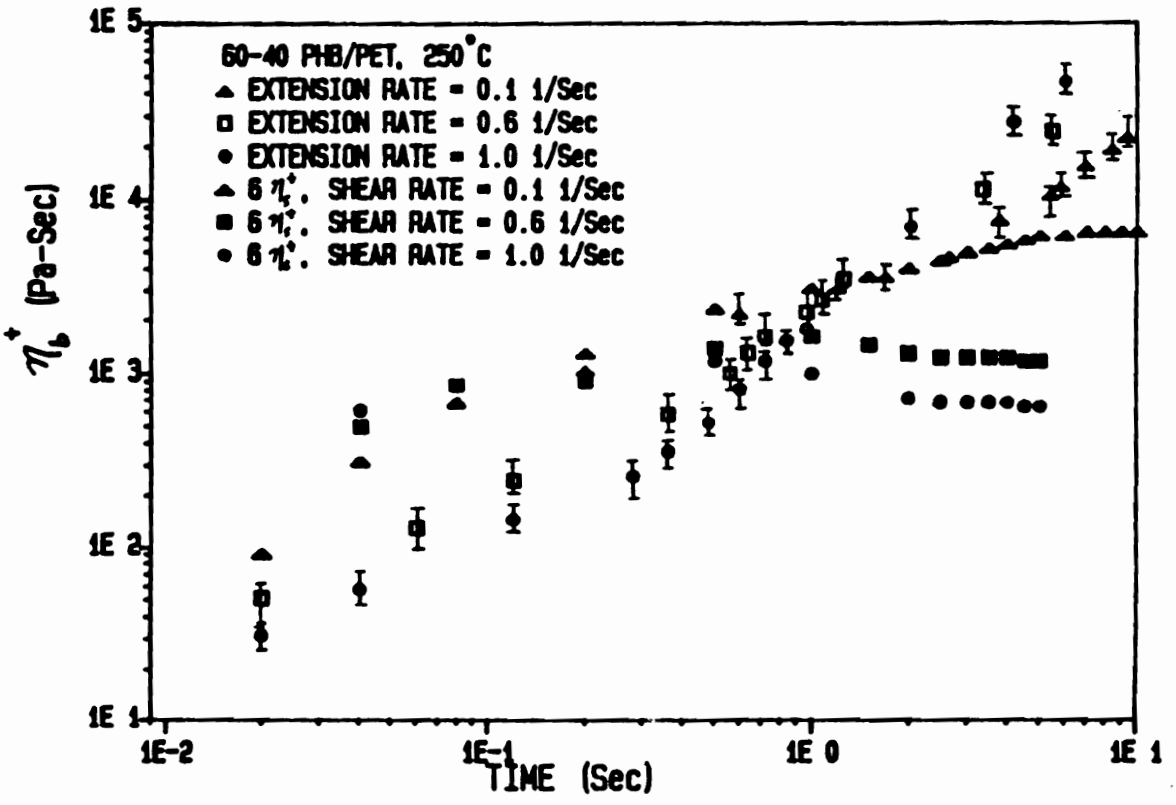

Figure 14. Equibiaxial extensional viscosity of the 60HBA/PET copolyester at 250°C. [20].

solutions showed a rate independent extensional viscosity and a Trouton ratio of 9, but it is highly questionable whether these results represent steady flow behavior. In contrast, the transient elongational viscosity behavior of liquid crystalline HPC melts showed rate thinning behavior, but this could be explained by a yield stress in the material at the temperature used. The equibiaxial extensional viscosity of thermotropic copolyesters has been reported, but there is some uncertainty as to whether these results represent the behavior of the liquid crystalline state or are controlled by the presence of crystallinity. Clearly, there is a definite need for further work to reliably determine the extensional behavior of LCPs.

2.2 Structure and Morphology of LCPs

In Chapter One, the structure of liquid crystalline polymers was introduced and it was shown that in their equilibrium state there is a high degree of molecular orientation on a local scale, but macroscopically they are isotropic. At the same time it is possible to process LCPs into articles with a high global degree of molecular orientation and an oriented or fibrillar structure, resulting in exceptional physical properties. This section is therefore devoted to a review of the development of orientation and structure in LCPs. Specifically, focus is placed on how processing parameters affect the LCP morphology. In the first part (2.2.1), the fundamental concepts for characterizing the orientation and polydomain texture of LCPs are presented. Next, the development of molecular orientation and structure during processing are reviewed with emphasis being placed on the effect of deformation type and thermal history. Finally, the method of small angle light scattering is reviewed for use in the characterization of structure in LCP's during flow.

2.2.1 Orientation and Structure in LCPs

2.2.1.1 Order Parameter Tensor

In the Chapter 1 the order present in the nematic mesophase was briefly described and it was shown that the molecules are preferentially oriented about a certain direction, defined as the director, **n**. However, the molecules are not perfectly aligned along **n** but take on a distribution of orientations and a parameter is needed which can describe this distribution of orientations (assuming the molecules are rigid rods and neglecting chain flexibility). The order parameter tensor , S_{ij}, is such a parameter and is defined as [4]:

$$S_{ij} = \int f(u_i,t)(u_i u_j - \frac{1}{3}\delta_{ij})d\mathbf{u} \qquad (2.2.1)$$

where **u** is a unit vector which describes the orientation of a rigid rod molecule and f(**u**,t) is the orientation distribution function. The integral is over the surface of a sphere defined by $|\mathbf{u}| = 1$.

The order parameter tensor has a few properties worth noting. It is deviatoric, and therefore its trace must be equal to zero. Its eigenvalues or principal values (S_1,S_2,S_3), which define the principal axes of orientation, also must add to zero. If all three are equal, then $\mathbf{S} = 0$ and the material is isotropic. Finally, if two of the eigenvalues are equal then the system is axially symmetric and S_{ij} can be represented by [39]

$$S_{ij} = S(n_i n_j - \frac{1}{3}\delta_{ij}) \qquad (2.2.2)$$

where S is the scalar order parameter and is equivalent to the Hermans orientation function with **n** as the reference direction. Therefore, the range of S is $-1/2 < S < 1$, where the values

of -1/2, 0, and 1 represent perfect biaxial orientation, random orientation, and perfect uniaxial orientation, respectively.

The order parameter was described here because of its importance in the molecular theories for and experimental characterization of rodlike polymers and liquid crystals. As will be seen in section 2.3, S_{ij} is an important quantity in Doi's theory for the molecular dynamics of rod-like polymers and S is useful for evaluating thermodynamic theories like that of Flory [10,65] for mesophase formation. Techniques which have been used to measure the scalar order parameter of nematic polymers in the liquid crystalline state include analysis of refractive index data, magnetic susceptibility experiments, NMR lineshape analysis, electron spin resonance spectra simulation, wide angle x-ray scattering (WAXS), infrared (IR) dichroism, and ultraviolet (UV) dichroism [103].

While a review of these techniques is not possible here, it is instructive to consider some general results. A more detailed review has been given by Noel [103]. Typical values of S for LCPs fall within the range of 0.4-0.9 and depend on many factors [103]. Introducing chain flexibility into the polymer by adding flexible spacing groups tends to decrease the values of S, and a large odd-even effect is seen as a function of the spacer length (i.e. number of carbon atoms in the chain backbone of the spacer unit). The value of S generally increases with molecular weight up to an assymptotic value. Thus polymeric LCs have higher order parameters than their low molecular weight analogs. The order parameter decreases as a LCP approaches its nematic-isotropic transition and generally falls to within the range of 0.4-0.7 as predicted by Flory [65]. High values of S, in the range of 0.8-0.9, have been observed in thermotropic systems which were aligned by high external magnetic fields. Finally, the order parameter is affected by deformation of the system. A discussion of the effect of flow on the orientation in LCPs is given in section 2.2.2.

2.2.1.2 Polydomain Texture of Liquid Crystalline Polymers

The use of the order parameter, S, to describe the molecular orientation in nematic liquid crystals was discussed in the last section and it was implied there that the material is uniform throughout. However, this is not the case for LCPs, which typically display what is referred to as a polydomain structure. In this section, a description of the polydomain structure of nematic liquid crystalline polymers is given.

The defect structure of low molecular weight liquid crystals has been described by de Gennes [4] and similar behavior has been seen in a number of polymeric systems. In the case of nematic liquid crystals, the polydomain structure is characterized by a spatial variation in the director which results from a combination of twist, bend, and splay defects as well as discontinuities in the director field (disclinations). When viewed under crossed polarizers in the optical microscope, the polydomain texture of nematic liquid crystals has been described as being "threadlike", and is often referred to as a Schlieren texture. The Schlieren texture of a sample of the 60HBA/PET copolyester, formed after an isotropic film was quickly brought to 240 ^{0}C and annealed for a few minutes [104], is shown in Figure 15.

As can be seen, the texture is made up of dark brushes which meet at distinct points, called disclinations. Disclinations in nematics are either in the form of points or lines, depending on sample thickness and surface effects, and represent discontinuities in the director field. In the case of point disclinations, they are characterized by the parameter s, the strength of the disclination [104]. The value of s is equal to one fourth of the number of dark brushes contacting the disclination and the sign is based on the direction the individual brushes rotate as the crossed polarizers are rotated relative to the sample. When the brushes rotate in the same direction as the polarizers, the sign is positive. Examples of disclination types are given in Figure 16.

A high degree of molecular orientation exists between the disclinations and this is usually what is referred to as a domain. Since the size of these regions is on the order of that of visible light, nematic liquid crystals are tremendous scatterers. De Gennes [4] has shown

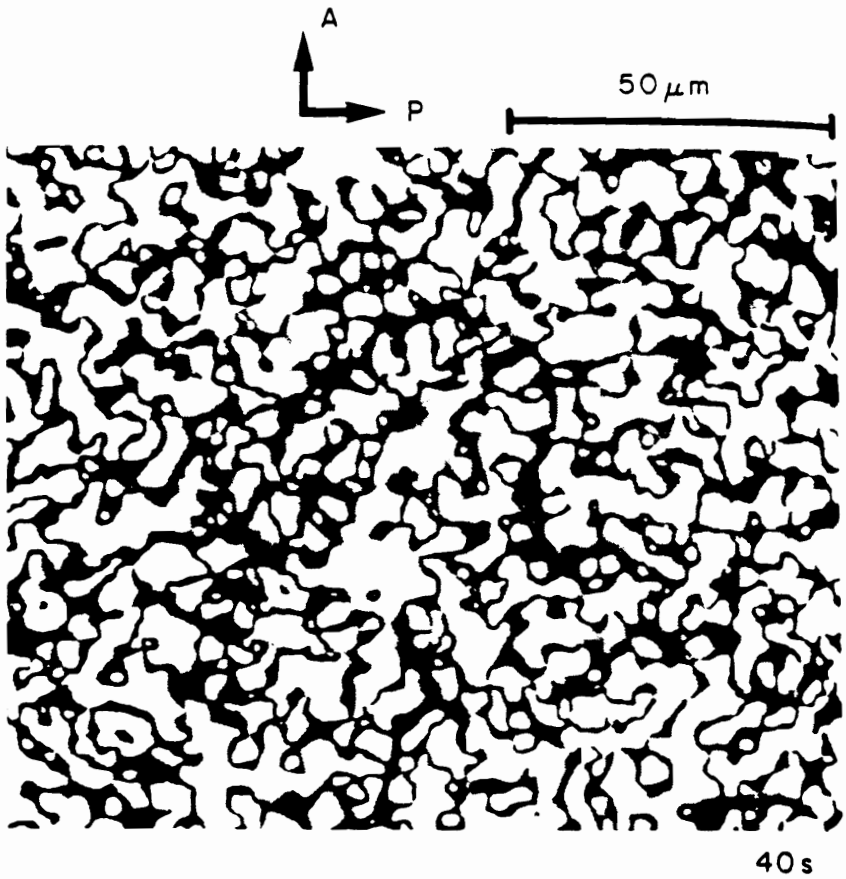

Figure 15. Schlieren texture of 60HBA/PET copolyester at 240 °C [104].

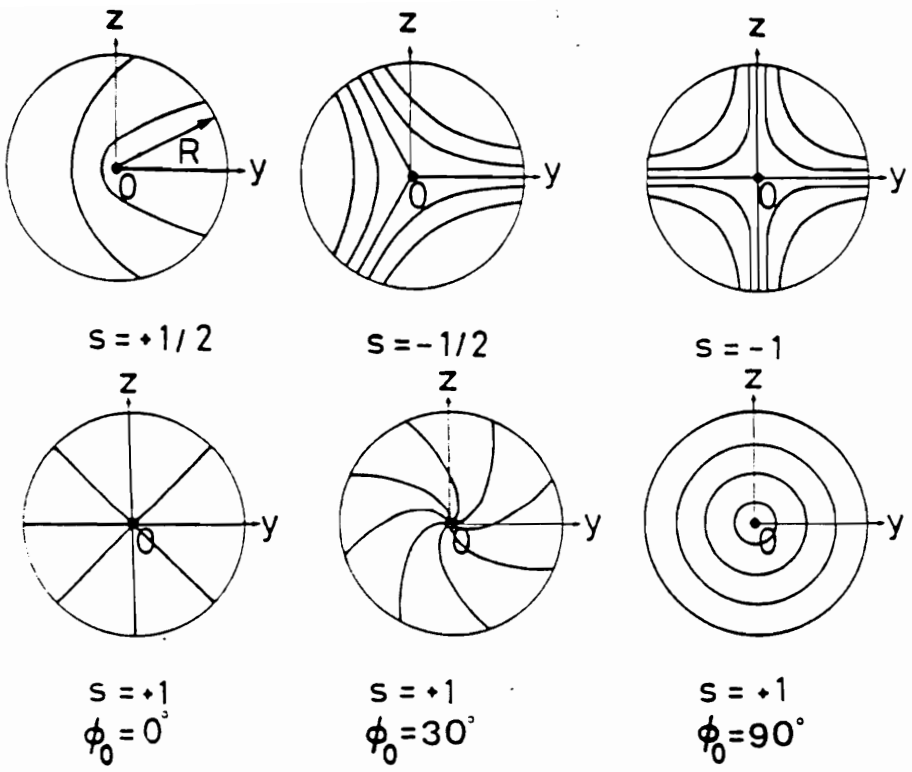

Figure 16. Definition of disclinitions in nematic LCs by their strength s [149]. The lines describe the director orientation.

that the scattering power of a material in the nematic state is on the order of 10^6 times that of the material in the isotropic state. For this reason, the use of rheo-optical techniques for the characterization of liquid crystalline polymers is restricted to samples with a very small thickness, on the order of 50 μm or less.

One final point should be made about the polydomain texture. As noted above, the polydomain texture is associated with defects in the director field, which gives the system an excess free energy. In the process of minimizing this free energy nearby disclinations of opposite sign can coalesce, wiping each other out. By doing so the number of disclinations in a LCP under quiescent conditions tends to decrease, causing an enlargement of the domains [104] with time. On the other hand, mechanical energy can be stored during flow in LCP systems by an increase in the number of disclinations or decrease in domain size. Therefore, the actual structure present in LCPs depends on its previous history and this is discussed next.

2.2.2 Development of Orientation and Structure

The description of the polydomain texture of nematic LCPs given in the last section is somewhat idealized and the texture shown in Figure 15 on page 60 is seen in practice only by careful annealing or aging of the material [16]. The actual orientation and texture observed in processed LCPs are much different and depend greatly on the thermal and deformation histories experienced by the LCP during processing. In this section the processing of LCPs will be reviewed and an effort is made to establish the effect of the above factors on LCP orientation and morphology. Therefore, focus is placed on the relative effects of shear versus extensional deformation and also the effect of thermal history. While an attempt is made to separate these two processing parameters in the review, an understanding of much of the experimental work presented requires both to be considered simultaneously. Finally, some effort is made to relate the structure and orientation present in the material during flow to the rheological behavior of the material described in section 2.1.

2.2.2.1 Kinematics of Deformation

In order to appreciate the role of kinematics of deformation on the development of molecular orientation and structure obtained in a material, it is necessary to define the velocity field for each flow type. In general, shearing flows are those flows for which non-diagonal elements of the rate of deformation tensor are nonzero. A elementary case is simple shear flow, for which the velocity field can be given as:

$$v_x = \dot{\gamma}_{xy} y; \quad v_y = 0; \quad v_z = 0. \tag{2.2.3}$$

On the other hand, extensional flows are often called shear-free flows and represent the case where only the diagonal elements of the rate of deformation tensor are non-zero. The general velocity field for extensional flow is defined by:

$$v_x = -\frac{1}{2}\dot{\varepsilon}(1 + b)x$$

$$v_y = -\frac{1}{2}\dot{\varepsilon}(1 - b)y$$

$$v_z = \dot{\varepsilon} z \tag{2.2.4}$$

where the variable $\dot{\varepsilon}$ is the extension rate and the parameter b defines the flow type. The three special types of extensional flows are elongational (or uniaxial extensional) flow with ($b = 0$, $\dot{\varepsilon} > 0$), biaxial extensional flow with ($b = 0$, $\dot{\varepsilon} < 0$), and planar extensional flow with ($b = 1$).

Next, consider the effect of flow type on the shape of an element of material which is initially square, as shown in Figure 17. It can be seen for shear flow that at a constant strain rate, the characteristic dimension of the element changes linearly with time, and part of the deformation is rotational. At the same time, for elongational flow it can be seen that the length of the fluid element changes exponentially with time at a constant strain rate. Tanner [105] considered the behavior of a hypothetical molecule acting like an elastic dumbbell in such flow fields and determined that elongational flows are much more effective than shear flows in stretching out the molecules. Therefore, he concluded that extensional flows are strong flows, while shear flow is a weak one.

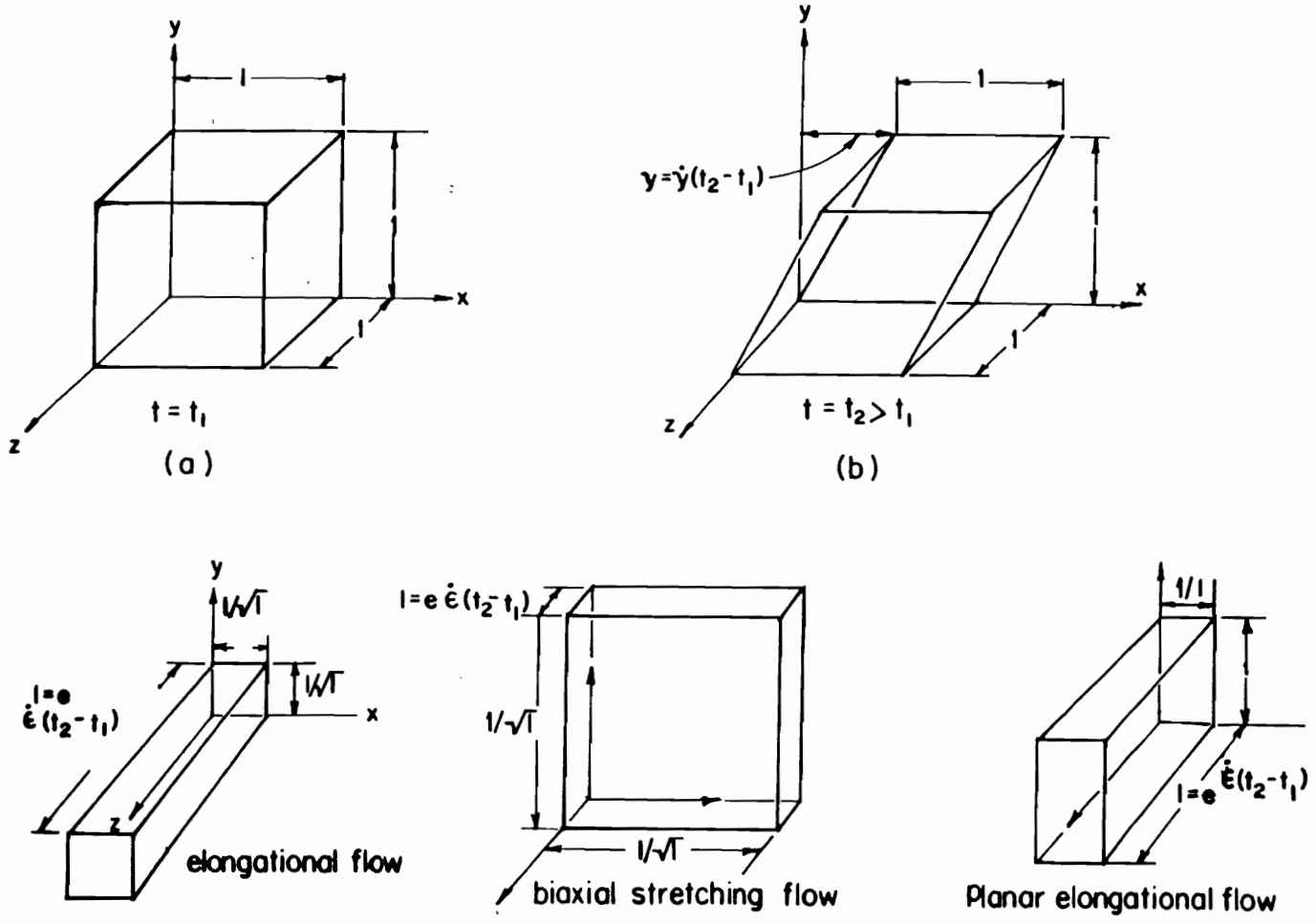

Figure 17. Deformation of a) a unit cube of material by b) steady shear flow and c) extensional flows, after [72].

Additionally, Larson [131] has put forth the idea that the ability of a flow to align molecules (versus stretch them) is also an important flow property and classifies the ability of different flows to align molecules using the invariants of the Finger Tensor (I_1,I_2,I_3). When $I_1 > I_2$, the flow is strongly aligning; when $I_1 = I_2$ the flow is neutrally aligning; and when $I_1 < I_2$ the flow is weakly aligning. According to this classification elongational flows are strongly aligning and shear flows are neutrally aligning.

From the demonstration of the action of flow type and the ideas of Larson. it is apparent that kinematic arguments predict elongational flow to produce a higher degree of molecular orientation in LCPs than shear flow. However, the existence of the polydomain texture in LCPs adds uncertainty to these predictions. Experimental studies on LCPs are examined next in order to determine whether these predictions are valid.

2.2.2.2 Processing Studies

Fiber Spinning. In view of the industrial importance of high strength and modulus LCP fibers, a great deal of work has been done to study the effect of processing variables on the physical and mechanical properties of drawn fibers. Studies on the spinning of fibers from TLCPs include those on the 60HBA/PET copolyester by Acierno [122], Tealdi [123], Muramatsu [124], Sugiyama [59], Lewis and Fellers [30], and Cuculo [125]; on a copolyester composed of 80 mole % HBA and 20 mole % PET (80HBA/PET) by Zachariades [132]. Reports on the spinning of fibers from other TLCPs have been reported by Ide [27] for a copolyester of 60 mole% HBA/ 20% 2,6-naphthalene diacetate (NDA)/ 20 % TA system, by Shimamura [57] for HPC, by Kenig [126] for both PPTA and several copolyesters based on naphthalenic moities, by Amano [127] for several HBA/PET copolyesters, by Zhou [128] for a HBA/NDA/HQ/PET copolyester, by Itoyama [129] for a copolyester of p-HBA/m-HBA/p,p-biphenol/ClHQ/TA and one based on HNA supplied by Celanese, and by Sarlin [130] for the 73HBA/HNA copolyester (Vectra A900). Processing parameters commonly investigated include of draw ratio, die diameter and L/D,

shear rate in the die, extrusion temperature, pre-extrusion thermal history, and thermal conditions during post extrusion draw. While a complete review of all of these studies would be unwieldy, a point is made to use specific examples to illustrate general trends in the literature. More detailed comparisons can be found in the following monographs [20,30,31,133].

A feature common to nearly all of the studies cited is the strong dependence of the tensile strength and modulus as well as molecular orientation on the spin draw ratio (DR), defined as the ratio of final fiber velocity to velocity of the polymer at the die exit (V_f/V_0) or alternately, as the ratio of die cross section to the final cross section of the fiber. An example of this relation is shown in Figure 18 for fibers of a 60HBA/20NDA/20TA copolyester extruded at 340 °C ($T_m = 300°C$) from a die with a diameter of 0.030" and a L/D of 33. As can be seen from Figure 18, both the modulus and strength increase rapidly from a draw ratio of 1 (no post extrusion elongation) to a plateau value at a higher draw ratio, where the modulus and strength show little or no dependence on DR. The value of draw ratio at which the mechanical properties reach their ultimate values does vary considerably between studies and ranges from as low as 8 [126] to as high as approximately 2000 [122] and depends on the material, processing conditions, and even seemingly the particular investigator.

In several of the studies cited above [27,59,122,124,127,128], techniques such as wide angle x-ray scattering or birefringence were used to study the molecular orientation as a function of draw ratio. Ide [27] used WAXS to show that the extrudate with no post extrusion draw showed nearly random molecular orientation, while a high degree of molecular orientation was measured in fibers with DRs as low as 3. Amano [127] showed the dependence of birefringence on draw ratio in fibers of a 50HBA/PET copolyester as seen in Figure 19. Likewise, other researchers have used WAXS to show the orientation in extruded fibers [124,128], with results similar to those of Ide. Zhou [128] observed that very little orientation was obtained in an undrawn copolyester extrudate even for die shear rates as high as 1173 s^{-1}, while a high degree of orientation was obtained in drawn fibers. These investigators explained the above results as indicating that elongational flow during post extrusion draw was responsible for the producing a high degree of molecular orientation and high mechanical properties, with

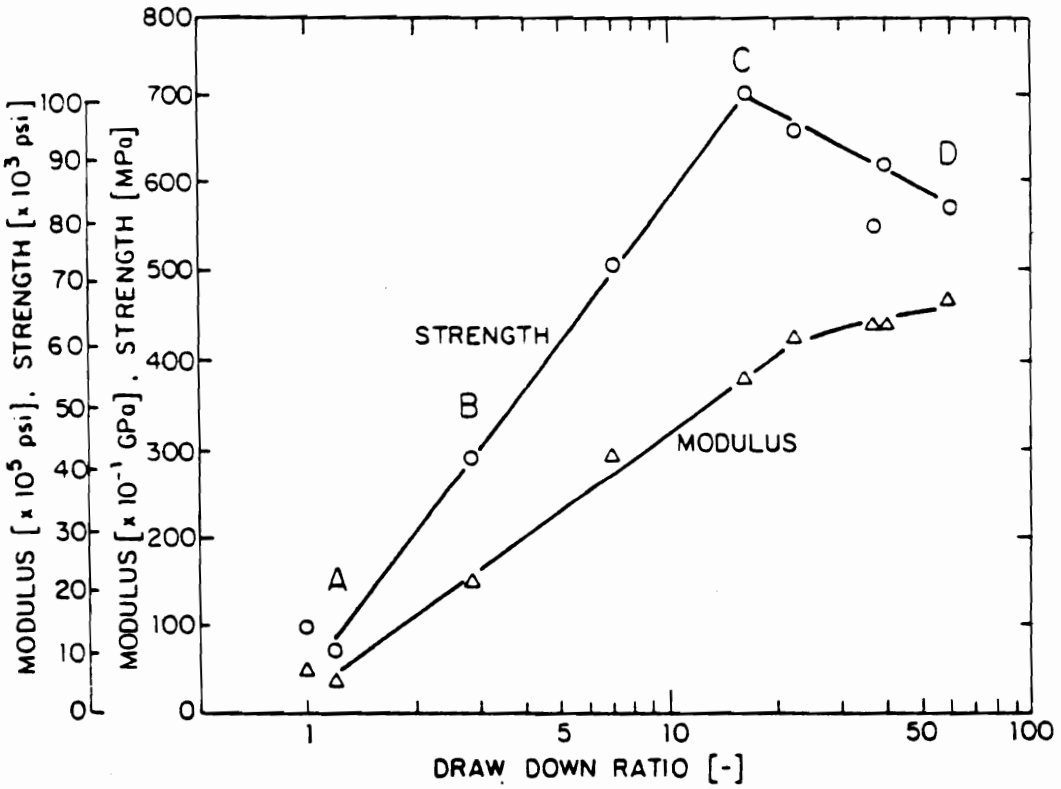

Figure 18. Mechanical properties of filaments of 60/20/20 HBA/NDA/TA copolyester at different draw ratios [27].

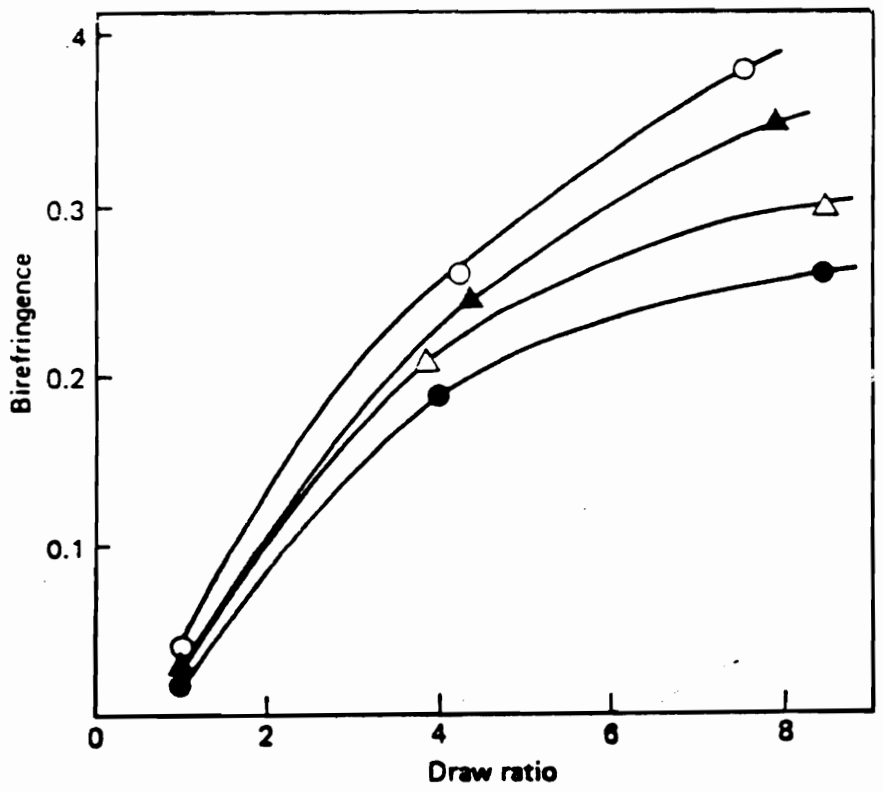

Figure 19. Dependence of birefringence on DR for several HBA/PET copolyester compositions. Top curve is 50HBA/PET [127].

relatively little contribution of shear flow in the die to either. Also, it should be noted that a much higher degree of orientation is obtained in the drawn fibers of the LCPs than would be obtained for conventional polymers drawn under similar conditions.

In addition to a high degree of molecular orientation being seen at high draw ratios, highly drawn fibers have been seen to have a very fibrillar morphology [134]. Therefore, at some point the liquid crystal domains in the material must become highly elongated to form this oriented texture. Studies on the morphology of both undrawn and drawn extrudates have been carried out [27,57,59,125,127,134]. In general, the undrawn extrudates are found to have a skin/core structure. The skin layer is typically fibrillar and oriented while the core is unoriented and shows domains with uniform aspect ratio. On the other hand, in highly drawn fibers, a uniform morphology is seen throughout the fiber with a very fibrillar structure. A schematic of a typical structure in such highly drawn fibers has been presented by Sawyer and Jaffe [134] and is shown in Figure 20, showing a hierarchical structure in which many different levels of molecular structures are present. In the study by Muramatsu [124], it was further noted that the oriented skin layer increased with draw ratio. These results then indicate that some post extrusion draw is necessary for the formation of an oriented and fibrillar microstructure in TLCP fibers.

While the conclusion stated above appears to be general for LCP drawn fibers, a couple of opposing results should be noted. Sugiyama [59] and Lewis [30] studied the spinning of fibers from the 60HBA/PET copolyester and reported that post extrusion draw gave only a small increase in the modulus (E) and Hermans orientation function f_H. At the same time they noted that for temperatures below 250 °C, increasing the shear rate in the die gave some increase in molecular orientation. Sugiyama and coworkers explained that high shear rates and shear stresses in the die were necessary to form permanent orientation in the fibers. In the study on the fiber spinning of 60HBA/PET by Muramatsu [124] reported on the effect of capillary L/D while holding other conditions constant. He found that increasing the capillary L/D increased the orientation and modulus of the fiber. Since the fibers drawn from the longer L/D die would be expected to show less influence from the elongational flow associated with the converging

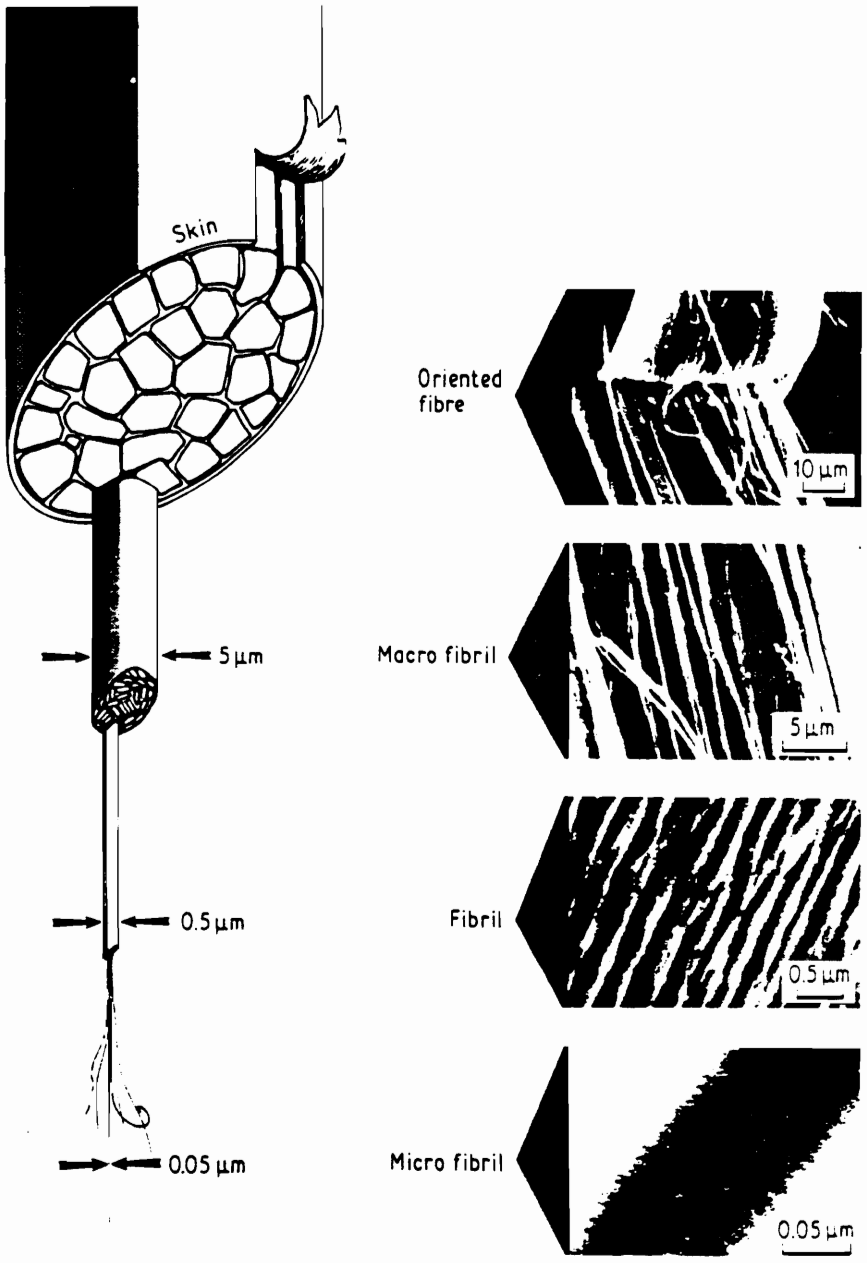

Figure 20. Hierarchical structural model for oriented LCP fibers [134].

section than a short L/D die, it is indicated that shear flow must be responsible for some improvement in properties. At the same time Muramatsu noted that at fixed L/D, increasing the die shear rate had little effect on fiber modulus, and some post-extrusion draw was necessary to obtain maximum mechanical properties and orientation.

In order to explain the discrepancy discussed above, it is necessary to look at other factors besides just type of deformation. For example, in Sugiyama's work there was only a difference in orientation as a function of die shear rate at temperatures below 250 °C, where the material is known to contain residual crystallinity (T_m = 255 °C). Increasing the flow rate would not only have caused increased shear stress in the die but also increased the extensional stress due to converging flow at the die entrance, both of which could act to break down any elastic structure in the material and allow the material to become oriented. At the same time, the lack of an increase in properties due to post-extrusion draw could be explained by the resistance of unmelted HBA crystallites to deformation during flow. In the case of Muramatsu's work (done at 260 °C), the increased shear flow in the die could have acted to break down and melt crystallites which were still not melted. The polymer would then have a more homogenous consistency, which then allowed easier alignment as a result of post extrusion draw. In fact, Muramatsu notes a more fibrillar texture in the higher L/D die. Further support for this hypothesis comes from the discussion of thermal history effects below.

Several researchers have also investigated the effect of thermal conditions on the structure and orientation in LCP fibers. Many of the researchers found that the best mechanical properties and highest orientation were obtained when the extrusion temperature was above the highest crystalline melting endotherm [59,123-125,128,132]. Muramatsu [124] suggested for the 60HBA/PET material that by melting out all crystallinity a more readily oriented nematic state exists in the melt. Furthermore, when the results were compared for samples whose only difference had been the level of residual crystallinity in the melt (one batch had a more blocky sequence distribution), it was found that the material with a higher content of residual crystallinity gave lower mechanical properties and orientation. Yet when processed at a temperature where both materials should have been free of residual crystallinity, me-

chanical properties were similar. This hypothesis is supported by Zachariades' study [132] of 80HBA/PET fibers. SEM, TEM, and micro-wide angle x-ray scattering were used to show that undeformed p-HBA domains remained in the fibers spun below 328 °C. In fibers spun above 328 °C, a uniform fibrillar texture was observed. Also, the mechanical properties were higher for the fibers drawn down above 328 °C than those drawn down below 328 °C.

In contrast to the result just stated, some researchers report a decrease in fiber properties as the extrusion temperature increased [122,129,130]. Acierno [122] reported the modulus of fibers spun from 60HBA/PET at temperatures from 225 to 285 °C, with the highest mechanical properties reported at 225 °C for all DR. Muramatsu notes that Acierno used lower extrusion rates and higher draw ratios in his work and hypotheses two regimes, but fails to explain how this would justify the differences. While differences in the batch of material used also could affect results, this explanation also seems unsatisfactory.

One final spinning parameter worth noting is the thermal condition along the spinline. Lewis and Fellers [30] varied this condition for fibers spun from 60HBA/PET using a heated collar at the die exit. They found that fibers spun where the spinline and die temperature were equal (isothermally) had lower mechanical properties and values of f_H than those of fibers spun at ambiant conditions. Thus, relaxation of orientation is also possible under certain thermal conditions.

As shown above, both deformation and thermal history have been shown to be important factors in the development of orientation and structure during fiber spinning. It was shown that fiber properties depend highly on the post-extrusion draw ratio, indicating the importance of elongational flow in producing a high degree of molecular orientation and a fibrillar morphology. At the same time, there were indications that shear flow, coupled with appropriate thermal conditions, could also be responsible for the development of orientation and texture. Finally, thermal history was shown to significantly affect the morphology of fibers both through the effects of residual crystallinity (or lack of it) in the melt and through relaxation processes.

Injection Molding. Several studies have been reported on the properties and morphology of injection molded bars and plaques [25,26,135-138]. Ophir and Ide [25] studied injection molded bars of the 60HBA/20NDA/20TA copolyester and noted a distinct skin-core morphology with 4 different layers from the skin to the core. It was observed that the skin was highly oriented in the flow direction, while the other layers showed a much lower degree of orientation. The origin of the layers was explained in terms of the flow and thermal conditions in the mold filling process. The skin layer was formed from material which had undergone elongational flow at the melt front, and was then quickly cooled by the mold walls, locking in the orientation. The center layers underwent mainly shearing or plug flow, and had more time to relax, thereby showing a lesser amount of orientation.

Joseph and coworkers [135] studied the orientation and texture produced in injection molded plaques of the 60HBA/PET copolyester, using both center and end gates. For plaques molded with the end gate mold, they found five distinct layers throughout the thickness direction, a skin layer, a intermediate region, and a core region. The skin layer was found to have a high degree of molecular orientation and a fibrillar morphology. The intermediate region showed much lower orientation, and slightly oriented domains. The core showed only a small degree of molecular orientation and an undeformed domain structure. These results are consistent with those of Ophir and Ide and further back up the flow mechanism described.

The results described above have been further verified in other studies on injection molded LCP articles [136-138]. In all cases, it is clear that elongational flow in the melt front is responsible for a high degree of orientation. At the same time, shear flow in the subskin and core regions seems to result in very little orientation. However, since the core region has a much longer cooling time than the skin region the lack of orientation in th core could also be due to relaxation following flow.

Other studies. Other studies on the processing of LCPs have been reported in order to better define the conditions under which an oriented structure is obtained. Zachariades and Logan [132] studied the relative effect of shear and elongational flow by comparing the structure and orientation obtained in sheared films and drawn fibers of the 80HBA/PET copolyester.

The films were sheared between parallel plates while the material was allowed to cool. It was found that a moderate degree of molecular orientation and a moderately elongated domain structure could be obtained during shearing. At the same time, a much higher degree of orientation, more fibrillar morphology, and higher mechanical properties were obtained in the drawn fibers.

In order to more precisely separate the effect of shear and elongational flow and also thermal history effects Viola and Baird [8,28,139] studied sheared disks and extended films of the 60HBA/PET copolyester. Sheared disks were prepared between parallel plates by heating the material to 275 °C and then shearing at an edge shear rate of 10 s^{-1} to a large strain value. The disks were either cooled after cessation of shear flow or sheared and cooled simultaneously. The extended films were made by extrusion through a flat film die with post extrusion draw applied by a set of takeup rollers. For the disks sheared then cooled, a very low degree of molecular orientation was seen, even at high shear rates. Likewise, the morphology (as seen by SEM) showed a sheet-like texture with no indication of orientation [28]. However, in the sheared while cooled disks a moderate degree of molecular orientation was obtained. In comparison with the sheared disks, films extruded with comparable extension rates (2.5 s^{-1}) were found to have a much higher level of molecular orientation and a more fibrillar morphology. Therefore, while a higher degree of orientation was obtained by extensional flow versus shearing, simultaneous deformation and cooling were also shown to be necessary for locking in flow induced orientation.

2.2.3 Rheo-optical studies

In the processing studies reviewed above the morphology of solidified LCP articles was examined in respect to thermal and flow history. However, those studies did not answer the question of exactly what state of structure exists in the material during flow. Yet this knowledge is necessary for a thorough understanding of the rheological studies presented earlier

and provides a further basis for evaluating constitutive models. Therefore, several researchers have conducted *in situ* rheo-optical studies [17,34,80,104,140-154] using the methods of polarized optical microscopy (POM), birefrigence, or light scattering to determine the structure and orientation of LCPs during flow.

One of the first studies reported in the literature on the structure of flowing LCP systems was carried out by Kiss and Porter [80] on lyotropic solution of PBG in m-cresol using a specially constructed parallel plate device. The plates were made of quartz windows which allowed the polymer to be viewed in an optical microscope set up with the analyzer and polarizer oriented 90° apart and at a 45° angle with the shear direction. They reported three different textures present in the material during shearing, depending on the rate. At rates less than 1-3 s^{-1}, they noted bright streaks running parallel to the flow direction. At rates in the range of 3-100 s^{-1} they observed a coarser texture with streaks running perpendicular to the flow direction, and at higher rates the field of view was a featureless gray. Furthermore, it was noted that the ranges at which these textures were found coincided with positive values of N1 at low shear, negative values of N1 at medium shear rate, and positive values of N1 at high rates.

In the same study, Kiss and Porter also report on the structure present during relaxation of the solution following steady shear. It was found that the streak structure formed at low rates relaxed over several minutes, going steadily toward one with large speckles. However, relaxation from the two higher rate ranges occurred faster and went to a banded texture with bands lying perpendicular to the flow direction. The higher the shear rate the faster the texture relaxed with better band definition and thinner bands. A banded texture was also produced in films prepared by shearing then drying off the solvent. Using a red plate at 45° to the crossed polarizers they were able to show that the molecular orientation in the bands was alternately $\pm 45°$ to the shear direction. Kiss and Porter summarized their observations by proposing that three different textures are formed during shear flow in LCPs, depending on the shear rate. In the range of lowest shear rates, molecules orient in the flow direction. At moderate to high rates, the molecules orient at $\pm 45°$ to the shear direction with stored elastic energy respon-

sible for the negative normal stresses. Finally, at the highest rates the domains break up and tumble. While this model does describe the behavior observed, it seems unlikely that a high degree of molecular orientation could be obtained in the LCP at low rates, only to be lost as rates are increased to moderate levels. Also, it relies upon the assumption that molecular orientation in the dried film was the same as during flow at moderate rates, even though it is know from melt studies that molecular orientation in sheared LCP samples does relax.

Asada and coworkers [13,141,142] used light transmittance to study changes in structure in lyotropic solutions of PBLG during steady shear flow. Three different polarizer conditions were used and these are shown in Figure 21a, while measured values of the transmitted light intensities for the different polarizer conditions (I_E, I_{II}, and I_X) are shown in Figure 21b. First, consider the quantity I_E as a function of shear rate. At low rates I_E is independent of rate and of moderate values, indicating a globally random orientation. As rate increases I_E goes through a range of decrease and then levels off at a low value, signifying a high degree of orientation along the shear direction. At the same time, it can be shown from the values of I_{II} and I_X that a domain texture exists at the lower rates but that a monodomain texture develops at the highest rates [17]. Not only do these results contradict those of Kiss and Porter at low and moderate rates, but they also support the structure part of the 3 region flow curve proposed earlier in section 2.1. One explanation for this discrepancy is that Kiss and Porter used optical microscopy, which focuses on a local layer of material in a shear plane, while the work by Asada and coworkers used optical transmittance which gives more of a bulk measurement of properties.

In support of the results of Asada and coworkers, Graziano and Mackley [141] have reported on the changes in optical texture during oscillatory shear flow of several thermotropic LCPs (maximum strain is about ten units). Many of these materials were oligomeric and only the highest molecular weight sample is described here. Two distinct regions of texture were seen as a function of angular frequency. At lowest frequencies, they observed a texture with a large number of domains where individual domains shifted but the overall texture was constant. At only low frequencies, a polydomain or as they describe "worm" texture exists in the

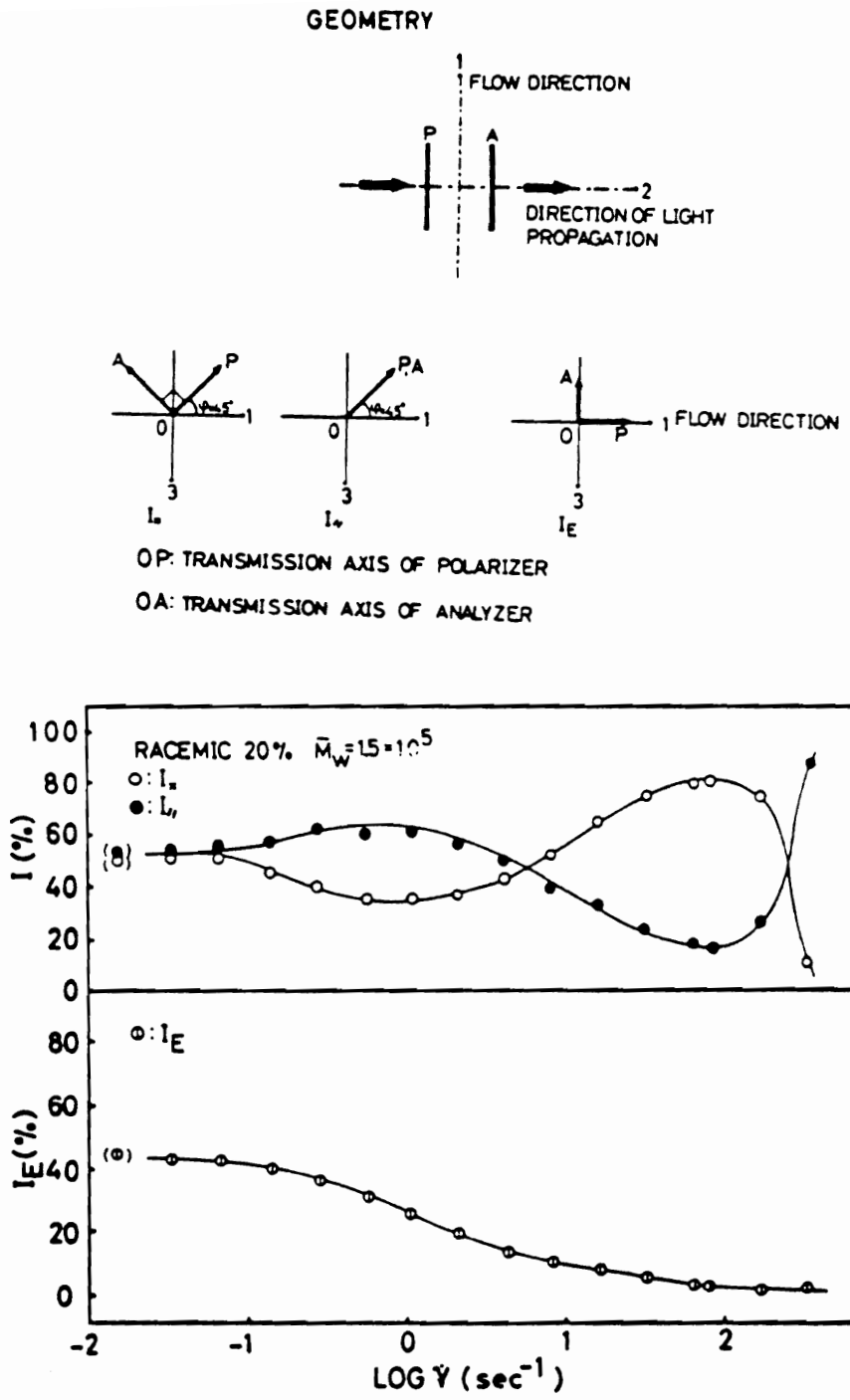

Figure 21. Geometry of polarizers (a) and variation of I_X, I_{II}, and I_E (b) with shear rate for 20% PBLG in m-cresol [17].

polymer. At angular frequencies above 0.1 rad/s, the texture becomes highly ordered in the flow direction, with no indication of domains. The relaxation of the structure of this material was very similar to that observed above by Kiss and Porter.

Onogi and coworkers [34] used birefrigence to follow the orientation in lyotropic solutions of HPC in water during both shear and elongational flow. Of particular interest were transient shear stress growth/relaxation experiments, an example of which is shown in Figure 22. In that figure it can be seen that for isotropic solutions, the stress and birefringence are directly proportional at all times. However, the stress and birefringence in the lyotropic solutions are not proportional with the time scale for relaxation of the stress being much faster than the time scale for relaxation of orientation. Furthermore, at lower shear rates a transient overshoot of birefringence was seen which was attributed to a breakdown of cholesteric structure into an oriented nematic structure, where domain boundaries disappear. In the case of elongational flow (in gravity spinning), no domain texture was observed and a high degree of molecular orientation was seen. Furthermore, the orientation developed very quickly upon exit from the spinning die with the maximum orientation obtained at the point where the velocity profile just leveled off. At distances further along the spinline the extension rate was zero and the orientation showed some relaxation. Also, a monodomain type texture was observed as a result of elongational flow.

In the studies above one common feature of LCP systems was a banded texture appearing in the material as a result of shear flow as shown in Figure 23a. Recent studies by several investigators [142-148] have shown that the structure and orientation is one of elongated LCP domains, which lie in a zig-zag pattern such that the molecules alternately are oriented $\pm$20-45^0 [80,144,146,147] with respect to the shear flow direction. An example of such a morphology is shown in Figure 23b for a thermotropic copolyester based on hydroquinone and 4,4′-dicarboxy-1,10-diphenoxydecane [148]. Not all of the studies show such a fibrillar texture, but all do show the zig-zag in molecular orientation.

While the banded structure has been shown to be a common feature in sheared LCP films, the early studies of Kiss [80] and Graziano [141] failed to show whether the texture was

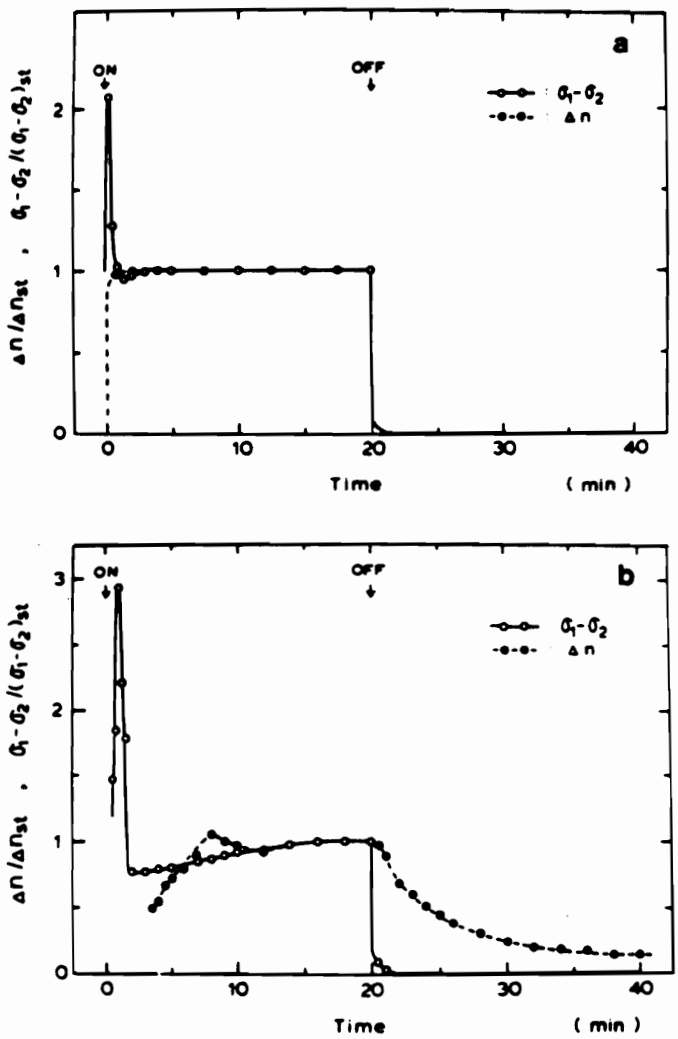

Figure 22. Relation of stress and birefringence for a) isotropic and b) anisotropic solutions of HPC/water [34].

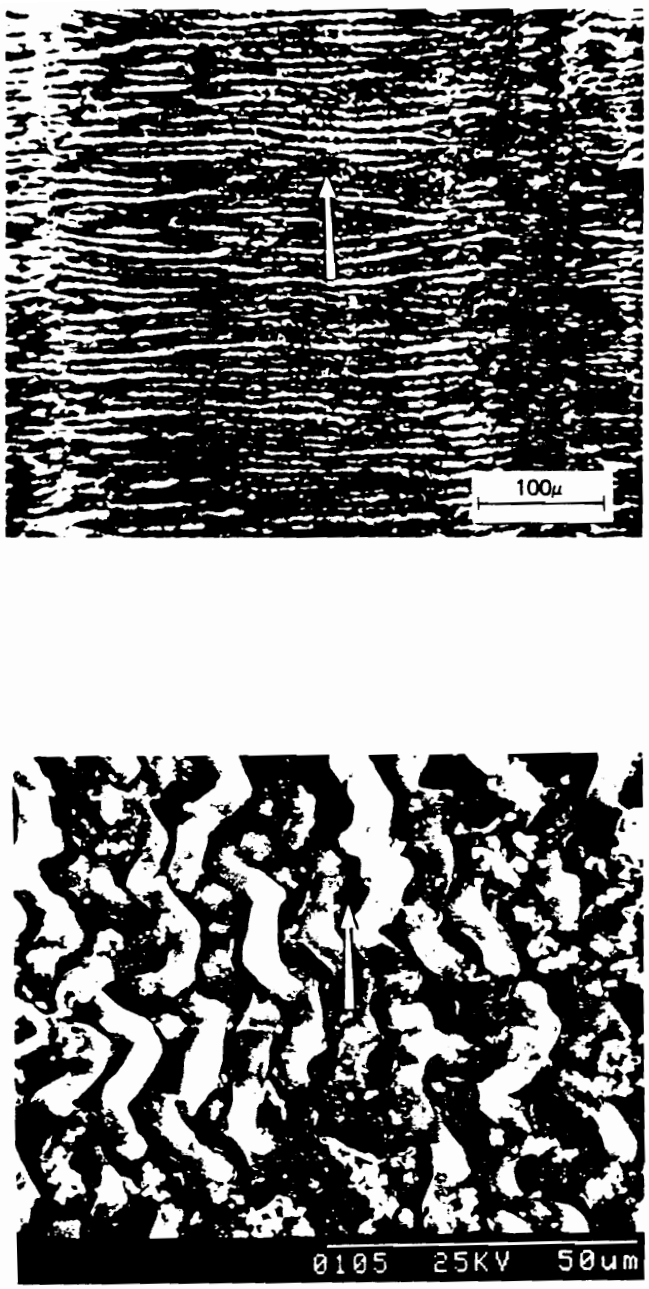

Figure 23. Optical micrograph (a) and SEM photomicrograph (b) of banded texture in a thermotropic copolyester [148].

present during shear flow or was formed during relaxation. Some recent studies [150-154] have been made using the technique of small-angle light scattering (SALS) to probe structural changes during and after shear flow. In all cases tests were performed on lyotropic solutions of HPC, PMDG, or PBLG. A typical set of SALS patterns for steady state shear flow at a range of shear rates is shown in Figure 24along with the corresponding viscosity curve. The theoretical and experimental basis for the evaluation of SALS patterns is not presented here but presented in Appendix A in detail. The important result is that a banded structure would likely result in a SALS pattern similar to (h) of Figure 24, but with distinct lobes and rotated 90^0 with respect to that pattern. No such pattern is seen during shear in any of the studies, while such a pattern is seen during relaxation following shear flow [150-152]. Additionally, Hashimoto has shown that the appearance of the banded texture coincided with the first portion of the stress relaxation curve for PMDG solutions. Therefore, the banded texture seen in LCPs is a result of a relaxation process and is not a flow feature.

In this section rheo-optical studies on the macromolecular structure present in LCPs during flow were reviewed. While the 3 region flow curve proposed by Onogi and Asada [17] was shown to poorly describe the viscosity behavior of LCP systems, the proposed structural model is consistent with the results presented here. For shear flow it was shown that domains are present at low rates but break up at high rates into an oriented monodomain texture. While there has been very little work done on the evolution of structure during elongational flow, there is some indication that a monodomain structure is easily formed. At the same time, very little has been done to show how the structure develops on the startup of flow in shear flow and nothing reported for elongational flow. Since most flows involved with polymer processing are transient in nature, this is somewhat surprising. Finally, the method of small angle light scattering was shown here to be useful for characterizing the structure present in LCPs during flow. A detailed review of the method of SALS is therefore given in Appendix A.

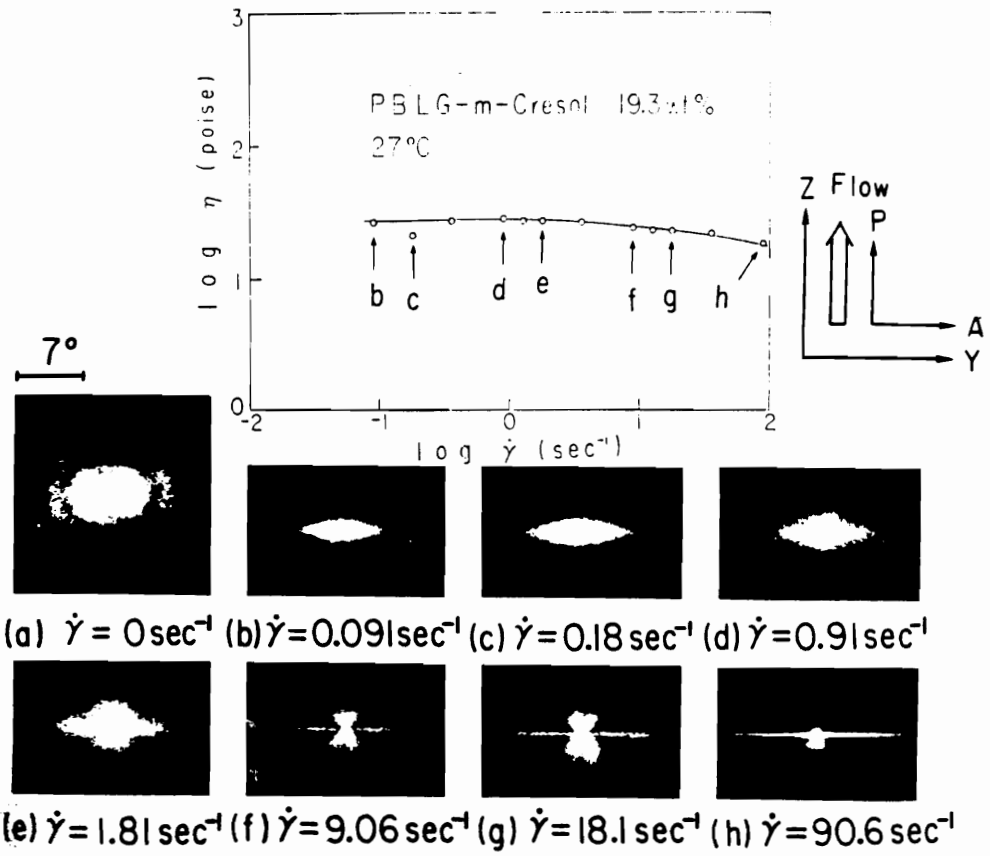

Figure 24. Steady state shear viscosity and H_V SALS patterns as a function of shear rate for 20% PBLG in m-cresol [154].

2.3 The Doi Theory

In Chapter One the requirements for constitutive models to adequately describe LCPs were given; namely, that the model be capable of describing both the stress and orientation state in the material as a function of deformation history. Two theories which satisfy this requirement are the continuum model of Ericksen and Leslie [35,36] and the molecular model of Doi [39,180]. However, the Ericksen theory has been shown to be incapable of describing the transient shear flow behavior of a thermotropic copolyester [8,95] and is encumbered by the necessity of fitting 5 constants. On the other hand the Doi theory, which is based on molecular dynamics, has only two parameters to be fit and has not been fully evaluated for its ability to predict either steady or transient shear and extensional flow behavior. Therefore, the Doi theory appears to be the most promising one to date for use in modelling the flow of LCPs and is therefore examined here in some detail.

2.3.1 Doi Theory for Rodlike Polymers

Doi's theory for the molecular dynamics of concentrated solutions of rod-like polymers is reviewed in this section. First, a brief development of the theory is given, including the important assumptions, approximations, and extensions. The predictions of the theory are then compared with the experimentally observed behavior of LCPs as described in section 2.1. The theory predicts the nonlinear viscoelasticity of both isotropic and anisotropic solutions as well as the phenomenological coefficients from molecular parameters. However, an important limitation is that the theory fails to consider the case where there is a spatial variation of the director, **n**.

2.3.1.1 Development of Theory

Doi's theory for the molecular dynamics of rod-like polymers in concentrated solutions [39,180] is an extension of the theory of Doi and Edwards [181,182] for isotropic semi-concentrated solutions. The theory considers the dynamics of a rigid rod with length L, diameter d, and orientation **u** with respect to cartesian coordinates (x,y,z). For very dilute solutions ($c \ll L^{-3}$) there is no interaction between rods and the rotational motion is described by the theory of Kirkwood and Auer [183]. The resulting kinetic equation for the orientation distribution function $f(\mathbf{u},t)$ is then given by

$$\frac{\partial f}{\partial t} = D_{ro}\nabla_{\mathbf{u}}\bullet\nabla_{\mathbf{u}}f + \nabla_{u}\bullet\dot{\mathbf{u}}f \qquad (2.3.1a)$$

where

$$D_{ro} = k_B T \ln \frac{(L/d)}{3\pi\eta_s L^3} \qquad (2.3.1b)$$

and D_{ro} is the rotational diffusivity of a rod in dilute solution, k_B is Boltzmanns constant, η_s is the solvent viscosity, ∇_u is the gradient operator over the solid angles θ and ϕ, and $\dot{\mathbf{u}}$ is the rate of change of **u** due to flow and given by

$$\dot{\mathbf{u}} = \mathbf{K}\bullet\mathbf{u} - (\mathbf{u}\bullet\mathbf{K}\bullet\mathbf{u})\mathbf{u} \qquad (2.3.2)$$

where **K** is the velocity gradient tensor ($\mathbf{K} = \partial v_\alpha/\partial x_\beta$).

For concentrations greater than $(1/L^3)$ the rotational motion of the rods is restricted by interactions with neighboring rods. The rod is now essentially restricted to a tube of space with the same length as the rod and radius a. By undergoing translational motion along the tube the rod changes its direction by a small amount $\Delta\theta \approx a/L$. In a unit time the process will be repeated D_{ro} times so that the overall rotational diffusion constant is now [39]

$$D_r = D_{ro}(\Delta\theta)^2 \tag{2.3.3}$$

Estimating the tube radius from the distance of the rod to its nearest neighbor and inserting this into the equation for the rotational diffusion coefficient Doi and Edwards obtained [182]

$$\tilde{D}_r = \nu_1 D_{ro}(cL^3)^{-2}\left(\frac{4}{\pi}\int f(\mathbf{u}, t)\sin(\mathbf{u}, \mathbf{u}')d^2\mathbf{u}'\right)^{-2} \tag{2.3.4}$$

where $\tilde{D}_r$ is now the rotational diffusion coefficient for a single rod in solutions with $c > L^{-3}$, ν_1 is an undetermined constant, and $(\mathbf{u},\mathbf{u}')$ is the angle between two rods. The rotational diffusion $\tilde{D}_r$ can be used in the kinetic equation, which now becomes

$$\frac{\partial f}{\partial t} = \nabla_u \bullet \tilde{D}_r \nabla_u f + \nabla_u \bullet \dot{u} f \tag{2.3.5}$$

Although equation 2.3.5 takes into account molecular interactions, its use is restricted to systems which are isotropic at equilibrium, i.e. $f_{eq} = 1/4\pi$. Doi [39] now uses Onsager's expression for the free energy of a solution of rods [184] to generalize for higher concentrations where the material can become liquid crystalline. Now instead of stipulating that the system be isotropic at equilibrium, the orientation in the system at rest is determined by a minimization of the Helholtz free energy *A*. The free energy is minimized with respect to f, the orientation distribution function, which now becomes

$$f(\mathbf{u}) = \text{const}\ \exp[-V(\mathbf{u})/kT] \tag{2.3.6}$$

where $V(\mathbf{u})$ is the mean field potential which acts on a rod by the neighboring rods and is given in [39]. Doi now generalized the kinetic equation to include the effect of the potential $V(\mathbf{u})$:

$$\frac{\partial f}{\partial t} = \nabla_u \bullet \tilde{D}_r\left(\nabla_u f + \frac{f}{k_B T}\nabla_u V\right) + \nabla_u \bullet \dot{u} f \tag{2.3.7}$$

Equation 2.3.7 is the basic equation in the Doi theory and generally describes the dynamics of rod-like polymers for $c > L^{-3}$.

In order to simplify the mathematical analysis, Doi [39] expanded the term $\sin(\mathbf{u},\mathbf{u}')$ in the expression for $V(\mathbf{u})$ in terms of the irreducible tensors equivalent to spherical harmonics. By truncating the expansion for terms higher than fourth rank tensors, Doi obtained

$$V(\mathbf{u}) = -\frac{3}{2} U k_B T (u_\alpha u_\beta - \frac{1}{3}\delta_{\alpha\beta}) S_{\alpha\beta}(t) \tag{2.3.8}$$

where U (sometimes written as C in papers) is a constant and

$$S_{\alpha\beta}(t) = \int f(\mathbf{u},t)(u_\alpha u_\beta - \frac{1}{3}\delta_{\alpha\beta})d\mathbf{u} \tag{2.3.9}$$

is the orientational order parameter tensor, which was described in section 2.2. The constant U is equal to $\nu_2 c d L^2$, where ν_2 is a numerical constant, and characterizes the intensity of the interaction potential.

In order to determine the rheological properties from the theory, Doi [39] considered a small deformation for an individual rod. The net effect of the deformation is to change the orientation of the rod and this will change the free energy, which in turn generates a stress. This method is well known [39] and results in the following equation for stress:

$$\sigma_{\alpha\beta} = 3ck_BT\{S_{\alpha\beta} - U[S_{\alpha\mu}(S_{\beta\mu} + \frac{1}{3}\delta_{\beta\mu}) - \langle u_\alpha u_\beta u_\mu u_\nu \rangle S_{\mu\nu}]\} \tag{2.3.10}$$

It should be noted here that the equation above for the stress tensor only contains terms due to the intermolecular potential and Brownian motion, as Doi drops terms for solvent contributions and hydrodynamic drag, arguing that the stress contribution from these terms is small compared to the other two [182].

The stress tensor, $\sigma_{\alpha\beta}$, represents a deviatoric stress, which is sufficient here since an isotropic stress should have no effect on the orientation or flow. Also, the stress tensor in equation 2.3.10 is symmetric since the effects of external fields were not considered. Doi [185]

carried out the derivation for the case where a magnetic field was present, but this is not considered here since magnetic fields are expected to have a relatively small effect on polymeric liquid crystals.

Two further approximations were made in order to obtain a closed form solution for $S_{\alpha\beta}$. The first was to replace the rotational diffusion coefficient for a rod in a concentrated solution tilde sub r with an averaged one $\bar{D}_r$, which is obtained by expanding the expression in the integral of equation 2.3.4 in terms of the irreducible tensors equivalent to spherical harmonics [39]:

$$\frac{4}{\pi}\int f(\mathbf{u}_1,t)f(\mathbf{u}_2,t)\sin(\mathbf{u}_1,\mathbf{u}_2)d\mathbf{u}_1 d\mathbf{u}_2 \approx 1-\frac{3}{2}S_{\alpha\beta}(t)^2 \quad \text{and} \tag{2.3.11a}$$

$$\bar{D}_r = D_r\left(1-\frac{3}{2}S^2_{\mu\nu}\right)^{-1/2} \tag{2.3.11b}$$

where $D_r = \nu_1 D_{ro}(cL^3)^{-2}$. The coefficient 3/2 on the right side replaces the coefficient of 15/16 obtained from the expansion using spherical harmonics [39] in order to fulfill the case for perfect alignment. The second approximation involves the decoupling of the fourth order tensor average in equation 2.3.10. Doi arbitrarily chooses the form

$$< u_\alpha u_\beta u_\mu u_\nu > = < u_\alpha u_\beta >< u_\mu u_\nu > \tag{2.3.12}$$

This leads to

$$\frac{\partial S_{\alpha\beta}}{\partial t} = F_{\alpha\beta}(\mathbf{S}) + G_{\alpha\beta}(\mathbf{S}) \tag{2.3.13}$$

where

$$F_{\alpha\beta}(\mathbf{S}) = -6\bar{D}_r[(1-\frac{U}{3})S_{\alpha\beta} - U(S_{\alpha\mu}S_{\beta\mu} - \frac{\delta_{\alpha\beta}}{3}S^2_{\mu\nu}) + US_{\alpha\beta}S^2_{\mu\nu}] \tag{2.3.14a}$$

$$G_{\alpha\beta}(\mathbf{S}) = \frac{1}{3}(K_{\alpha\beta} + K_{\beta\alpha}) + (K_{\alpha\mu}S_{\mu\beta} + K_{\beta\mu}S_{\mu\nu} - \frac{2}{3}\delta_{\alpha\beta}K_{\mu\nu}S_{\mu\nu}) - 2K_{\mu\nu}S_{\mu\nu}S_{\alpha\beta} \quad (2.3.14b)$$

and $K_{\alpha\beta} = \partial v_\alpha / x_\beta$. Physically, the functions $F_{\alpha\beta}$ and $G_{\alpha\beta}$ represent the effects of Brownian motion and the macroscopic flow field, respectively, on the rod orientation. The stress tensor now becomes

$$\sigma_{\alpha\beta} = 3ck_BT[S_{\alpha\beta}(1 - \frac{U}{3}) - U(S_{\alpha\mu}S_{\beta\mu} - \frac{1}{3}\delta_{\alpha\beta}S^2_{\mu\nu}) + US_{\alpha\beta}S^2_{\mu\nu}] \quad (2.3.15)$$

The desired rheological constitutive equations of the Doi model are then given by equations 2.3.13 to 2.3.15. In order to solve these equations the velocity field and the parameters U and D_r are first specified, as well as initial values of $S_{\alpha\beta}$ for orientation. One then obtains a set of coupled differential equations for $S_{\alpha\beta}$, which are solved by a numerical integration method [45]. The components of stress can then be calculated from equation 2.3.15.

2.3.1.2 Predictions of the Doi Theory

Prilutski [45] used the procedure described above to calculate the stress response for both steady shear and elongational flows. For the case of shear flow, the theory predicts a Newtonian region at low rates followed by a power law region at higher rates. The Doi theory, in the form of equations 2.3.14 to 2.3.15, actually predicts that the stress passes through a maximum as rate increases at high rates. While some LCP systems have shown indications of a zero shear viscosity at low rates, this contradicts experimental observation of power law indices in the range of 0.5 at moderate rates. Metzner and Prilutski [42] also noted that transient shear predictions do not agree with the experimentally observed behavior in the HPC/acetic acid system they investigated. At the same time their calculations were based on

the use of only one initial condition and they appear to have made no effort towards investigating other physically realizeable situations.

For the case of elongational flow the Doi theory again predicts a constant extensional viscosity, a Trouton ratio equal to about 9 at low rates ($< 1\ s^{-1}$), and a saturation of the elongational stress at higher rates. The steady state stress and scalar order parameter predicted for elongational flow are shown in Figure 25 and Figure 26. While there is still some question as to whether Prilutski's elongational flow results for the HPC/acetic acid solutions are general for LCP systems, it can be seen from Figure 13 that there is good agreement between experiment and the predictions of the theory. However, neither the transient flow response nor the development of orientation have been verified for elongational flow.

2.3.2.3 Modifications of the Doi Theory

Two modifications to the Doi theory have been proposed in the literature and are reviewed in this section. First, Doraiswamy and Metzner [186] have proposed keeping the term in the stress equation with accounts for the contribution to the stress for the solvent, a term which Doi had discarded as being unimportant relative to the stress resulting from the free energy density associated with the anisotropic distribution of rods. The second modification is that due to Marrucci and Grizzuti [187,188], who attempt to modify the theory to account for the effect of polymer polydispersity.

Doraiswamy and Metzner [186] have analyzed the discrepancy between theoretical predictions and experimental results at high shear rates and concluded that this arises due to the neglecting of the solvent contribution to stress, which could be significant at high rates. A term was then added to the stress to account for this interaction and is of the form $\eta_r\eta_s(V_{\alpha,\beta} + V_{\beta,\alpha})$, where η_r is the relative viscosity defined as $\eta_r = (\frac{1-\Phi}{\Phi_0})^{-2}$, with Φ equal to the volume fraction of LCP and Φ_0 an empirical constant. Because of the semi-empirical nature of the added term and the numerous approximations made in the Doi theory, Doraiswamy and

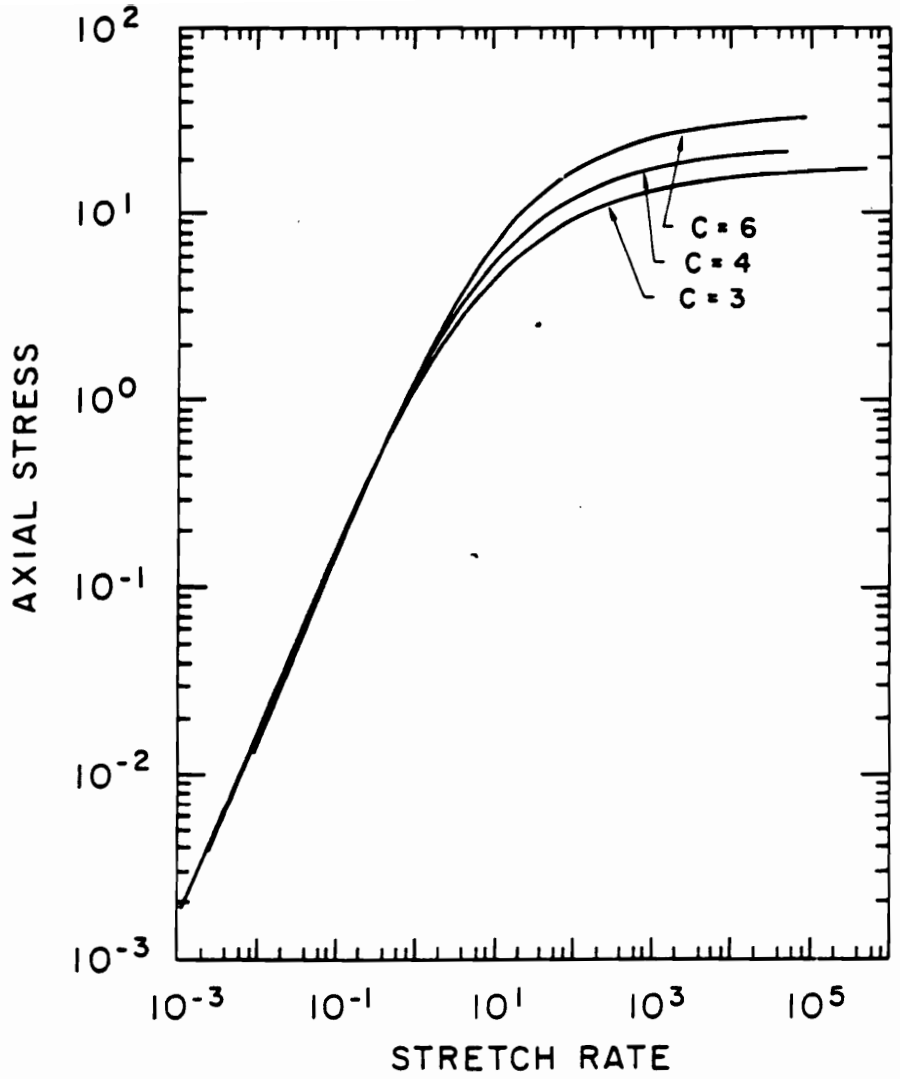

Figure 25. Prediction of axial stress for elongational flow by the Doi Theory [42].

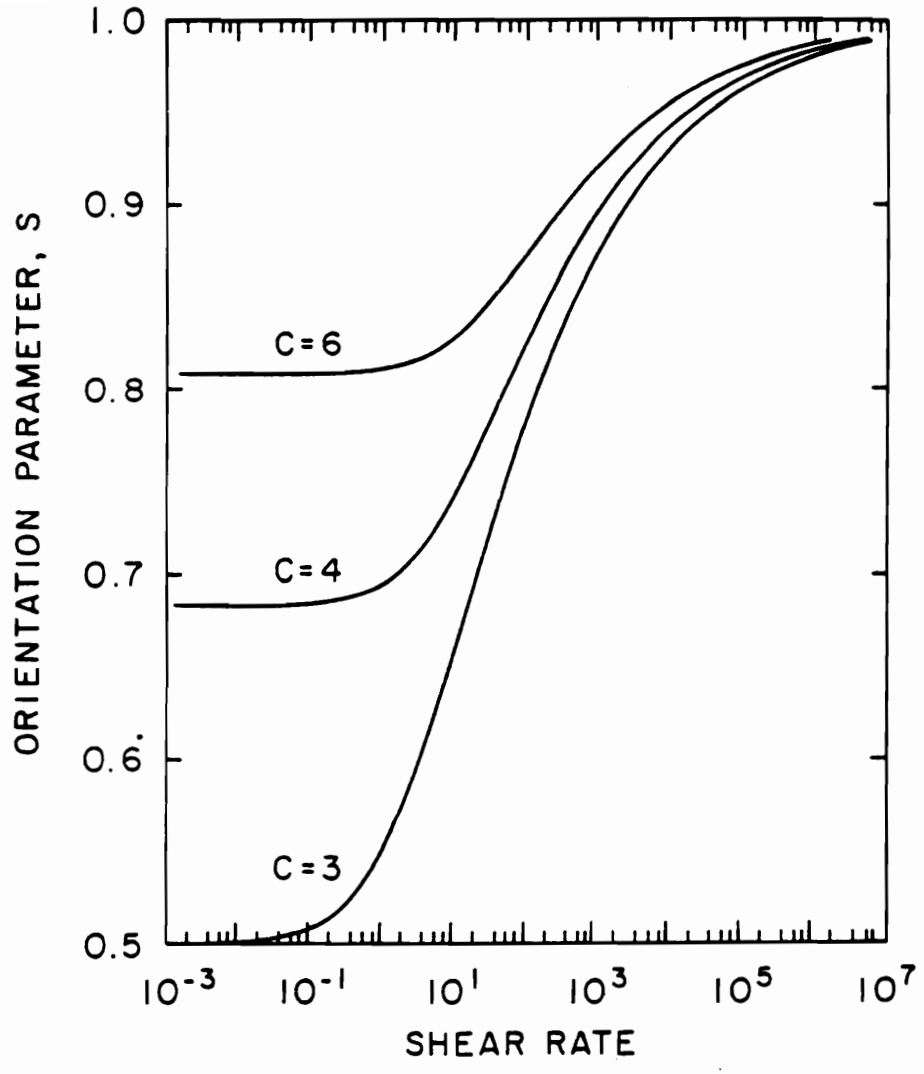

Figure 26. Prediction of the order parameter during steady elongational flow by the Doi Theory [42].

Metzner [186] have condensed the physical constants into four constants which can be determined empirically.

The effect of adding the solvent contribution term above is only significant at high deformation rates. For both shear and elongational flow, the stress no longer saturates and the material is predicted to exhibit an upper Newtonian plateau. Doraiswamy and Metzner [186] have shown that the Doi theory modified with this new term could adequately model the steady shear flow viscosity behavior of a lyotropic HPC solution up to moderately high rates. Additional support for the theory comes from evidence of a second "Newtonian" plateau in the viscosity versus shear rate curve at very high rates [44,178]. At the same time, it was earlier shown in section 2.1 that the slope of the viscosity versus rate curve in many TLCPs is about -0.5, while this theory predicts a slope of -1 in the moderate rate range where shear thinning is predicted. Also, the addition of this term only creates the need to evaluate one more constant. Therefore, the proposed modification by Doraiswamy is not kept for further consideration.

In the original derivation of the Doi theory all rigid rods are assumed to be the same length. In order to make the theory more applicable to real LCPs, Marrucci and Grizzuti [187, 188] have extended the Doi theory to account for polydispersity, the new theory being called the Doi-Edwards-Marrucci-Grizzuti (DEMG) theory. The theoretical details are extensive and are not given here, but some results are considered.

Marrucci and Grizzuti [188] and Fuller and coworkers [189-191] have examined the predictions of the DEMG theory for semi-dilute solutions and compared them to experimental results. Marrucci and Grizzuti [188] state that the results for steady shear flow and for stress relaxation upon cessation of steady shear flow using a bimodal distribution are very similar to the experimental data of Berry and coworkers [75,192,193]. In a more detailed study, Fuller and coworkers [189-191] used the rheo-optical method of two color flow birefringence to measure the orientation present in semi-concentrated collagen solutions during steady and transient shear flow. The collagen solutions were well characterized and showed bimodal polydispersity. A comparison of experimental results with the predictions of the DEMG model

show excellent qualitative and good quantitative agreement. Furthermore, the quantitative differences have been shown to be partly due to flexibility of the rod.

While the predictions of the DEMG model show good agreement with experimental behavior for semi-dilute solutions, extension of the theory to concentrated solutions adds tremendous difficulty to the calculations and none are available at this time. Additionally, such calculations are beyond the scope of the work proposed here. However, polydispersity is known to have a tremendous influence on the rheology of flexible chain systems [72] and this review would be incomplete without mention of this consideration.

One additional modification of the theory has not been effectively dealt with in the literature. The original equations from which the Doi theory is derived include a contribution to the stress for rod-solvent friction. This term is given in equation 2.3.16 [186]. Doi [39] justifies dropping the term by comparing the relative magnitudes of the coefficients and Doraswamy [186] further justifies dropping the term by stating that the same effects can be absorbed into the term for solvent contributions discussed above. Still, consideration of the term is mathematically simple and no convincing argument has been given for dropping it.

$$\frac{ck_BT}{2D_{ro}} < v_{\gamma\delta} u_\gamma u_\delta u_\alpha u_\beta > \qquad (2.3.16)$$

The Doi theory was developed and it was shown that the steady shear behavior of LCPs can be modelled by the theory over limited shear rate ranges. While the data of Prilutski [45] for elongational flow is questionable, the Doi theory was shown to be capable of modelling that behavior. However, the Doi theory in its present form can not accurately model the shear flow behavior of LCPs at high rates. At the same time a complete evaluation has not been made of the theory for its ability to predict or model transient flows. While modifications to the Doi theory have been proposed, they have either been proven not to improve agreement with experiment or have not yet been evaluated. Finally, it was noted that the Doi theory does not take into account spatial variations in the director which are known to be present in LCP systems. In view of the structural studies reviewed in section 2.2, modification of the theory

to account for multiple domains seems to be a requirement for accurate modelling of LCPs, at least for transient flows.

2.4 Objectives

In the first chapter liquid crystalline polymers were introduced and the general objectives of this work were given. Areas of the literature pertaining to these objectives were then reviewed in some detail in this chapter. These ideas are briefly discussed here in order to more fully explain the justification for the proposed research. The research objectives are then restated very specifically at the end of the section.

In this chapter it was shown that elongational flow is more effective than shear flow in producing a high degree of molecular orientation than shear flow in LCP systems. While a great deal of rheological characterization has been done on LCP systems in shear flow, almost nothing has been reported on the elongational flow behavior of LCPs. At the same time the industrial importance of TLCPs is growing and a knowledge of this behavior is necessary for optimization of equipment design, especially where complex flows are involved.

The shear flow behavior of these materials was reviewed and it was shown that the behavior measured is very much dependent on the state of the material, i.e. isotropic, liquid crystalline, or biphasic (LC + isotropic, LC + residual crystallinity). In view of those results a detailed knowledge of the shear flow behavior of a material should provide valuable information about the state of the material, and also would provide an indication as to whether the extensional flow behavior of a specific material could be generalized to other systems.

The structure of liquid crystalline polymers was reviewed and it was shown that the structure depends strongly on deformation and thermal history. The steady state structure present during shear flow and upon cessation of shear flow was reported, but only Onogi and coworkers [34] reported on the structure developed during elongational flow. Additionally, the

study was conducted on a drawn fiber, which already had some structure developed during flow through the capillary. Nothing has yet been reported on the development of structure in LCPs during the startup of steady elongational flow, yet a knowledge of the minimum strain necessary to break down the domain structure would be valuable for process design.

In view of the discussion above and the objectives stated in chapter 1, section 5, the following specific research objectives were developed:

1. to design and construct an extensional rheometer capable of measuring the extensional stress growth behavior of polymeric melts, particularly thermotropic liquid crystalline polymer (TLCP) melts;

2. to determine the extensional stress growth behavior of various TLCPs under isothermal conditions and at conditions where the material was preheated before testing at a lower temperature, and to establish whether this behavior is different from that determined for isotropic flexible chain melts;

3. to determine the extensional viscosity growth behavior of a material in both anisotropic and isotropic melt states and thereby establish whether the behavior is controlled by the rodlike conformation of the molecule or the anisotropic nature of the melt;

4. to determine the dynamic shear flow and transient shear stress growth/relaxation behavior of the same TLCPs which were tested in extension in order to help establish the nature of the melt (i.e. liquid crystalline (LC), LC with residual crystallinity, etc.);

5. to establish whether the shear behavior of the TLCPs determined above is specific to the systems investigated or general for all LCPs, implying that the extensional flow results could also be general;

6. to determine whether the Doi theory, in its original or in a modified form, is able to qualitatively and/or quantitatively model the extensional and shear stress growth behav-

ior of TLCPs and to establish whether the adjustable parameters determined from experimental shear flow behavior can be used in the theory to predict the extensional flow behavior;

7. to determine the effect of extensional flow on the orientation and morphology of extruded LCP films as a function elongational strain, which would effectively establish an upper limit for the orientation and structure changes which could be brought about during isothermal extension in the extensional rheometer;

8. to determine whether the method of small angle light scattering can give useful information about the changes in LCP domain geometry (in terms of size and aspect ratio) during uniaxial elongation in the extensional rheometer.

3.0 Experimental and Numerical Methods

In this chapter the experimental and numerical methods are described for fulfilling the research objectives stated in the last chapter. In section 3.1 the properties of the LCP materials used in this study are presented and other characterization studies carried out on the materials are described. Next, shear characterization tests for the LCPs are detailed. In section 3.3 the design of the extensional rheometer is briefly described and a general test procedure is given. The equipment and tests for the morphological characterization of drawn LCP films is presented in section 3.4. Finally, section 3.5 describes the method used for solving the equations representing the Doi theory. Additionally, modifications to the theory for the addition of a rod-solvent friction contribution to stress and for a multidomain average over stress are also described.

3.1 Materials and Characterization

The materials used in this study were a copolyester of 60 mole % HBA and 40 mole% PET (referred to as 60HBA/PET), hydroxypropylcellulose (HPC), a copolyester of 73 mole %

HBA and 27 mole % HNA (referred to as HBA/HNA), and linear low density polyethylene (LLDPE). The materials were chosen for a number of reasons including availability, suitability for use in available instruments, and availability of knowledge about the materials from previous studies. Each one of the materials is described below and a summary of pertinent material properties of the LCPs is given in Table 3, with the chemical structure of the repeat units given in Figure 27. Each of the materials used here came from a single production batch in order to eliminate any effects due to changes in molecular weight, molecular weight distribution, composition, and sequence distribution which could vary between different batches.

3.1.1 Materials

The first LCP used in the study was 60HBA/PET, a thermotropic copolyester supplied by Eastman Chemical Company with the nominal composition given above. 60HBA/PET was synthesized by a melt condensation reaction as described by Jackson [26]. It is believed to have a number average weight of approximately 20,000 and a polydispersity ratio ($\overline{M}_W/\overline{M}_N$) of about 2, as would be expected for a condensation type polymer [26]. The sequence distribution of the polymer is reported to be random [194], however, later work has shown that some HBA blockiness can develop by transesterification if the material is annealed below 255 °C [179], the melting point of residual HBA crystallinity. 60HBA/PET has a complex melt structure which likely consists of both liquid crystalline HBA rich domains and isotropic PET rich domains [195], yet was used here because of relatively low melt temperature, availability, and the wealth of previous work performed on this material. Because of the potential for chain scission by hydrolysis in 60HBA/PET, the material was always dried in a vacuum oven for a minimum of 24 hours at 120 °C prior to processing or rheological testing.

The second material used was hydroxypropylcellulose (HPC), which was used because of its relatively low melting point and because it is possible to test the material in both the LC and isotropic melt states. HPC is a cellulose ether and was prepared by the

Table 3. Properties of TLCPs Used in this Study

Property	60HBA/PET	HPC EF	HPC G	HBA/HNA
Source	Eastman Chemical	Aqualon	Aqualon	Hoechst Celanese
Commercial Name	X7G	Klucel EF	Klucel G	Vectra A900
$\overline{M}_w$	40,000[1]	80,000[1] 116,000[2] 102,000[3]	370,000[1] 470,000[2]	30,000[1]
$\overline{M}_w/\overline{M}_N$	2[1]	3.34[3]	5-8[1]	2[1]
Composition	62.8% HBA 37.2% PET	MS 3.16	MS 4	73% HBA 27% HNA
Tg [°C]	62[4]	94[4]	97[4]	97[4]
Tm [°C]	252	150-160	150-160	283
Tni [°C]	420	197[4]	201[4]	-
ρ [g/cc]	1.4 (25°C)	1.15 (25°C) 1.015(190°C)	1.17 (25°C) 0.995 (240°C)	1.39 (25°C) 1.27 (320°C)
$\alpha_l \times 10^4$ [K^{-1}]	-	2.3	2.3	1.42

[1]Nominal values
[2]Determined from intrinsic viscosity
[3]Determined from GPC.
[4]Determined from DSC.

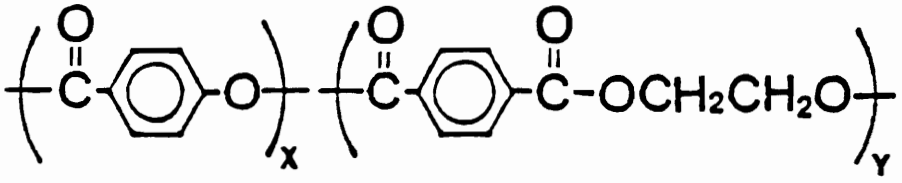

a) 60HBA/PET (x=0.60, y=0.4)

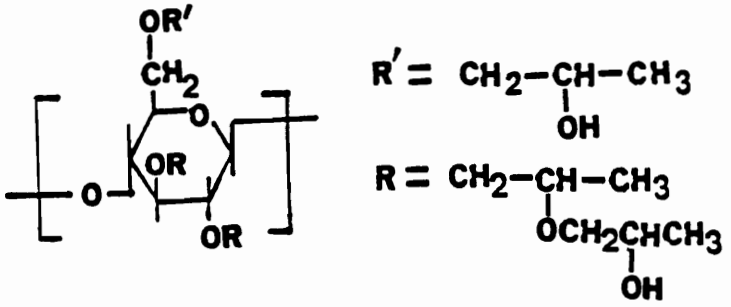

b) HYDROXYPROPYLCELLULOSE (MS=4)

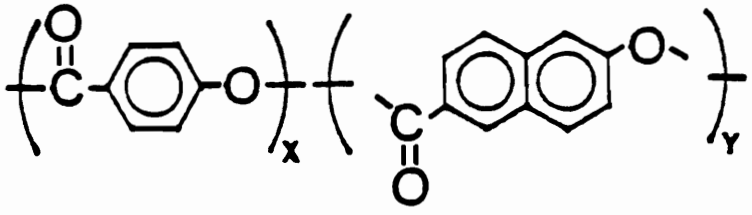

c) HBA/HNA (x=0.73, y=0.27)

Figure 27. Chemical structures of a) 60HBA/PET, b) HPC, and c) HBA/HNA.

hydroxypropylation of cellulose as described by Klug [196]. Two different molecular weight samples of HPC were obtained from the Aqualon Company (Wilmington, DE) and used in this study, HPC EF and HPC G. HPC EF has a nominal $\overline{M}_w$ of 80,000 (value of 102,000 measured by means of GPC and value of 116,000 measured by means of intrinsic viscosity as described later) and molecular substitution of 3.16 (MS = number of hydroxypropyl groups per repeat unit) [197,198], while HPC G has a nominal $\overline{M}_w$ of 370,000 (value of 470,000 measured by intrinsic viscosity) and MS of 4. The polydispersity ratio of both materials is reported to be in the range of 5-8 [198], however, a value of 3.34 was found for HPC EF from a GPC trace [197]. HPC is hydroscopic and was therefore dried for at least 8 hours at 110 °C in a vacuum oven prior to processing or rheological testing.

The third polymer used was HBA/HNA, supplied by Hoechst Celanese and produced commercially under the name Vectra A900. HBA/HNA has a weight average molecular weight of ca. 30,000 and polydispersity ratio of about 2 [178]. The synthesis of HBA/HNA is by melt condensation as detailed by Calundann [7]. The sequence distribution of the HBA and HNA moities has been reported to be completely random [7,199]. HBA/HNA is a fully aromatic copolyester and the melt is believed to wholly nematic [7]. For this reason the behavior of the HBA/HNA material is expected to be more characteristic of the nematic liquid crystal state and therefore this material was also used. HBA/HNA samples were always dried at 125 °C under vacuum for a minimum of 24 hours prior to processing or rheological testing in order to minimize chain scission by hydrolysis.

The last material used was LLDPE, a linear low density polyethylene supplied by the Mobil Company under the name NTA 101. The LLDPE was reported to have a $\overline{M}_w$ of 120,000 and a polydispersity ratio of 4.1 [204]. This material was used in this study as a standard for evaluating the performance of the ER. It was chosen for number of reasons, including 1) the possibility of testing it in the ER, in the Rheometrics Extensional Rheometer (RER), and in the RMS; 2) the material is linear and its melt is thought to behave in a linearly viscoelastic manner up to moderate deformation rates; and 3) its shear viscosity is of the same magnitude as that of the LCPs studied.

3.1.2 Material Characterization

Because of the variation in material properties between batches and the necessity of accurately knowing thermal transitions, DSC measurements were made on each of the polymers used. DSC measurements were carried out on a Seiko DSC 210 instrument. The materials were put through two heating and cooling cycles in order to remove thermal history effects, with a heating/cooling rate of 20 to 40 °C per minute used for the first cycle and a rate of 10 to 20 °C per minute used for the second cycle. Thermal transitions were then determined from the second heating curve.

In order to better establish the state of the TLCP melts, films of the polymers were observed in the optical microscope as the temperature of the material was raised through the melting and liquid crystal to isotropic state transitions. This work was conducted on a Zeiss optical microscope on polymer films of 25 to 100 μm thickness and photographically recorded. Heating rates were typically on the order of 5 °C per minute.

Intrinsic viscosity measurements were made on solutions of the two HPC resins in order to get an accurate value of molecular weight, which is obtained from the correlation $\overline{M}_w = 38{,}500\,[\eta]^{1.093}$ determined by Wirick [200]. Three solutions of each polymer were prepared in the concentration range of 0.05 to 0.4 g/dl using a 50 volume % mixture of ethanol in water as a solvent. Viscosity measurements were made using a Cannon-Fenske Routine Viscometer for Transparent Solutions at 25 °C following the standard method as described by Rodriguez [201]. Results for HPC EF were confirmed by comparison with GPC results performed at the Aqualon Company [197]. No such measurements were made on the thermotropic copolyesters because of their insolubility in common solvents.

Wide angle x-ray scattering patterns were taken of HPC disks which had been quenched from different melt temperatures in an attempt to determine whether there was residual crystallinity in the melt. Samples were annealed for 10 minutes in the RMS oven under nitrogen at temperatures of 190 and 210 °C for HPC EF and 200 and 240 °C for HPC G, representing

the liquid crystal and isotropic melt states for each material, respectively. Upon removal from the oven samples were quenched in liquid nitrogen and stored at room temperature until testing. WAXS patterns were taken with a Phillips PW 1720 x-ray generator set at 40 kV and 20 milli-amperes and photographically recorded using a Wahrus camera. Exposure times varied from 2 to 4 hours, depending on sample thickness. Calculations of d-spacings were made using Braggs law ($n\lambda = 2d\sin\theta$), where n is a positive integer, λ is the wavelength of radiation ($\lambda = 1.541$ Å), and 2θ is the scattering angle.

3.2 Shear Rheology

The LCPs were characterized via two types of transient flow tests. Dynamic oscillatory shear flow tests were conducted on the LCPs in order to determine the general viscosity versus angular frequency relationships and also in order to help determine the melt state of each material at the temperatures used for elongational flow tests. Transient shear tests were performed for a comparison with extensional viscosity growth tests and also as an additional criteria for evaluation of the Doi theory. Most shear testing was performed on a Rheometrics Mechanical Spectrometer (RMS) model 800, with some earlier testing done on a model 605. Generally, parallel plate geometry was used for oscillatory flow tests while cone and plate geometry was used for the shear stress growth/relaxation tests. The plates were 25 millimeters in diameter and a 1 millimeter gap was used for parallel plate testing, while a 0.1 radian cone was used for cone and plate testing. The instruments measure the torque, normal force, and displacement of a sample as a function of time. The equations relating these quantities to the rheological quantities reported below can be found in [72,105] and general test procedures are given in [202]. The reproducibility of the results was confirmed by running 2 or 3 separate tests at each test condition.

The materials tested in shear were prepared in the following way. Those materials which were received in pellet form were inserted into the appropriate fixture and molded in the test fixtures just prior to testing. This was the case for LLDPE, 60HBA/PET, and HBA/HNA. Since the HPC was received in powder form, it was compression molded into 25 millimeter diameter 1 millimeter thick disks for RMS testing. The disks were molded in a hot press under approximately 2000 psi pressure and at 160 °C. Care was taken not to expose the HPC disks to the atmosphere and they were dried in a vacuum oven at 110 °C for 8 hours prior to testing.

3.2.1 Dynamic Oscillatory Shear Rheology

Several dynamic oscillatory shear tests were performed on the TLCPs as background work for the transient shear and elongational flow stress growth experiments and to help determine the state of the LCP melts. Tests were conducted at each of the temperatures used for extensional testing. The dynamic tests performed were strain sweeps, frequency sweeps, time sweeps, and temperature sweeps (only on the HPC materials) with each of these described below.

Dynamic strain sweep tests were performed in order to determine the range of strains for which the material response is strain independent, thereby determining the range of strain that the material behaves in a linear manner (i.e. the stress and strain curves have the same shape), which is a necessary condition for the test to be valid. The strain levels used in the other dynamic oscillatory tests were then kept within this linear range. Sweeps were conducted on the materials using a cone and plate geometry and at frequencies of 1, 10, and 100 Hz while strains ranged from 0.001 to 0.5 strain units.

Dynamic frequency sweep tests were conducted in order to determine the general viscosity versus angular frequency behavior of the material and also to help determine whether there was any residual crystallinity in the melt state as evidenced by the behavior of G' and G'' at low frequencies. The measured quantities were generally the dynamic

viscosity (η^*), the dynamic storage modulus (G′), and the dynamic loss modulus (G″) versus frequency. Tests were conducted over the frequency range of 0.1 to 100 rad/s, with the lower frequency limit of 0.1 used both because of the limited sensitivity of the force transducer and because of the large times necessary for testing at lower rates, which could result in material degradation or loss of material from the gap between plates. A parallel plate geometry was used and maximum strain at the plate edge varied according to the material.

Dynamic time sweeps were also done in order to confirm the stability of the polymer melts at the test temperatures as a function of time. Again, the quantities examined were η^*, G′, and G″. Sweeps were carried out in the parallel plate geometry using the same strain amplitude as the frequency sweeps and for a duration of 30 to 60 minutes. Frequencies of 10 rad/s were also used. By following the values of η^*, G′, and G″ as a function of time evidence was obtained for determining whether degradation and/or melt crystallization occur in the LCP melts during aging.

As discussed in Chapter 2 section 1, the viscosity of the isotropic melt of a polymer can be higher than the viscosity of the nematic state. Dynamic temperature sweep tests were therefore carried out in order to better define this transition. Also, there has been some question of whether or not the HPC material is in a nematic or a cholesteric state when anisotropic melts have been observed. Since the cholesteric state has been found to have a higher viscosity than the isotropic state in low molecular weight liquid crytals, the observation of a lower melt viscosity in the anisotropic versus the isotropic melt states would provide evidence that the anisotropic HPC melts are nematic. The temperature ranges used for testing were 160 to 220 °C for HPC EF and 160 to 240 °C for HPC G, which range from the softening point of the materials to well into their isotropic melt states. The sweep rate was 5 °C per minute, and sweeps in both directions were carried out to determine whether there was hysteresis, which would be a strong sign of the presence of residual crystallinity. Tests had to be carried out in a parallel plate geometry because of changes in the gap dimension due to thermal expansion. A frequency of 10 rad/s was used in all cases and maximum strain amplitude at the plate edge was 4 % for HPC EF and 2 % for HPC G.

3.2.2 Transient Shear Tests

Transient stress growth/relaxation experiments were carried out on the LCPs at the same temperatures and deformation rates as were used for elongational flow tests, a summary of which is given in Table 4. A cone and plate geometry (25 millimeter diameter, 0.1 rad cone) was used so that the material was subjected to a homogeneous deformation. Care was taken to give the polymer samples approximately the same thermal history as experienced by samples placed in the extensional rheometer. The quantities of interest in these tests are the shear stress (or equivalently the shear viscosity) and the first normal stress difference.

The procedure used in the transient tests is briefly described here because of its non-standard nature. Samples were placed in the pre-heated fixtures of the RMS and molded. The gap was set, and samples were allowed to relax so that there was a total time period of 10 minutes from the time the sample temperature first reached test temperature until the run was started. The shear history applied to the material is demonstrated in Figure 28. At the start of the run the sample was subjected to a steady shear rate deformation which lasted for a period of time equal to 20 (in some cases 40) strain units. Deformation was then stopped and the material relaxed for the same period of time. Finally, a second period of flow was applied to some of the materials in order to better test the normal stress behavior. New samples were used for each run and at least 2 runs were made at each of the conditions.

3.3 Extensional Rheology

The main objective of this work was to determine the uniaxial extensional flow behavior of LCPs. Transient elongational viscosity growth tests were conducted on the HPC materials and also on also on HBA/HNA to to fulfill that objective. Tests were were carried out using a

Table 4. Conditions for Transient Elongational and Shear Flow Tests.

Material	Temp. [°C]	Rate [s^{-1}]
60HBA/PET#	275	0.053, 0.2, 0.53
HPC EF	190	0.0249, 0.0643, 0.141, 0.487
	210	0.0239, 0.0638, 0.168, 0.510
HPC G	200	0.00784, 0.0158, 0.142
	240	0.00848, 0.0170, 0.164
HBA/HNA	300	0.0290, 0.0840, 0.151, 0.482
	320	0.054, 0.173, 0.450

No successful elongational flow tests were made on 60HBA/PET.

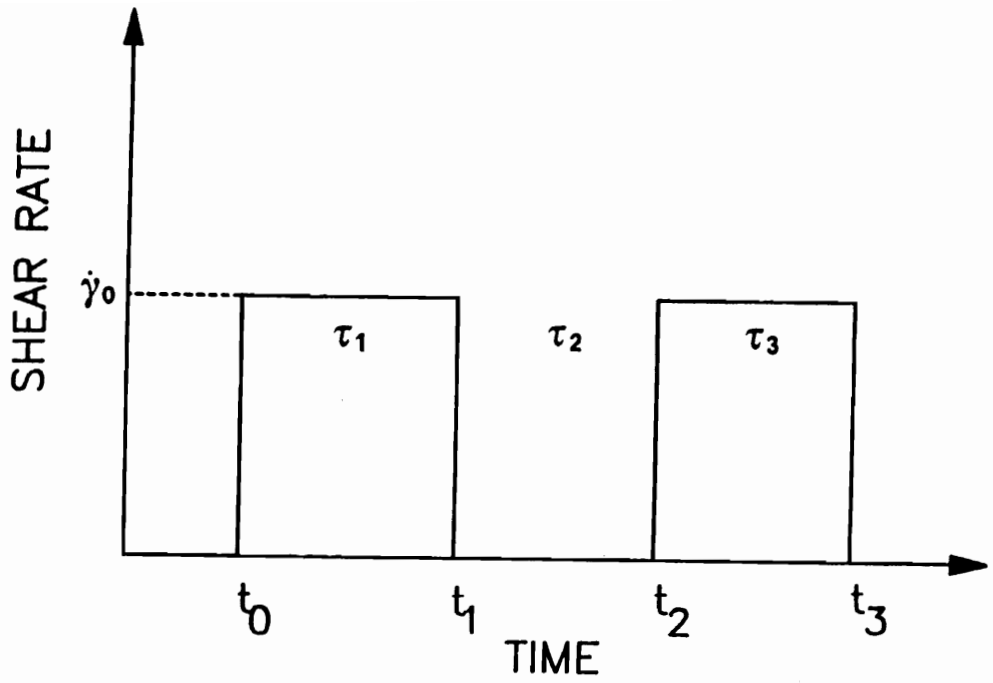

$$\tau_1 = \tau_2 = \tau_3 = \frac{20}{\dot{\gamma}_0}$$

Figure 28. Deformation applied to a LCP during transient shear stress growth/relaxation test.

newly designed dual rotary clamp extensional rheometer, referred to hereafter as the ER. A schematic of the basic design of the ER is shown in Figure 29 and a photograph of the actual device is shown in Figure 30. Details of the design and operation of the ER as well as procedures for collecting and processing data are deferred until Appendix B, so that they can be given adequate treatment. Only a brief description of these are given in this section.

While many of the design features of the ER are due to Meissner [40,203] and Laun and Münstedt [41], the rheometer also has one key feature not included in those rheometers. The ER is capable of operation up to temperatures of about 320 °C, almost 100 °C higher than previously used by Meissner [40,203], Laun and Münstedt [41], or others [120,121]. Several design features make this possible, including building materials, choice of immersion oil, and location of the LVDT outside of the oil reservoir. One additional feature not previously seen by the author was to conduct tests with the polymer sample located at the interface between two mutually immiscible oils, one with a higher density and one with a lower density than the polymer melt. Doing so provided for a much more uniform temperature in the sample and also prevented contact with air, which decreased polymer degradation.

Another modification to the ER with respect to the rotary clamp rheometers of Meissner [203] and Laun and Münstedt [41] was to have one end glued to an aluminum clip and held fixed, as was previously done by Ide [121] and Carter [120]. This configuration provided for an order of magnitude increase in the sensitivity of force measurement over the dual rotary clamp setup. Therefore, the "fixed end" configuration was used for collection of all of the data presented in this dissertation.

The sample geometry and preparation of the polymer samples used for elongational flow tests are briefly described next, while a more detailed description is given in Appendix B. The sample geometry was cylindrical, with samples approximately 9" long and 0.39" in diameter. Samples were prepared either by molding in the barrel of an Instron Model 3211 Capillary Rheometer (LLDPE and HBA/HNA) or by extrusion from a Killion 1" laboratory extruder through a 1/4" capillary die with a 15.4 L/D ratio (HPC EF and HPC G). Samples were then glued to aluminum T-clips on one end using either epoxy cement (LLDPE and HPC materials)

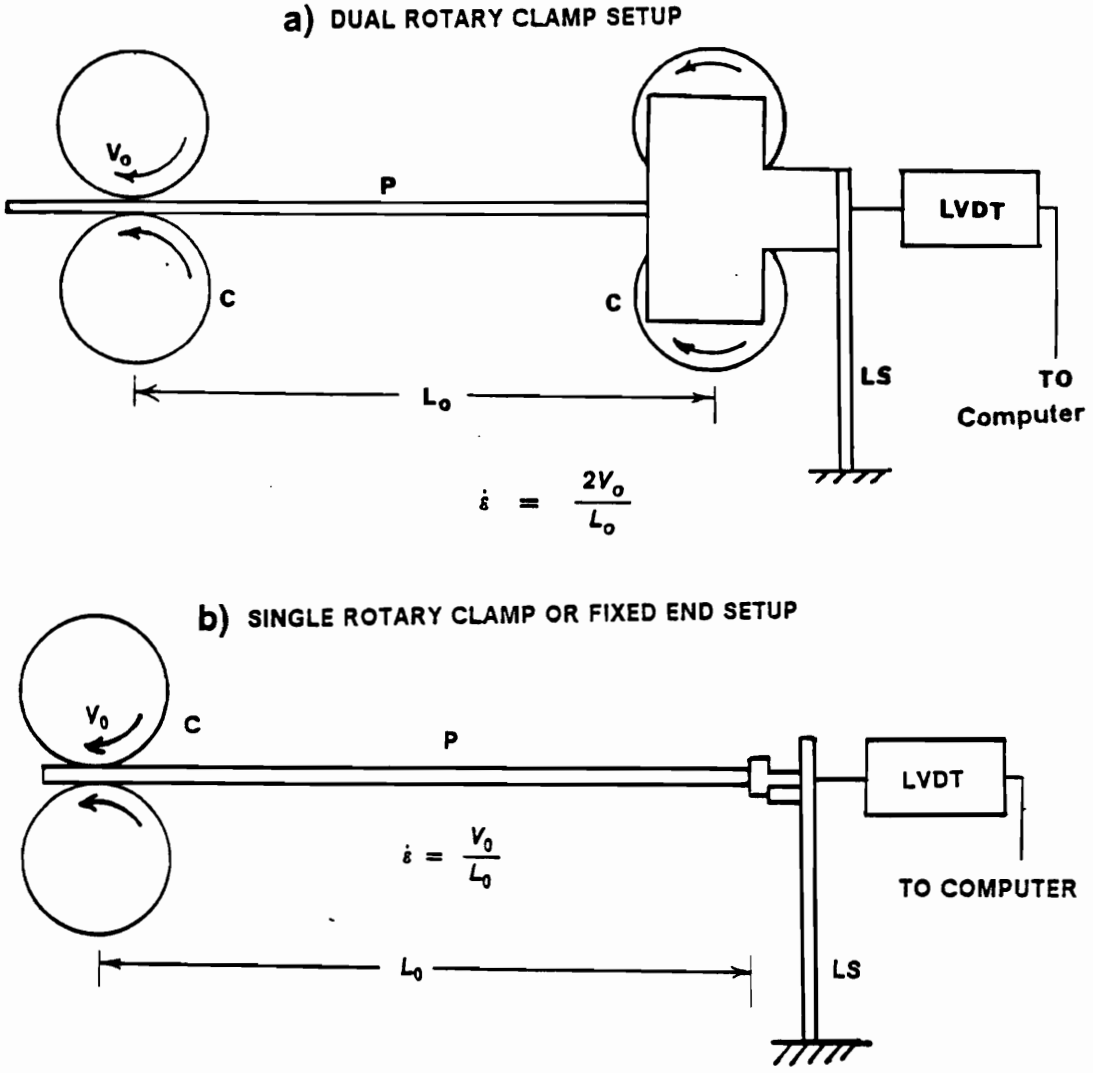

C - rotating clamps
LS - leaf spring
LVDT -linear voltage displacement transducer
P - polymer sample
L_o - length of sample

Figure 29. Basic design of the ER in a) dual rotary clamp and b) single rotary clamp configurations.

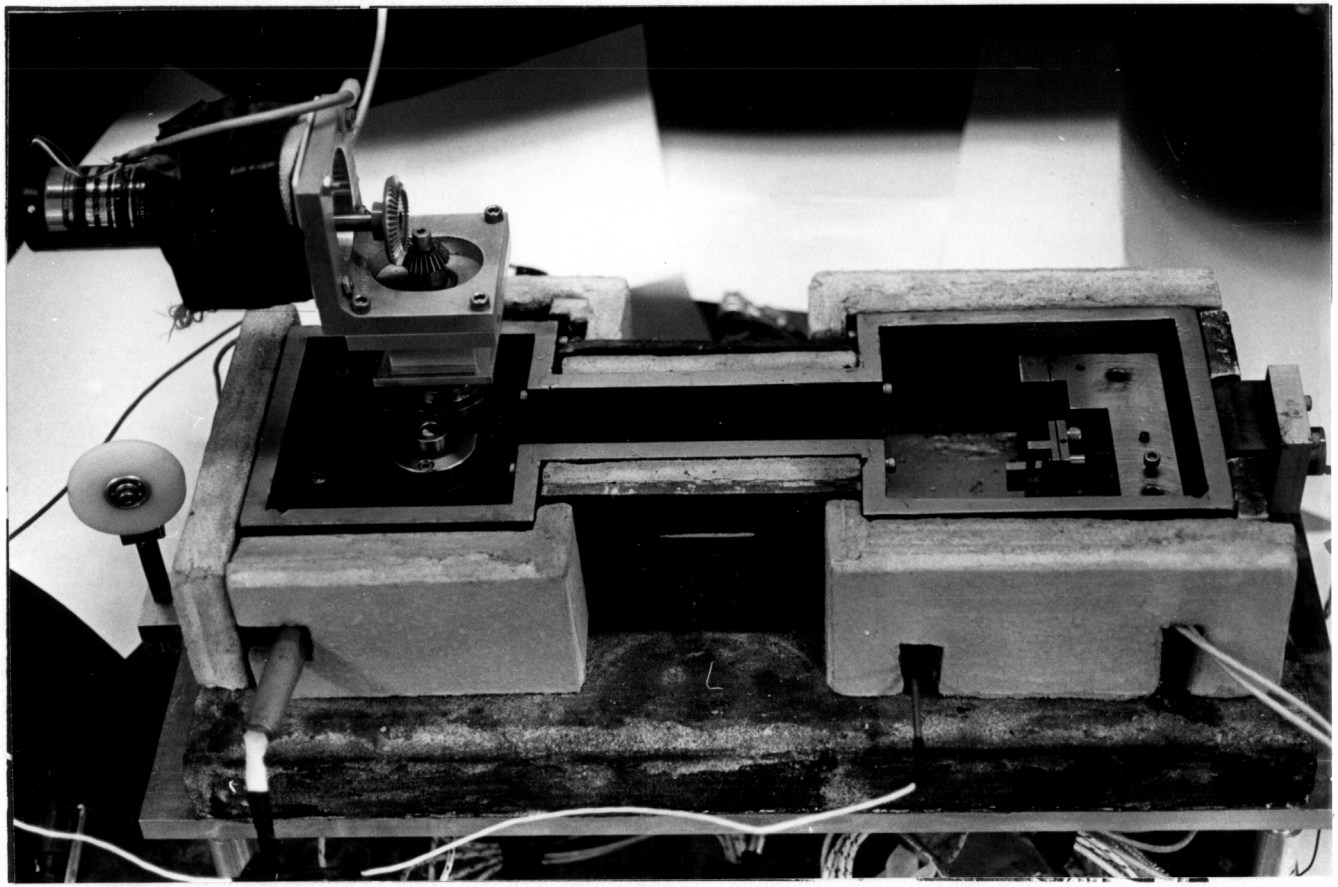

Figure 30. Photograph of the extensional rheometer (ER) constructed at VPI in single rotary clamp configuration.

or using a high temperature bismaleimide adhesive (Crest #4446). Before elongational testing the samples were always dried as previously described for each material in order to reduce degradation and bubble formation (in HPC materials).

Here the test procedure is briefly summarized for extensional testing of LCP materials with the ER set up in the single rotary clamp configuration shown in Figure 30:

1. The ER oil reservoir was heated up to test temperature;
2. The leaf spring was calibrated using a set of weights;
3. A sample was inserted into the rheometer oil reservoir and attached to the leaf spring.
4. The elongational flow test was run on the sample, with data output to a computer and stored as displacement versus time. A video recording of the cross sectional area of the sample was also recorded using a video camera and stored on video tape;
5. Post collection noise reduction was performed on the ER LVDT displacement data using Fast Fourier Transforms;
6. Video data was analyzed to determine true deformation rate.
7. Calculations were performed the data (after noise reduction), including corrections for deformation rate, with final results in the form of transient elongational viscosity versus time.

A couple of other details about the test procedure and results should be noted. First, the elongational flow tests on the LCPs were carried out at constant temperature and at constant elongation rate. Second, in order to ensure reproducibility for the LCPs, at least three separate runs were made for each material at each temperature and at each rate. Generally, the tests are reproducible within $\pm 20\%$ up to moderate strains, where fracture or necking occurs. The final results reported in Chapter 4 are then the average values of the 3 best runs for each material and condition. A summary of test conditions is given in Table 4 on page 107.

In order to establish the absolute accuracy of the extensional rheometer, tests were conducted on a sample of LLDPE (the NTA 101 material previously described) in the ER, in the Rheometrics Extensional Rheometer (RER Model 9000), and also transient shear tests were

conducted in the RMS as described in section 3.2. All tests were conducted at 170 °C and at deformation rates ranging from 0.01 to 0.5 s^{-1}.

Since elongational flow testing is not yet considered a routine type of test, the RER Model 9000 instrument is briefly described here. The RER Model 9000 is a Münstedt type extensional rheometer with a basic design as described in [72]. The polymer sample is glued at each end to an aluminum clip and is placed into a heated oil bath, with the oil chosen to have approximately the same density as the polymer melt. At the start of the test the material is drawn on one end and the other is attached to a force transducer. Constant elongation rate tests were conducted, which result in the sample length increasing exponentially as a function of time. The calculation of the transient extensional viscosity as well as other details of the test procedure can be found in [72,205].

A comparison of the results from the ER, the RER, and $3\eta^+$ (from the RMS) are shown in Figure 31 at a deformation rate of 0.02 s^{-1}. At such low rates the LLDPE is expected to behave in a linearly viscoelastic manner, i.e. $\bar{\eta}_e^+ = 3\eta^+$, where $\bar{\eta}_e^+$ is the elongational viscosity growth function. The ER results are shown as solid lines while the others are represented by symbols as defined in Figure 31. It can be seen that there is good agreement between the results from the three different instruments. Results at other rates not shown give nearly as good agreement. Therefore, ER is shown be able to accurately measure the elongational viscosity of a polymer melt. Further information on the range of operation is given in Appendix B.

3.4 Drawn Film Characterization

A study of the morphology of drawn LCP films was carried out as background work for the *in situ* SALS tests which were attempted. The drawn films represent the maximum degree of orientation which could be expected in the isothermally extended material. Also, the

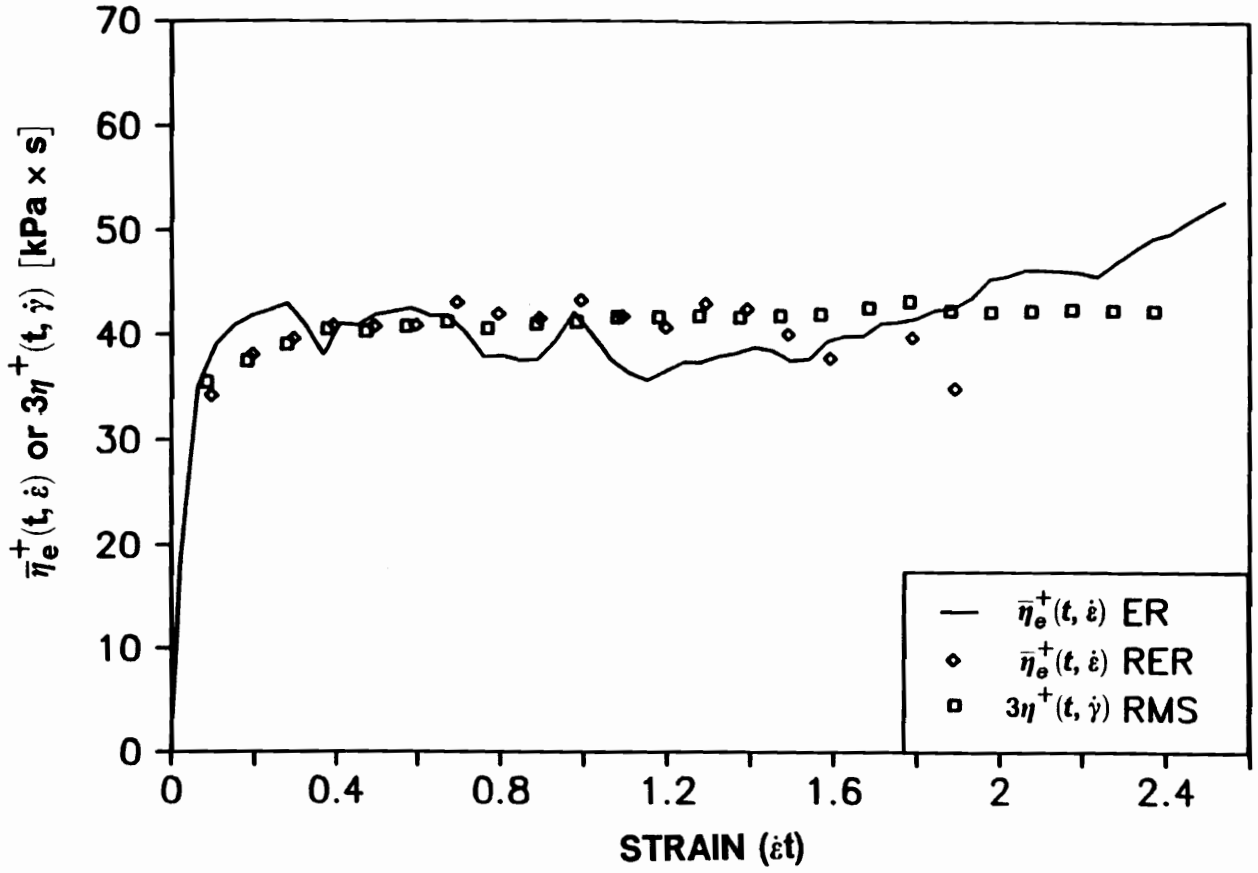

Figure 31. Elongational and shear viscosity growth for NTA 101 LLDPE at 170 °C and 0.02 s^{-1}.: Data denoted by solid line for $\bar{\eta}_e^+$ (ER), ◇ for $\bar{\eta}_e^+$ (RER), and □ for $3\eta^+$ (RMS).

morphology of the solid films can be characterized with several different methods so that a more definite structure can be assigned to SALS patterns determined from LCP melts.

In order to reduce the scope of the study to a manageable level only films of 60HBA/PET and HBA/HNA were produced and characterized. Films were made by extruding the polymers through a 0.030" by 4" flat film die attached to a Killion 1" Laboratory extruder and then drawing the samples using a set of takeup wheels. The temperatures of the three extruder zones and in the die were 200, 260, 260, and 190 ^{0}C for 60HBA/PET and 200, 280, 280, and 232 ^{0}C for HBA/HNA, respectively. The resulting films had draw ratios (cross sectional area of the die divided by the cross sectional area of the film) of approximately 3 to 110. Three different films of each material, each with a different draw ratio, were characterized in this study.

The extruded films were characterized by several methods. First, wide angle x-ray scattering (WAXS) was used to obtain a qualitative measurement of the degree of molecular orientation in the films. The theoretical basis for measurement of molecular orientation is discussed by Mitchell [206]. WAXS patterns were taken on the same equipment described in section 3.1, with exposure times ranging from 4 to 24 hours depending on film thickness. Films were aligned so that the direction of the beam was perpendicular to the plane of the film. Also, patterns were taken on one of the film samples in three orthogonal directions: 1) beam perpendicular to the film plane, 2) beam along the width direction of the film and 3) beam along the draw or length direction. This was done in order to determine whether the molecules were oriented predominantly within the plane of the drawn film.

Polarized optical microscopy (POM) was used in order to characterize the geometry of supermolecular structures such as the LCP domains. Samples of the films were microtomed to a thickness of 5 microns and placed between a glass slide and coverslip. Samples were observed in a Zeiss optical microscope between crossed polarizers at magnifications of 125x and 250x. Also, samples were examined with the draw directions both at 0^{0} and 45^{0} with respect to the polarizer directions. Optical textures were recorded photographically.

The texture present in the drawn films was also examined by scanning electron microscopy (SEM). The film samples were examined with a Cambridge Stereoscan 200 mi-

croscope. Fracture surfaces of the films were prepared by fracturing in liquid nitrogen with fracture occurring in the plane of the film. For the case of 60HBA/PET films, samples were etched in n-propylamine for 4 hours to remove PET rich regions, leaving mainly HBA rich LC domains as determined by Joseph [135]. A 150 Angstrom gold film was coated onto the sample surfaces in a sputter coater prior to examination in the SEM to prevent charge buildup.

Small angle light scattering (SALS) patterns were taken of the same microtomed films examined in the optical microscope. Samples were placed on glass slides and a drop of immersion oil with approximately the same refractive index was placed on the sample. A second slide was then placed on top and the slides were taped together. SALS patterns were taken with a setup similar to that shown in Figure A1 of Appendix A, using a HeNe laser light source providing polarized monochromatic light at a wavelength of 6328 Angstroms. The sample to film distance was 15.4 cm and patterns were recorded using a Polaroid camera. SALS patterns were only taken in H_V mode since V_V patterns would be affected by density fluctuations in the immersion oil.

3.5 Numerical Work

The Doi theory, both in its original and in modified form, was evaluated for its ability to both predict and model the steady and transient shear and elongational flow behavior of TLCPs. By "predict" it is meant that parameters were calculated from molecular characteristics as specified in the theory. By "model" it is meant that parameters were experimentally determined in order to obtain the best possible fit. Parameters which were examined in this way include the product ckT, the interaction potential U, the rotary diffusion coefficient D_r, and a parameter given as A ($=D_r/D_{ro}$) which is a front factor for the rod-solvent contribution to the stress tensor as discussed.

The evaluation of the Doi theory was limited in scope to a comparison with the HPC EF material at 190 °C (liquid crystal state), HPC EF at 210 °C (isotropic state), and the HBA/HNA copolyester at 320 °C. It was felt that this provided for a thorough evaluation of the theory with respect to experimental behavior.

3.5.1 Modified Equations

As previously shown in section 2.3, the equations making up the Doi theory are given in equations 2.3.13 to 2.3.15. Modifications of the theory were discussed in section 2.3 and two are examined here. The first simply involves retaining the rod-solvent friction term given in equation 2.3.16 in the stress tensor equation (2.3.15). In order to do this the fourth order average in equation 2.3.16 was decoupled as in equation 2.3.12, giving the following for the components of the stress tensor :

$$\sigma_{\alpha\beta} = 3ckT\left[S_{\alpha\beta}(1-\frac{U}{3}) - U(S_{\alpha\mu}S_{\beta\mu} - \frac{1}{3}\delta_{\alpha\beta}S^2_{\mu\nu}) + US_{\alpha\beta}S^2_{\mu\nu}\right] + \frac{AckT}{2D_r} v_{\mu,\nu}(S_{\mu\nu}+\frac{1}{3}\delta_{\mu\nu})(S_{\alpha\beta}+\frac{1}{3}\delta_{\alpha\beta}) \quad (3.5.1)$$

where A is the ratio D_r/D_{ro} and lies in front of the term for rod-solvent friction. The second modification examined is using a multidomain average in order to simulate the actual structure initially present in LCP melts. A number of domains, n, is chosen such that the overall orientation in the system is random, or stated more exactly:

$$\sum_{k=1}^{n} S^k_{\alpha\beta}(t=0) = 0 \quad \text{for all values of } \alpha \text{ and } \beta \quad (3.5.2)$$

where $S_{\alpha\beta}$ is the orientation order parameter tensor.

In order to determine the components of stress, a choice has to be made for the addition of the stress contributions from the different domains. If interdomain effects are ignored, the same two limits can be defined which were used by Larson [209] for oscillatory flow. These are the Voigt and Reuss averages. In the Voigt average each domain experiences the same deformation rate (and strain), while in the Reuss average each domain experiences the same stress state. The first case represents the upper limit of stress and the components of the stress tensor are simply given by:

$$\sigma_{\alpha\beta} = \sum_{k=1}^{n} \sigma_{\alpha\beta}^{k} \tag{3.5.3}$$

The second case represents the lower limit of stress for this model, but was not calculated.

The equations for the derivatives of $S_{\alpha\beta}$ which must be solved are written out here in full form. Since calculations are made for transient flows, all five independent components of $S_{\alpha\beta}$ must be kept, with the third diagonal term presented as a completeness. For simple steady shear flow, these equations are:

$$\begin{aligned}\frac{\partial S_{11}}{\partial t} &= -6\bar{D}_r\left[(1-\frac{U}{3})S_{11} - U(S_{11}^2 + S_{12}^2 + S_{13}^2 - \frac{1}{3}S_{\mu\nu}^2 - S_{11}S_{\mu\nu}^2)\right] \\ &\quad + \dot{\gamma}S_{12}(\frac{4}{3} - 2S_{11})\end{aligned} \tag{3.5.4}$$

$$\frac{\partial S_{22}}{\partial t} = -6\bar{D}_r\left[(1-\frac{U}{3})S_{22} - U(S_{12}^2 + S_{22}^2 + S_{23}^2 - \frac{1}{3}S_{\mu\nu}^2 - S_{22}S_{\mu\nu}^2)\right] - \dot{\gamma}S_{12}(\frac{2}{3} + 2S_{22})$$

$$\frac{\partial S_{33}}{\partial t} = -6\bar{D}_r\left[(1-\frac{U}{3})S_{33} - U(S_{13}^2 + S_{23}^2 + S_{33}^2 - \frac{1}{3}S_{\mu\nu}^2 - S_{33}S_{\mu\nu}^2)\right] - \dot{\gamma}S_{12}(\frac{2}{3} + 2S_{33})$$

$$\frac{\partial S_{12}}{\partial t} = -6\bar{D}_r\left[(1-\frac{U}{3})S_{12} - U(S_{11}S_{12} + S_{12}S_{22} + S_{13}S_{23} - S_{12}S_{\mu\nu}^2)\right] + \dot{\gamma}(\frac{1}{3} + S_{22} - 2S_{12}^2)$$

$$\frac{\partial S_{13}}{\partial t} = -6\bar{D}_r\left[(1-\frac{U}{3})S_{13} - U(S_{11}S_{13} + S_{12}S_{23} + S_{13}S_{33} - S_{13}S_{\mu\nu}^2)\right] + \dot{\gamma}S_{12}(S_{23} - 2S_{12}S_{13})$$

$$\frac{\partial S_{23}}{\partial t} = -6\bar{D}_r\left[(1-\frac{U}{3})S_{23} - U(S_{12}S_{13} + S_{22}S_{23} + S_{23}S_{33} - S_{23}S_{\mu\nu}^2)\right] - \dot{\gamma}2S_{12}S_{23}$$

where $\bar{D}_r$ was defined in equation 2.3.11b as $D_r[1 - 3/2S_{\mu\nu}^2]^{-2}$, and assumming symmetric $S_{\alpha\beta}$, $S_{\mu\nu}^2$ is given by:

$$S_{\mu\nu}^2 = \mathbf{S}.\mathbf{S} = S_{11}^2 + S_{22}^2 + S_{33}^2 + 2S_{12}^2 + 2S_{13}^2 + 2S_{23}^2 \tag{3.5.5}$$

For elongational flow with the kinematics given in equation 2.2.4, the derivatives of $S_{\alpha\beta}$ are given by:

$$\begin{aligned}\frac{\partial S_{11}}{\partial t} &= -6\bar{D}_r\left[(1-\frac{U}{3})S_{11} - U(S_{11}^2 + S_{12}^2 + S_{13}^2 - \frac{1}{3}S_{\mu\nu}^2 - S_{11}S_{\mu\nu}^2)\right] \\ &\quad + \dot{\varepsilon}(\frac{2}{3} + S_{11} - 3S_{11}^2)\end{aligned} \tag{3.5.6}$$

$$\begin{aligned}\frac{\partial S_{22}}{\partial t} &= -6\bar{D}_r\left[(1-\frac{U}{3})S_{22} - U(S_{12}^2 + S_{22}^2 + S_{23}^2 - \frac{1}{3}S_{\mu\nu}^2 - S_{22}S_{\mu\nu}^2)\right] \\ &\quad - \dot{\varepsilon}(\frac{1}{3} + S_{11} + S_{22} + 3S_{11}S_{22})\end{aligned}$$

$$\begin{aligned}\frac{\partial S_{33}}{\partial t} &= -6\bar{D}_r\left[(1-\frac{U}{3})S_{33} - U(S_{13}^2 + S_{23}^2 + S_{33}^2 - \frac{1}{3}S_{\mu\nu}^2 - S_{33}S_{\mu\nu}^2)\right] \\ &\quad - \dot{\varepsilon}(\frac{1}{3} + S_{11} + S_{33} + 3S_{11}S_{33})\end{aligned}$$

$$\frac{\partial S_{12}}{\partial t} = -6\bar{D}_r\left[(1-\frac{U}{3})S_{12} - U(S_{11}S_{12} + S_{12}S_{22} + S_{13}S_{23} - S_{12}S_{\mu\nu}^2)\right] + \dot{\varepsilon}S_{12}(\frac{1}{2} - 3S_{11})$$

$$\frac{\partial S_{13}}{\partial t} = -6\bar{D}_r\left[(1-\frac{U}{3})S_{13} - U(S_{11}S_{13} + S_{12}S_{23} + S_{13}S_{33} - S_{13}S_{\mu\nu}^2)\right] + \dot{\varepsilon}S_{13}(\frac{1}{2} - 3S_{11})$$

$$\frac{\partial S_{23}}{\partial t} = -6\bar{D}_r\left[(1-\frac{U}{3})S_{23} - U(S_{12}S_{13} + S_{22}S_{23} + S_{23}S_{33} - S_{23}S_{\mu\nu}^2)\right] - \dot{\varepsilon}S_{23}(1 + 3S_{11})$$

3.5.2 Solution

The Doi Theory was evaluated by first solving equations 3.5.4 for shear flow or 3.5.6 for elongational flow to give the time evolution of $S_{\alpha\beta}$, then values of $S_{\alpha\beta}$ are inserted into equations 3.5.1 to calculate the components of the stress tensor. The equations above for $S_{\alpha\beta}$ represent a set of coupled non-linear ordinary differential equations and must be solved numerically. This was done using the IMSL differential equation solver, DGEAR. DGEAR uses Adam's predictor-corrector method to calculate the solution to an initial value problem as discussed in [8]. Separate programs were written for shear and elongational flow calculations, DOIT6 for shear and DOIE3B for elongation. A copy of both programs is given in Appendix C.

In order to solve the above equations for the Doi theory several parameters (ckT, U, D_r, and A), the kinematic flow field, and initial conditions for $S_{\alpha\beta}$ must be specified. The parameters above were either calculated from molecular properties or treated as experimentally fitted constants, both cases being treated in Appendix C. The specification of the kinematic flow field is straightforward and has already been inserted into equations 3.5.4 (shear) and 3.5.6 (elongation). Initial values for the components of $S_{\alpha\beta}$ were set to zero as is the case for an isotropic system.

In contrast, the specification of initial values of $S_{\alpha\beta}$ for an anisotropic system ($U \geq 3$) is not so straightforward and several different initial conditions were examined. First, calculations were made with all components of $S_{\alpha\beta}$ set initially to zero, which actually defies the physical basis of the equations. Next, an effort was made to find initial values for $S_{\alpha\beta}$ which are physically realistic, and this was done as follows. The order parameter tensor $S_{\alpha\beta}$ was assumed to be axially symmetric in the system at rest and given by equation 2.1.1, i.e. $S_{\alpha\beta} = S(n_\alpha n_\beta - \frac{1}{3}\delta_{\alpha\beta})$. Now Doi [42] also gives a relation between S and U for a system at equilibrium, namely,

$$S = \frac{1}{4} + \left(1 - \frac{8}{3U}\right)^{1/2} \qquad (3.5.7)$$

The value of S is therefore determined by specifying U. By specifying the initial director $\mathbf{n}(t=0)$, the initial values of $S_{\alpha\beta}$ are then determined.

Several different initial director orientations were used and all of these are listed in Table 5. The first director orientations investigated were those which occur in the limit of zero deformation rate, occurring spontaneously at the slightest deformation in the system. For shear flow the orientation occurs in the x-y plane and the components of the director are calculated according to Doi [39] as

$$n_1 = \cos(\theta) \text{ and } n_2 = \sin(\theta) \tag{3.5.8}$$

where $\tan(\theta) = \left(\frac{1-S}{1+2S}\right)^{\frac{1}{2}}$ and depends only on the value of U specified. For the case of elongational flow the initial director orientation is in the flow direction and is then independent of U.

Six other initial director orientations were used for both shear and elongational flow and are given by the last six director orientations specified in Table 5. These directions were chosen so as to represent a wide range of initial directions and also because collectively they satisfy equation 3.5.2. It is then possible to use the solutions obtained with these initial director orientations in the proposed multidomain average.

Table 5. Initial Director Components Used in Numerical Work

Other Conditions‡	n_1 (t = 0)	n_2 (t = 0)
S, U = 3 †	0.89443	0.44721
S, U = 4 †	0.93907	0.34372
S, U = 6 †	0.96541	0.26075
S, U = 10 †	0.98120	0.19300
S, U = 25 †	0.99303	0.11790
S, E	1.00000	0.00000
S, E	0.00000	1.00000
S, E	0.00000	0.00000
S, E	0.81650	0.00000
S, E	-0.40825	0.70711
S, E	-0.40825	-0.70711

†Initial conditions for limit of very slow flow.
‡S = Shear flow, E = Elongational flow.

4.0 Experimental Results and Discussion

The experimental methods used for fulfilling the set research objectives were described in detail in the last chapter (and Appendix B). In this chapter the experimental results are presented and discussed. The chapter is divided into four major sections. In the first section (4.1) the material characterization work is presented. The purpose of this work is to establish the state of the materials at the temperatures used for rheological testing and provide some of the necessary material parameters for the numerical modelling. The test results presented are those described in section 3.1 (DSC, intrinsic viscosity, optical microscopy, and WAXS). Also, dynamic shear testing of the LCPs is presented there in order to show melt stability as well as establish whether residual crystallinity is present in the LCP melts. The transient shear stress growth/relaxation results for the TLCPs are then presented in section 4.2. These results are used to establish whether the TLCPs studied here behave in a manner similar to other TLCPs reported on in the literature, which allows some assertions to be made about the generality of the transient elongational flow behavior. Also these results are used for comparison of shear to elongational flow behavior and for evaluation of the predictions of the Doi theory. In section 4.3, the transient elongational viscosity growth results are presented. The behavior determined from these results is compared to that known for flexible-chain isotropic melts as well as for isotropic melts of rod-like polymers. Finally, the morphological studies on

drawn LCP films are presented in section 4.4. The purpose of these measurements is to demonstrate the degree of molecular orientation and elongation of the liquid crystalline domains which can be obtained in the LCPs undergoing elongational deformation. Furthermore the technique of small-angle light scattering is evaluated for its potential use in the determination of charges in the supermolecular structure present in the TLCPs resulting from elongational flow. The results of the numerical studies are deferred until Chapter 5, where they are presented and discussed in detail.

4.1 Material Characterization

In the literature review (Chapter 2) it was shown that the rheological behavior of a LCP depends a great deal on the actual state of the melt; i.e. whether the material is liquid crystalline, isotropic, or biphasic (liquid crystal and isotropic, liquid crystal and residual crystallinity, etc.) The main purpose of the results presented in this section is therefore to establish the state of the LCPs studied at the temperatures used for shear and elongational flow tests and to determine whether any changes in the materials take place during testing due to crystallization or degradation. Results are presented for the techniques of differential scanning calorimetry (DSC), optical microscopy, wide angle x-ray scattering (WAXS), and dynamic shear flow.

In addition to the tests given above, intrinsic viscosity measurements were carried out on the HPC materials in order to provide molecular weight values. These values are necessary for the determination of some parameters in the Doi theory and also provide a better basis for comparison of the transient flow results for HPC to those given in the literature [56-59,115,116,171]. Additionally, the intrinsic viscosity measurements were used to determine whether degradation occurred in the HPC materials during rheological testing.

4.1.1 Characterization Results

Intrinsic viscosity measurements were made on various samples of the HPC EF and G materials in order to determine their molecular weights and thus provide information for the numerical work and also determine whether degradation occurred during rheological testing. The results for both HPC EF and HPC G are tabulated in Table 6 for both as received material and material which had been tested in the ER. The corresponding molecular weights of the samples were calculated from the correlation given in section 3.1.2 and are also shown, with the molecular weight values being equal to $\overline{M}_w$ to a good approximation since the exponent in the Mark-Houwink equation for HPC is 0.915 [200]. The values of $\overline{M}_w$ shown in Table 6 show a slight decrease in $\overline{M}_w$ as a result of testing in the ER for the HPC material (the decrease is outside of experimental error limits), while the values obtained for HPC G are the same within experimental error. Therefore, it appears that no significant degradation occurred in the HPC materials during rheological testing.

DSC measurements were carried out on the LCPs in order to determine thermal transitions in the materials and to look for indications of residual crystallinity. The tests were carried out using two heating and cooling cycles with the first cycle used mainly to erase previous processing history. In all cases the first heating was to a temperature above the highest melting transition known for the materials. The second heating cycles were then used to determine transition temperatures and these are shown in Figure 32 for 60HBA/PET and HBA/HNA, and in Figure 33 for the HPC materials. The transition temperatures determined from these curves are given in Table 7. It is worth noting that the copolyesters show no signs of residual crystallinty above their previously established melting points. Also, the HPC materials show no solid to liquid melting transition but show a broad first order transition at the liquid crystal to isotropic phase transition, with the transition occurring over a range of about 30 ^{0}C for each material.

Table 6. Results of Intrinsic Viscosity Measurements on HPC Materials.

Material	Process History	$[\eta]$ dl/g	$\overline{M}_w$
HPC EF	As Received	1.124	116,000
	In ER at 190°C for 15 min.	1.009	104,000
	In ER at 210°C for 15 min.	1.044	108,000
HPC G	As Received	4.02	469,000
	In ER at 200°C for 15 min.	3.97	463,000
	In ER at 240°C for 15 min.	3.946	458,000

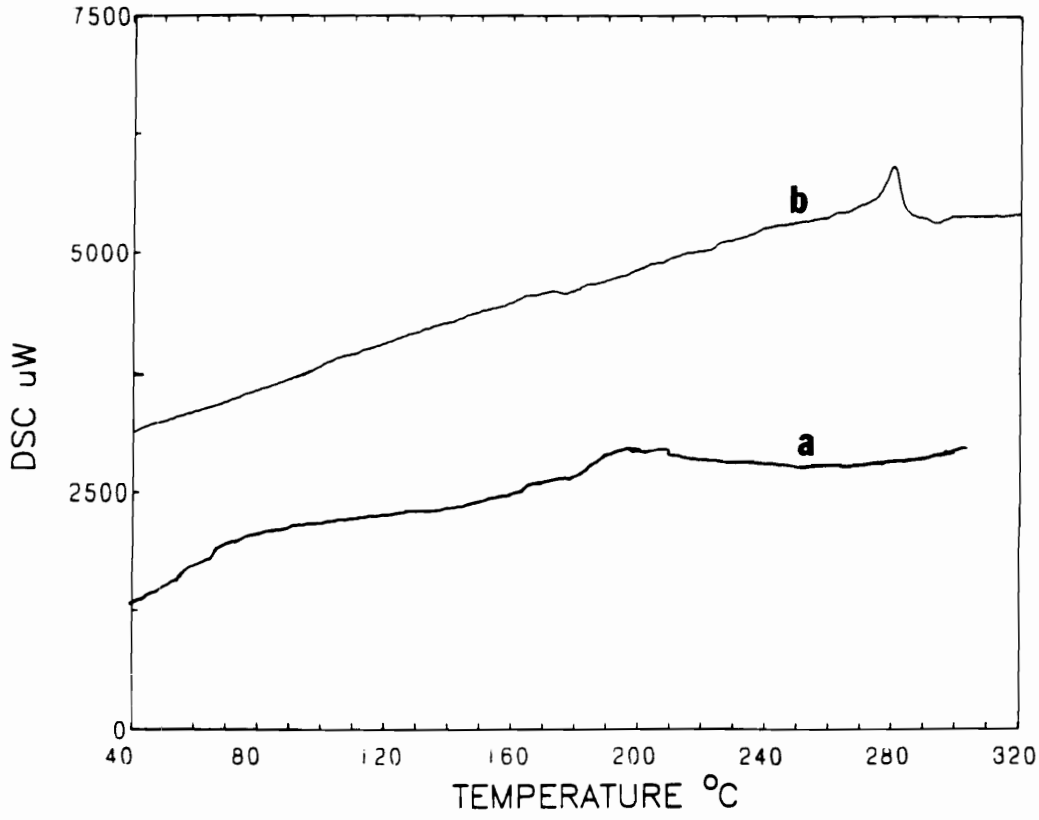

Figure 32. Second heating cycle for (a) 60HBA/PET and (b) HBA/HNA copolyesters. Heating rate is 20 °C/minute.

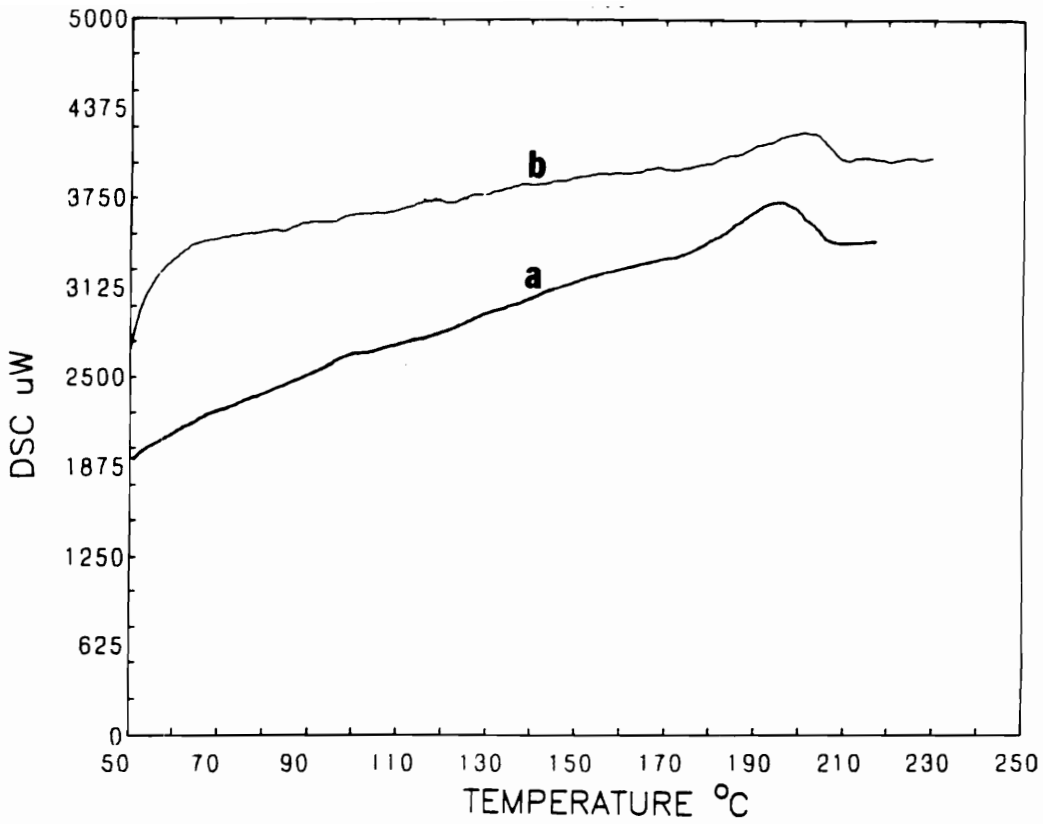

Figure 33. Second heating cycle for (a) HPC EF and (b) HPC G. Heating rate is 10 °C/minute.

Table 7. Thermal Transitions from DSC, Optical Microscopy, and Dynamic Shear Flow.

Material	Tg [°C]	Tm [°C]	Tni [°C]
60HBA/PET (1)	62	196‡, 257	-
HPC EF (1)	94	-	173-206 (197†)
(2)	-	-	190-200
(3)	-	150-160	189-202
HPC G (1)	97	-	180-209 (201†)
(2)	-	-	200-215
(3)	-	150-160	190-217
HBA/HNA (1)	-	280†	-

(1) determined from DSC († peak value)
(2) determined from polarized optical microscopy.
(3) determined from dynamic shear (sweep up).
‡ Corrosponds to point where material first flows.

Optical microscopy was used as a complementary technique for the determination of the liquid crystal to isotropic phase transition for the HPC materials, since the liquid crystal phase is birefringent while the istropic phase is not. The disappearance of birefringence during heating then determines the transition. Sample films were prepared as discussed in Chapter 3 and observed while the temperature was raised at a rate of 5 °C per minute. While photographs of the transmitted light were taken, the images were mostly featureless. Therefore special care was taken to record visual observations with regard to the intensity of transmitted light. For the HPC EF material, it was found that the intensity started to noticeably decrease just below 190 °C and a completely dark field was seen at just above 200°C. Therefore, from optical microscopy the HPC EF material was determined to be anisotropic below 190 °C, biphasic from 190 to 200 °C, and isotropic above 200 °C. The HPC G material had a more defined texture (salt and pepper type) and the transitions were more easily seen. The HPC G material was found to be liquid crystalline below 195 °C, biphasic from 195 to 215 °C, and isotropic above 215 °C. These results are tabulated in Table 7 for comparison with transitions determined from other methods. It is worth noting that no determination could be made of whether the birefringence at the lower temperatures was due to a liquid crystalline or crystalline phase from optical microscopy because of limited image resolution.

Wide angle x-ray scattering studies were done on the HPC resins in order to determine whether there was any residual crystallinity in the materials at the temperatures used for rheological testing. Samples of HPC EF were annealed at 190 and 210 °C and were then either quenched in liquid nitrogen or slow cooled (at 5 °C/minute). The same was done with HPC G except temperatures were 200 and 240 °C. The resulting WAXS patterns are shown in Figure 34 and Figure 35 for HPC EF and HPC G, respectively. Two broad rings are seen in all of the samples at values of 2θ of 7.8° and 20.0° and are presumably due to scattering from amorphous material. At the same time, these rings are seen to be sharper in the HPC EF sample annealed at 190 °C than for the samples annealed at the higher temperatures, indicating closer intermolecular spacing at that temperature and supporting the assertion of a liquid crystalline state for HPC EF at 190 °C. In addition to the amorphous rings a weak but

sharp ring can be seen at $2\theta = 17.8^0$ for both materials annealed at the lower temperatures and quenched and possibly also in both materials slow cooled from the upper temperatures. This ring is due to a small amount of crystallinity in the material, which is presumably present in the materials at the annealing temperatures for samples which were quenched after the annealing. At the lower temperatures it thus appears that HPC EF and G materials have residual crystallinity present.

4.1.2 Dynamic Oscillatory Shear Results

Dynamic oscillatory shear testing was performed as described in section 3.2 in order to provide background information on the materials and also to help determine the physical state of the materials at the temperatures used for the transient shear and elongational flow tests which are listed in Table 4 on page 107. The dynamic tests which were run include dynamic strain sweeps, time sweeps, frequency sweeps, and temperature sweeps (just for HPC materials). In the isothermal testing the samples were loaded into the rheometer and subjected to approximately the same thermal history as samples loaded into the extensional rheometer and tested. This meant treating the samples to a small amount of thermal overshoot upon loading (2-5 °C for about 3 minutes) and waiting 10 minutes from the time the temperature in the RMS oven first reached the test temperature until the tests were started. Additionaly two or three measurements were made on each material at each test condition to check reproducibility. Unless indicated by error bars, the deviation between tests was within the size of the symbols.

Dynamic strain sweep tests were performed on all materials at all of the temperatures of interest in order to determine the range of strain for which the materials behaved in a linear manner. It was found that all of the materials showed a linear range of strain (i.e. η^*, G′, and G″ independent of strain) at all temperatures and all frequencies investigated, which for most

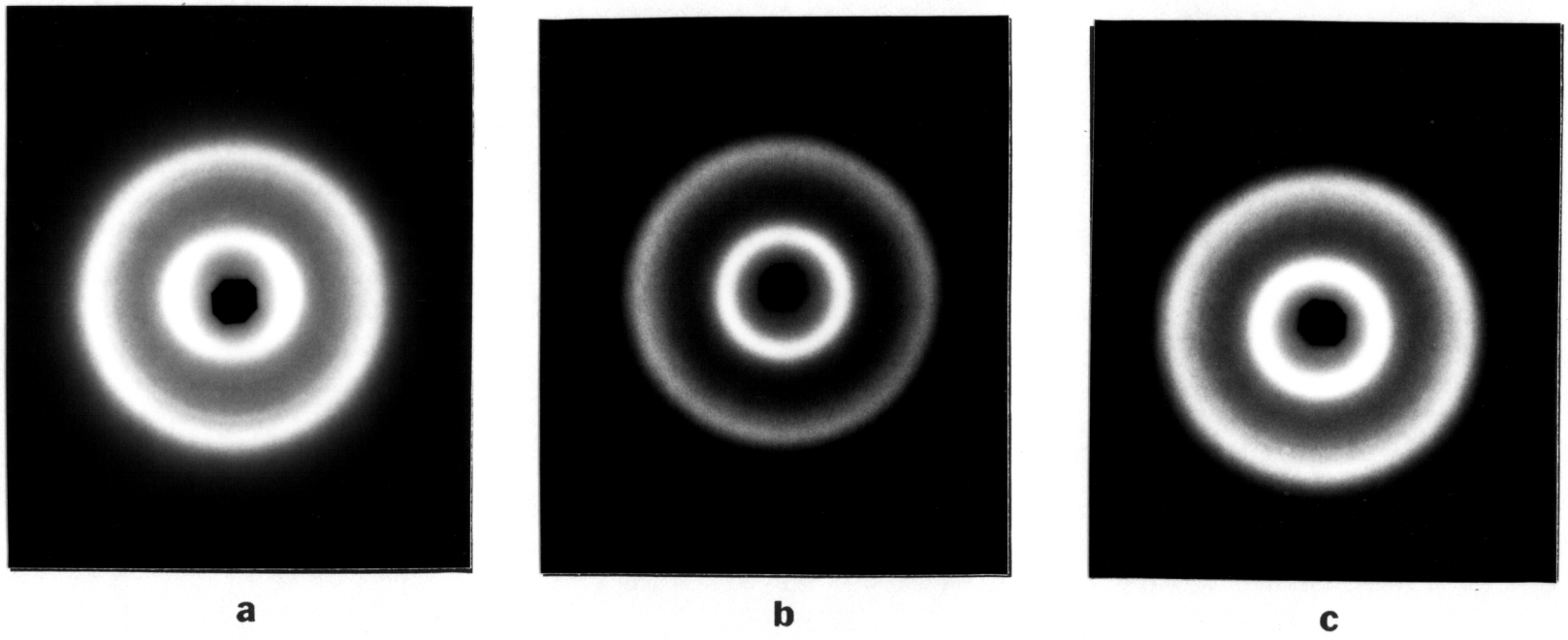

Figure 34. WAXS patterns of HPC EF samples annealed at: (a) 190 °C and then quenched, (b) 210 °C and then quenched, and (c) 210 °C and then slow cooled.

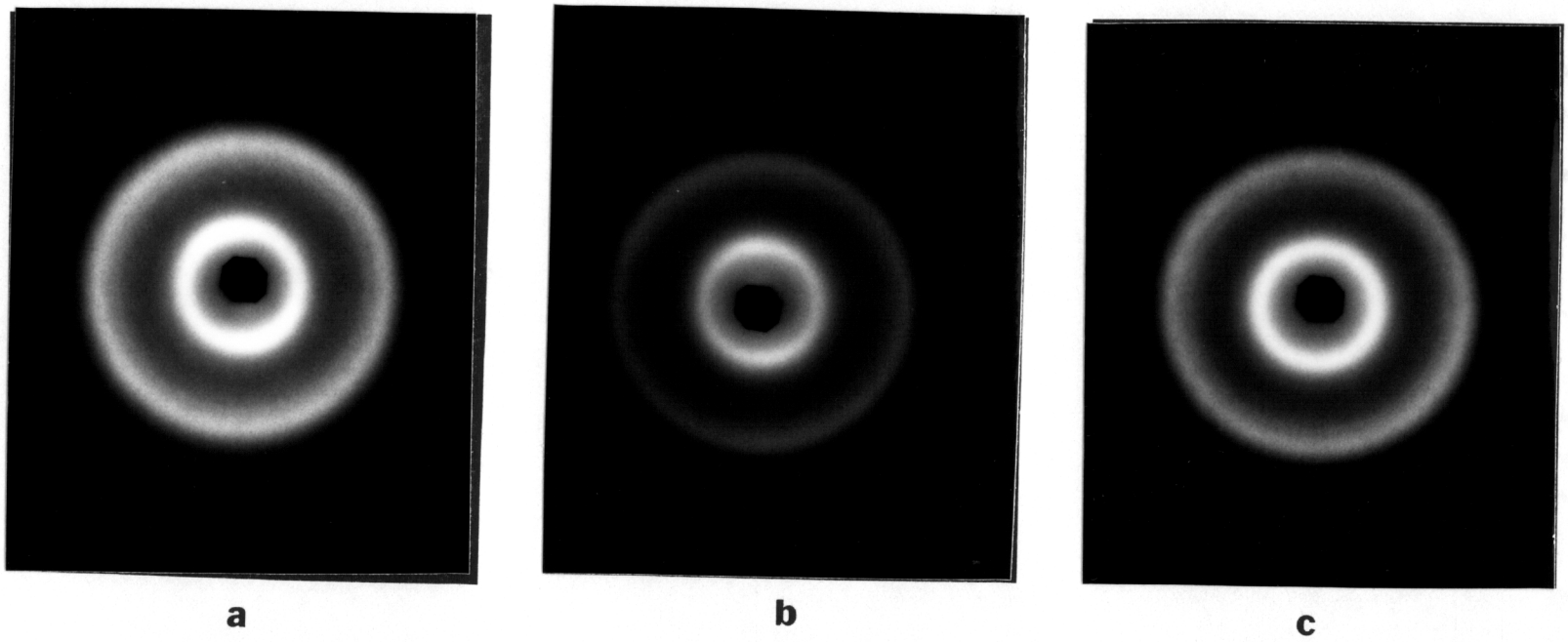

Figure 35. WAXS patterns of HPC G samples annealed at: (a) 200 °C and then quenched, (b) 240 °C and then quenched, and (c) 240 °C and then slow cooled.

of the materials was up to approximately 10 % strain. The strains used for other dynamic tests were then kept within the linear region.

Dynamic time sweep tests were performed on all of the materials in order to test the melt stability, with changes in the values of η^* or tanδ (G″/G′) being indicative of degradation, crystallization, or even changes in the microstructure of the melt due to flow. A decrease in the value of tanδ shows an increase in the elastic nature of the material and is due to the formation of an elastic network as a result of processes such as crystallization or crosslinking. On the other hand, an increase in the value of tanδ results from the destruction of an elastic network as would occur due to the melting of residual crystallinity or degradation by chain scission. At the same time it might not be possible to determine which process is responsible for changes in the melt using time sweeps alone.

The results of the dynamic time sweep tests are shown in Figures 37 and 38 for HPC EF and HBA/HNA, respectively, while time sweep data for all of the LCPs are tabulated in Appendix D. In Figure 36 the time sweep results are shown for HPC EF at 190 and 210 °C. At 190 °C the dynamic viscosity is seen to grow about 25 % over a period of approximately 45 minutes while tanδ remains nearly unchanged. Although this degree of change is greater than that expected due to instrument drift, it is relatively small compared to what would be expected for any significant crystallization, which can be ruled out since no change is seen in tanδ. At 210 °C, the dynamic viscosity of HPC EF shows no significant change, while the value of tanδ decreases now over 50%, indicating a relative increase in the elastic nature of the melt. Since no change in the molecular weight of HPC was seen previously this would have to be due to either crystallization or intermolecular hydrogen bonding. An increase in melt elasticity is also seen in HPC G at 240 °C, which is above the equilibrium melting temperature for HPC of 234 °C [171], indicating that hydrogen bonding is likely to be the responsible process. In contrast to the results for HPC, no changes are seen in the values of η^* or tanδ for HBA/HNA at 301 or 320 °C, as is shown in Figure 37. The HBA/HNA material is, therefore, seen to have a stable melt at these temperatures.

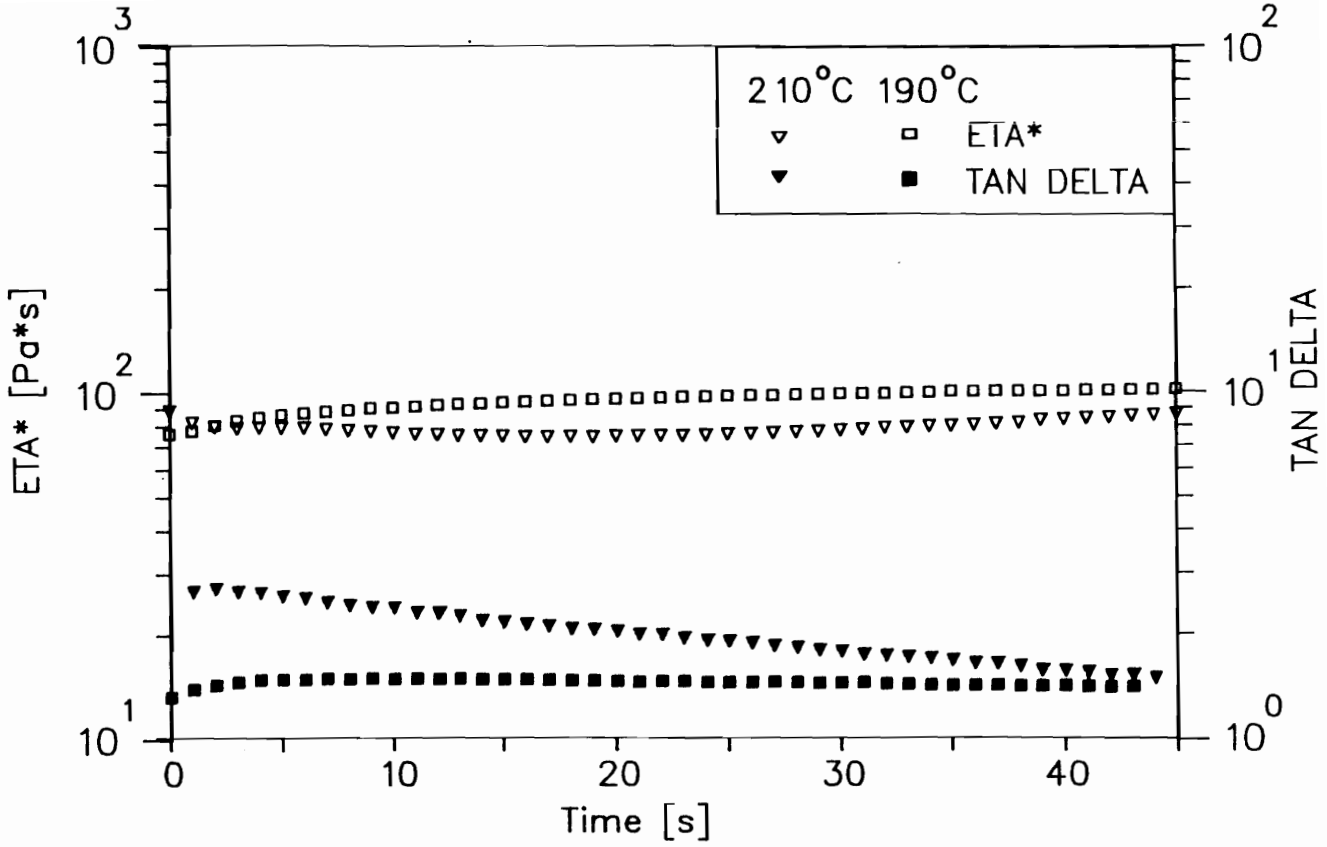

Figure 36. Dynamic time sweeps of HPC EF at 190 and 210 °C, ω= 10 Hz. Symbols described in figure.

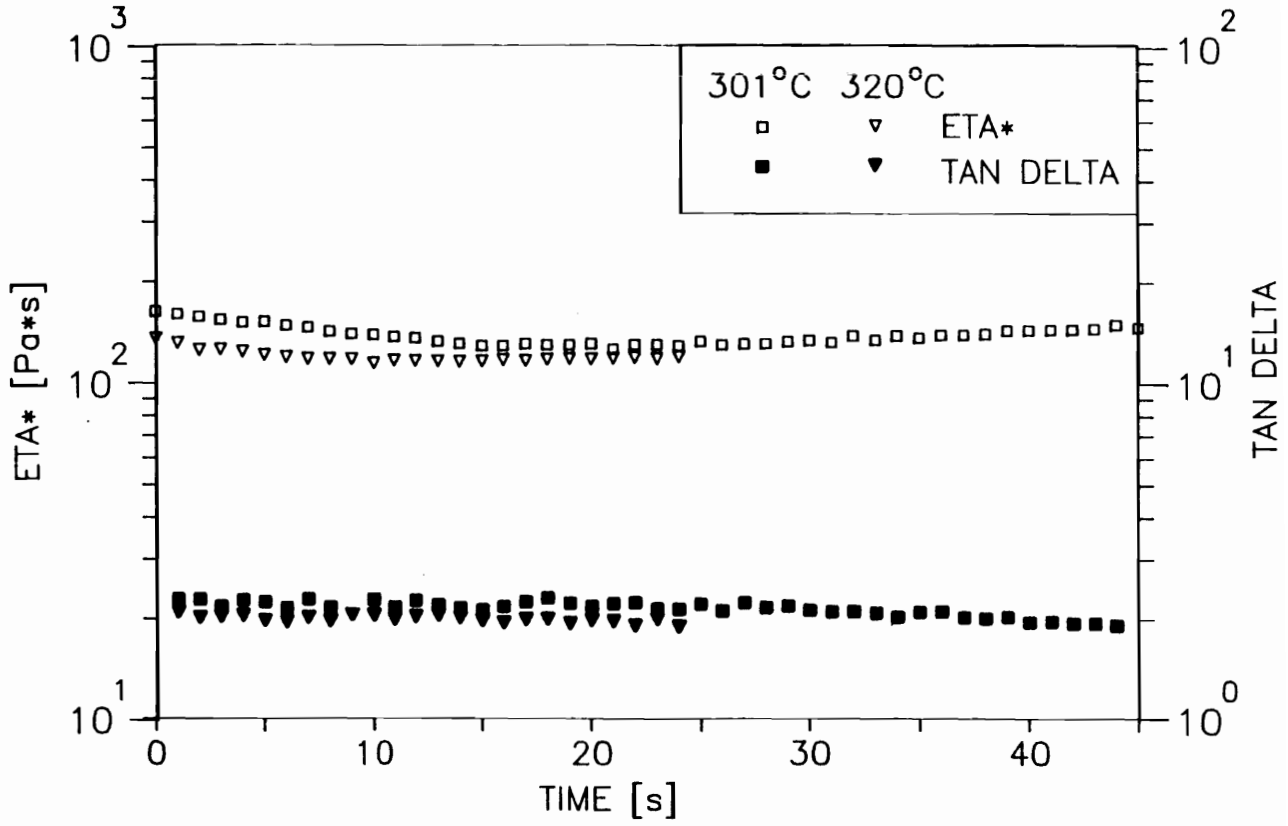

Figure 37. Dynamic time sweeps of HBA/HNA at 301 and 320 °C, ω= 10 Hz. Symbols described in figure.

Dynamic frequency sweeps were run on the LCPs at the temperatures of interest in order to determine the frequency dependence of the complex viscosity. Such information was necessary for an initial estimate of the stresses that were encountered in the elongational flow testing and also to help determine whether there is residual crystallinity in the materials. For example, shear thinning at low frequencies and high values of G′ relative to G″ at low frequency show a material to have a high degree of elasticity, which along with yield stresses have been associated with crystallinity in TLCP melts [18,110].

Frequency sweep results are shown for 60HBA/PET, HPC EF, HPC G, and HBA/HNA in Figures 39 to 42, respectively. The results for 60HBA/PET at 275 °C are shown here for comparison with the other LCPs, even though no elongational flow tests were run on this material. The features worth noting are the appearance of a Newtonian plateau in the dynamic viscosity at low shear rates and relatively low values of G′ relative to G″ at low frequencies, indicating low melt elasticity. Such a lack of melt elasticity at low frequencies implies the absence of residual crystallinity in the melt and this has been previously noted for 60HBA/PET at 275 °C [29,195].

The frequency sweep behavior of the other LCPs in the liquid crystalline state (HPC EF at 190 °C, HPC G at 200 °C, and HBA/HNA at both 301 and 320 °C) is seen to be different from that for 60HBA/PET in a number of ways. All of these materials show a frequency thinning dynamic viscosity over the entire frequency range with no sign that the dynamic viscosity will level off at lower rates. HPC EF at 190 °C, HPC G at 200, and HBA/HNA at 301 and 320 °C also show values of G′ which are approximately the same or even larger than the value of G″, indicating an unusually large degree of elasticity. Furthermore, the value of G′ appears to be leveling off as the angular frequency decreases for HPC EF at 190 °C and for HBA/HNA at both temperatures, indicating the possibility of a yield stress. This behavior is consistent with the presence of residual crystallinity in these materials.

The frequency sweep results for the HPC materials in the isotropic states (HPC EF at 210 °C and HPC G at 240 °C) were also studied. At 210 °C, the behavior of HPC EF is very different than at 190 °C, showing a Newtonian plateau and low values of G′ relative to those of G″ at low

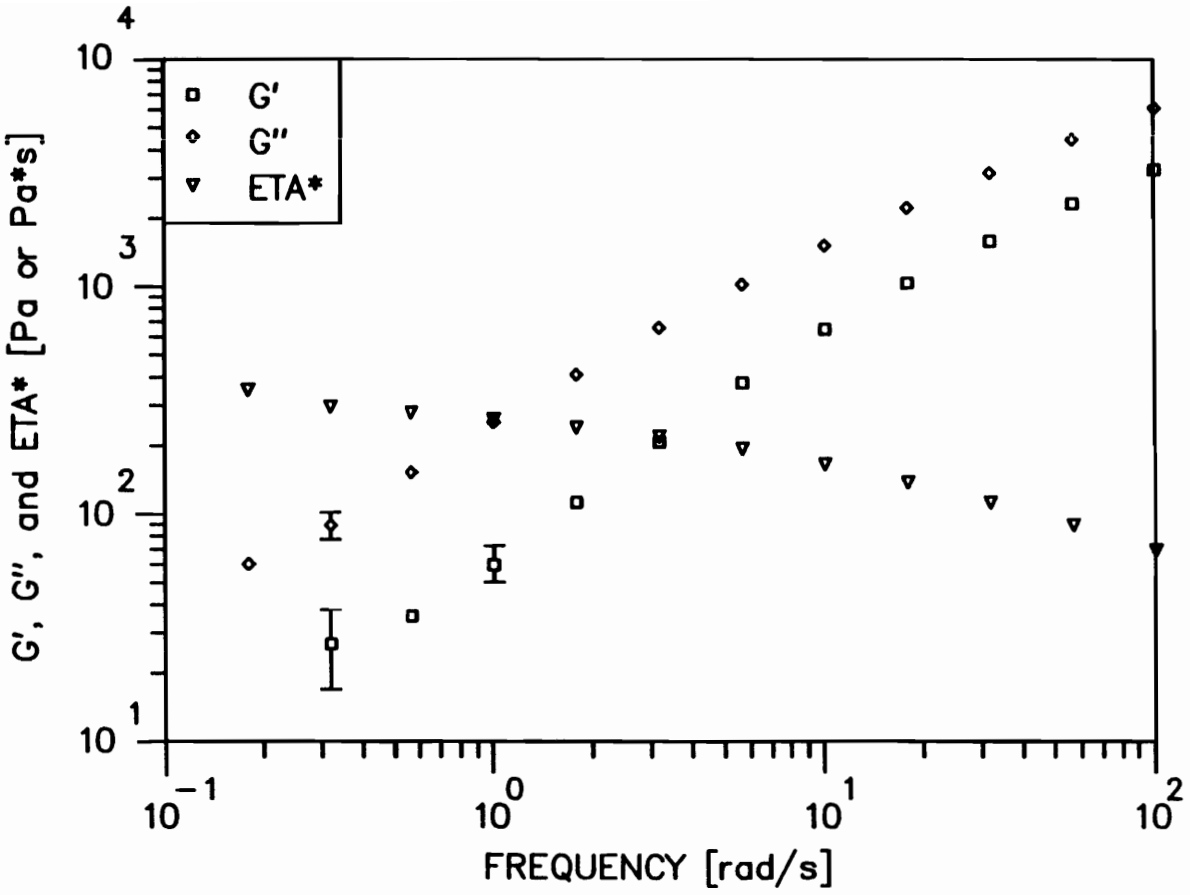

Figure 38. Dynamic frequency sweep of 60HBA/PET at 275 °C. Symbols described in figure.

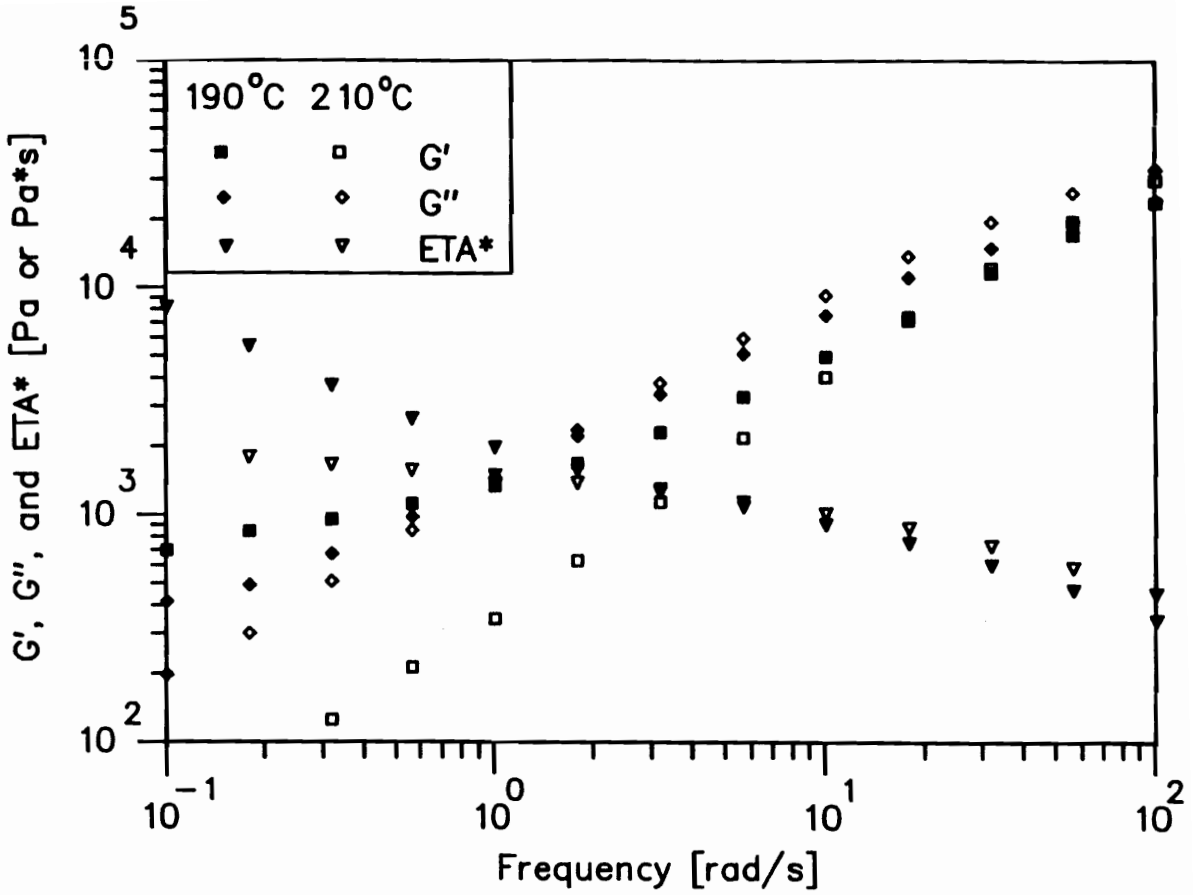

Figure 39. Dynamic frequency sweep of HPC EF at 190 and 210 °C. Symbols described in figure.

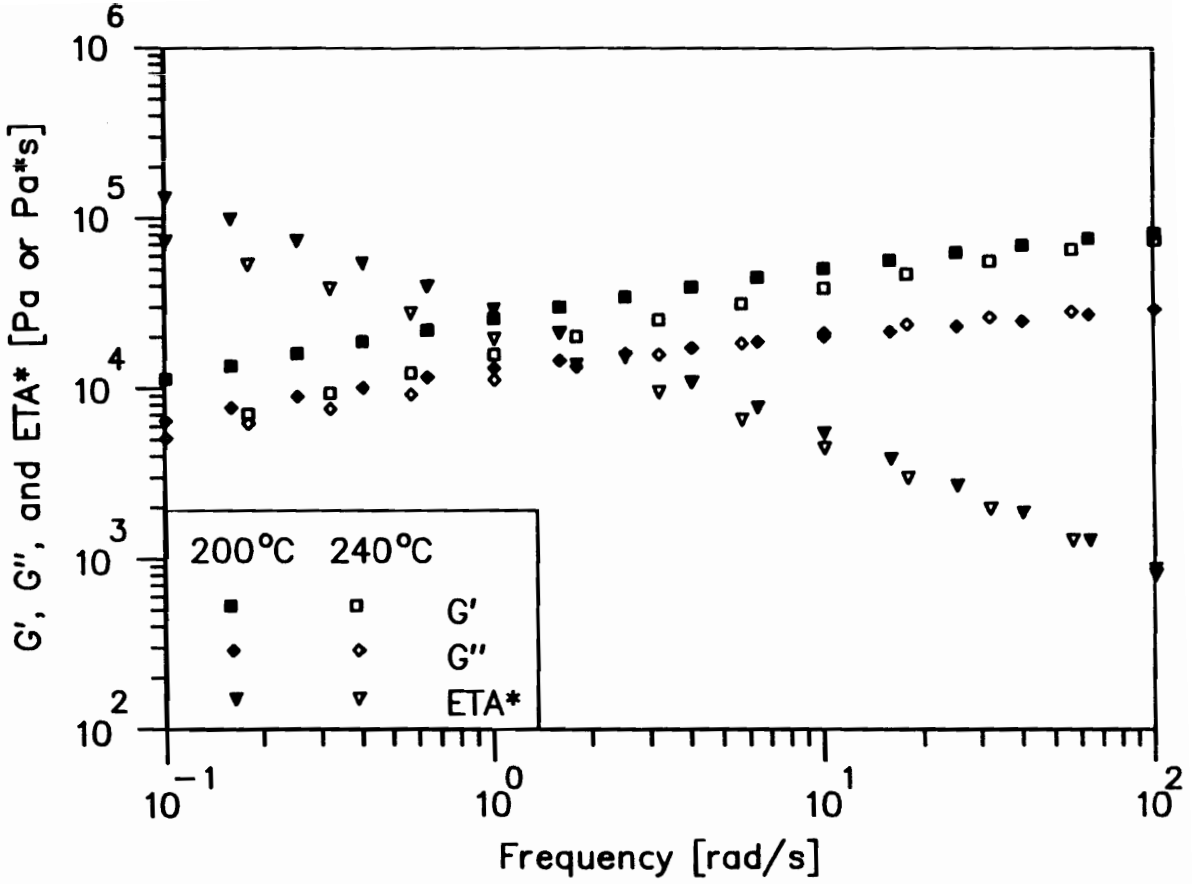

Figure 40. Dynamic frequency sweep of HPC G at 200 and 210 °C. Symbols described in figure.

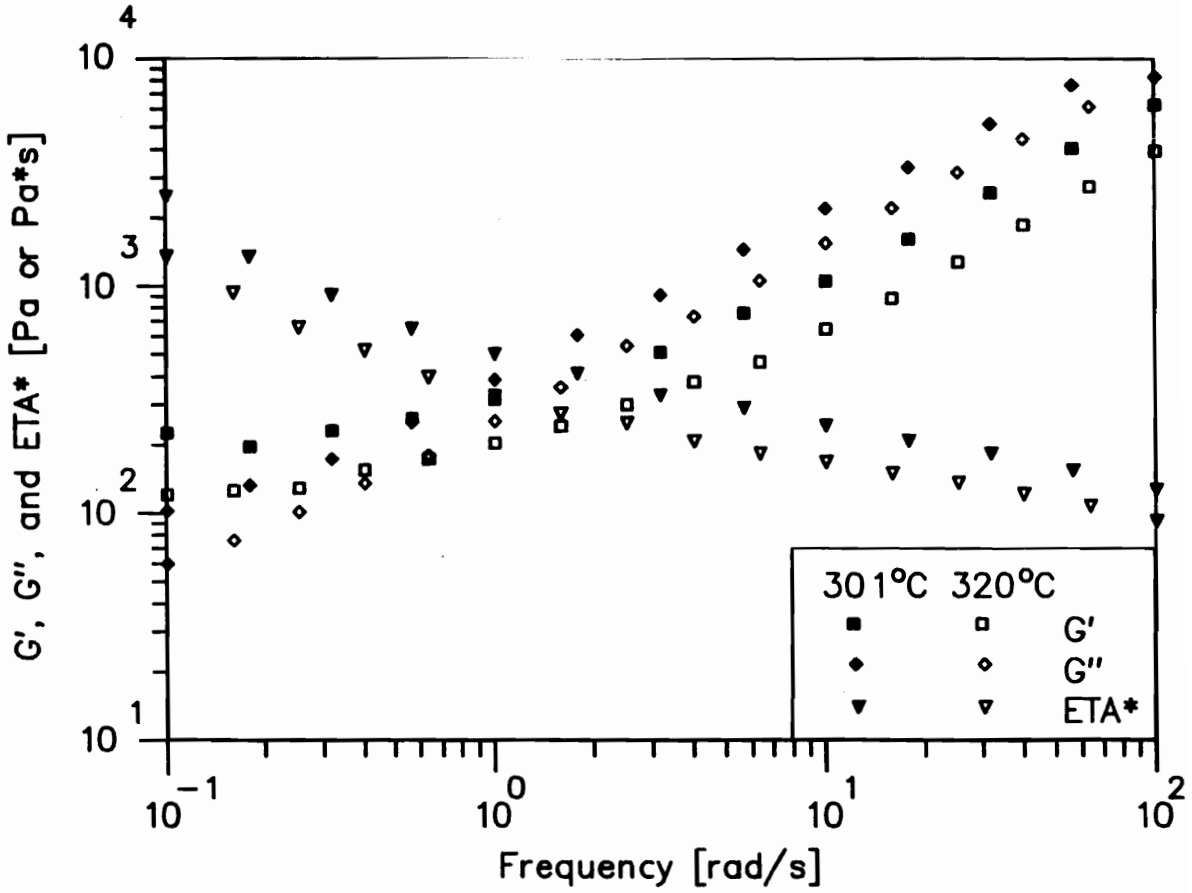

Figure 41. Dynamic frequency sweep of HBA/HNA at 301 and 320 °C. Symbols described in figure.

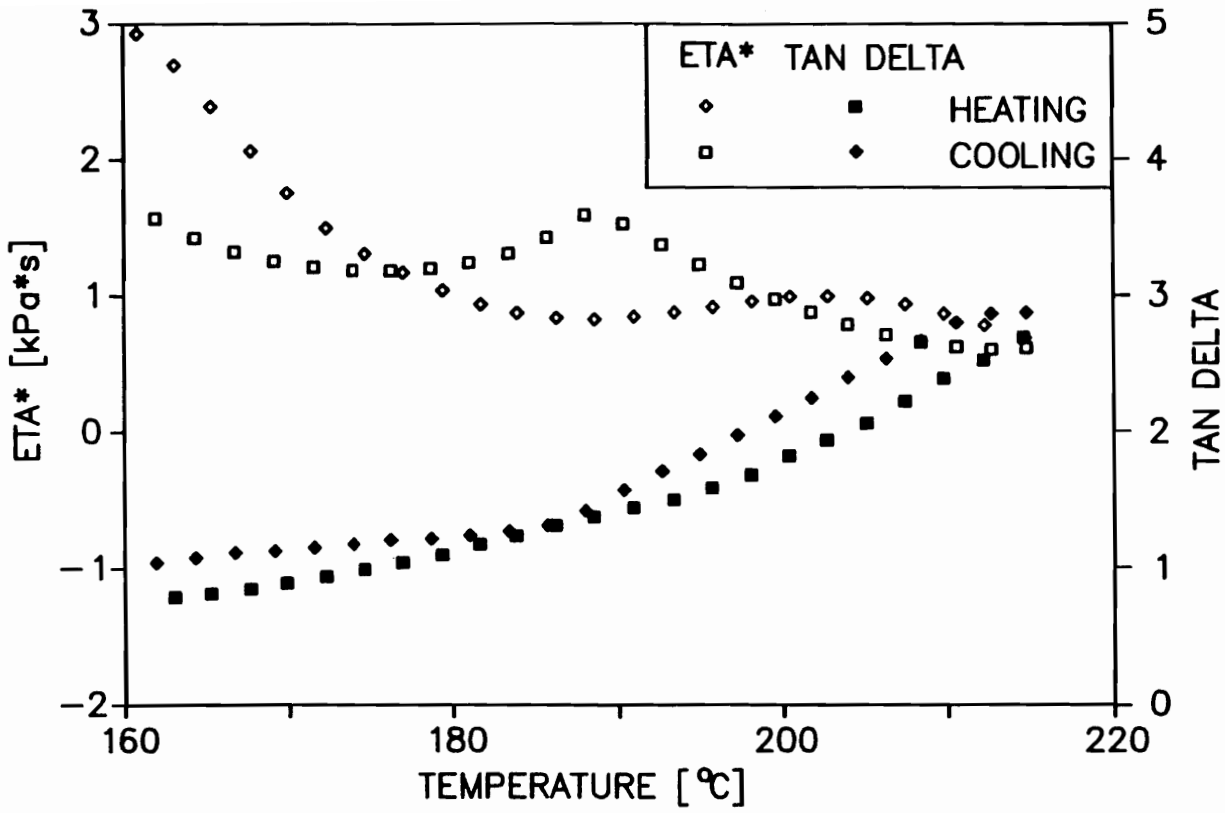

Figure 42. Dynamic temperature sweep of HPC EF, rate = 5 °C/minute and ω = 10 Hz. Symbols described in figure.

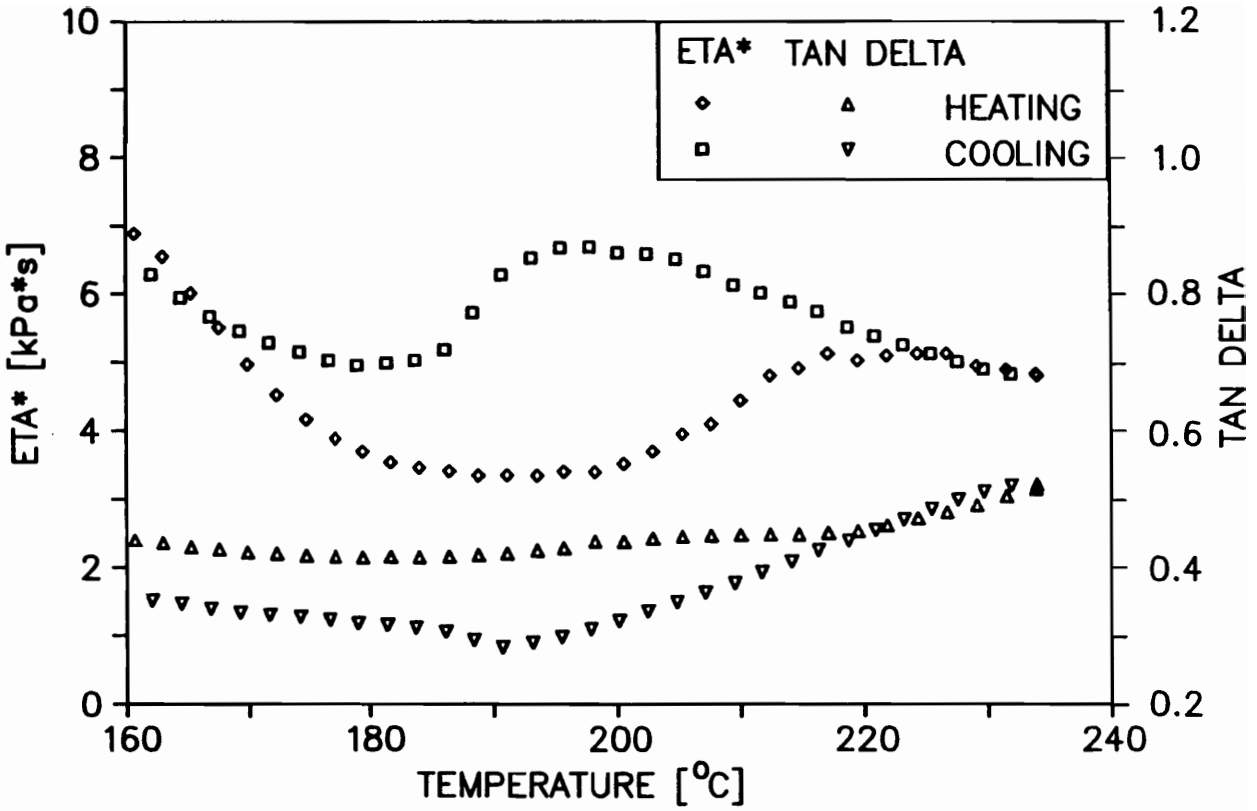

Figure 43. Dynamic temperature sweep of HPC G, rate = 5 °C/minute and ω= 10 Hz. Symbols described in figure.

angular frequency. Such behavior indicates the lack of residual crystallinity in HPC EF at 210 °C. In contrast, the behavior of the HPC G material at 240 °C is very similar to that of the same material at 200 °C, except for lower values of G' at low frequencies. Again, this could indicate the absence of residual crystallinity in HPC G at 240 °C. At the same time such similar behavior for a material thought to be in two different physical states could be an indication that flow is dominated by molecular relaxations because of the high molecular weight.

Temperature sweep tests were run on the HPC materials in order to help determine the temperatures or temperature ranges for the liquid crystal to isotropic transition occurring in the material. Results for HPC EF are shown in Figure 42 and those for HPC G are shown in Figure 43, with the transition temperatures obtained from these results tabulated in Table 6 on page 126. The beginning of the liquid crystal to isotropic phase transition was assumed to occur at the minimum in the curve in analogy to that for lyotropic systems, while the transition was assumed to be complete at the curve maximum. Also, it can be seen that the transition range depends on whether the test was carried out in a heating or cooling sweep. The transition temperatures used were obtained from the heating curve for two reasons. First, the cooling transition has been observed to be shifted to lower temperatures in another LCP system due to supercooling [34], and therefore the cooling curve transitions are likely inaccurate. Second, the materials tested in the transient type tests were heated up from room temperature and therefore undergo a thermal history similar to the material tested in the heating curve.

4.1.3 Discussion of Materials State

The determination of the physical state of the LCP melts used in this study was necessary for the critical examination of the transient flow results, for being able to extend this transient flow behavior to other LCP systems, and for the critical evaluation of the predictions of the Doi theory. Therefore, the results just presented are examined here and conclusions

are drawn as to the physical state of the LCPs at the conditions used for transient shear and elongational flow tests. A summary of these conclusions is given in Table 8.

The melt state of 60HBA/PET is established here since it was used in transient shear stress growth/relaxation tests. The 60HBA/PET copolyester has been extensively examined in the literature [8, 26, 28, 30, 44, 60, 87, 95, 117, 124, 135, 138, 194, 195] and is well known to exist as a biphasic material at 275 °C, with the major phase a HBA rich nematic mesophase and the minor phase a PET rich isotropic phase. Also, it is reported to be free of residual crystallinity at 275 °C [29,195], and this has been confirmed by the use of dynamic frequency sweep tests as previously shown.

The physical state of the HPC melts are considered next. First, it is established that HPC exhibits a liquid crystalline melt state within a certain temperature range and arguments are given for the type of mesophase exhibited. The phase transition in HPC from the liquid crystal to the isotropic state is then discussed. Finally, the aspect of residual crystallinity in the HPC EF melts is examined.

Both HPC materials were found to exhibit a liquid crystalline melt within certain temperature ranges. While the material begins to flow between 150 and 160 °C, examination via optical microscopy shows birefringence until much higher temperatures. Additionally, the observation of a minimum and maximum in the dynamic shear viscosity versus temperature curve can not be explained in any other way, since crystallization can be ruled out as this phenomenon is seen for both heating and cooling cycles. Similar observations have been noted in HPC melts by other investigators [57-59,115,116]. A plot of the relative intensity of light transmitted through an HPC film situated between crossed polarizers versus temperature is shown in Figure 44. Again, it can be seen that birefringence persists well above the flow temperature. By definition, such behavior is indicative of a liquid crystalline state.

The determination of the mesophase type in HPC is also important and evidence for establishing the mesophase type is discussed here. Two experimental techniques were relied upon for this: optical microscopy and dynamic temperature sweeps. Using optical microscopy, it was observed that the color of transmitted light changed with increasing temperature from

Table 8. Physical State of the LCPs Used in Transient Flow Tests.

Material	Temperature [°C]	Physical State
60HBA/PET	275	Biphasic - nematic major phase and isotropic minor phase.
HPC EF	190	Liquid crystal major phase, some isotropic phase and residual crystallinity
	210	Isotropic phase with possibility of residual nuclei
HPC G	200	Liquid crystal major phase, some isotropic phase and residual crystallinity.
	240	Isotropic
HBA/HNA	301	Nematic major phase and some residual crystallinity
	320	Nematic major phase and some residual crystallinity or crystal nuclei.

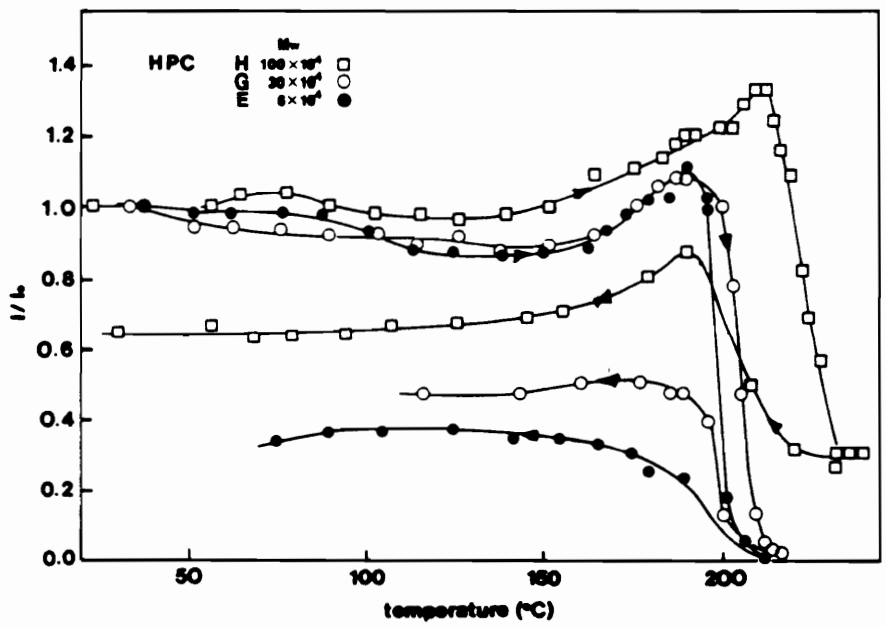

Figure 44. Light intensity I/I_0 due to HPC between crossed polars as a function of temperature [57].

170 °C to about 185 °C, where no further changes occurred. Such changes are well known for low molecular weight cholesteric systems and are due to changes in the cholesteric pitch due to thermal expansion [4]. Furthermore, HPC has been shown to exhibit a cholesteric mesophase in aqueous solutions [34,144]. In materials which are both lyotropic and thermotropic similar mesophase types are typically displayed under both conditions [4,9]. On the other hand, the dynamic viscosity versus temperature curve was seen to display a minimum and maximum with rising temperature which shows that the liquid crystalline phase has a lower viscosity than the corresponding isotropic phase. In low molecular weight liquid crystals, only the nematic mesphase has a lower viscosity than the corresponding isotropic phase [4]. While it is unclear whether this behavior is a characteristic of polymeric liquid crystals, it could indicate that there is a phase transition to a nematic state under flow conditions. Such flow induced transitions have been reported in lyotropic solutions of HPC [34,224] and PBLG [53] when the material was sheared at moderate to high rates ($\dot{\gamma}$ greater than the order of 1 s^{-1}). Therefore, the the HPC materials appear to exist in a cholesteric mesophase at equilibrium in the anisotropic melt state, but could undergo a transition to the nematic state under flow at high deformation rates.

One aspect of the physical state of HPC that has not been well defined is the liquid crystal to isotropic transition. Examination of the transition ranges reported for the HPC materials in Table 7 on page 129 shows the transition range to vary widely, depending upon the method used. The most accurate method, DSC, shows the widest transition range while the least accurate, optical microscopy, shows the tightest range. In any case, DSC, optical microscopy, and dynamic temperature sweep tests indicate that the HPC materials contain both liquid crystal and isotropic phases at the lower temperatures used for transient flow tests, i.e. HPC EF at 190 °C and HPC G at 200 °C. At the same time both the DSC peak temperatures and the dynamic temperature sweep data indicate that the major phase at the temperatures just given is the liquid crystal phase. Additionally, under flow conditions the transition temperature could be effectively increased for each material due to entropic effects and this would

increase the relative amount of material in the liquid crystalline versus the isotropic state during flow.

Another aspect of the state of the HPC melts to be considered is the presence of residual crystallinity. Evidence for the presence of residual crystallinity comes mainly from the WAXS patterns and dynamic frequency sweep tests. Both HPC EF at 190 °C and HPC G at 200 °C showed definite signs of having residual crystallinity as evidenced by the sharp diffraction rings at $2\theta = 17.8^0$ shown in Figures 34 and 35, and this is further substantiated in HPC EF by the high values of G′ at low frequency. At the same time, HPC EF at 210 °C and HPC G at 240 °C show no signs of having residual crystallinity by any of the techniques used. While the presence of very small quantities of residual crystallinity cannot be ruled out in HPC EF at 210 °C, its presence in HPC G at 240 °C is very unlikely, since Samuels [171] has determined the equilibrium melting point of HPC (T_m^0) to be 234 °C.

One final aspect of the HPC materials which is important for this study is the aspect of chain flexibility. HPC exists as a rigid helical molecule due to intramolecular hydrogen bonding, which exists up to at least 250 °C [171]. At the same time solution studies [200] indicate that the chain has some flexibility, which tends to make the molecule less rod-like as the molecular weight increases [200]. This brings into question whether the behavior observed in HPC G ($\overline{M}_w = 470{,}000$) will be dominated by conformational changes, such as those which occur in flexible-chain polymers, or by molecular scale rotational and translational motions as those which occur in a perfectly rigid rod. The dynamic frequency sweep behavior of the HPC G material was very similar to what is seen for high molecular weight flexible-chain polyolefins (for example Fig. 3.4-3 of [72]). At the same time the frequency sweep behavior of HPC EF is very similar to that of the HBA/HNA copolyester, which has a very rigid molecule. Thus, differences in the overall chain conformations of HPC EF and HPC G could result in differences in their flow behavior.

The melt state of HBA/HNA at both 301 and 320 °C is thought to be nematic with the presence of a small amount of residual crystallinity. The determination that HBA/HNA is liquid crystalline comes from the observation of birefringence in the melt state. The establishment

of a nematic state is derived both from the observation of a Schlieren texture in the melt, the rod-like nature of the molecule because of its wholly aromatic composition, and the lack of chirality of HBA/HNA molecules which is necessary for the formation of a cholesteric mesophase [4]. Evidence for residual crystallinity comes from the high values of G′ measured at low frequencies. Neither degradation nor the polydomain structure of the material could possibly result in such high values of G′ (Wissbrun [18] has shown this to be true using the elastic contribution to the stress tensor from the Leslie-Ericksen theory) and this leaves only residual crystallinity as a cause. Furthermore, studies by Lin and Winter [100] have shown that crystallinity is possible in the melt up to 320 °C, and Kamal [212] has determined the value of T_m^0 for HBA/HNA of 372 °C. While Kamal's value of T_m^0 could vary between batches because of the effect of composition and sequence distribution, it is sufficiently high to show that residual crystallinity is possible at the temperatures used for transient flow studies, i.e. 301 and 320 °C. At the same time, the level of residual crystallinity in HBA/HNA should be lower at 320 °C than at 301 °C, since a smaller amount of material could be in the crystalline state at equilibrium as dictated by statistics for a random sequence distribution.

The role of degradation should be considered in the HBA/HNA material since testing in the RMS uses a nitrogen atmosphere while the sample in the ER is exposed to hot oil. Dynamic frequency sweeps were run on as received and post ER tested samples of HBA/HNA at 330 °C. Thermal history effects due to residual crystallinity should be minimal at this temperature and any differences in the frequency sweep results would be strong evidence for degradation. While results are not shown, it was found that measurements on the two samples showed agreement well within 5 %. Therefore, it is concluded that no degradation occurred during rheological testing for the HBA/HNA copolyester.

In closing, it should be noted that the materials used in this work have been shown to exhibit complex melt states. In nearly all cases, more than one phase is present in the materials at each thermal condition investigated (i.e. liquid crystalline phase, isotropic phase, and crystallinity). In view of this it should be cautioned that the rheological behavior determined for the materials and presented in the next two sections can not be considered to represent

that of all LCPs. Only by establishing that the transient shear flow behavior of the materials investigated here agrees well with the behavior previously determined in LCPs with well defined states can any degree of generality be proposed for the elongational flow behavior determined in this work (and presented in section 4.3).

4.2 Transient Shear Results and Discussion

Transient shear stress growth/relaxation tests were carried out on the LCPs for a number of reasons. First, by comparing the resulting behavior of the TLCP systems investigated here to the behavior of other LCP systems reported in the literature, assertions can be made about the generality of the elongational behavior determined for the same materials (presented in section 4.3). Second, a comparison of the transient shear flow behavior of the LCPs with that for isotropic melts of flexible-chain polymer and isotropic melts of polymers with rod-like molecules is used in an attempt to establish whether the behavior of LCPs is fundamentally different from that for the isotropic systems. This is discussed at the end of the section. Third, the direct comparison of the transient shear and elongational flow behavior shows whether the two are simply related as is found for the shear and elongational flow behavior of linear flexible-chain polymers at low deformation rates. Finally, the transient shear flow results are used for the evaluation of the Doi theory (presented in Chapter 5).

4.2.1 Shear Stress Growth/Relaxation Behavior

The transient shear stress growth/relaxation behavior of several TLCPs was investigated at the conditions previously listed in Table 4 on page 107 and using the test procedure described in section 3.2. The precision of the tests was estimated to be within ± 14 % for stress

levels above 50 Pa using a crude error analyses. Additionally, the reproducibility of the tests was determined by running 2 or 3 samples at each condition and in all cases, except for the 60HBA/PET material, the agreement between runs was within ±15%. For the 60HBA/PET material at the lower rates, the agreement relative errors as large as 25 % were found.

The stress growth behavior of all of the liquid crystalline melts showed similar behavior and a representative set of results is shown in Figure 45 to demonstrate the behavior observed over an entire test. Several features of the shear stress growth/relaxation behavior are seen to be common to all of the rates investigated. Upon the startup of steady shear flow, there is an initial stress overshoot, after which the stress approaches a constant value. The stress is then seen to relax quickly after the cessation of shear flow, usually reaching values which cannot be differentiated from zero with the force resolution of the RMS transducer. Finally, upon the second startup of steady shear, the stress again shows an initial overshoot, but now the overshoot is lower than that for for the first deformation period. Again, similar results were found for HBA/HNA at 320 °C, for 60HBA/PET at 275 °C, and for HPC EF at 190 °C.

In order to better analyze the similarities in the stress growth/relaxation behavior measured for the different materials, the results have been plotted in reduced form in Figures 46 to 53, showing both the first stress growth period and the following stress relaxation. It was found that all of the materials showed an initial overshoot peak upon the startup of steady shear flow and that the strain ($\dot{\gamma}t$) at which this peak occurs is roughly independent of deformation rate for each material with peaks occurring at about 2 to 3 strain units. Furthermore, it was found that the reduced magnitude of the overshoot peak was independent of rate for HBA/HNA and for HPC EF at 190 °C at lower rates, though the fact that this was not seen in 60HBA/PET at 275 °C could be due to error in the magnitude of the shear stress. The stress relaxation behavior of the TLCPs also showed similarities with the time needed for the reduced shear stress to relax to a certain value decreasing as the rate of prior shearing increased. In fact, over the range of rates investigated the stress relaxation time scales directly with the reciprocal of the prior shear rate, as is demonstrated in Figures 52 and 53 for HPC

EF at 190 °C and HBA/HNA at 301 °C with similar results seen in 60HBA/PET and HBA/HNA at 320 °C.

While the transient stress growth/relaxation behavior of the LCPs was shown to be similar for the materials in the anisotropic melt state, the behavior measured for the isotropic HPC EF melt (at 210 °C) shows some differences from that described above (see Figures 48 and 53). The stress overshoot peaks observed upon the startup of flow are relatively small in magnitude. They do not occur at the same strain level for different shear rates and the magnitude of the overshoot peaks depend on the shear rate. At the same time the stress relaxation behavior is somewhat similar to that of the anisotropic melts. The reduced shear stress is observed to relax at an increasing rate as the rate of prior shear increases and the values of the reduced stress are found to lie upon the same curve (within experimental error) when plotted versus reduced time ($\dot{\gamma}_o t$).

4.2.2 Transient First Normal Stress Difference

The transient first normal stress difference, $N1(t, \dot{\gamma})$, was also measured for some of the LCP systems at the same conditions as the transient shear stress with the results shown in Figures 54 to 57 ($N1(t, \dot{\gamma})$ was too small to be accurately measured for 60HBA/PET and was not reproducible for HPC G). Although the results from single runs are shown, they are qualitatively reproducible. Unlike the transient shear stress behavior, there is is no general transient N1 behavior for the different materials and the behavior is even rate dependent for HBA/HNA. Both anisotropic HPC (190 °C) and HBA/HNA show initial overshoot in N1, with the magnitude of the overshoot increasing with increasing shear rate. Another similarity is that the values of N1 go highly negative after the initial overshoot. However, after this time the behavior is not common and while the value of N1 for HPC EF levels off during steady flow, the value of N1 for HBA/HNA levels off at low rates and shows a continued increase at the highest rate. Upon cessation of flow, again no general behavior is seen. Although the values of N1 are

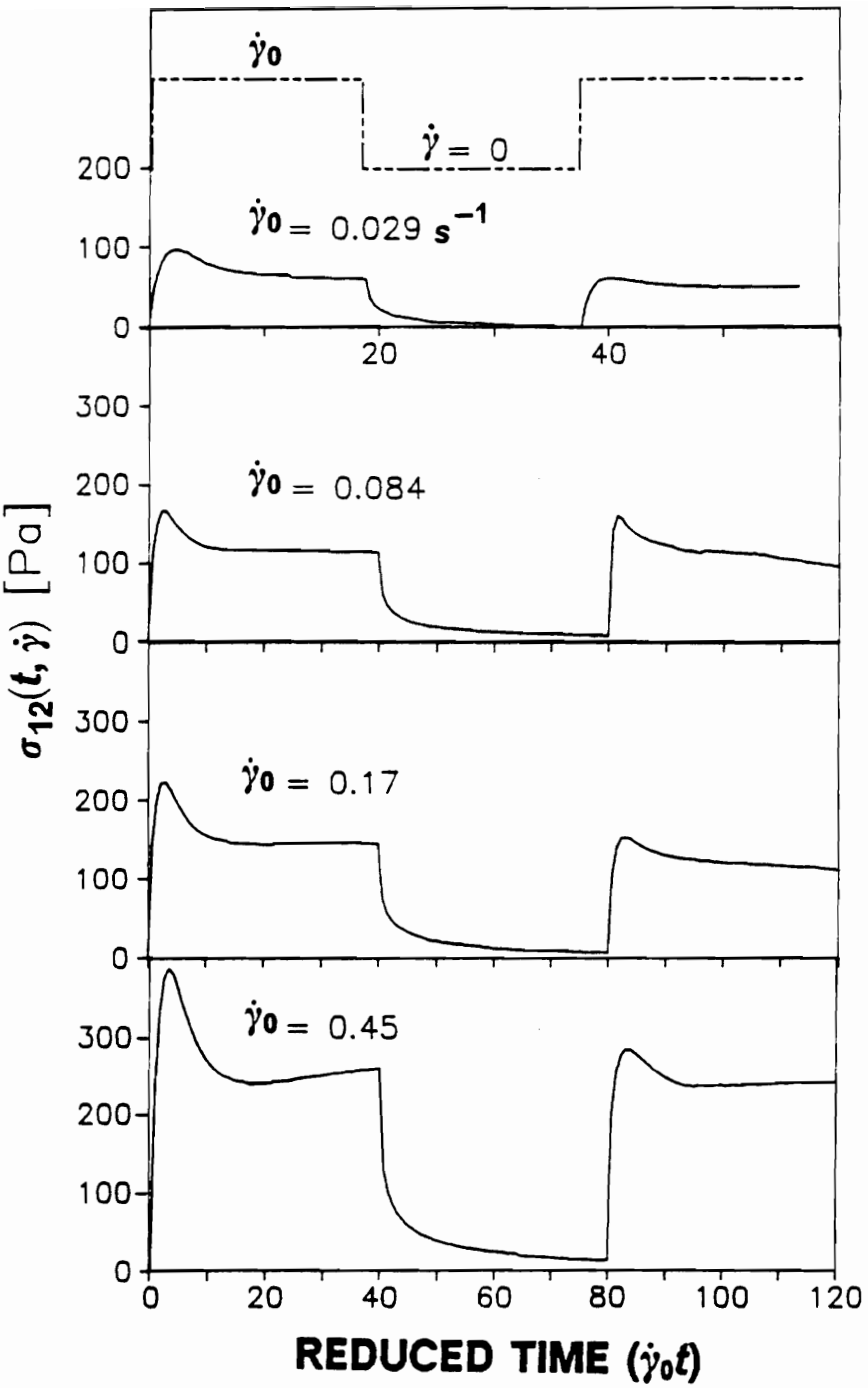

Figure 45. Transient shear stress growth/relaxation of HBA/HNA at 301 °C: Shear stress plotted versus the product of shear rate and time for each rate $\dot{\gamma}_0$.

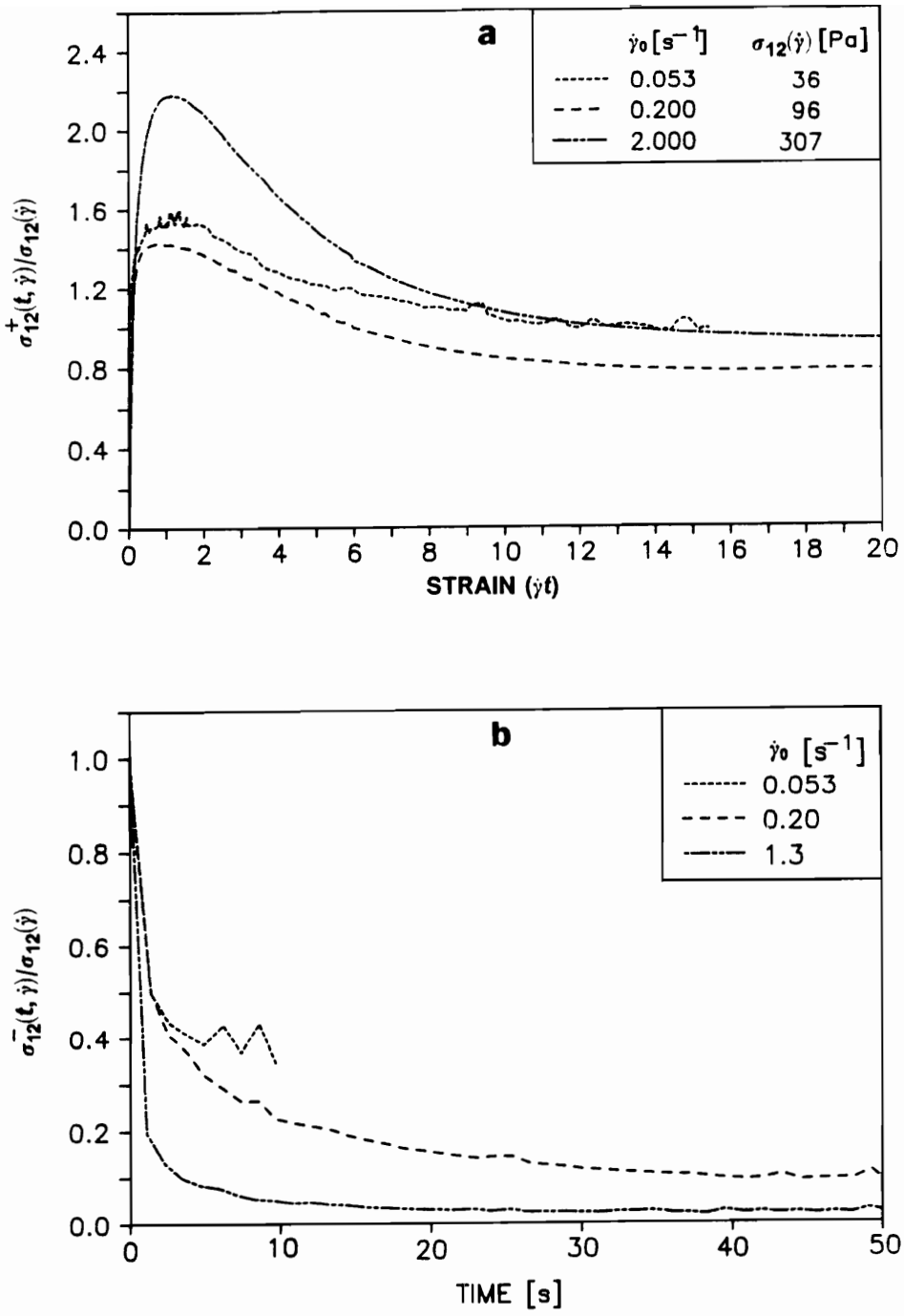

Figure 46. Transient shear stress (a) growth and (b) relaxation of 60HBA/PET at 275 °C: The shear stress is reduced by the steady state value at each rate $\dot{\gamma}_0$.

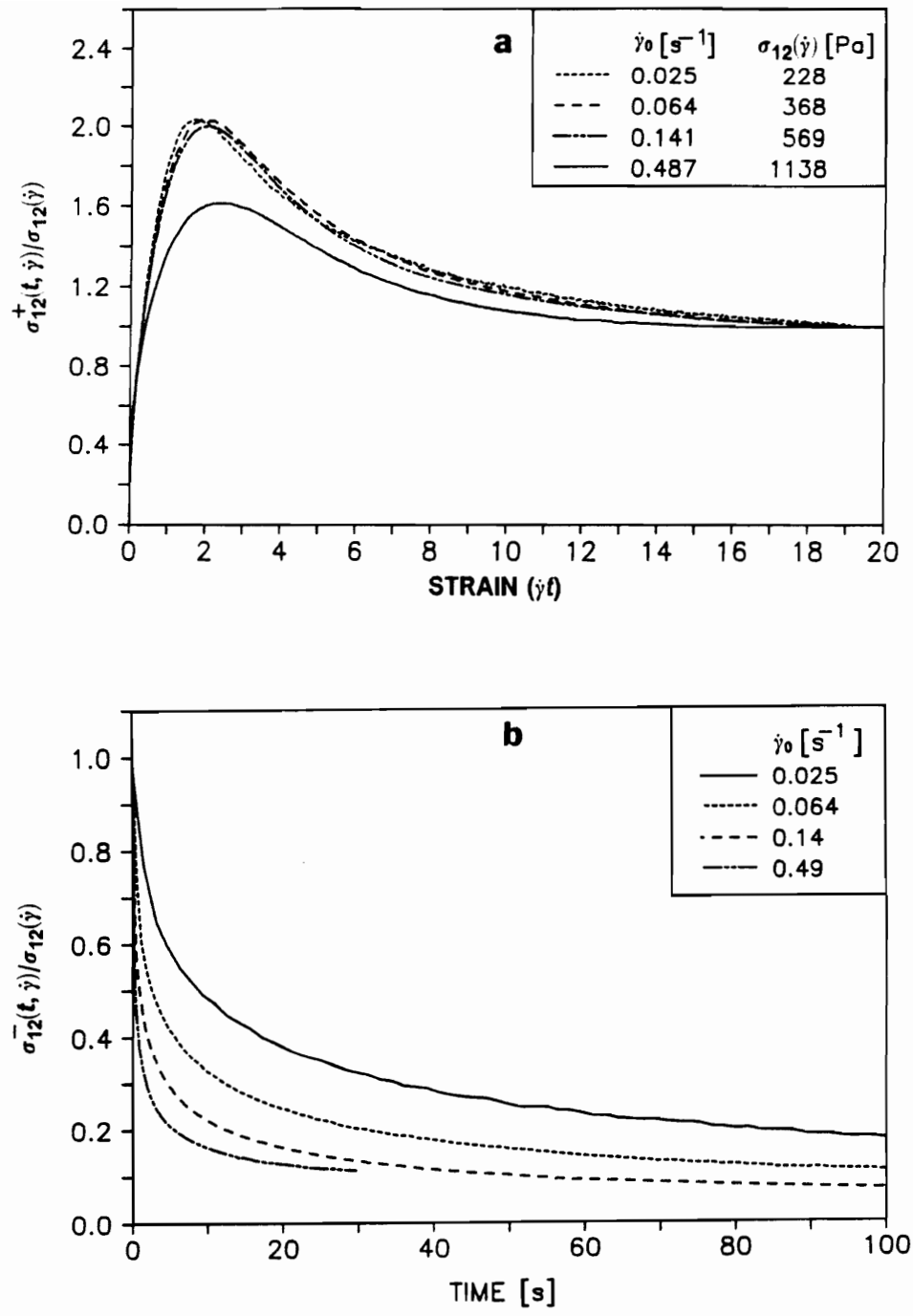

Figure 47. Transient shear stress (a) growth and (b) relaxation of HPC EF at 190 °C: The shear stress is reduced by the steady state value at each rate $\dot{\gamma}_o$.

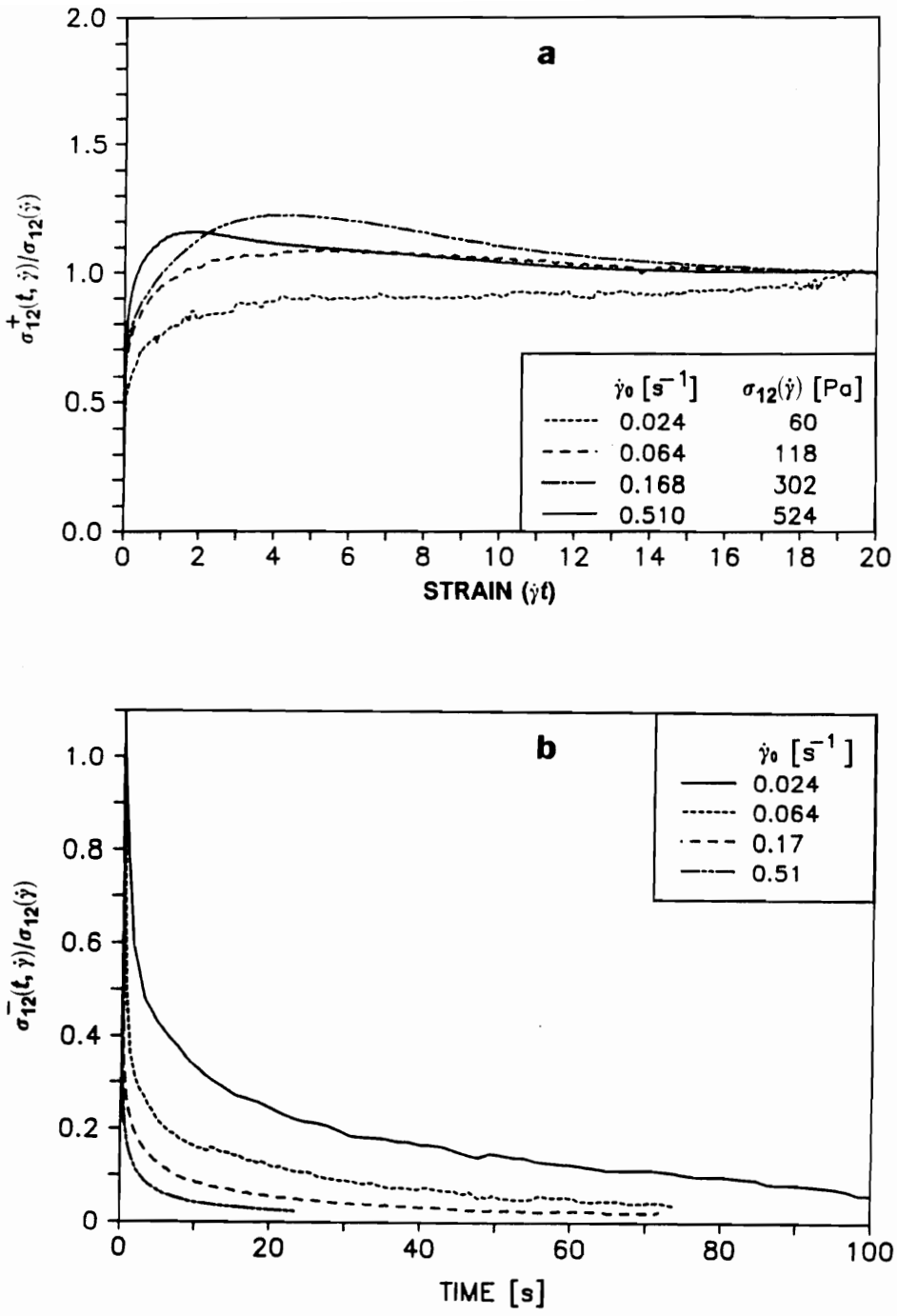

Figure 48. Transient shear stress (a) growth and (b) relaxation of HPC EF at 210 °C: The shear stress is reduced by the steady state value at each rate $\dot{\gamma}_0$.

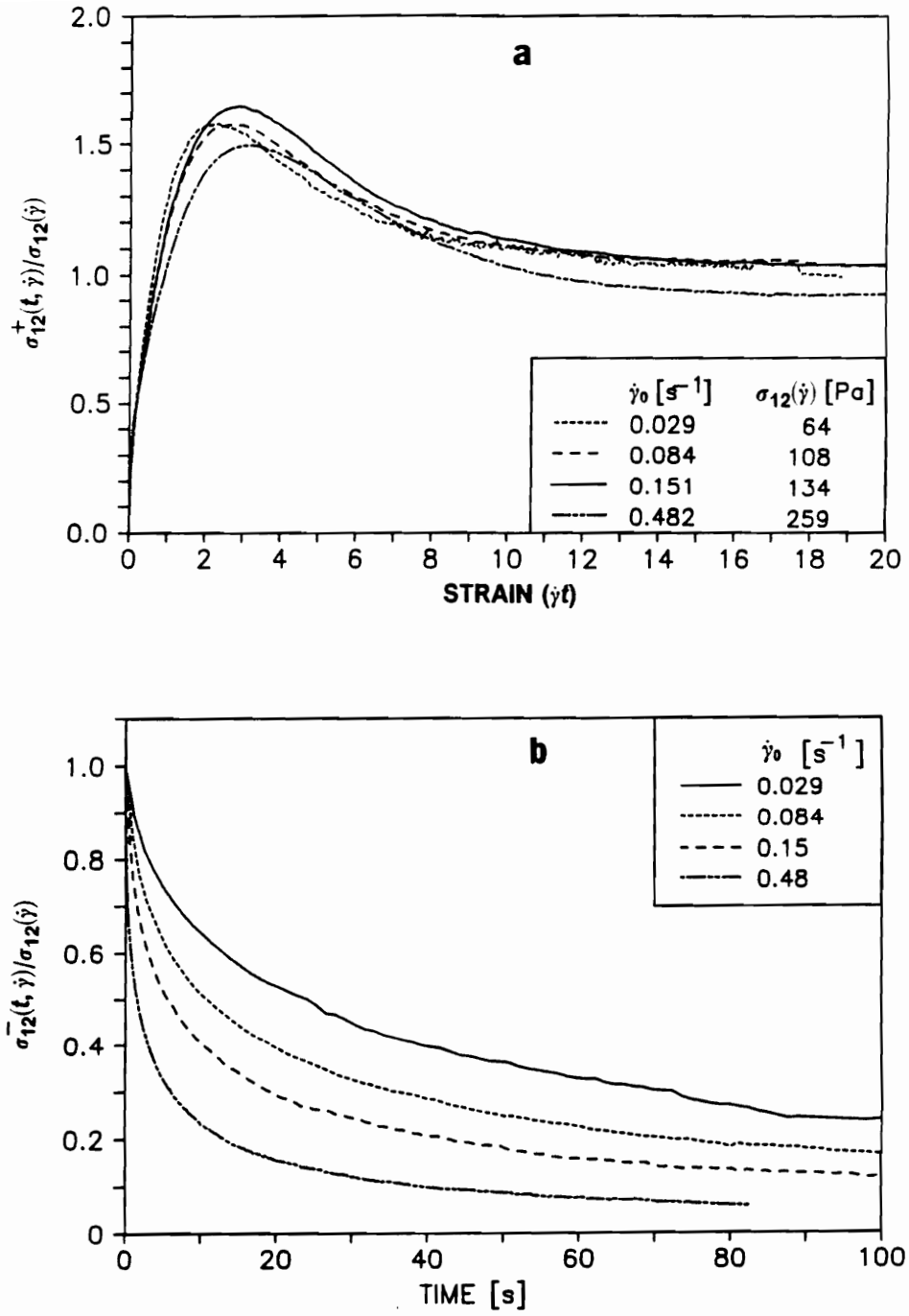

Figure 49. Transient shear stress (a) growth and (b) relaxation of HBA/HNA at 301 °C: The shear stress is reduced by the steady state value at each rate $\dot{\gamma}_o$.

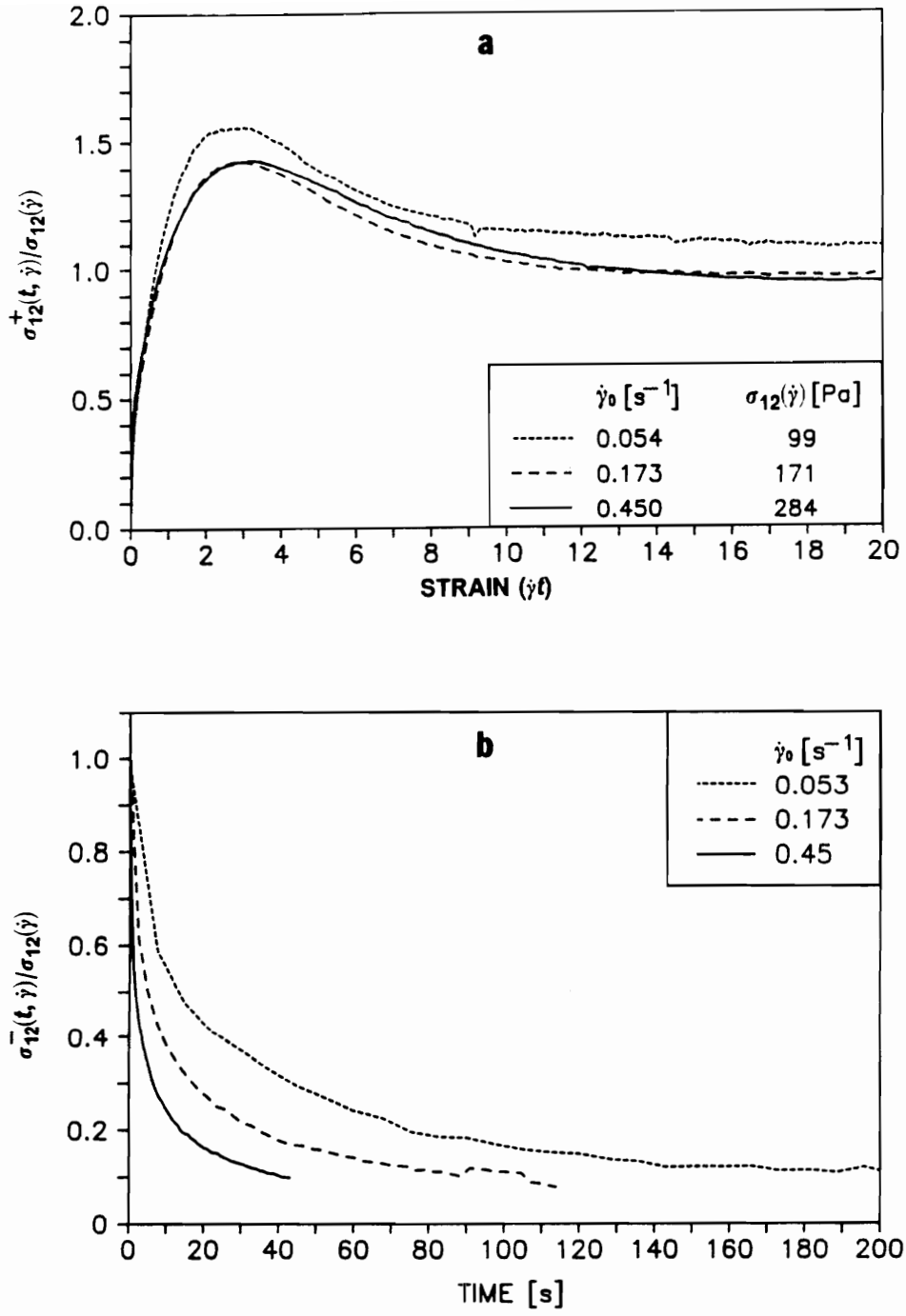

Figure 50. Transient shear stress (a) growth and (b) relaxation of HBA/HNA at 320 °C: The shear stress is reduced by the steady state value at each rate $\dot{\gamma}_o$.

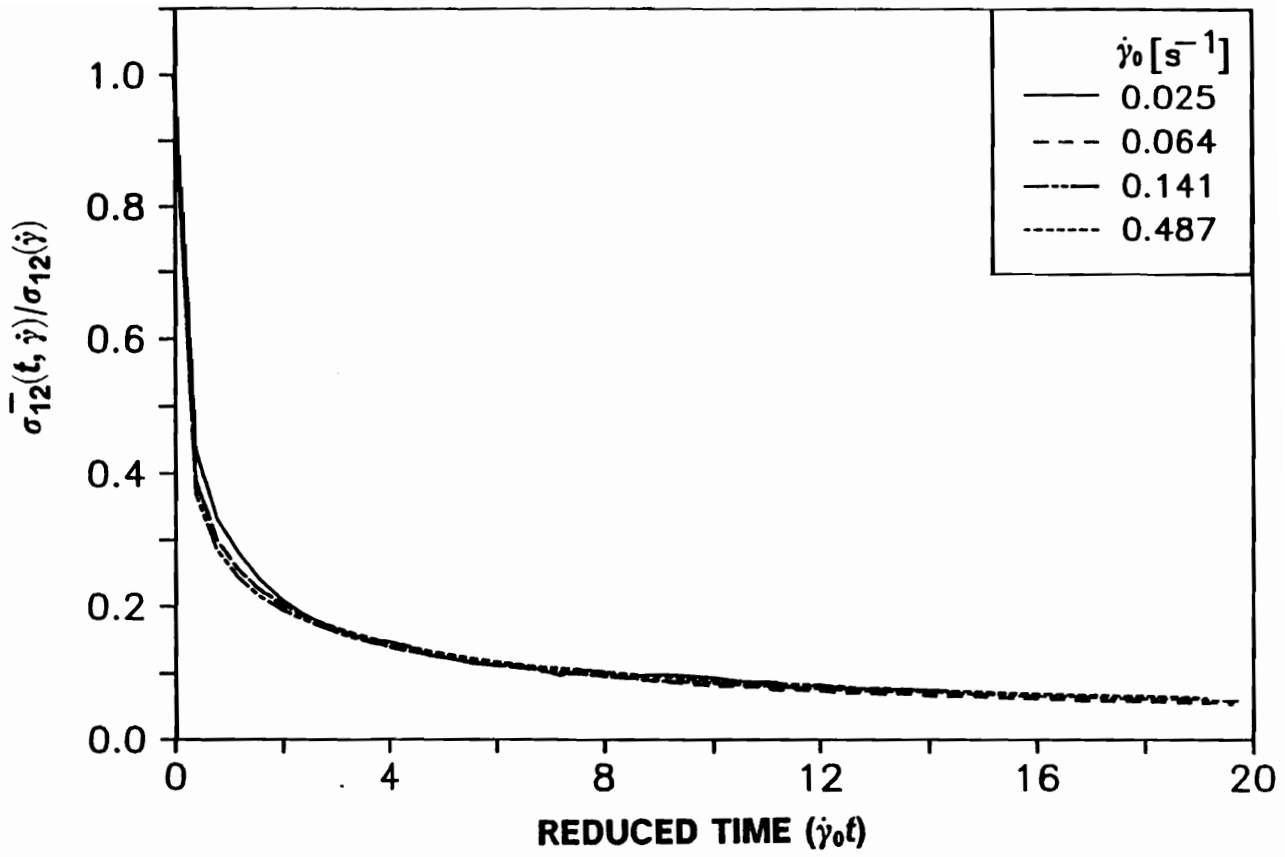

Figure 51. Transient shear stress relaxation after cessation of steady flow in HPC EF at 190 °C: Reduced stress plotted versus product of prior shear rate and time ($\dot{\gamma}_0 t$).

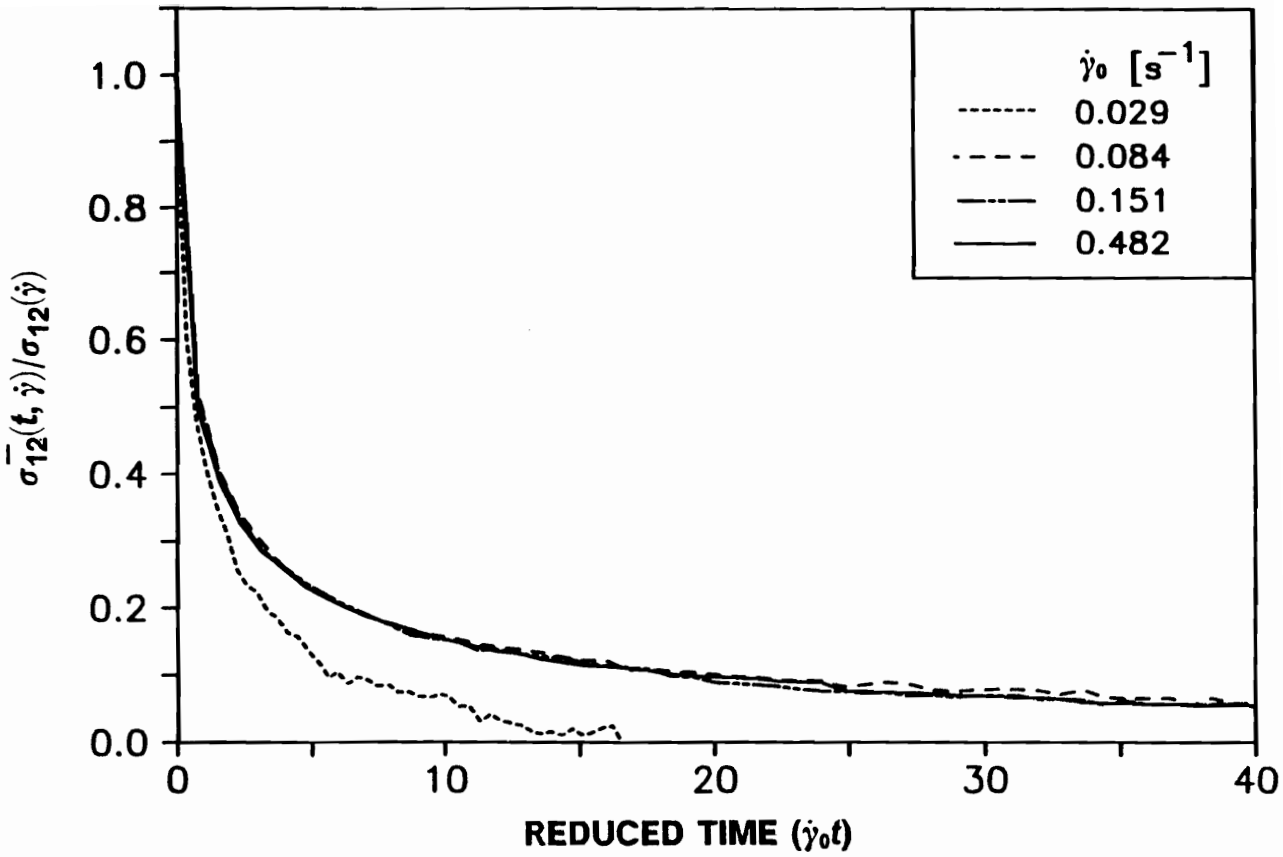

Figure 52. Transient shear stress relaxation after cessation of steady flow in HBA/HNA at 301 °C.: Reduced stress plotted versus product of prior shear rate and time ($\dot{\gamma}_o t$).

negative for HPC EF at 190 °C, upon cessation of shear the values become even more negative. By taking the normal force baseline to be that after the cessation of flow, it is found that the value of N1 in anisotropic HPC is actually positive. When the results for HBA/HNA are treated in this manner negative values of N1 are seen at low shear rates and positive values are seen at the highest rate. In comparison to these the results for HPC EF and HBA/HNA, only positive values of N1 were measured for 60HBA/PET at 275 °C which confirms of the results reported by Gotsis [87,89].

The transient first normal stress difference behavior was also determined for two isotropic melts, namely, HPC EF at 210 °C and for the flexible-chain polymer LLDPE. Positive values of N1 were determined for both materials at all of the deformation rates where the normal force was large enough to be detected, with results shown in Figure 57 for HPC EF at 210 °C. It was found that the values of N1 for the isotropic HPC EF melt were 30 % larger than 2G′ which is within the experimental error for values of N1 at the rates investigated. The equality of 2G′ to N1 could not be rigorously tested for the isotropic HPC EF melt at the rates investigated. At the same time values of N1 were found to be equal to those of 2G′ for LLDPE at 170 °C over the limited range of rates tested, indicating proper operation of the RMS during testing.

4.2.2 Discussion of Transient Shear Behavior

The transient shear stress growth/relaxation behavior determined for the TLCPs investigated suggests that the behavior of liquid crystal polymer systems follows certain scaling laws. In this study the magnitude of the reduced stress σ_r ($\sigma_r = \sigma^+_{12}(t, \dot{\gamma})/\sigma_{12}(\dot{\gamma})$) was found to be independent of the shear rate when plotted as function of strain (the strain referred to in this discussion is Hencky strain, $\dot{\gamma}t$), within the range of rates investigated. Such scaling behavior has been noted in several other LCP systems by other investigators: Mewis and Moldenaers [96,213] found similar scaling for the reduced stress upon the inception of steady shear flow

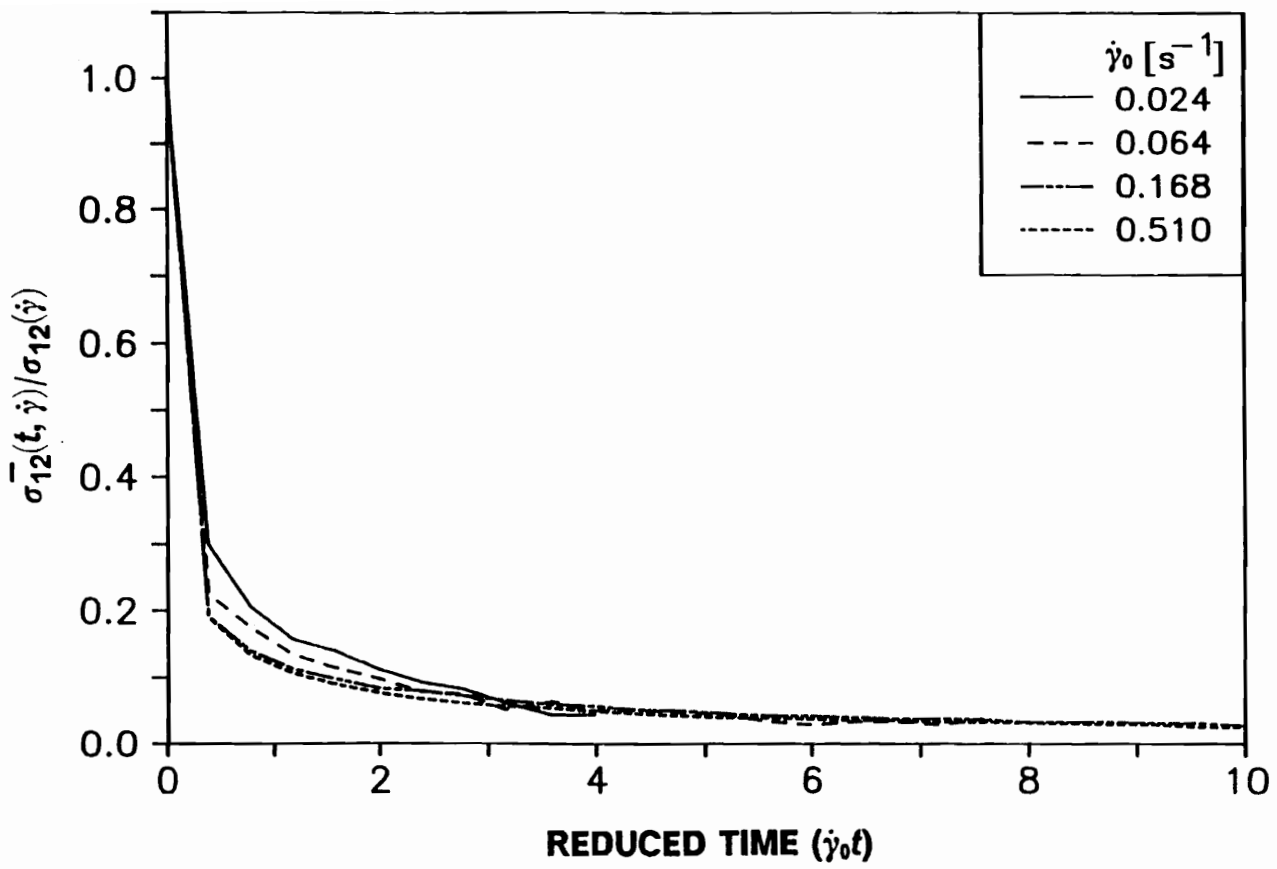

Figure 53. Transient shear stress relaxation after cessation of steady flow in HPC EF at 210 °C: Reduced stress plotted versus product of prior shear rate and time ($\dot{\gamma}_0 t$).

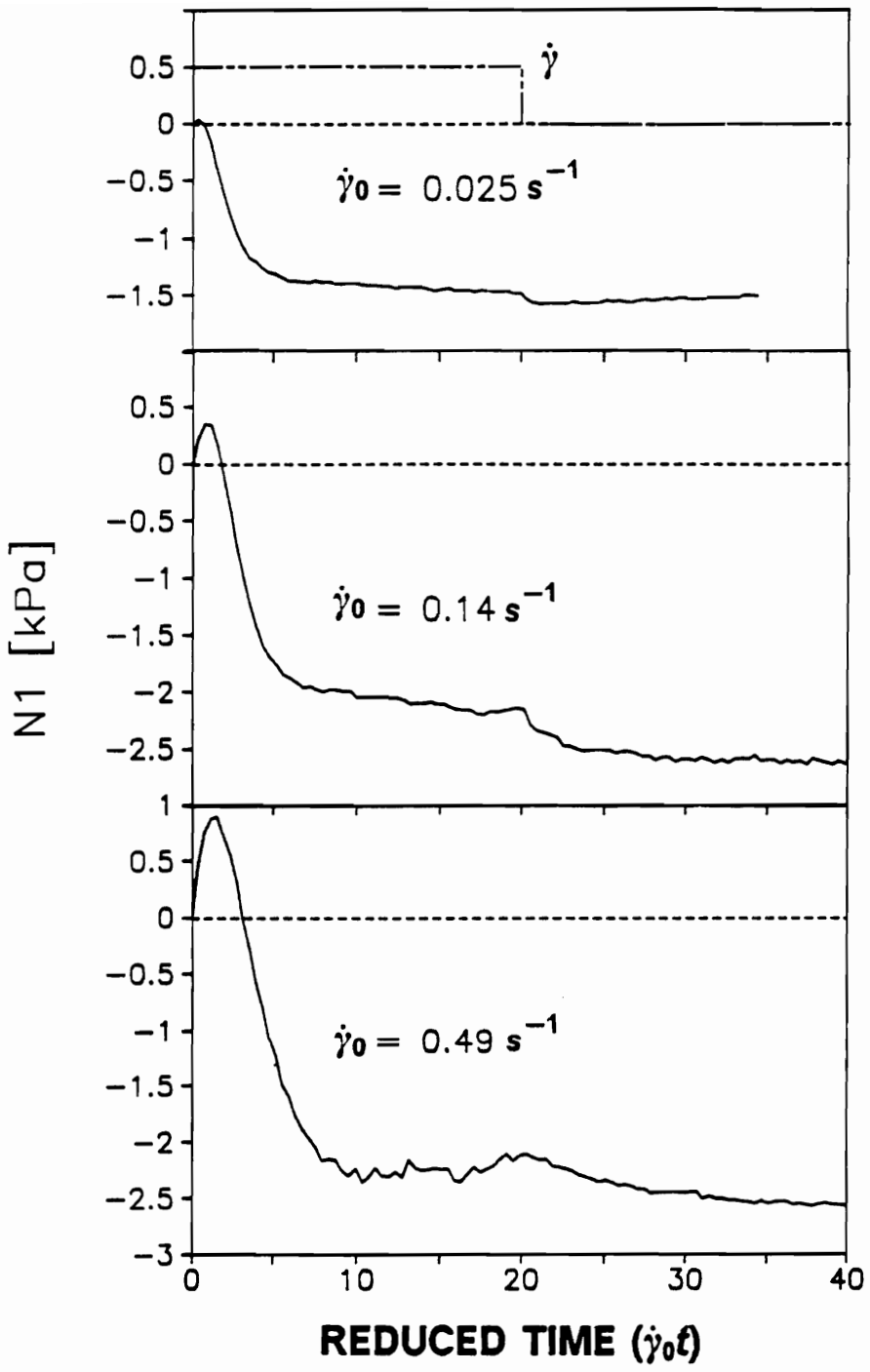

Figure 54. Transient N1 behavior for HPC EF at 190 °C. Time scale reduced by shear rate ($\dot{\gamma}_0$).

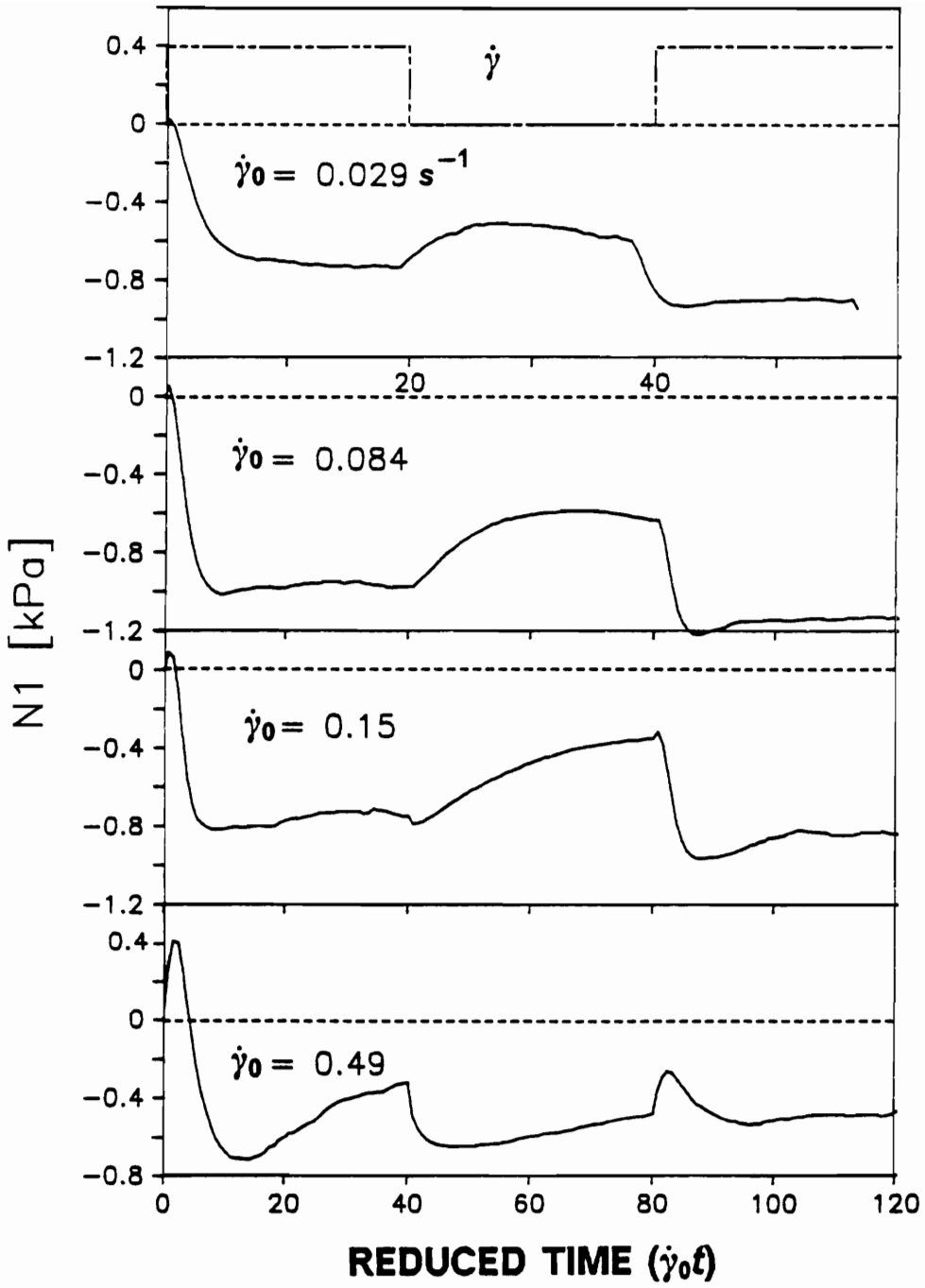

Figure 55. Transient N1 behavior of HBA/HNA at 301 °C. Time scale reduced by shear rate ($\dot{\gamma}_0$).

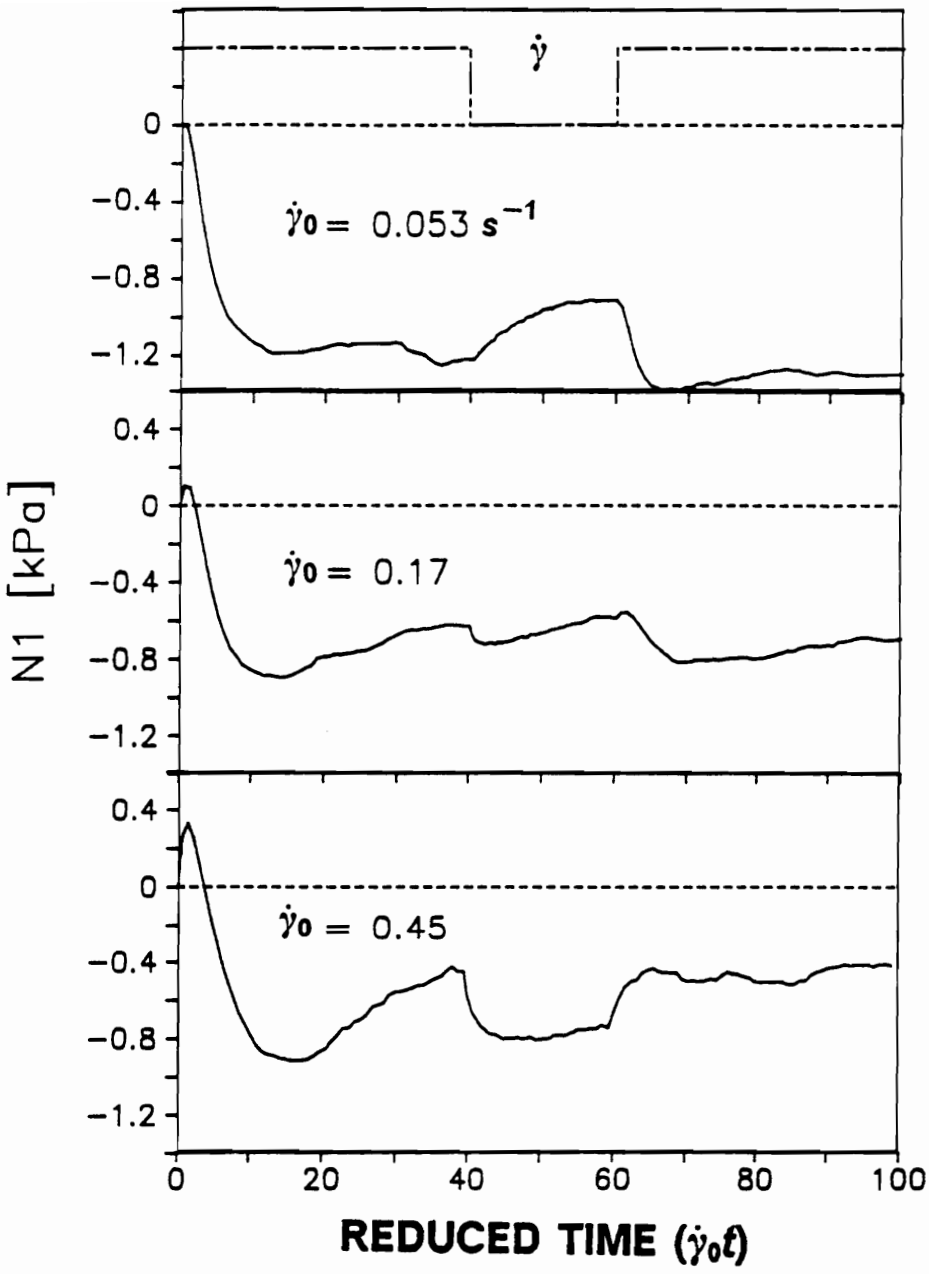

Figure 56. Transient N1 behavior of HBA/HNA at 320 °C. Time scale reduced by shear rate ($\dot{\gamma}_0$).

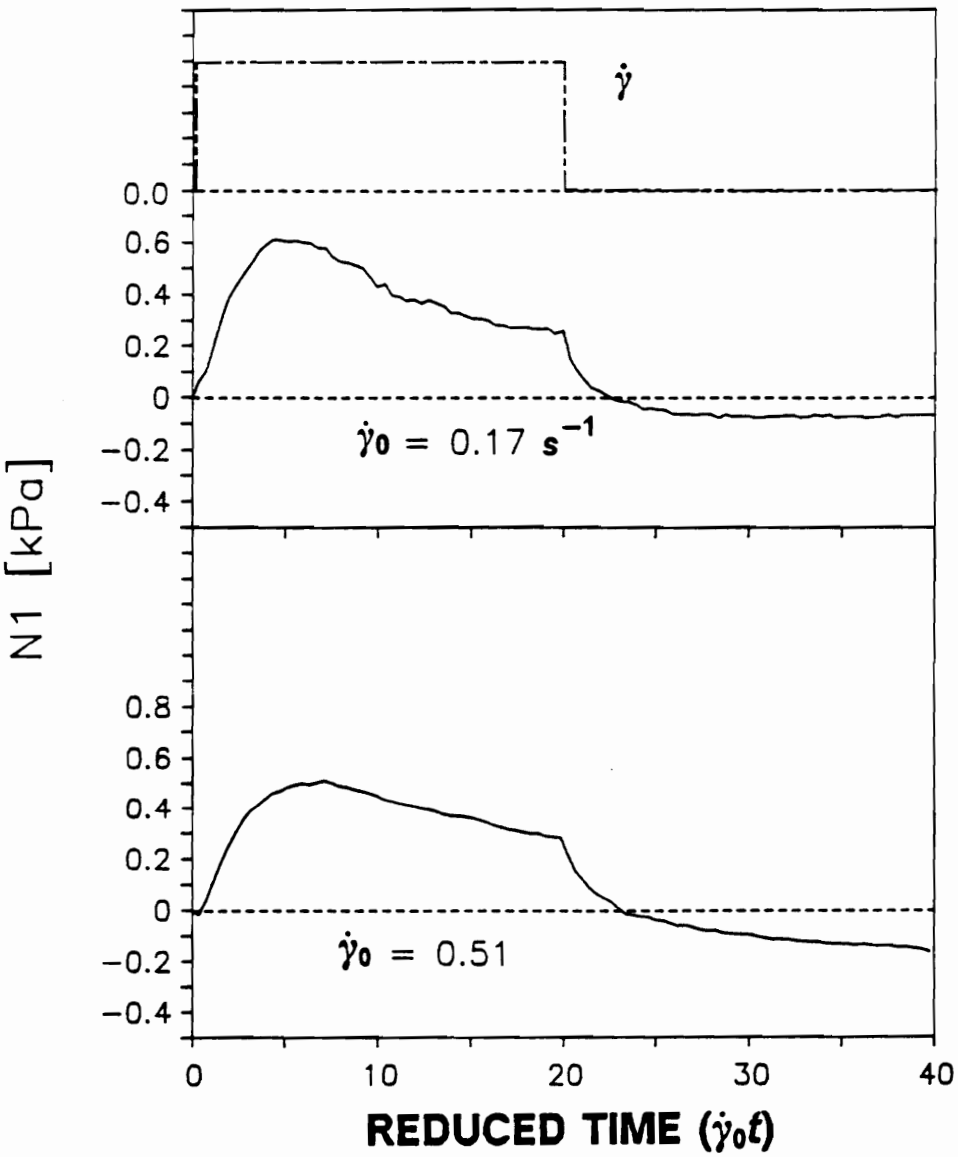

Figure 57. Transient N1 behavior of HPC EF at 210 °C. Time scale reduced by shear rate ($\dot{\gamma}_0$).

in lyotropic PBLG solutions, but found that such scaling was valid for stress relaxation only at strains greater than about 0.5; Larson and Mead [111] reported that the strain recovered upon the cessation of shear flow for lyotropic HPC and PBLG solutions also depends only on strain; Doppert and Picken [118] again noted that reduced stress was only dependent on strain for the inception of steady shear flow in PPTA/H_2SO_4 solutions; Guskey and Winter [214] noted for HBA/HNA that the shapes of the transient viscosity and first normal stress curves were similar for different rates when plotted versus strain.

The question of whether there are fundamental differences in the transient behavior of LCPs and that for isotropic systems of either flexible-chain or rigid chain polymers is considered next. Flexible-chain systems have been reported to display an overshoot peak which occurs at a constant level of strain [72,105] and also stress relaxation which occurs over a time scale which decreases with increasing prior shear rate. Additionally, such behavior has also been reported for by Baird [225] for isotropic solutions of PPTA is concentrated sulfuric acid. However, in all of the isotropic systems it has been observed that the magnitude of the overshoot peak in σ_r upon the startup of steady shear flow increases with increasing shear rate in contrast to the behavior seen in the LCP systems. The relative times for the evolution of the shear stress and the first normal stress difference can also be used to compare the different systems. In the LCPs investigated here, the overshoot or undershoot peaks in the shear stress and first normal stress difference do not occur at similar times but the values of the two quantities appear to approach steady state values at roughly the same time. This contrasts with the behavior reported for flexible-chain isotropic systems [105], where it is found that the overshoot peak for $\sigma\dagger_2(t, \dot{\gamma})$ occurs at roughly half the time as the overshoot peak for $N\dagger$ For the case of isotropic systems of rod-like molecules as evidenced by the isotropic HPC EF melt no consistent behavior is seen between different rates. However, the results reported by Baird [225] for PPTA solutions shows behavior similar to that for the isotropic flexible-chain systems. While further work is needed to confirm the comparisons made here between the behavior of the isotropic and anisotropic systems, it appears that some aspects of the behavior of LCPs are fundamentally different from that isotropic polymer systems.

In view of the discussion above the question arises as to whether the scaling behavior seen for the transient shear stress of the LCPs is due to structural changes occurring in the material. For LCPs, both the evolution of molecular orientation through changes in the local director and changes in the polydomain texture are possible. First, the role of director orientation changes are considered. Viola [8] has shown that the Leslie-Ericksen theory can predict a stress overshoot upon the inception of flow due to the evolution of molecular orientation as seen by changes in the director orientation. However, he also showed that relatively low degrees of molecular orientation were obtained in sheared 60HBA/PET using shear rates much higher than those used in this study, with similar results obtained obtained rheo-optically by other investigators [17,140,141]. Additionally, the magnitude of the overshoot peak was seen to depend on the shear rate for both isotropic HPC EF melts and isotropic PPTA/H_2SO_4 solutions [225]. It then appears that the transient shear flow behavior of TLCPs cannot be due solely to the orienting of individual molecules during flow.

On the other hand, there is evidence for changes in the polydomain structure of LCPs on the startup of flow as was discussed in section 2.2 of the literature review. Larson [111] has shown that such scaling relationships can be predicted by the use of a phenomelogical model which describes the evolution of domain size and domain distortion. Also, Burghardt and Fuller [222] and Larson and Doi [223] have separately shown that the Leslie-Ericksen theory can predict such scaling for transient flows when applied to polydomain systems. Therefore, over the range of rates studied (i.e. low rates), it appears that transient stress growth and relaxation of LCPs is governed by changes in the polydomain texture of the material.

In contrast to the transient shear stress, no general type of behavior was determined for the first normal stress difference of the different LCPs. In order to attempt an explanation of the observed behavior, both errors in the experimental technique and the individual contributions to N1 from the polymer melts are considered. Errors in the experimental technique are mainly those due to error in the baseline. Contributions to normal stresses in polymer melts include those due to fluid inertia, those due to flow induced changes in chain conformation, those due to density changes in the fluid itself, and those due to flow induced changes in the

orientation distribution function (in rigid polymers) [92,217,218]. Each of these contributions to N1 are considered next with respect to the measurements shown in Figures 54 to 57.

In order to avoid confusion, the sign convention used in the discussion of N1 is defined and discussed here. For the purpose of this discussion, tensile stresses are considered to be positive and compressive stresses are negative so that values of N1 measured for flexible-chain polymer systems are positive (this is opposite to the sign convention used in Bird, Armstrong, and Hassager [72] but consistent with mechanics notation). For the test method used and a cone and plate geometry compressive forces acting on the material at the plate surfaces produce positive values of N1 and tensile forces pulling on the fluid surface will produce negative values of N1.

First, errors in the baseline of the force transducer are considered. The baseline of the normal force transducer is set to zero for the RMS 800 at the start of the transient test, regardless of whether there is actually a zero normal force. Residual stresses in a polymer sample at the start of the test would then cause an error in the baseline assumed by the instrument. Such residual stresses will be present when the material has not been properly allowed to relax or might also occur because of the presence of yield stresses. Since the samples tested are compressed before upon loading into the test fixtures the residual force will be negative and the baseline will be shifted to a positive value. Upon the startup of flow the release of these residual stresses would then cause N1 to go negative. Since both HPC EF at 190 ^{0}C and HBA/HNA are thought to contain residual crystallinity it is likely that residual stresses were present in the materials at the start of the tests. Therefore, at least part of the negative undershoot in the values of N1 in those two materials is expected to be due to baseline errors.

The effect of fluid inertia on N1 has been thoroughly discussed by Kiss [80] with regard to PBLG solutions. While the contribution to N1 is negative for a cone and plate geometry, the magnitude of the contribution was found to be insignificant at rates comparable to those used here. A calculation of the contribution to N1 from fluid inertia was made for the HPC EF material and at a rate of 0.5 s^{-1}, the contribution is found to be 0.06 Pa. This is 3 to 4 orders of

magnitude lower than the negative values of N1 observed. Therefore, inertial forces are negligible at the conditions investigated.

Flow induced changes in chain conformation can produce contributions to N1 in flexible-chain molecules through an entropic force, which acts to restore the molecule to its equilibrium conformation. For flexible-chain polymers, the contribution to N1 resulting from this force is positive under the sign convention used here. For the case of HPC there might be sufficient chain flexibility to that this type of contribution to N1 is significant. At the same time no an estimation of such contributions is not possible here. In contrast to the HPC materials, the HBA/HNA copolyesters is thought to be very rigid and contributions to N1 from conformational changes would be expected to be negligible.

Variations in material density are also expected to have a large effect on the normal stress measured for a polymer melt. For example, large fluctuations in N1 can be observed due to large thermal fluctuations [202]. Density changes due to flow would then also affect the normal stress measurement, with densification contributing negatively to the value of N1 in a cone and plate geometry. In order to quantify the magnitude of possible contributions to N1 from density changes, a sample calculation was made for the HPC material. Consider an HPC material which is largely liquid crystalline but contains 25 % isotropic material at the start of the test and assume that upon inception of flow the material becomes wholly liquid crystalline. Using densities obtained from Samuels [171], a 4 % reduction in density was calculated to result in a reduction of 0.018 mm in the thickness of a sample for for a cone and plate test geometry. As estimate of the compliance of the normal force transducer in the RMS 800 was made from the process of zeroing the plate gap and a value of 5E-6 mm/g was obtained. The contribution to N1 resulting from such a density reduction was calculated to be -140,000 Pa, which is 2 orders of magnitude larger than the negative N1 values observed in the LCPs. While the density change assumed here is somewhat exaggerated, it can be seen that even a 0.04 % density change could result in negative values of N1 of the order measured. However, it should also be pointed out that such values should be transient in nature since the stress generated is isotropic and will act to draw in the free surface of the material at the edge

of the plate. Therefore, density changes can not explain all of the negative values of N1 observed in the LCPs investigated.

Finally, the generation of contributions to the first normal stress difference from changes in the orientation distribution are considered. Both positive and negative contributions can be generated depending on whether the orientation distribution becomes sharper or broader as a result of the imposed flow as was discussed in chapter 2. While such changes in the orientation distribution might also be associated with density changes in the material, the stress generated is now anisotropic which allows a steady state contribution to N1. In view of the above discussion, it would be expected that the contribution to N1 from imposed changes in the orientation distribution is positive at large rates. However, it is not clear whether the distribution is broadened or sharpened in the range of rates investigated.

The experimentally determined N1 behavior of HPC EF and HBA/HNA is now considered in terms of the contributions to the normal force discussed above. The initial overshoot in the value of N1 upon the startup of flow occurs at roughly the same strain level as the shear stress overshoot, and is likely related to the breakdown of the fluid structure. From the discussion above the observation of a positive overshoot seems somewhat strange and the only explanation this author can come up with is some type of compressive force caused by rotation and breakup of domains, but this is pure speculation. Following this overshoot the value of N1 goes highly negative and the most likely reason is that there was a baseline error. The breakdown in structure associated with the first peak might then allow the normal force to relax an this effectively results in a negative value of N1. Additional negative contributions to N1 could result from either densification or broadening of the orientation distribution. In the case of HBA/HNA, where true steady negative values of N1 are observed, it seems likely that they are related to the broadening of the orientation distribution since densification should result only in transient negative values. In the case of HPC EF relatively steady values of N1 are also seen and therefore densification might not be significant. At the same time the true values of N1 for HPC EF are positive and orientation distribution effects might also be absent.

While the major features of the N1 behavior determined for the LCPs can be explained in terms of different contributions to the normal force, such explanations can not be proven at this time. For example, both changes in molecular conformation and a sharpening of the orientation distribution could result in positive values of N1, though no direct evidence exists for the determination of which contribution is responsible. Also, while negative values of N1 could be due to the broadening of the orientation distribution, no direct experimental evidence has proven this mechanism. Finally, it is still possible that an unknown mechanism exists for the generation of a negative contribution to N1.

In summary, the shear stress growth/relaxation behavior of several LCPs was determined and found to obey certain scaling relations, with the magnitude of the reduced shear stress independent of rate when taken to be a function of strain. Similar results have been previously reported in the literature for several other LCP systems. At the same time no general behavior for the transient growth/relaxation of the first normal stress was determined, though behavior similar to that measured here has been previously determined for other TLCP systems. The behavior determined for the LCPs was compared to that for isotropic systems of both flexible-chain and rodlike polymers. While many similarities were found between the behavior of the liquid crystalline and isotropic systems, a difference in the scaling of the magnitude of the shear stress overshoot peak with shear rate provides support for the assertion that structural changes are important for transient flows in LCPs. Finally, it should be noted that a limited number of transient flow studies have been reported for LCPs and the generality of much of the behavior presented here is still uncertain.

4.3 Elongational Behavior of TLCPs

The main objective of this work was given as the determination of the elongational flow behavior of TLCPs and establishing whether this behavior is different from that of isotropic

systems of either flexible-chain or rodlike polymers. In this section the results of transient elongational viscosity growth studies are presented and discussed. The studies were carried out on three thermotropic LCPs; namely HPC EF, HPC G, and HBA/HNA. Since very few similar results have been reported for LCP systems, the results are analyzed and discussed in relation to the behavior for both isotropic melts of flexible-chain polymers and for isotropic melts for polymers having rodlike molecules. In order to do so the elongational viscosity growth behavior is compared to the shear viscosity growth behavior and examined from the framework of linear viscoelastic behavior.

Before considering the elongational flow results for the LCPs, it is helpful to note the behavior predicted by linear viscoelastic theory. The elongational viscosity growth function, $\bar{\eta}_e^+(t, \dot{\varepsilon})$, of a linearly viscoelastic material is independent of deformation rate and equals three times the shear viscosity growth function, $\eta^+(t, \dot{\gamma})$. Such behavior is commonly seen in flexible chain polymer melts at low deformation rates, while positive deviations of $\bar{\eta}_e^+(t, \dot{\varepsilon})$ from 3 $\eta^+(t, \dot{\gamma})$ or strain hardening have been seen in many polymers at higher deformation rates and above a certain strain level [72,105].

In order to facilitate determination of deviations from linear viscoelastic behavior in the elongational flow results, the transient shear viscosity growth functions are plotted with the results for elongational flow (see Figures 58 to 66). It is noteworthy that the shear viscosity growth function itself shows linear viscoelastic behavior at the different rates up to a certain strain level, which turns out to be about 1 strain unit. In the analysis of the results it is assumed that the linear viscoselastic behavior for each material is represented by the curve of $\eta^+(t, \dot{\gamma})$ at the lowest rate and up to a strain of 1. The linear viscoelastic shear stress growth function will be denoted by $\eta_0^+(t)$ to distiguish it from the rate dependent quantitity $\eta^+(t, \dot{\gamma})$.

4.3.1 Elongational Flow Results

The extensional viscosity growth behavior of three LCPs was determined in the rotary clamp extensional rheometer using the methods described in Chapter 3 and Appendix B. The results shown in this section represent the average of three test runs. Generally, the values of $\bar{\eta}_e^+(t, \dot{\varepsilon})$ determined for the LCPs showed agreement within $\pm$ 15% and in some cases agreement was much better than this. Additionally, an error analysis for the test method indicates that the absolute values of $\bar{\eta}_e^+(t, \dot{\varepsilon})$ obtained in the ER are within $\pm$ 20% of their true values. At the same time the error observed in the values of $\bar{\eta}_e^+(t, \dot{\varepsilon})$ measured for the LLDPE standard were within this range.

The elongational viscosity growth functions of anisotropic melts of HPC EF (190 °C), HPC G (200 °C) and HBA/HNA (301 and 320 °C) measured in the ER are shown in Figures 58 to 61. Both linear (i.e. $\bar{\eta}_e^+(t, \dot{\varepsilon}) = 3\eta_0^+(t)$) and nonlinear viscoelastic behavior was observed in the the anisotropic melts, with linear behavior only seen at low strain values and in some materials also only at the lowest elongation rates. Deviation from linear viscoelastic behavior was seen as a positive deviation of $\bar{\eta}_e^+(t, \dot{\varepsilon})$ from $3\eta_0^+(t)$ and is also referred to here as strain hardening. The criteria used for determining the start of strain hardening was to determine the strain value at which deviations of $\bar{\eta}_e^+(t, \dot{\varepsilon})$ from $\eta_0^+(t)$ became larger than 20%. Strain hardening was seen to occur starting at low to moderate strain values (0.1 to 1) or throughout the entire test. At the same time the magnitude of the strain hardening behavior was low when compared to that seen in a material such as linear low density polyethylene, with the value of $\bar{\eta}_e^+(t, \dot{\varepsilon})$ usually no greater than twice $3\eta_0^+(t)$ at sample fracture. Finally, no steady state elongational viscosity was seen in any of the anisotropic melts with samples either necking or fracturing at the end of the test. However, since strain levels were in the range of 1.2 to 2 strain units at fracture, the existence of a steady state elongational viscosity could not be ruled out either.

In order to determine the generality of the results, the effect of residual crystallinity has to be considered. In order to do so it is intructive to compare the results for HBA/HNA at 301

°C and 320 °C as shown in Figures 60 and 61, since the HBA/HNA melt is likely to have a larger amount of residual crystallinity at 301 °C than at 320 °C as previously discussed. It can be seen that strain hardening occurs at lower strain levels for the HBA/HNA melt at 301 °C than at 320 °C, with strain hardening behavior occurring at some rates throughout the entire test in the former case. At the same time, at 320 °C it is observed that the melt behaves in a linearly viscoelastic manner at low strains, up to about 0.5 strain units, at all rates investigated. Furthermore, the behavior of HPC EF at 190 °C shows behavior similar to that of HBA/HNA at 301 °C, i.e. deviation of $\bar{\eta}_e^+(t, \dot{\varepsilon})$ from $3\eta_0^+(t)$ at the higher rates for the entire strain range, and it was shown by means of WAXS that the HPC melt contains a significant amount of residual crystallinity. Also, strain induced crystallization is a valid mechanism for strain hardening behavior in conventional polymer systems [201]. Therefore, it appears that residual crystallinity is a reasonalble explanation for some of the strain hardening behavior seen in the TLCPs studied.

Some insight into the question of whether the elongational flow behavior determined is general for other LCP systems comes from establishing whether scaling relationships exist for the elongational flow behavior as is found for the transient shear flow behavior of the same LCPs. In order to do so the viscosity growth behavior of melts of HPC EF at 190 °C and HBA/HNA at 320 °C were replotted as viscosity versus strain as shown in Figures 62 and 63, though no reduction of the extensional viscosity was possible since no steady state values of $\bar{\eta}_e^+(t, \dot{\varepsilon})$ were determined. It can be seen that the shapes of the curves for the different rates are somewhat similar to each other and could show some overlapping if the stress was reduced. Similar behavior is also seen in HPC G at 200 °C and HBA/HNA at 320 °C. Thus, the elongational viscosity growth behavior of the TLCPs investigated appears to scale with strain, which is an indication that the results might be general to other LCP systems.

Should the elongational viscosity behavior of LCPs be found to scale with strain this would indicate that structural changes occurring in LCPs during flow govern their transient flow behavior as is believed to be the case for transient shear flow. Additionally, the question arises as to whether changes are occurring on the same structure level in both elongational

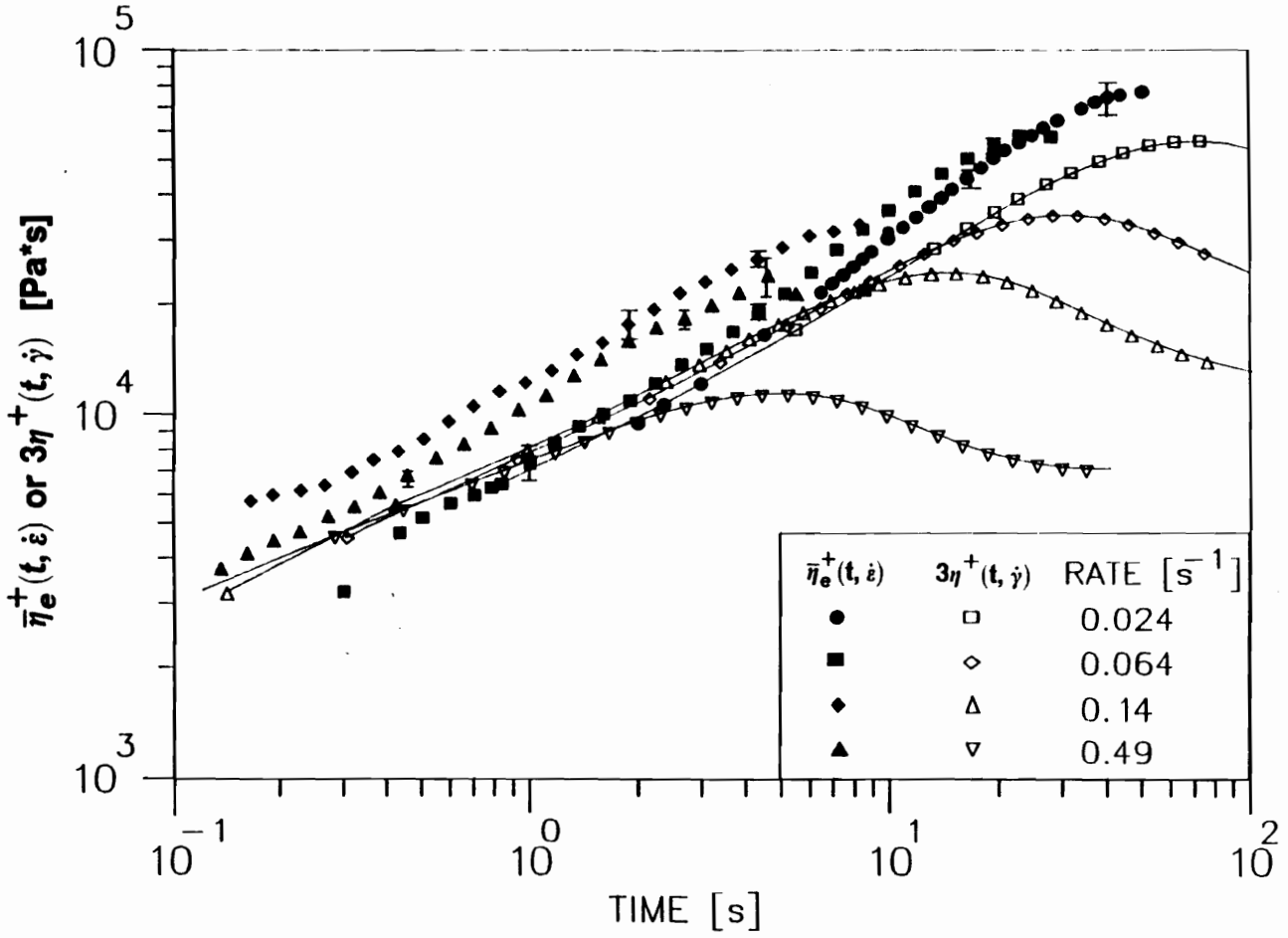

Figure 58. Transient elongational and shear viscosities of HPC EF at 190 °C: Lines are fitted to the shear data and symbols are described in the figure.

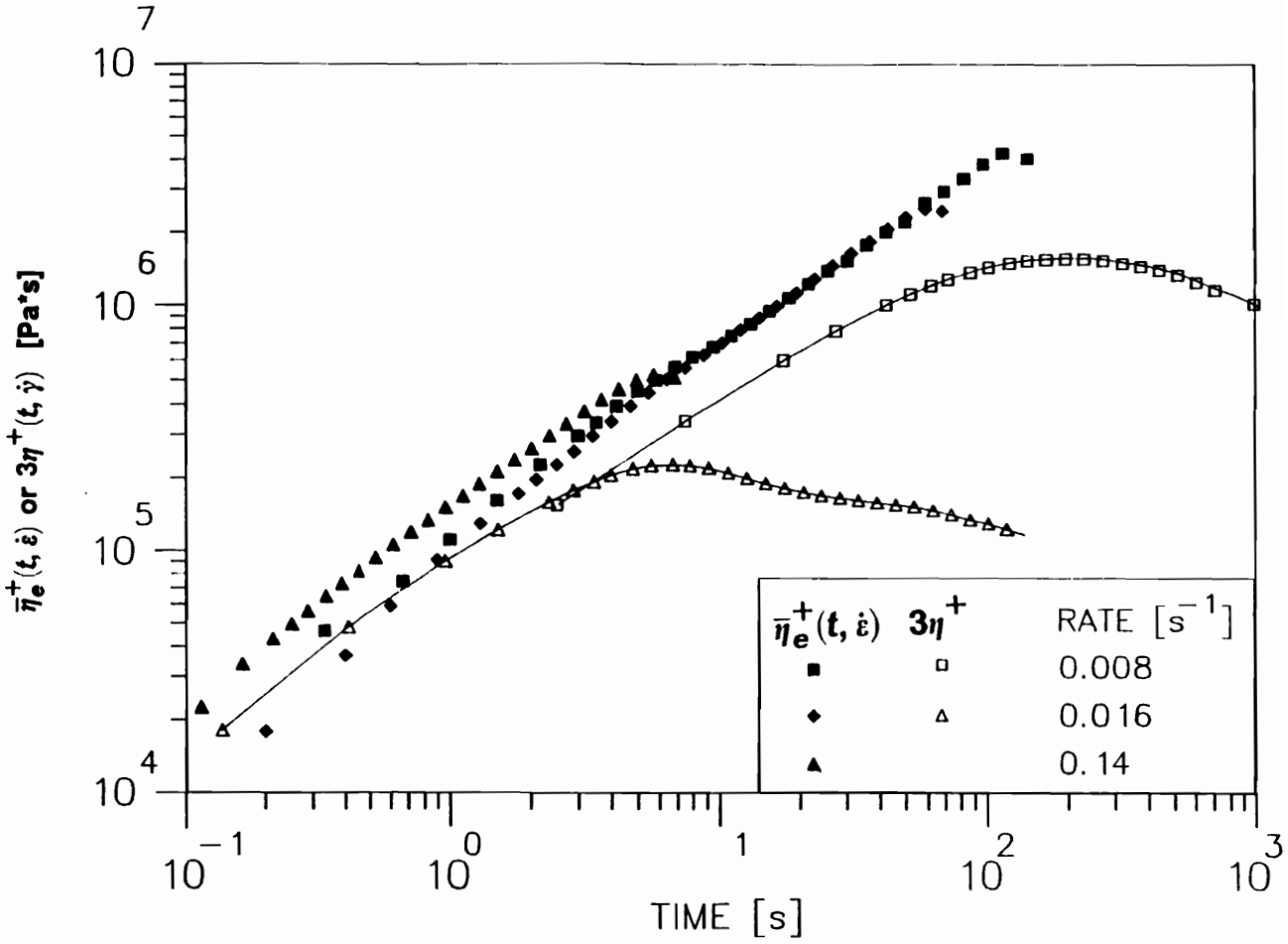

Figure 59. Transient elongational and shear viscosities of HPC G at 200 °C: Lines are fitted to the shear data and symbols are described in the figure.

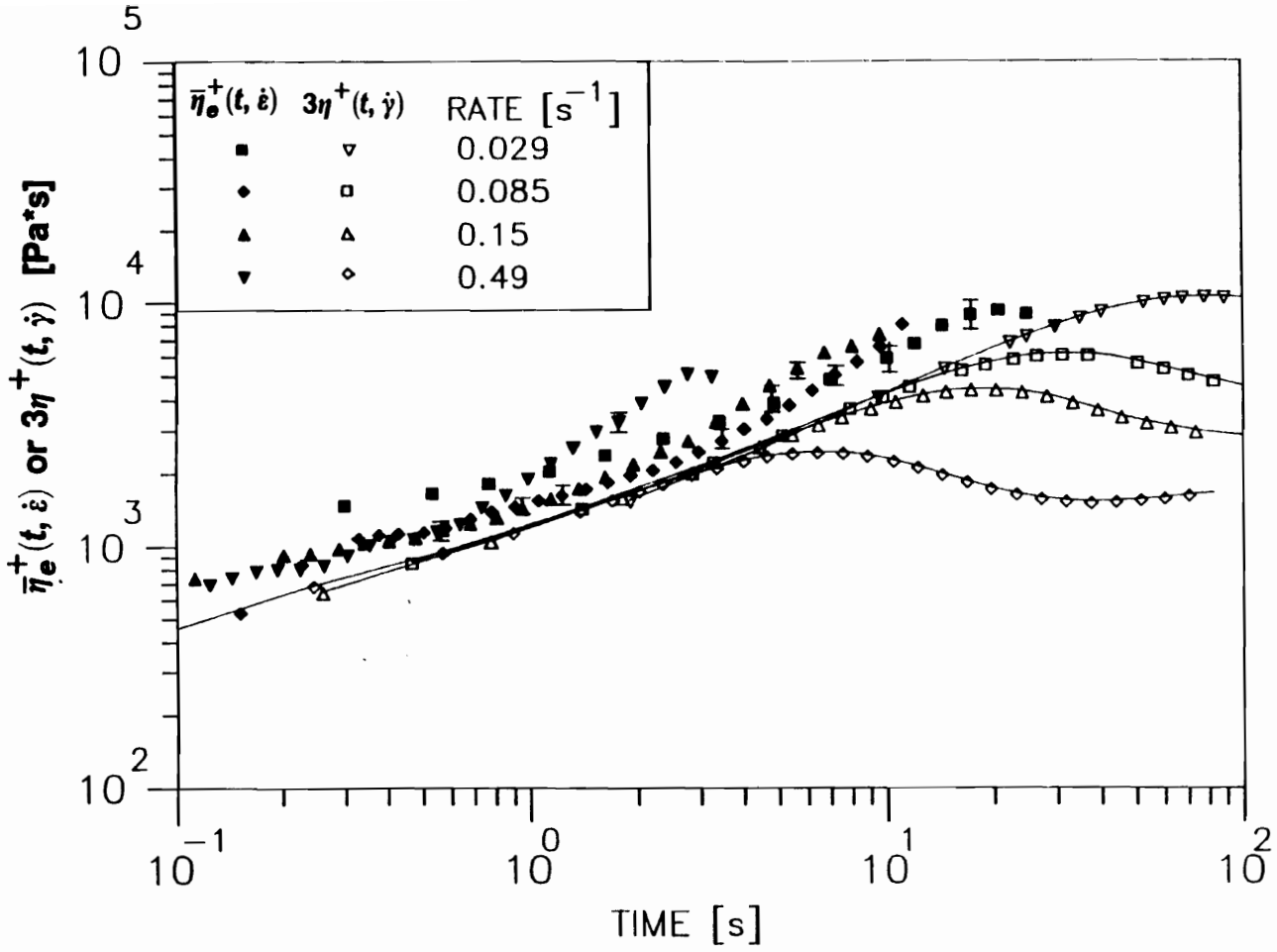

Figure 60. Transient elongational and shear viscosities of HBA/HNA at 301 °C: Lines are fitted to the shear data and symbols are described in the figure.

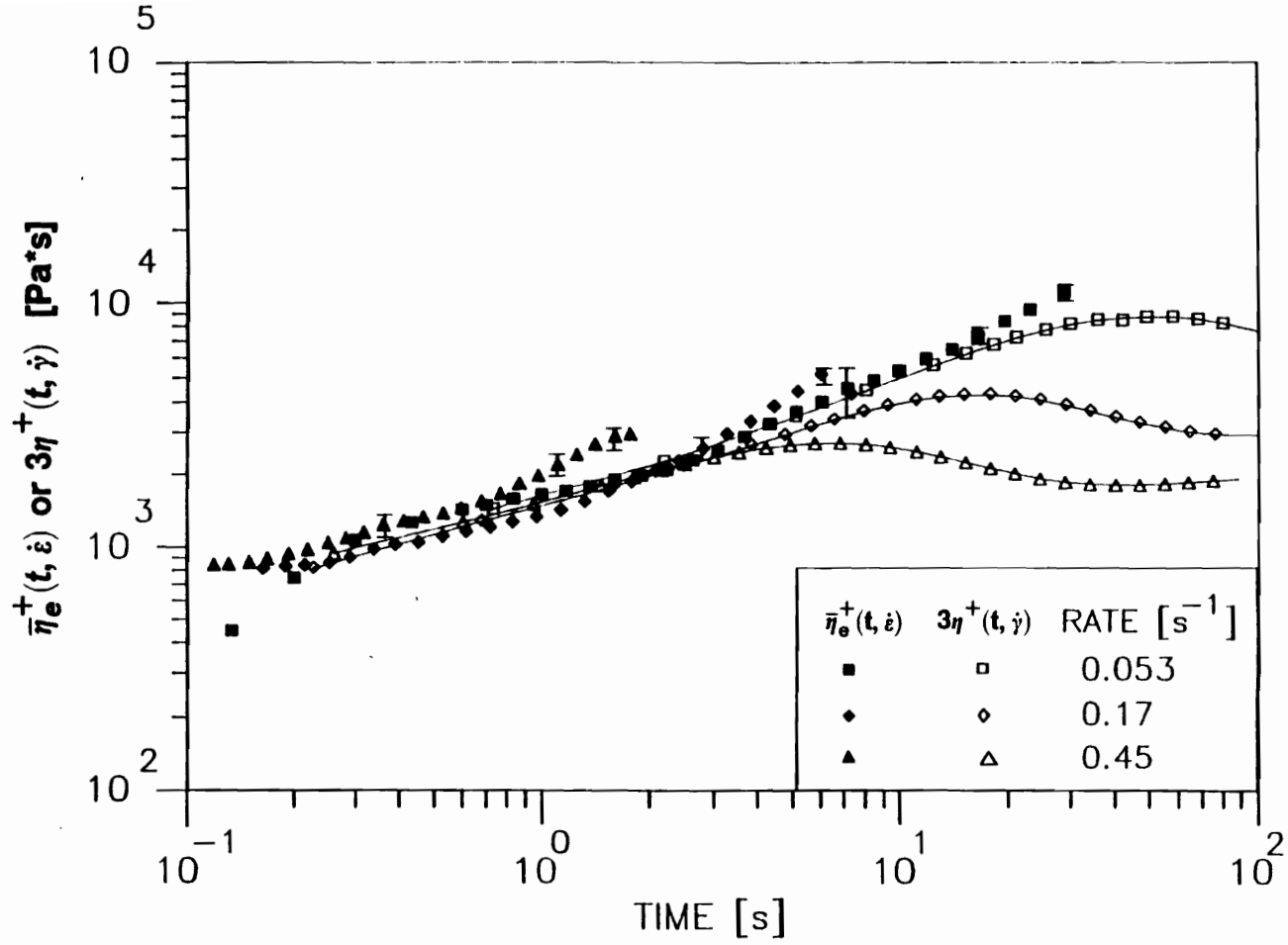

Figure 61. Transient elongational and shear viscosities of HBA/HNA at 320 °C: Lines are fitted to the shear data and symbols are described in the figure.

and shear type flows. While no direct evidence of structural change was obtained during testing, some insight is gained by a close comparison of the transient elongational and shear viscosities at the same deformation rates (see figures 58 to 61). It becomes apparent that the fracture of the samples undergoing elongational flow occurs at roughly the same level of strain as the maximum in the transient shear viscosity.

Another feature of the reduced plots shown in Figures 62 and 63 is a decrease in elongational viscosity with increasing rate when compared at equal values of *strain* (εt). While this is also expected for a linearly viscoelastic material at low strains (recall that for a linearly viscoelastic material $\bar{\eta}_e^+(t, \varepsilon)$ is independent of time at short times and therefore at higher rates the value of $\bar{\eta}_e^+(t, \varepsilon)$ is smaller at equal strain), the steady state elongational viscosity of such a material is rate independent. Additionally, the viscosity at which fracture occurs also decreases with increasing rate indicating that the steady state elongational viscosity of the LCPs, if one in fact exists, should be rate thinning.

The elongational viscosity growth functions of isotropic melts of the HPC materials were also determined in order to establish whether the elongational behavior of the materials was dependent on their physical state, with the results shown in Figures 63 to 65. In Figure 64, the elongational viscosity growth behavior of the isotropic HPC EF melt is seen to be markedly different from that for the anisotropic melt as shown in in Figure 58. For example, the value of $\bar{\eta}_e^+(t, \dot{\varepsilon})$ in the isotropic melt shows a steady value plateau at $3\eta_0$, with the value of the plateau found to be nearly independent of rate. Additionally, although strain hardening behavior is also seen in the isotropic melt, the value of strain at which it occurs in the isotropic melt is higher than that for the anisotropic melt. Also, The magnitude of strain hardening is seen to be much greater in the isotropic than the anisotropic melt. In contrast to the results for HPC EF, very little difference is seen between the elongational behavior of HPC G in anisotropic and isotropic melt states. However, it should be noted that the molecular weight of HPC G is very high and was noted as being more like a rubbery solid than a liquid in the melt, with elastic effects probably obscuring the viscous behavior.

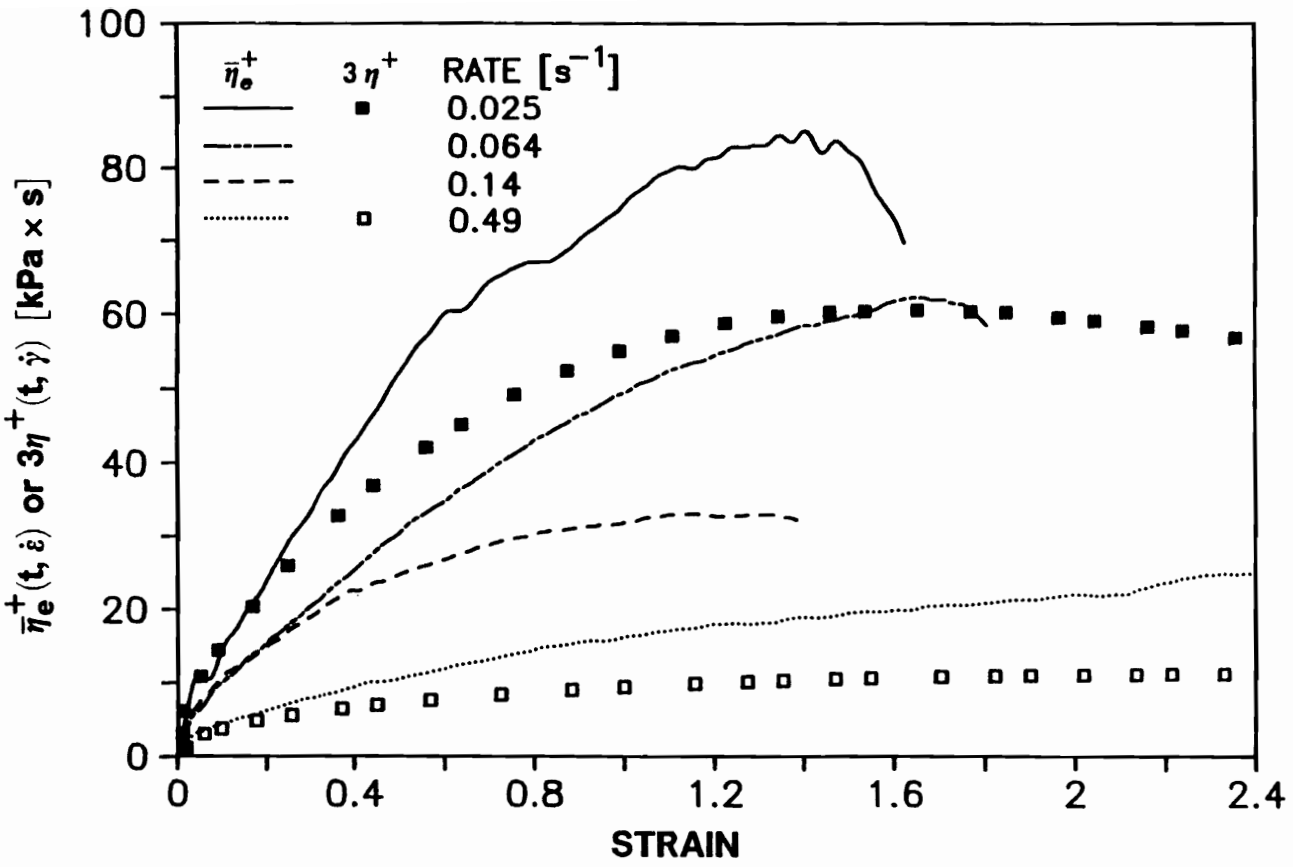

Figure 62. Transient elongational and shear viscosities of HPC EF at 190 °C: Lines denote $\bar{\eta}_e^+$ and symbols denote $3\eta^+$ at rates given in the figure.

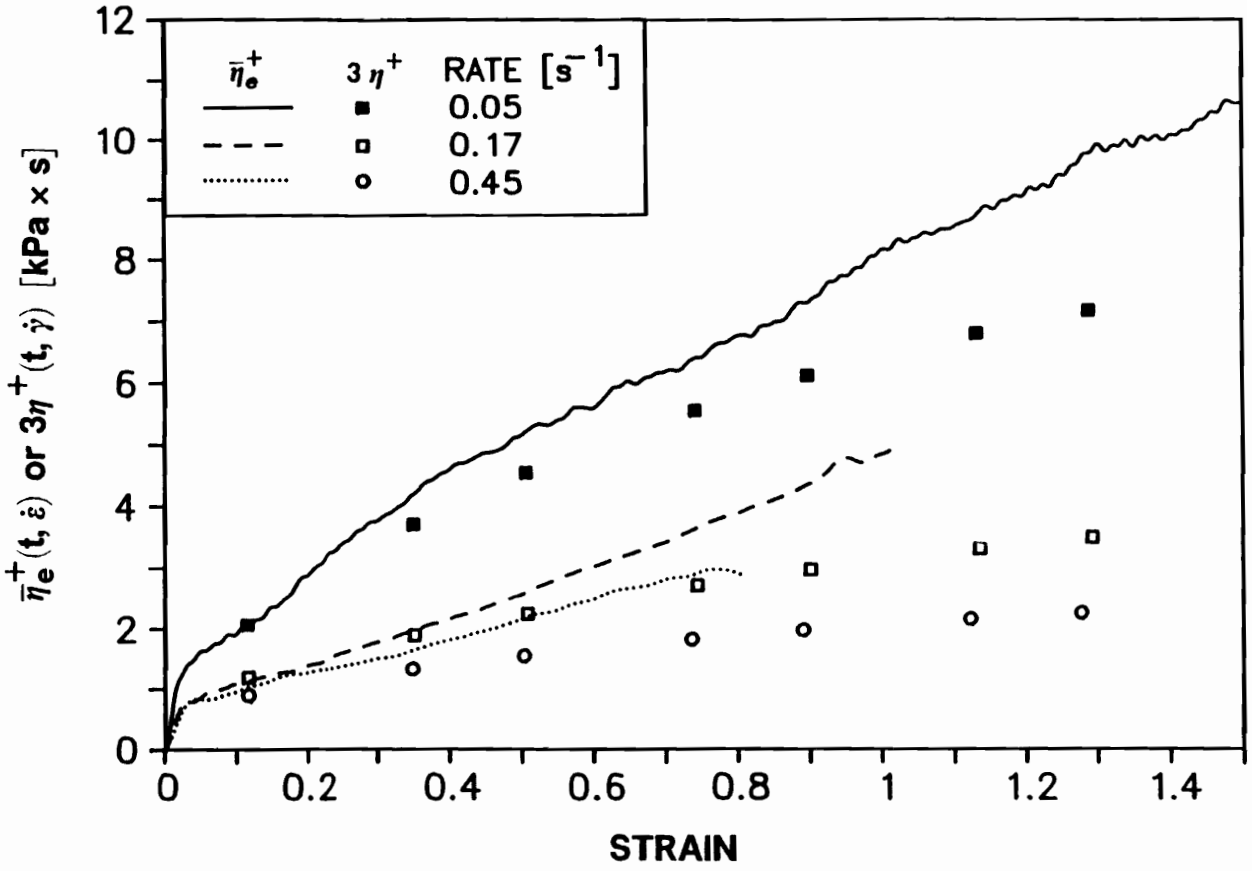

Figure 63. Transient elongational and shear viscosities of HBA/HNA at 320 °C: Lines denote $\bar{\eta}_e^+$ and symbols denote $3\eta^+$ at rates given in the figure.

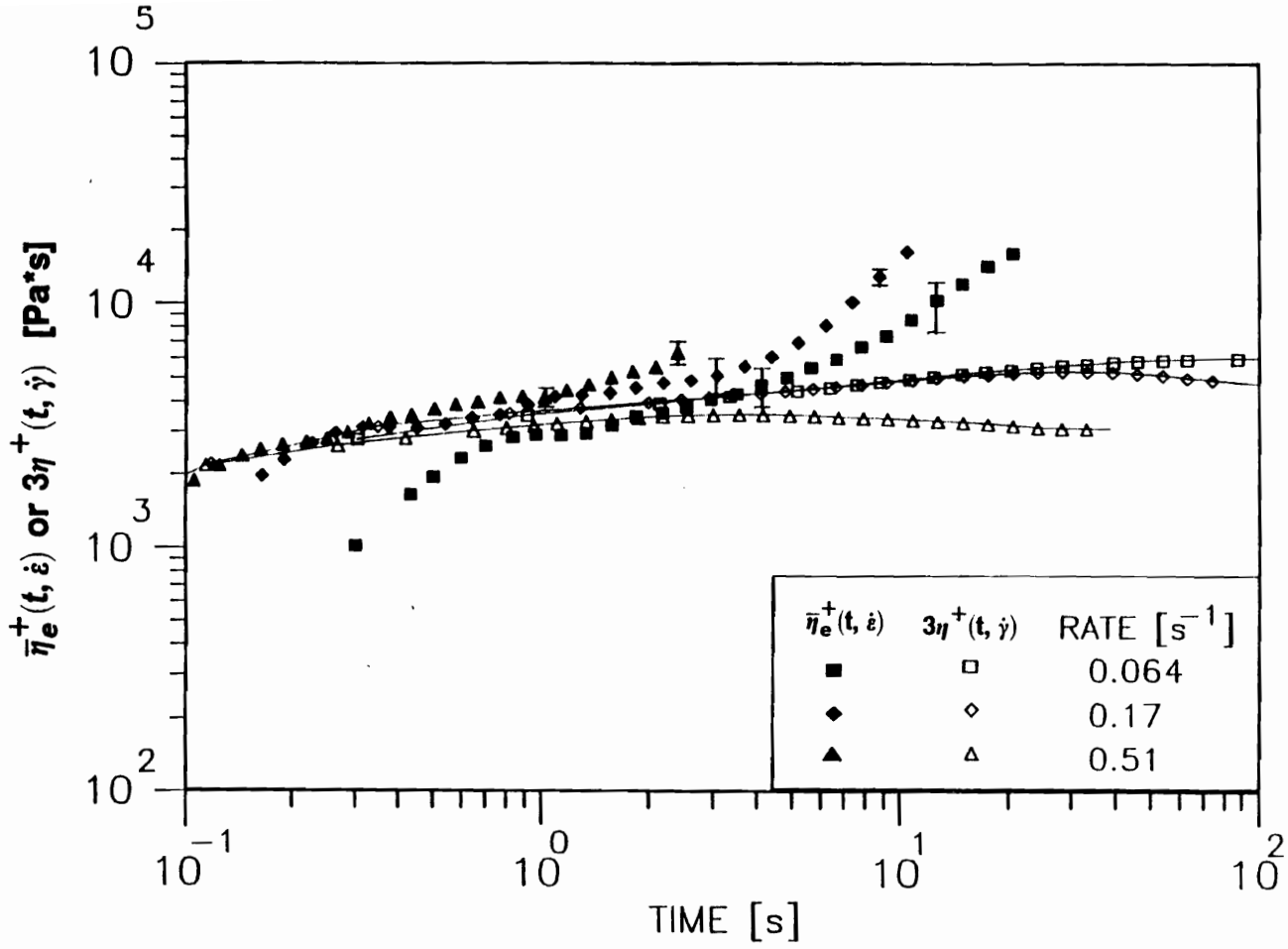

Figure 64. Transient elongational and shear viscosities of HPC EF at 210 °C: Lines are fitted to the shear data and symbols are described in the figure.

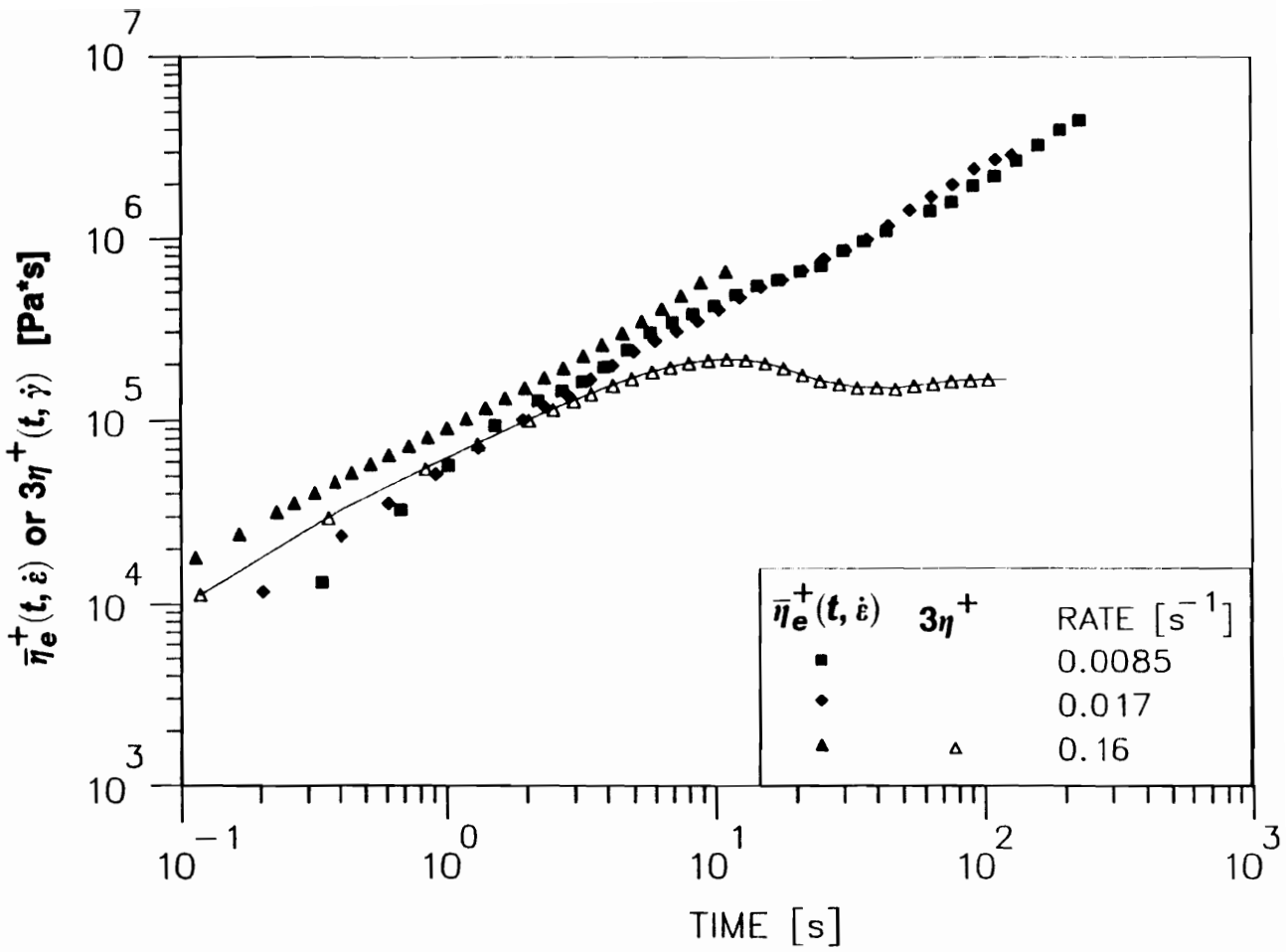

Figure 65. Transient elongational and shear viscosities of HPC G at 240 °C: Lines are fitted to the shear data and symbols are described in the figure.

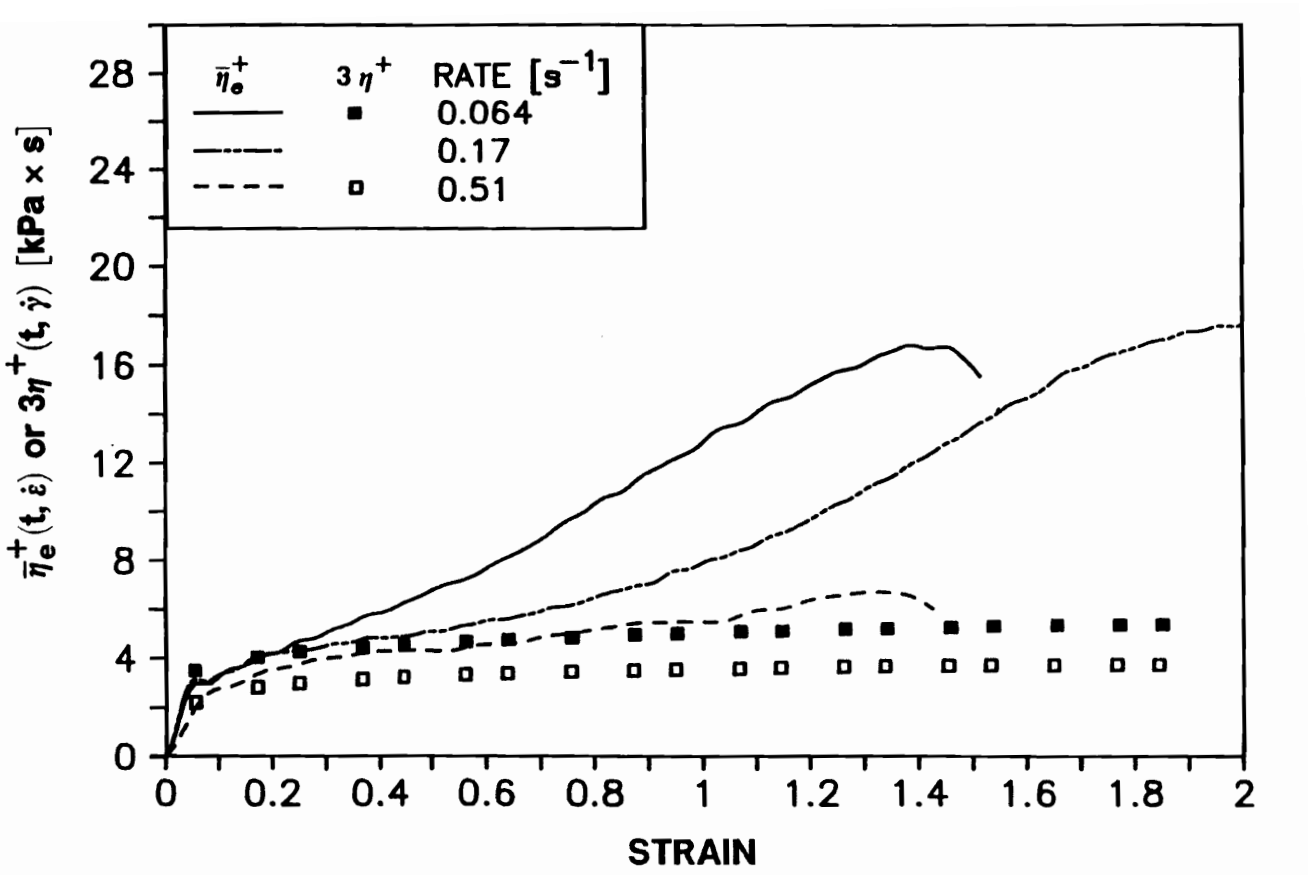

Figure 66. Transient elongational and shear viscosities of HPC EF at 210 °C: Lines denote $\bar{\eta}_e^+$ and symbols denote $3\eta^+$ at rates given in the figure.

The elongational viscosity growth functions of isotropic melts of HPC EF are also plotted versus strain in Figure 66 in order to determine whether any scaling relationships are found in the isotropic state. It can be seen that the curves are very similar at low strains, both in shape and magnitude. However, strain hardening behavior is seen at higher strains and the strain at which this occurs actually increases with increasing elongation rate. Thus, it appears that the elongational behavior of the isotropic melt does not scale with strain in agreement with the shear stress growth behavior of the material but in contrast to the anisotropic state in the same material.

4.3.2 Discussion of Elongational Behavior

The elongational viscosity growth behavior of three liquid crystalline materials was presented in this section. Certain similarities were seen in the behavior determined for the different LCPs. First, strain hardening was seen in the materials at all rates, apparently occurring at lower strains as rate increased. The degree of strain hardening seen in the materials was low to moderate, with no sign of unbounded stress growth as is seen in materials such as LDPE. At the same time, there was no direct evidence of a steady state elongational viscosity. The transient elongational viscosity growth curves for different elongation rates were seen to be similar in shape when plotted as a function of strain, with the viscosity decreasing with increasing rate when compared at the same strains. Finally, it was noted that the viscosity value at which the sample fractured also decreased with increasing rate.

Before considering whether the behavior determined for the TLCPs in this study is general to LCPs, it is instructive to compare the behavior to that determined for flexible-chain polymers, which is described in detail in a number of references [72,105,207,215]. The elongational flow behavior determined for the TLCPs in this study shows both similarities and differences from that known for flexible chain systems. In general, flexible-chain polymers display a steady state and rate independent elongational viscosity at low enough elongation

rates where the value of $\bar{\eta}_{\bullet}^{+}(t, \dot{\varepsilon})$ is equal to $3\eta_{o}^{+}(t)$. In contrast, no steady state values of $\bar{\eta}_{\bullet}^{+}(t, \dot{\varepsilon})$ were seen for the TLCPs investigated and there was evidence that the elongational viscosity is rate thinning as well. Some flexible-chain polymers are known to display strain hardening behavior as was found for the TLCPs. In fact, the degree of strain hardening seen in the TLCPs (i.e. the degree to which $\bar{\eta}_{\bullet}^{+}(t, \dot{\varepsilon})$ deviates from $3\eta^{+}(t, \dot{\gamma})$) was somewhat similar to that observed in certain samples of HDPE [141] and high molecular weight polystyrene [72]. The value of strain at which strain hardening behavior appears can also be compared. When this is done for the LCPs with the HDPE data determined by Ide and White [141] it is found that strain hardening occurs at about 1 strain unit. At the same time strain hardening behavior was seen to occur in the HBA/HNA melt (at 320 °C) at about 0.5 strain units. Although strain hardening was seen over the entire strain range for the TLCPs at some conditions, this might have been caused by the influence of residual crystallinity. Finally, it was hypothesized that TLCPs show rate thinning behavior based on the value of $\bar{\eta}_{\bullet}^{+}(t, \dot{\varepsilon})$ at sample fracture. At the same time rate thinning behavior has been seen in flexible-chain polymers only above a certain elongation rate [72]. Therefore, while the elongational behavior of the TLCPs shows some differences with that for flexible-chain polymer melts, there is no clear evidence at this time that the behavior is fundamentally different.

The question also arises as to whether the elongational behavior of rodlike polymers is different in the anisotropic and isotropic states. In order to answer this question the elongational flow behavior of isotropic and anisotropic melts of HPC EF was compared. Marked differences were found in the shapes of the curves and in the dependence of the elongational viscosity on deformation rate as previously described. Factors which could cause such differences in behavior are differences in chain flexibility, differences in test temperature, residual crystallinity, and differences in the material state (i.e. isotropic versus liquid crystalline). No differences are expected in the flexibility of the HPC EF chain at the two test temperatures. This is assumed since the molecule is helical and intermolecular hydrogen bonding hold the chain conformation in place [171]. Furthermore, infrared measurements indicated that this intramolecular hydrogen bonding is present to at least 250 °C [171]. Differences in be-

havior are also unlikely to be due to differences in the test temperature which are activation energy driven (such as in flexible-chain molecules [72]). The kinetic effect of changing the temperature should only affect the magnitude of the elongational viscosity and not the shape of the curve. The effect of residual crystallinity is more difficult to evaluate. It was shown in section 4.1 that there is a large difference in the amount of residual crystallinity present in the HPC EF melt at 190 and 210 °C. Some insight into the relative effect of residual crystallinity was shown by a comparison of the behavior of the HBA/HNA copolyester at the two temperatures used for testing and it was found that the only discernable effect was to cause strain hardening to occur at lower strain levels. At the same time the curves were still qualitatively very similar. It therefore appears that some of the differences seen in the elongational viscosity behavior of the isotropic and anisotropic HPC EF melts is due to a difference in state. At the same time the generality of this conclusion to other rodlike polymer systems has yet to be proven.

Finally, the generality of the elongational flow behavior of the TLCPs investigated to other LCP systems is considered. No comparable elongational flow results have been reported for other LCP systems and then no direct comparison to other systems is possible. However, the transient shear flow results presented in section 4.2 provide some insight into this question. The transient shear stress was seen to scale with the imposed shear strain, in agreement with the behavior determined by other investigators for several other LCP systems. Additionally, the elongational viscosity (or equivalently stress) also showed signs of scaling with strain. These results imply that both the transient shear and elongational flow behavior is governed structural changes occurring in the material as a result of flow. LCP systems having similar textures would then be expected to show similar transient flow behavior and it would be expected that the elongational flow behavior determined here is general for all LCP systems. However, the TLCP systems investigated in this study were also shown to contain small amounts of residual crystallinity. Residual crystallinity was shown to have a large effect on the rheological behavior determined for an LCP system (see Chapter 2), being correlated with anomalous types of behavior such as yield stresses, steady and transient nega-

tive values of N1, and deformation history effects. Additionally in the transient elongational flow tests just presented the presence of residual crystallinity was correlated with the tendency for strain hardening at lower strain values. Furthermore, the possibility that strain induced crystallization is responsible for the strain hardening behavior seen in the LCPs studied can not be ruled out. Therefore, at this time no generalization can be made about the transient elongational viscosity behavior determined in the TLCPs investigated.

4.3.3 Implications for Processing

While the behavior determined for the TLCP systems still leaves certain questions unanswered, there are certain implications in the results. First, strain hardening behavior has been associated with flow instabilities in the entry region to dies in flexible-chain polymer systems [105]. At the same time, the strain hardening behavior of the TLCPs investigated was seen to be aggravated by the presence of residual crystallinity. Therefore, the elimination of residual crystallinity in an LCP might help to reduce or eliminate such flow instabilities in the processing of the LCP where they are currently a problem.

Another aspect of the elongational flow behavior determined for the LCPs which has implications for processing is the observation that the elongational viscosity of LCPs is likely to be elongation rate thinning. Such behavior could cause necking and fracture in extrusion processes where some kind of post-extrusion draw is applied to the material. This might preclude the use of some processing methods with some LCPs or require that the properties of the LCP be modified through the use of appropriate thermal and deformation histories.

4.4 Morphology of Drawn LCP Films

The morphologies of drawn films of 60HBA/PET and HBA/HNA were studied at different draw ratios and the results are presented in this section, serving a dual purpose. First, the results serve to demonstrate the level of molecular orientation and elongation of liquid crystal domains which can be obtained in LCPs subjected to elongational flow, providing insight into possible structural changes occurring in the samples elongated in the ER. The second purpose was to correlate the morphology and orientation of the drawn films to their small angle light scattering (SALS) patterns. This was done in order to establish whether the technique of SALS could provide useful information about changes in the macromlecular structure of LCPs brought about by flow and was intended as background work for possible future in-situ studies.

4.4.1 Morphology Results

The molecular orientation and morphology of drawn films of 60HBA/PET and HBA/HNA were studied as described in section 3.4. Studies were made using the methods of WAXS, SEM, optical microscopy, and SALS. Both annealed and drawn films were studied. One film of each material was annealed well above the highest melting transition and quenched to represent the globally unoriented material in the quiescent melt state. The other three samples were drawn films, with three different draw ratios used for each film in order to determine the effect of varying elongational strain.

Wide angle x-ray scattering (WAXS) patterns were taken of the different TLCP films in order to qualitatively determine the level of molecular orientation present. The WAXS patterns of the films are shown in Figures 66 to 68. The WAXS patterns of the annealed and drawn films are shown for the copolyesters in Figures 66 and 67, with the x-ray beam in the direction

perpendicular to the film surface. The patterns for the annealed films are seen to show no overall molecular orientation as indicated by the rings in which the scattered beam intensity shows no dependence on the azimuthal angle. On the other hand the drawn films show a high degree of molecular orientation in the draw direction. Also, while a high degree of molecular orientation is seen in the drawn film for the case of the lower draw ratio, it can be seen that some improvement in orientation is obtained as the draw ratio increases. Since it has shown that shear flow is ineffective in producing a high degree of molecular orientation in LCPs [8], it is likely that the majority of the molecular orientation obtained in the drawn films is the result of elongational deformation.

While it is seen that a high degree of molecular orientation is obtained in the draw direction of the drawn films, it is not apparent from the results above whether the orientation is uniaxial in nature. In order to answer this question WAXS patterns were taken of a HBA/HNA drawn film with the x-ray beam directed in three orthogonal directions: namely, parallel to the draw, width, and thickness directions. The results of these tests are shown in Figure 69. Again, it can be seen that there is a high degree of molecular orientation in the draw direction. Additionally, from the pattern with the x-ray beam directed in the draw direction it can be seen that there is no preferential orientation in the width direction versus the thickness direction. The molecular orientation in the drawn films then appears to be uniaxial in nature.

SEM microscopy was used to study the morphology of supermolecular structures in the drawn copolyester films. Samples of the films were prepared by fracturing in liquid nitrogen and/or microtoming. Representative SEM micrographs of the films are shown in Figures 69 to 71. Also, it should be noted that the films of 60HBA/PET shown in Figure 70were etched in order to remove the isotropic PET rich phase, leaving HBA-rich liquid crystal domains. In the annealed films of both materials it can be seen that the domains are globular in shape with no preferred orientation. On the other hand, the drawn films are seen to have a fibrillar structure in which the liquid crystal domains have been elongated. Furthermore, in the etched 60HBA/PET films it can be seen that the aspect ratio (ratio of length to width) of the liquid crystal domains increases with the degree of post extrusion draw. At the same time all of the

drawn HBA/HNA films are highly fibrillar and no differences in the aspect ratios of the fibers are apparent for the films with different draw ratios.

The drawn copolyester films were also studied using the method of optical microscopy in order to examine the geometry of supermolecular structures present. The films studied were microtomed to a thickness of 5 μm and observed under crossed polarizers at a magnification of 250x. The results are shown in Figures 72 through 74 with the orientation of the polarizers in the vertical and horizontal directions. Also, the size scale is one centimeter in the figures equals 18 μm. For the drawn films of both materials, two separate optical micrographs are shown with the draw direction of the film at 0^0 and -45^0 to the horizontal direction. The annealed films of both materials are seen to display the threaded texture characteristic of nematic LCPs, with no preferred orientation seen for the liquid crystal domains. On the other hand, the optical textures of the drawn films are seen to depend very highly on the direction of the film with respect to the crossed polarizers. In the 45^0 orientation, the films are very highly birefringent, indicating a high degree of molecular orientation (known to be in the draw direction from WAXS). Also, the colored streaks seen in the films correspond to fibers, as can be seen when the optical micrographs are compared to the corresponding SEM micrographs. In contrast, the optical micrographs of the samples oriented at 0^0 to the crossed polarizers show textures somewhat similar to those seen in the unoriented materials only now there are some indications of elongation of the domains in the draw direction. Also, the degree of elongation of the domains increases somewhat with the draw ratio. It is noteworthy that the domains observed here are smaller than the macrofibrils and appear to exist within the fibers. Finally, in the highest draw ratio 60HBA/PET film some small bands are seen oriented perpendicular to the draw direction. Similar bands have been observed in highly drawn LCP fibers [134] and have been reported to be due to crystallite layers.

Small-angle light scattering (SALS) patterns were taken of the drawn copolyester films in order to determine whether the technique of SALS could provide information about changes in the geometry of supermolecular structures resulting from flow. The films used in the SALS studies were the same ones as were used for optical microscopy. Only SALS Hv patterns were

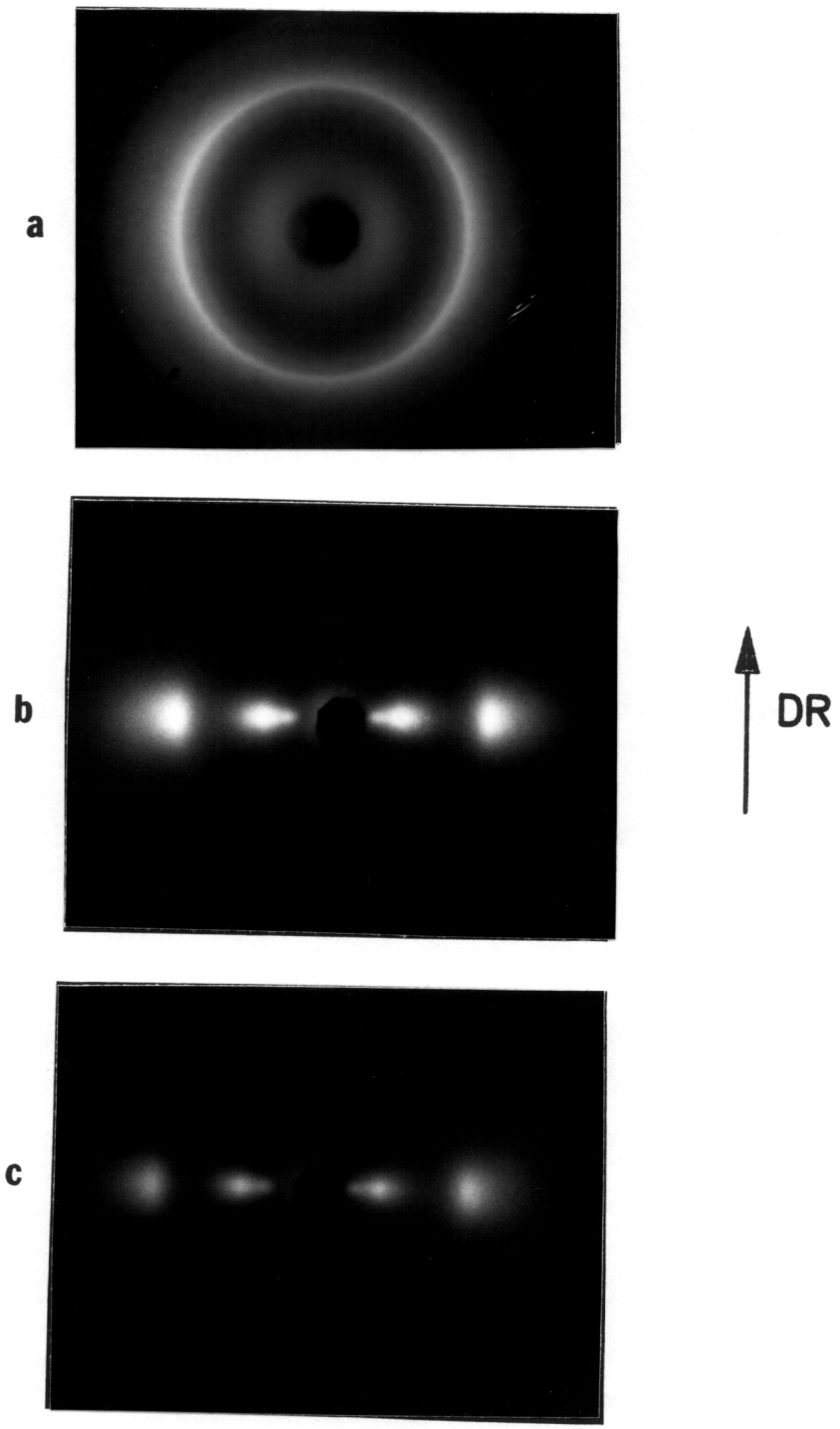

Figure 67. WAXS patterns of 60HBA/PET films (a) annealed, (b) DR=8.6, and (c) DR=21. Draw direction is vertical.

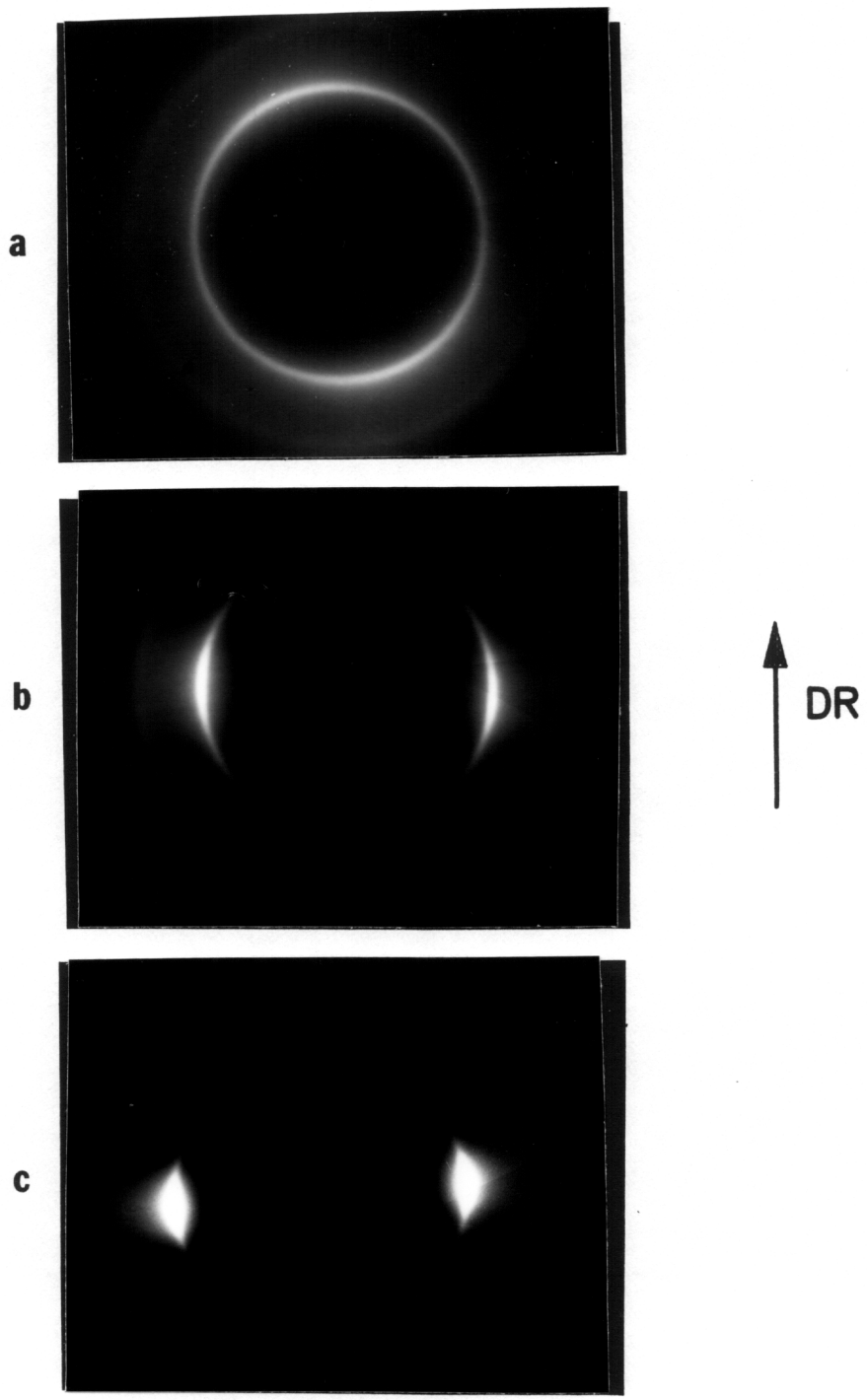

Figure 68. WAXS patterns of HBA/HNA films (a) annealed, (b) DR = 5.3, and (c) DR = 19. Draw direction is vertical.

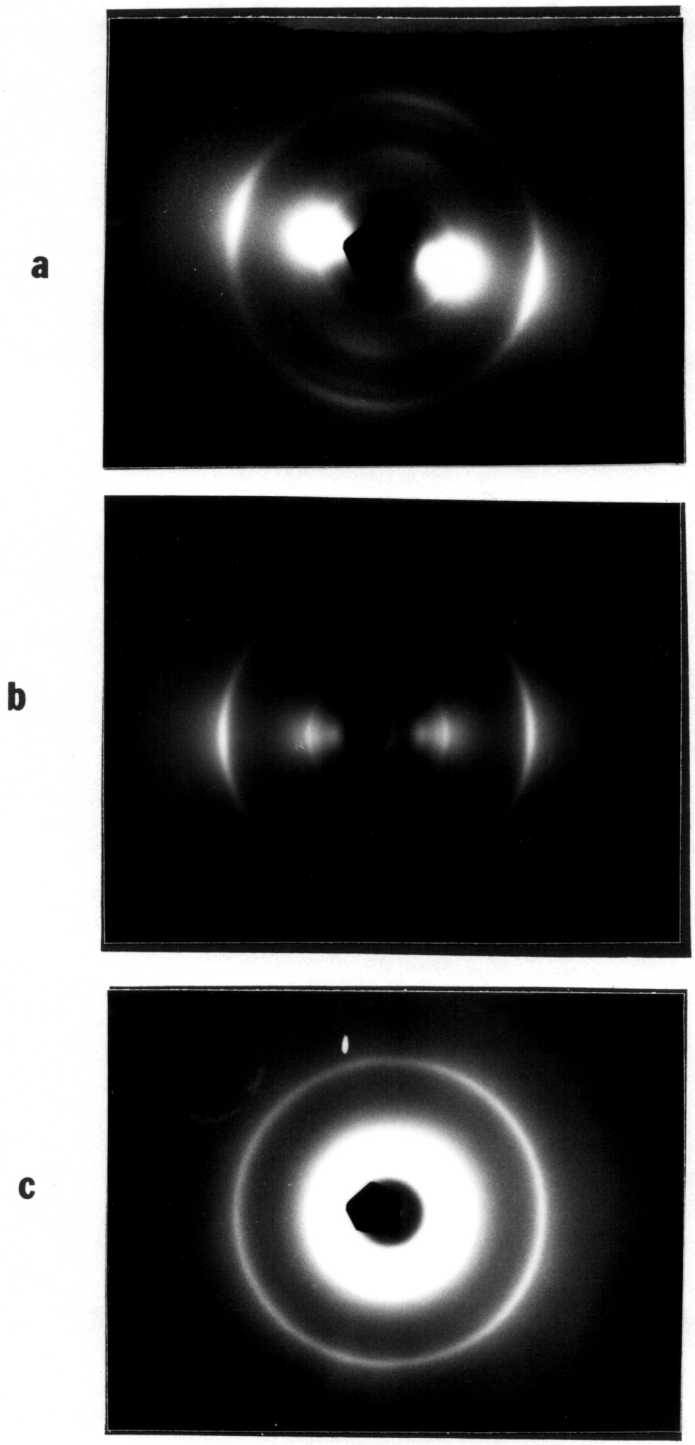

Figure 69. WAXS patterns of HBA/HNA film with DR=5.3. X-ray beam is oriented parallel to the: (a) thickness direction, (b) width direction, and (c) draw directions. Draw direction is vertical for (a) and (b).

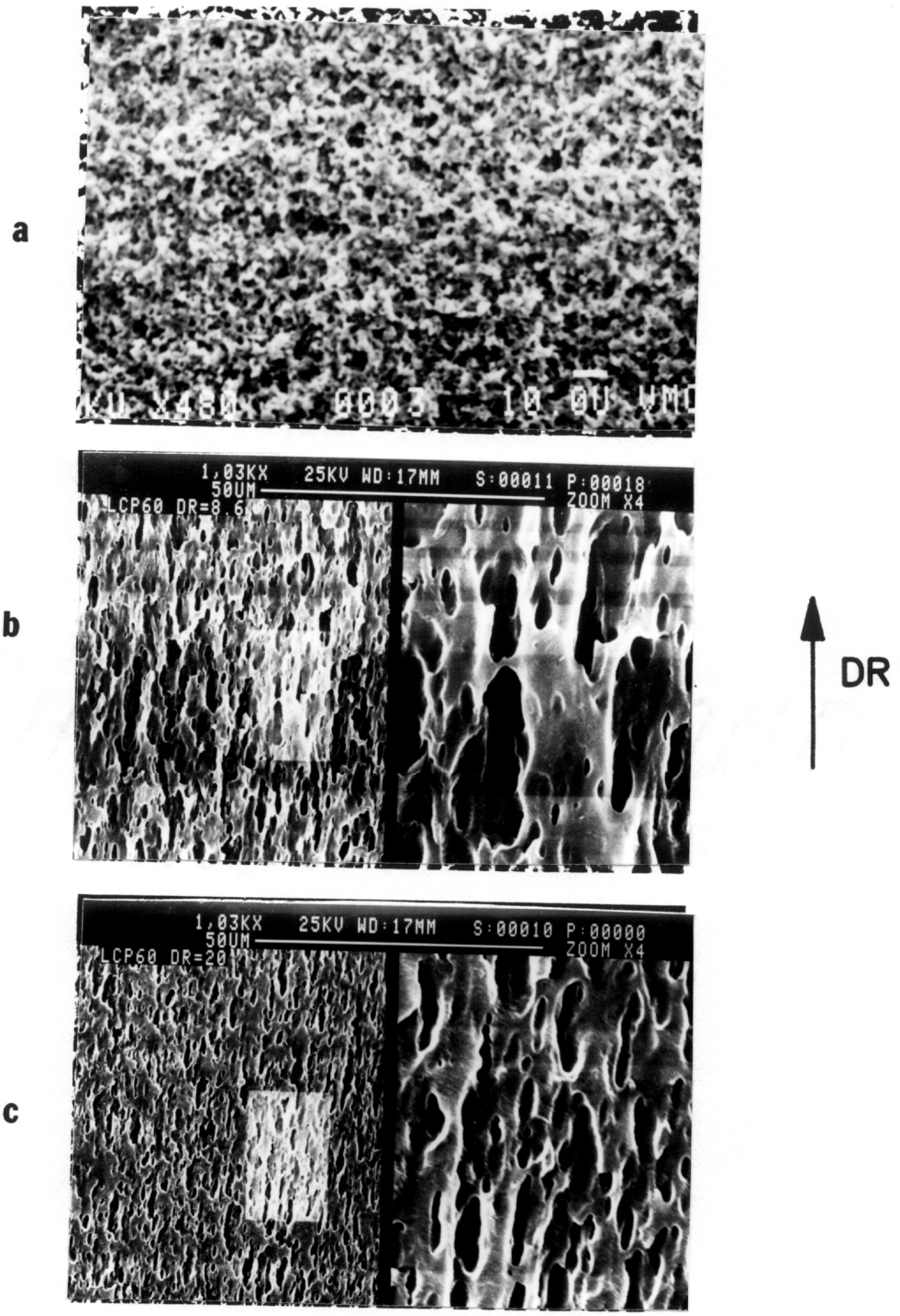

Figure 70. SEM micrographs of 60HBA/PET films etched to remove the isotropic phase and oriented with the draw direction vertical: (a) annealed, (b) DR=8.6, and (c) DR=21 Films were etched to remove the isotropic phase.

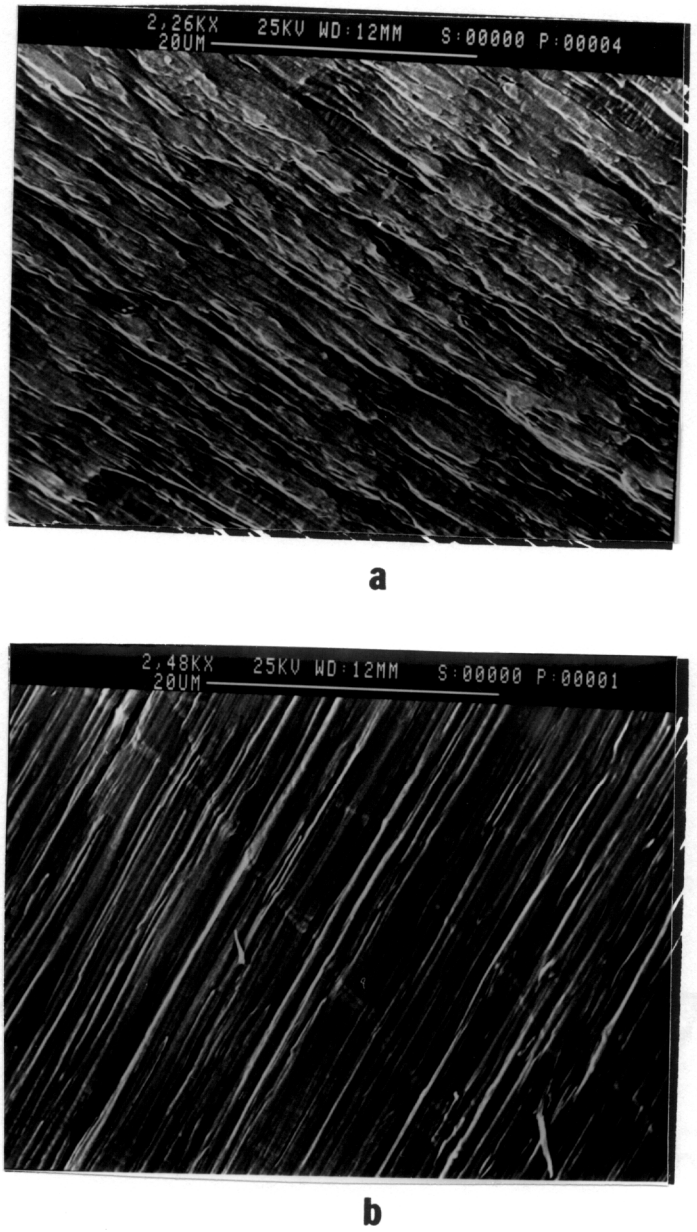

Figure 71. SEM micrographs of microtomed 60HBA/PET films with the draw direction along the fiber directions: (a) DR = 8.6 and (b) DR = 21.

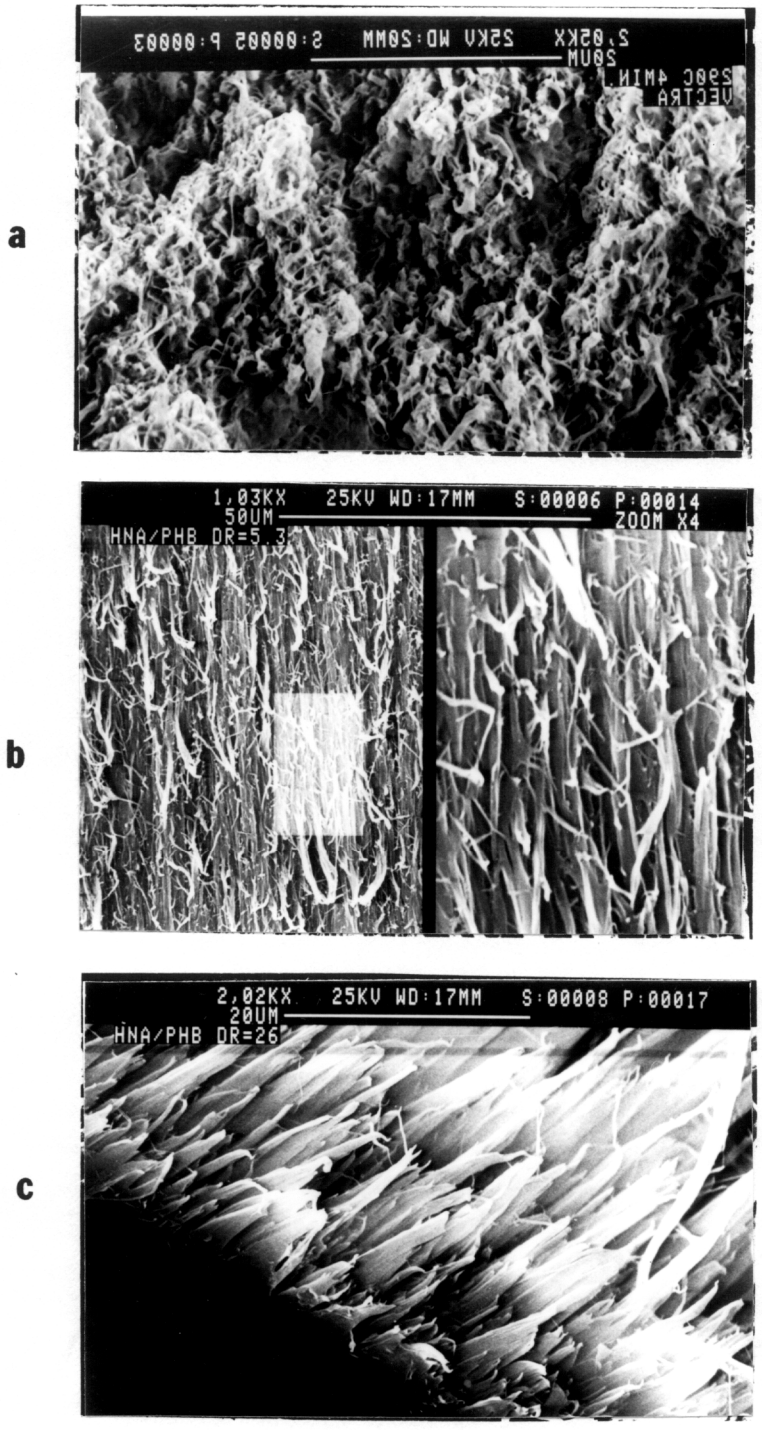

Figure 72. SEM micrographs of fractured HBA/HNA films with the draw direction along the fiber direction: (a) annealed, (b) DR = 5.3, and (c) DR = 26.

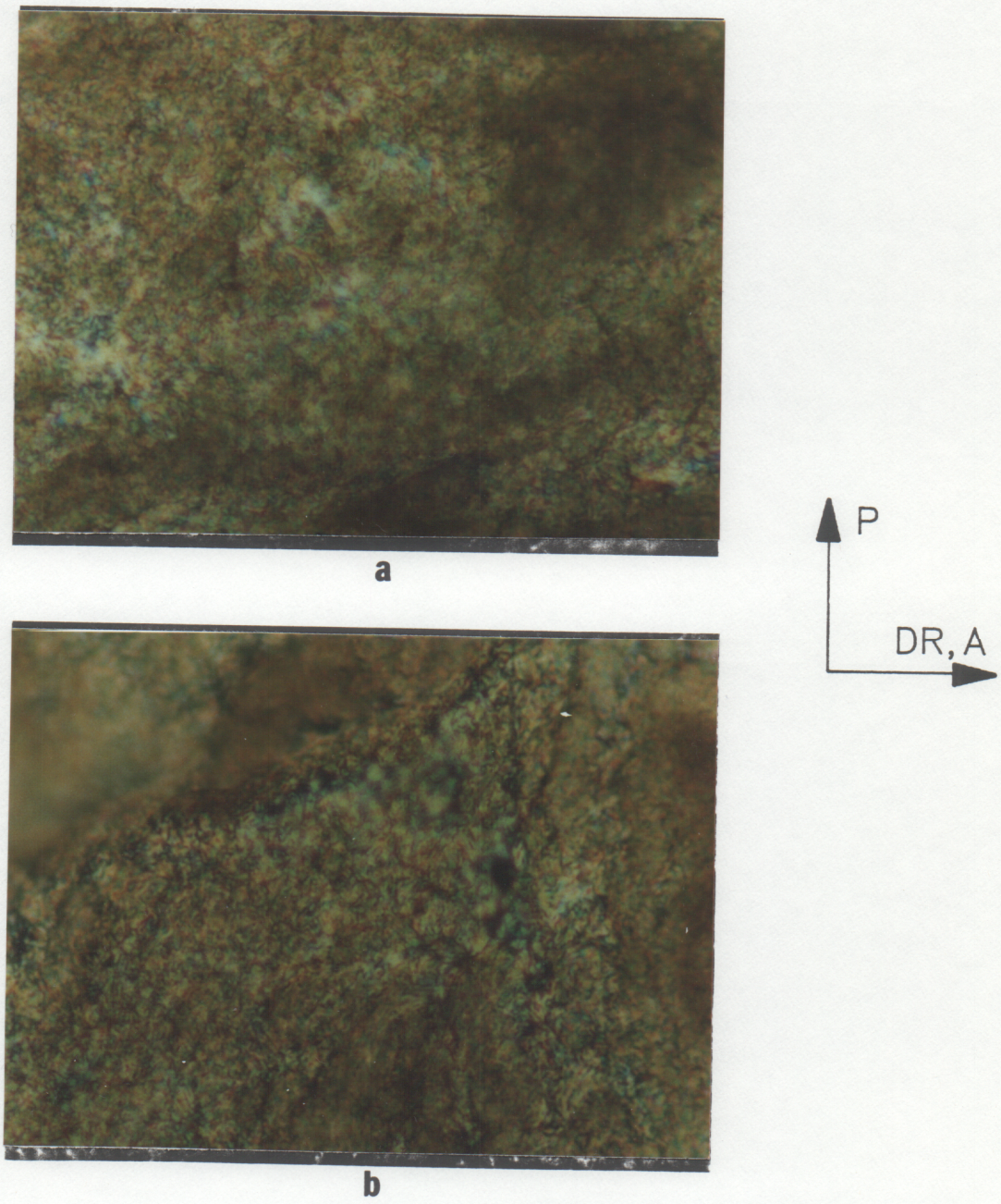

Figure 73. Optical micrographs of annealed films of a) 60HBA/PET and b) HBA/HNA. Crossed polarizers vertical and horizontal.

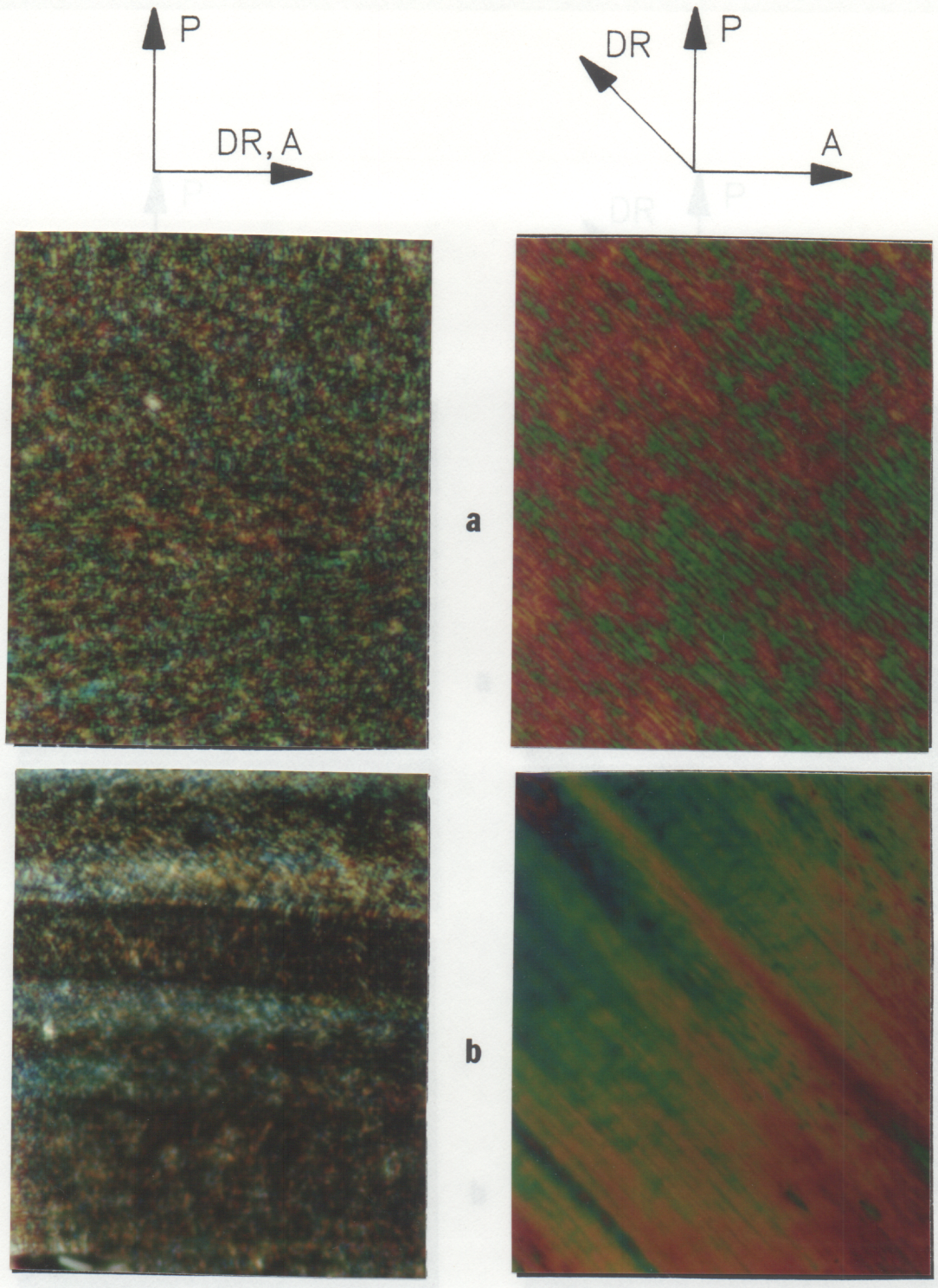

Figure 74. Optical micrographs of drawn 60HBA/PET films with polarizers oriented vertically and horizontally: (a) DR = 8.6, and (b) DR = 21. Draw direction at 0° (left) and -45° (right). Size scale 1 cm = 18 μm.

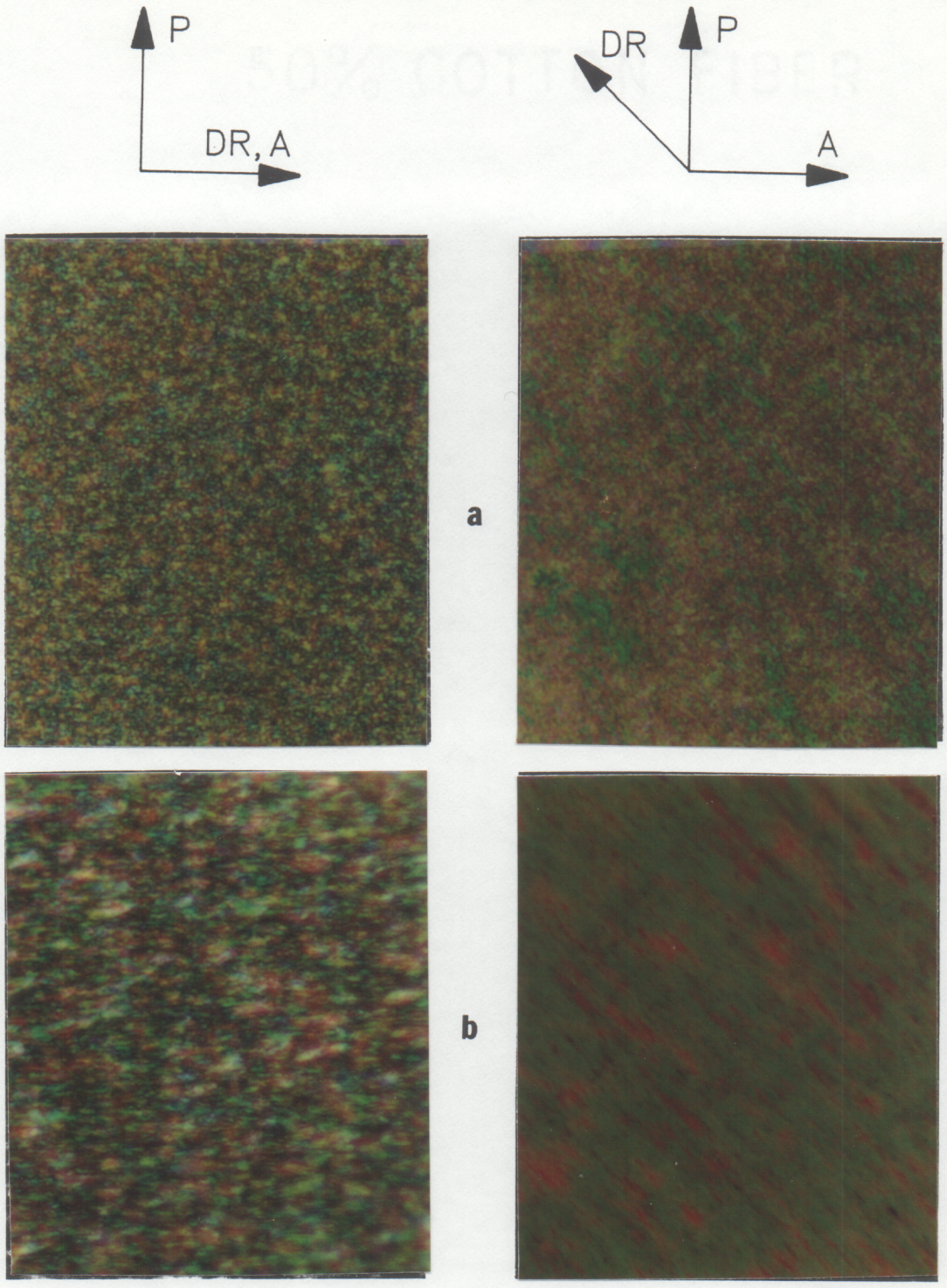

Figure 75. Optical micrographs of drawn HBA/HNA films with polarizers oriented vertically and horizontally.: (a) DR = 5.3 and (b) DR = 19. Draw direction at 0° (left) and -45° (right). Size scale 1 cm = 18 μm.

taken since isotropic scattering from density flucuations in both the LCP and immersion oil could obscure the Vv mode patterns. The resulting Hv patterns shown in Figures 75 and 76, with the patterns oriented so that the draw direction of the film is at -45° with respect to the horizontal direction. The patterns for the annealed LCP film are similar and show no azimuthal angle dependence of the scattered intensity. Also, the intensity decreases steadily with the Bragg angle 2θ. Such patterns can be simply interpreted based on statistical considerations and indicate structures with no net orientation in the plane of the film. Additionally, since no maxima are seen with respect to the 2θ direction the patterns indicate that there is no regular correlation distance in the domain geometries. This is consistent with a Schlieren texture. In contrast, the SALS patterns obtained for the drawn films are elongated with the long axis perpendicular to the draw direction. Since the angle of scattering is inversely related to the size of the scattering element, this indicates that the drawn films have elongated supermolecular structures with the long axis parallel to the draw direction. At the same time a lack of maxima in the 2θ direction indicates that there is a distribution of sizes. Finally, in the SALS pattern for the highest draw ratio 60HBA/PET film a maximum is seen with respect to the θ direction, with an elongated shape parallel to the center band. This would indicate that there is a regular correlation distance in the film in the draw direction, calculated to be 15 μm using Braggs law and the first order maximum. This could indicate that the domain lengths are very regular, but is more likely an artifact due to sample preparation by microtoming. Although regular bands were seen in the same sample by optical microscopy, the size of those bands was about 2 μm.

4.4.2 Discussion

The first objective of this study was to establish the degree of molecular orientation and elongation of liquid crystal domains occurring in the TLCPs as a result of elongational flow. While the results presented in this section are qualitative, it was shown that both a very high

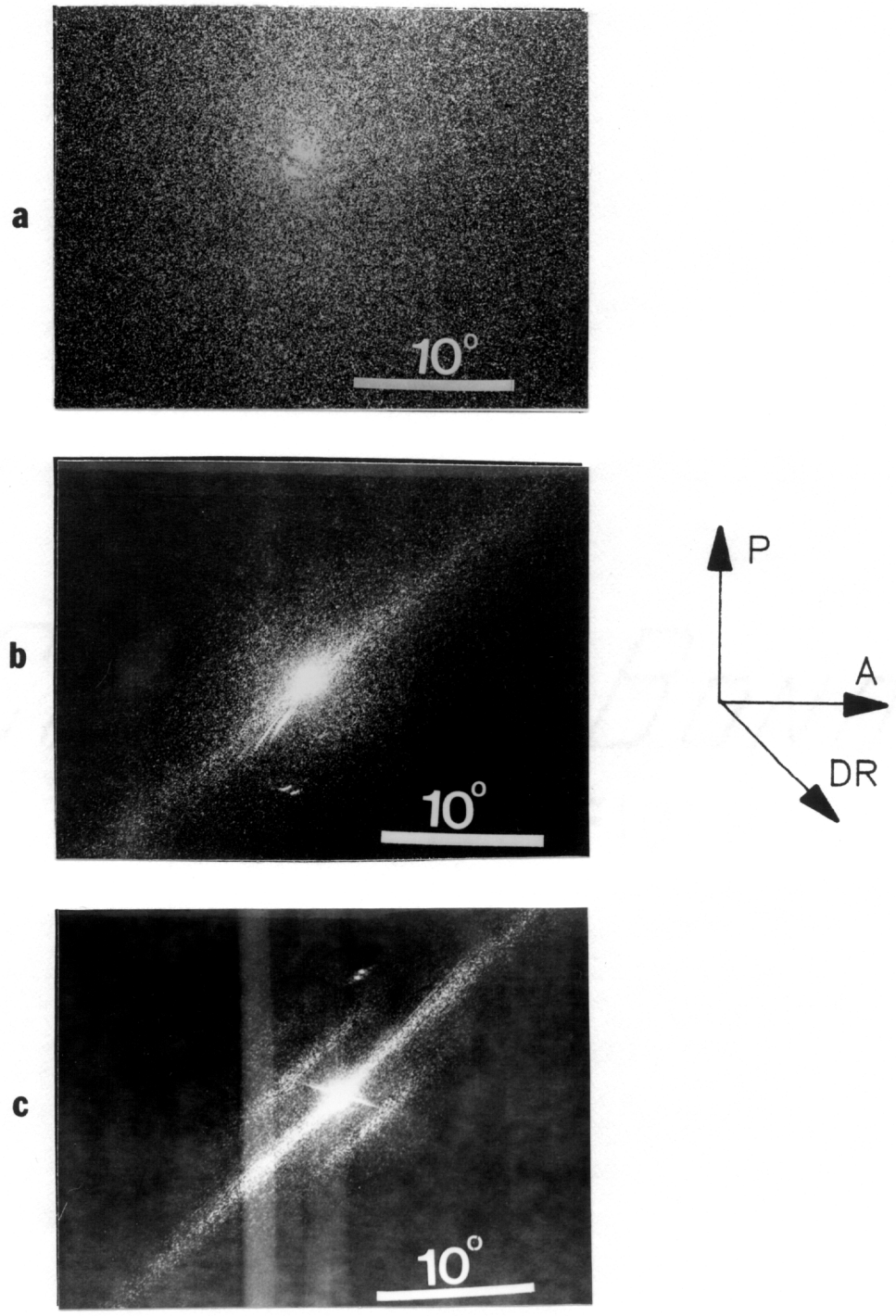

Figure 76. SALS Hv patterns of 60HBA/PET films a) annealed, b) DR=8.6, and c) DR=21. Draw direction at -45° to the horizontal dir.

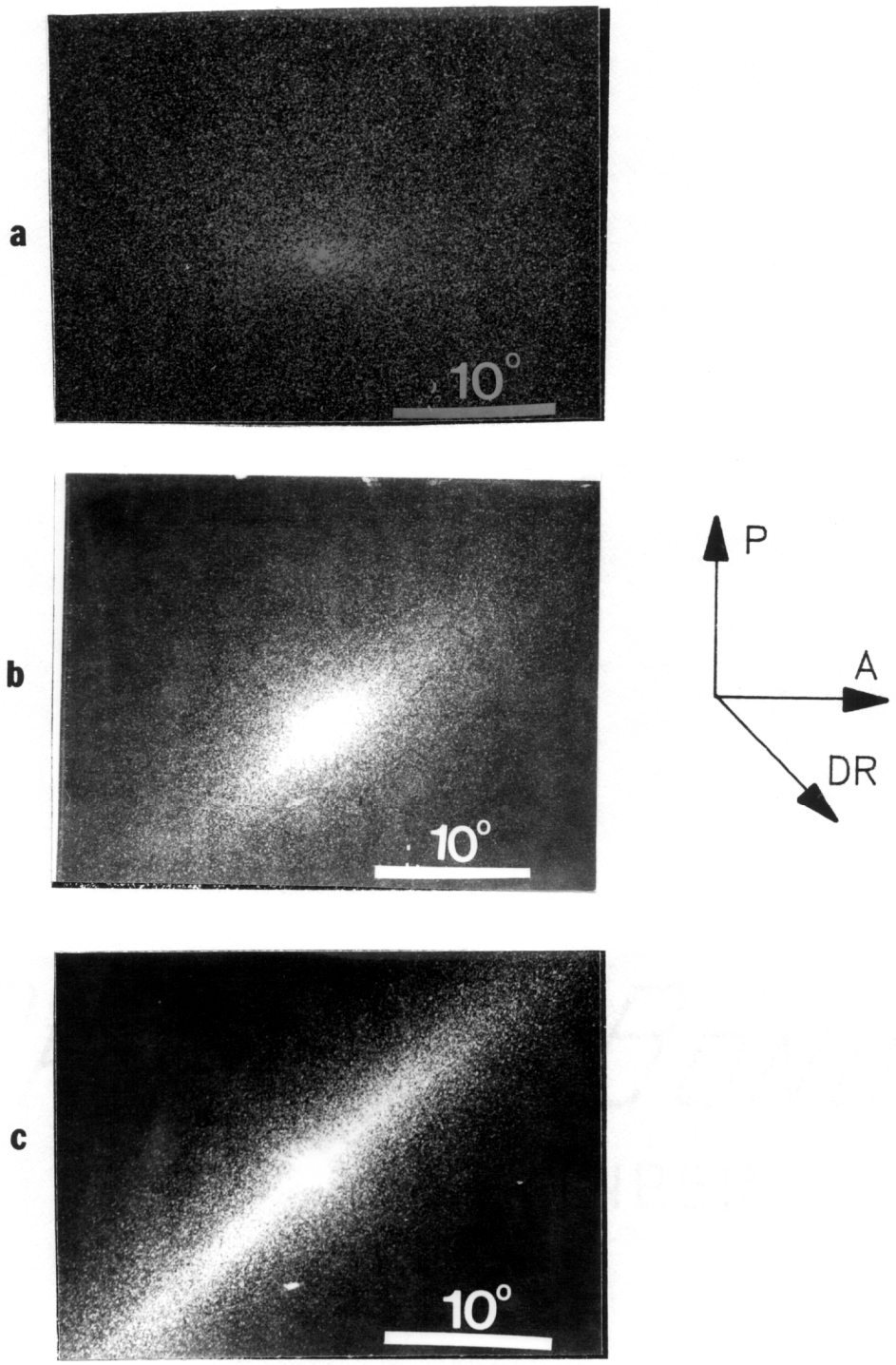

Figure 77. SALS Hv patterns of HBA/HNA films a) annealed, b) DR=5.3, and c) DR=19. Draw direction at -45° to the horizontal dir.

degree of molecular orientation and a morphology with elongated domains or fibers are obtained in the material subjected to extensional flow. Additionally, the degree of orientation and elongation of domains increases with increasing elongational deformation.

These results are important because they provide some insight into the structural changes with might be occurring in the samples tested in the ER. During such transient testing, it is possible that the structure of the material evolves from the globally unoriented texture seen in the quiescent melt to that seen in the drawn films. It should be noted that a highly oriented structure was seen in the drawn films for draw ratios as low as 5.3, corresponding to a Hencky strain of 1.6. At the same time, Hencky strains as high as 2 were obtained in the samples tested in the ER prior to fracture. Furthermore, such an oriented structure might be lower in viscosity than the unoriented equilibrium texture and thus contribute to necking and sample failure. However, it is unclear at this time whether such structural changes are occurring in the isothermally elongated materials because of possible relaxation processes. In any case, it appears that both changes in molecular orientation and in domain geometry are part of the structural changes occurring in LCPs during transient flow and likely influencing the transient elongational flow behavior of the materials.

The second objective of the morphological studies on the drawn film was to evaluate the technique of SALS for obtaining information about changes in the geometry of supermolecular structures in the LCPs occurring during flow. A comparison of the SALS results with those obtained by SEM and optical microscopy show good qualitative agreement between the different techniques. For example, both techniques show the elongated structures in drawn films, with the aspect ratio of the structures increasing with increasing draw ratio. While the results obtained for the films were qualitative and no determination was made of the ability of SALS to determine the absolute size of the structures, Effler [132] has shown that SALS could be used to determine the size of 60HBA/PET domains when interpreted using a statistical model. Therefore, it seems that the technique of SALS is useful in providing information about changes in the geometry of supermolecular structures in LCPs on a qualitative level and possibly on a quantitative level.

5.0 Evaluation of Doi Theory

In this chapter the Doi theory, in both original and modified forms, is evaluated for its ability to predict and model the experimental flow behavior of the TLCP materials investigated. By "predict," it is meant that the adjustable paramters in the Doi theory were calculated from molecular characteristics through the relations given by Doi and Edwards [182]. By "model," it is meant that the adjustable parameters were fit to experimental shear viscosity data. The chapter is divided into two sections. In the first section the numerical solutions obtained for equations 3.5.1 to 3.5.7 are presented and compared to the experimental behavior determined for HPC EF and HBA/HNA. It is there established whether the elongational flow behavior of the TLCPs can be predicted from parameters determined solely from shear flow data. In the second section, the Doi theory is examined and the question of whether the Doi theory describes the physical state of the material is discussed. An argument is made to justify the use of the rod-solvent interaction term in the stress equation (3.5.1). Also, the proposed multidomain average is examined and discussed in relation to other very recent work in the which the flow behavior of individual domains is modelled by the Leslie-Ericksen theory.

5.1 Doi Theory Results

Results for the Doi theory are presented in this section for both the shear and elongational flow behavior of isotropic and anisotropic systems of rodlike molecules. The results were obtained by numerical solution of equations 3.5.1 through 3.5.7 as described in Chapter 3 and Appendix C. First, the results for isotropic systems are evaluated using the experimental shear and elongational flow results for the isotropic HPC EF melt (at 210 ^{0}C). Next, the results for the anisotropic systems are evaluated using the experimental shear and elongational flow behavioro the experimental results for the anisotropic HPC EF melt (at 190 ^{0}C) and the HBA/HNA melt at 320 ^{0}C. Because of the large amount of results obtained and the similarity in results between those for anistropic HPC EF and HBA/HNA, only transient results for anisotropic HPC EF are shown for the evaluation of anisotropic systems.

5.1.1 Results for an Isotropic System

In Chapter 2 the derivation of the Doi theory was briefly recanted with the basis for the theory coming from the molecular dynamics of rod-like molecules in dilute solution. As the concentration regime of the systems increased, the number of approximations in the theory also increased. The predictions of the theory would then be expected to decrease in accuracy as the concentration regime of the systems increased. The Doi theory is therefore evaluated here first for a system which is isotropic at equilibrium. The experimental behavior of the isotropic HPC EF melt (210 ^{0}C) is used for this purpose.

The first objective in evaluation of the Doi theory was to establish whether the behavior of LCPs could be predicted when the parameters were determined only from molecular characteristics. The parameters U, &Dr, ckT, and A were determined in this way as described in Appendix C, with the resulting parameter values given in in Table 9. However, the value of

31.1 for U is outside the range of permissible values ($0 \leq U \leq 8/3$) for an isotropic system according to the Doi theory and no calculations using that value were made. Alternatively, values of U of 0, 2, and 2.5 were chosen to represent the range of realistic values and the remaining parameters were not changed. The results are then shown in Figures 78 to 81. In Figure 78 the predictions for the steady state shear viscosity are shown, and while it can be seen that the numerical results are close to experimental values, this is mainly due to the use of the zero shear rate viscosity for determining D_r. Also, it can be seen that the shear rate thinning behavior is not well predicted. The predictions for the steady first normal stress differences are shown in Figure 79 on page 214, where it can be seen that there is no agreement between the predictions and the experimental values of N1. The predicted shear stress and elongational viscosity growth are shown in Figures 80 and 81, respectively. It can be seen that the predicted response time is much too short. Though not shown, the curves for other values of U yield similar results. Therefore, the Doi theory cannot predict the experimental behavior of the isotropic HPC EF melt using parameters determined solely from molecular characteristics.

The second objective of the numerical work was to determine whether the Doi theory, in its original or modified form, could model the experimental shear and elongational flow behavior of LCPs. In this case the parameters U, D_r, ckT, and A are considered to be experimentally adjustable and fit to experimental steady shear viscosity data as described in Appendix C. First, a value of U was chosen and the other parameters were then determined. Again, values of U of 0, 2, and 2.5 were used to represent a wide range of molecular interaction and the resulting sets of parameters are given in Table 9. The steady and transient shear flow and transient elongational flow behavior calculated for some of these parameter sets is shown in Figures 81 through 84. It was found that the Doi theory could fit the steady shear viscosity behavior of the isotropic HPC EF melt in a semi-quantitative manner when rod-solvent interactions were retained as shown in Figure 82. At the same time, the combinations of the parameters (U,D_r,ckT) gave nearly identical predictions for the steady shear viscosity. The predictions for the steady state first normal stress difference are shown in Fig-

ure 83 for several combinations of (U,D_r,ckT). It can be seen that the solutions for the different parameter sets are nearly identical at low rates, but deviate somewhat at high rates with the plateau value of N1 depending on U. More importantly, the agreement between experiment and theory is remarkable considering that values of N1 were not used to fit the parameters.

The predictions of the Doi theory for transient shear stress and elongational viscosity growth for the isotropic HPC EF melt were determined next. Calculations were made using the parameters fit to the steady shear viscosity data (shown in Table 9) and the initial condition of random molecular orientation ($S_{\alpha\beta}(t=0)=0$ for all $\alpha\beta$). Representative results of these calculations are shown in Figures 83 through 86 for the sets of parameters characterized by $U=2$ and $U=2.5$. For the case of shear stress growth and the curves for $U=2$, which are shown in Figure 84, it can be seen that there is good qualitative agreement between theory and experiment. Similar behavior is obtained for values of U lower than 2. On the other hand, as U approaches 8/3 certain qualitative changes are seen in the predicted curves (see Figure 85 for $U=2.5$) and this appears to be due to a flow induced Transition from the isotropic to the liquid crystal state as evidenced by a dramatic increase in the order parameter S. The predictions for the elongational viscosity growth are shown in Figures 85 and 86 for the same two sets of parameters. The predictions for $U=2$ are shown in Figure 86, where is is seen that there is qualitative agreement at low strain values and at the lowest rate. However, the Doi theory does not predict strain hardening behavior. Also, it is seen in Figure 87 that changes occur in the shapes of the predicted curves as U approaches 8/3. In this case a steady state value of S of 0.64 was predicted, which indicates an isotropic to liquid crystal phase transition has occurred. One other feature of the transient elongational flow predictions worth noting is that the Doi theory predicts rate thinning behavior for the isotropic system. This contrasts with the relatively constant value of $\bar{\eta}_e^+(t, \dot{\varepsilon})$ at the plateau seen in the experimental curves.

Before closing the section some comments should be made about the effect of the rod-solvent contribution to the stress tensor. The agreement between experiment and theory was shown to extend to much higher rates (see Figure 82) when the rod-solvent term in retained in the stress tensor. Without the term, the predicted shear stress reaches a maximum as a

function of rate and a power law slope of $\leq$ -1 is predicted for the shear viscosity versus rate curve. Retention of the term can prevent saturation of the shear stress and results in a power law slope of -1/3 for the η versus $\dot{\gamma}$ curve, which is more realistic and fits the fits the dynamic viscosity versus frequency curve very well. While the dynamic viscosity and steady shear viscosity curves would not be expected to equal each other at high rates [72,105], this is nonetheless very encouraging. The addition of the rod-solvent interaction term also can be seen to prevent saturation in the values of N1, as shown in shown in curve 5 of Figure 83. However, no N1 data are available for the isotropic HPC EF melt with which to compare this. Finally, while nothing was shown here on the effect of the rod-solvent friction term on the transient flow response, it can be seen from the steady state results that the contribution from the term at the rates used for transient flow is almost negligible. Also, calculations were made to confirm this and it was found that there is no qualitative difference in the transient response when the rod-solvent term is retained.

5.1.2 Predictions for Anisotropic Systems

Results of the Doi theory were obtained for the case of anisotropic systems next. Experimental shear and elongational flow results for both an anisotropic HPC EF melt and a HBA/HNA melt were then compared to these results. Again, calculations were first made using parameters determined from molecular characteristics and evaluated using the steady shear flow behavior. Next, calculations were made with parameters obtained by choosing U and experimentally fitting the other parameters (D_r, ckT, and A) to the steady shear viscosity data. Additionally, the effect of varying the initial values of the components of the order parameter tensor was investigated for transient flow tests as described in Chapter 3. Finally, the use of a Voigt average [209] for the components of the stress tensor was investigated for the simulation of a multidomain system at the start of transient flows.

Table 9. Theoretically and Experimentally Determined Doi Theory Parameters

Material	Method of Determination†	U	D_r [s^{-1}]	ckT [Pa]	A
Isotropic HPC EF	T	31.1	12.2	132100	4.33E-4
	E	0	0.072	1015	~2
	E	2	0.022	3090	~2
	E	2.5	0.53	7330	~2
Anisotropic HPC EF	T	31.4	12.2	128000	4.41E-4
	E	3	0.0236	5770	~0.06
	E	4	0.00636	6030	~0.06
	E	6	0.00124	6860	~0.06
	E	10	0.000182	8490	~0.06
HBA/HNA (320°C)	T	161	1.94E-8	418000	2.31E-6
	E	4	0.069	1580	~0.01
	E	6	0.00136	1800	~0.01
	E	10	2.0E-4	2220	~0.01
	E	25	7.4E-6	3420	~0.01

†T = theoretical determination and E = experimental fit.

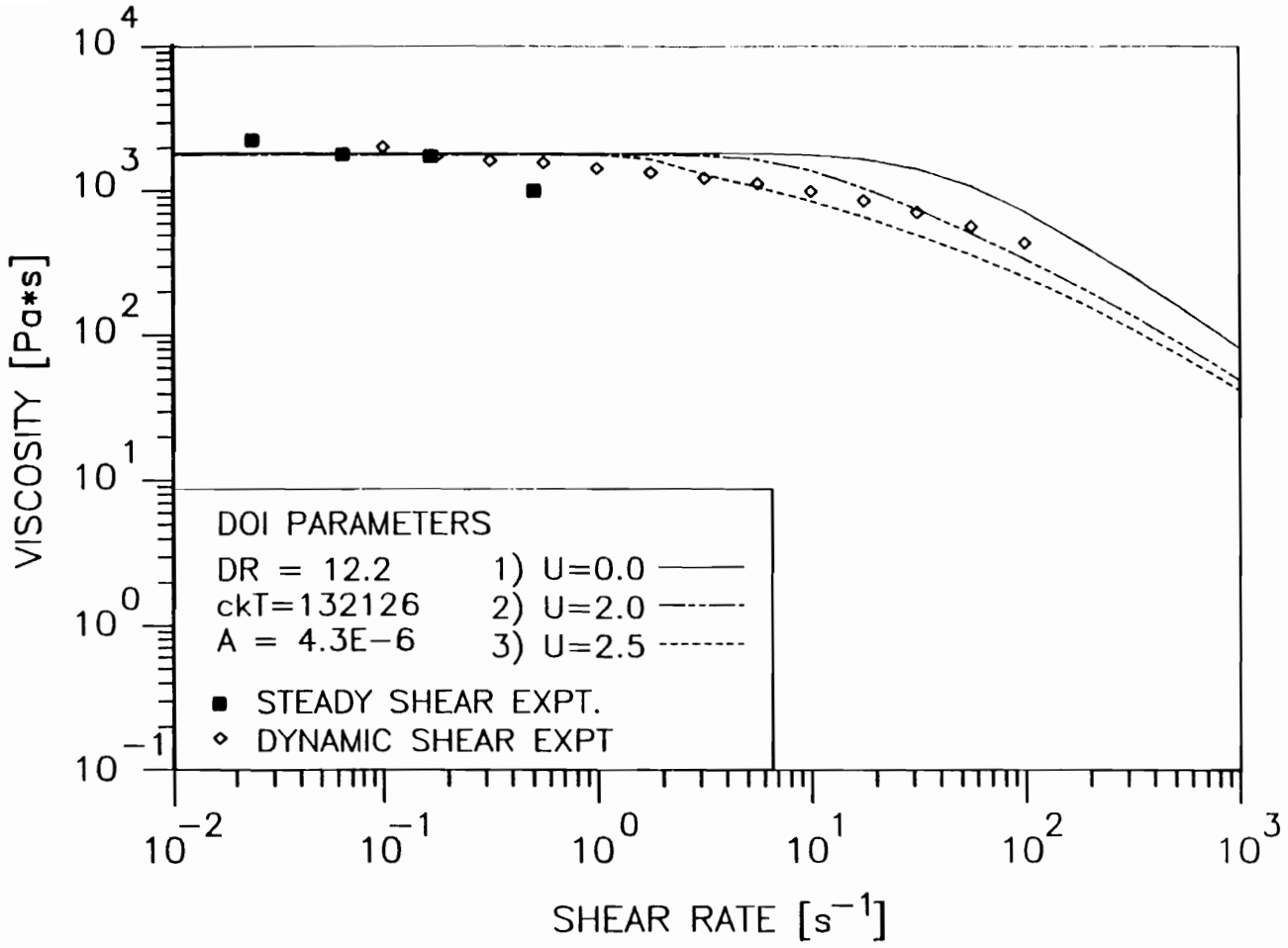

Figure 78. Doi theory predictions of the steady shear viscosity of an isotropic HPC EF melt: $D_r = 12.2$, ckT = 132100, A = 4.33E-4, and U = 0, 2, and 2.5. Theory given by lines and experimental data by symbols.

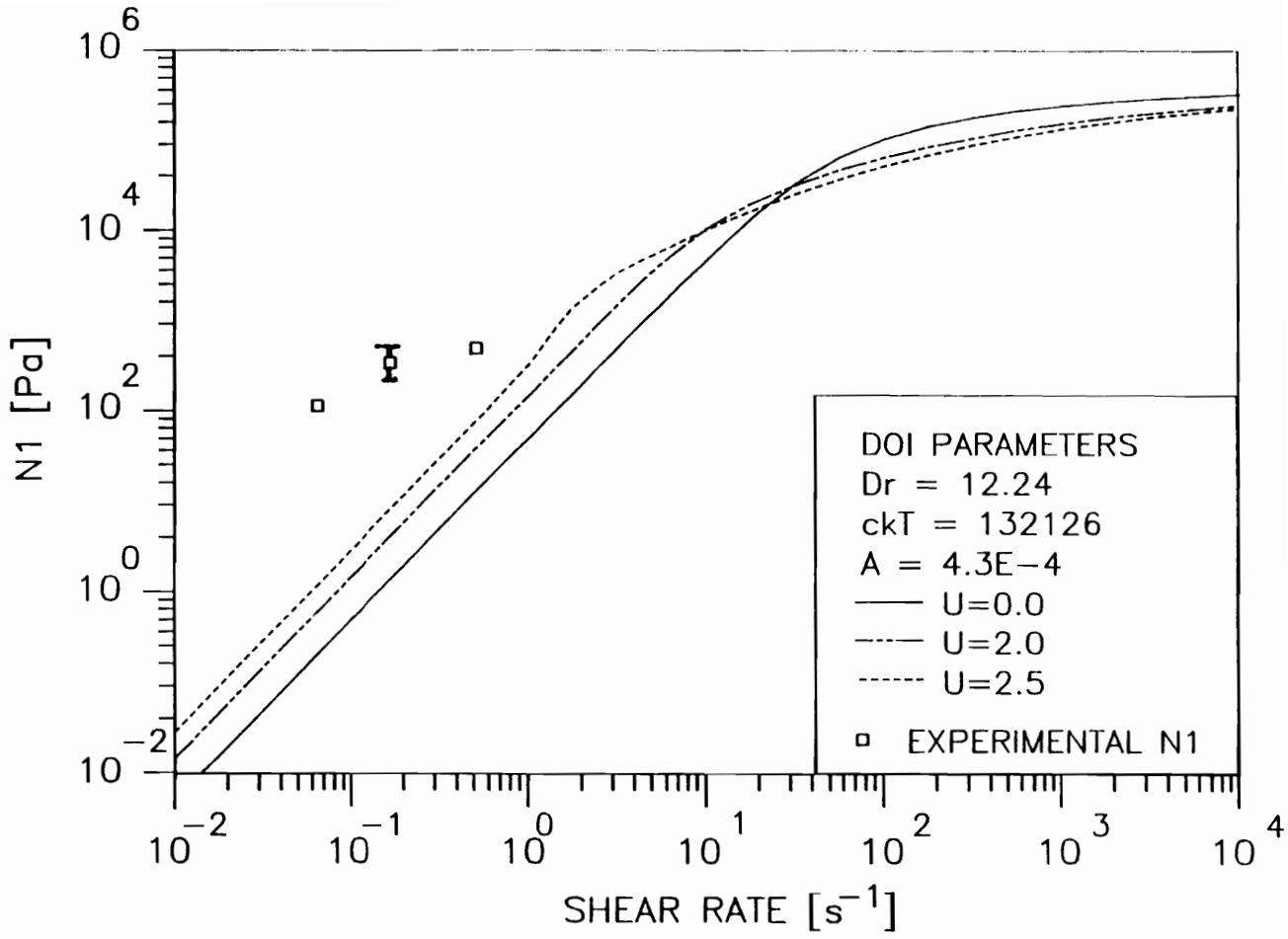

Figure 79. **Predictions of the Doi theory for the steady state first normal stress difference in an isotropic HPC EF melt: D_r=12.2, ckT=132100, A=4.33E-4, and U=0, 2, and 2.5. Theory given by lines and experimental data by symbols.**

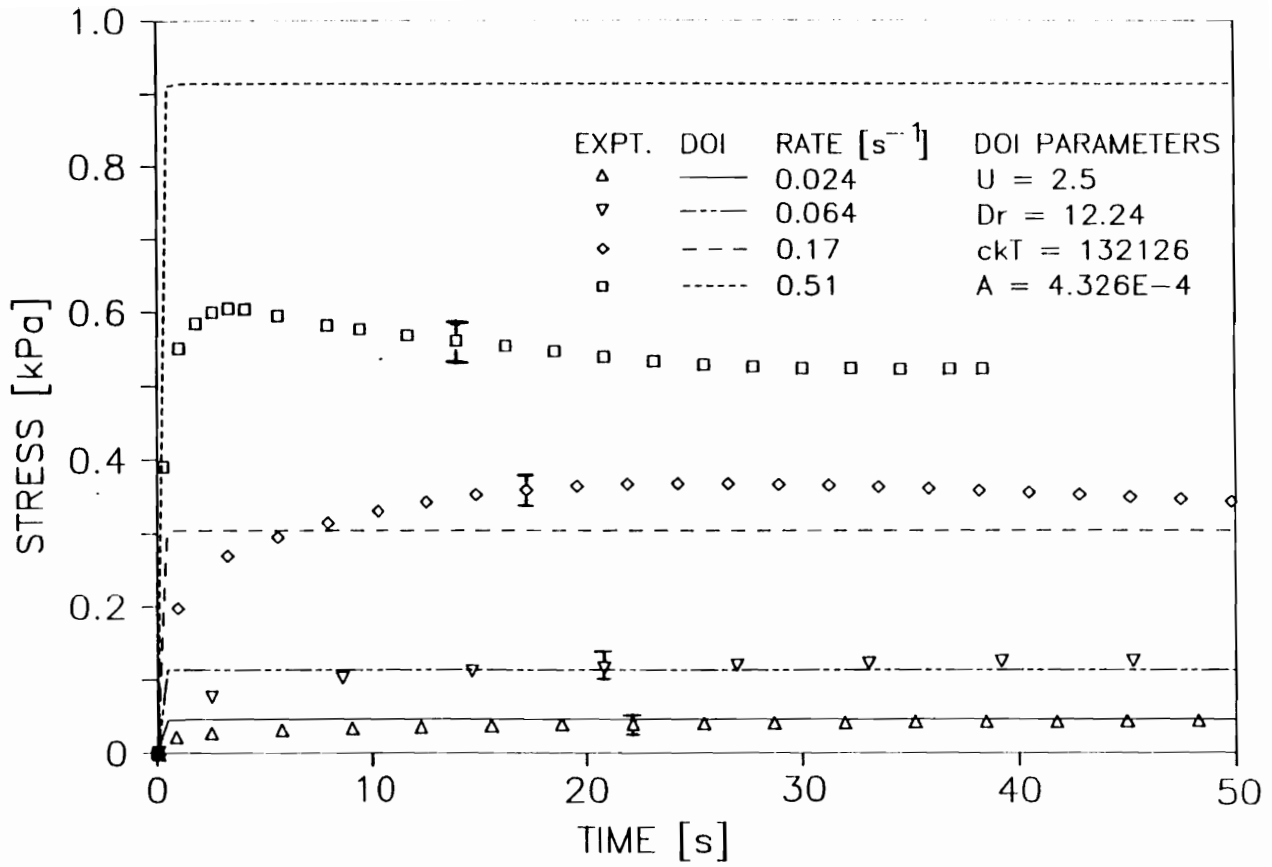

Figure 80. **Predictions of the Doi theory for transient shear stress growth of an isotropic HPC EF melt: U=2.5, D_r=12.2, ckT=1.32E5, A=4.3E-4.Theory given by lines and experimental data by symbols.**

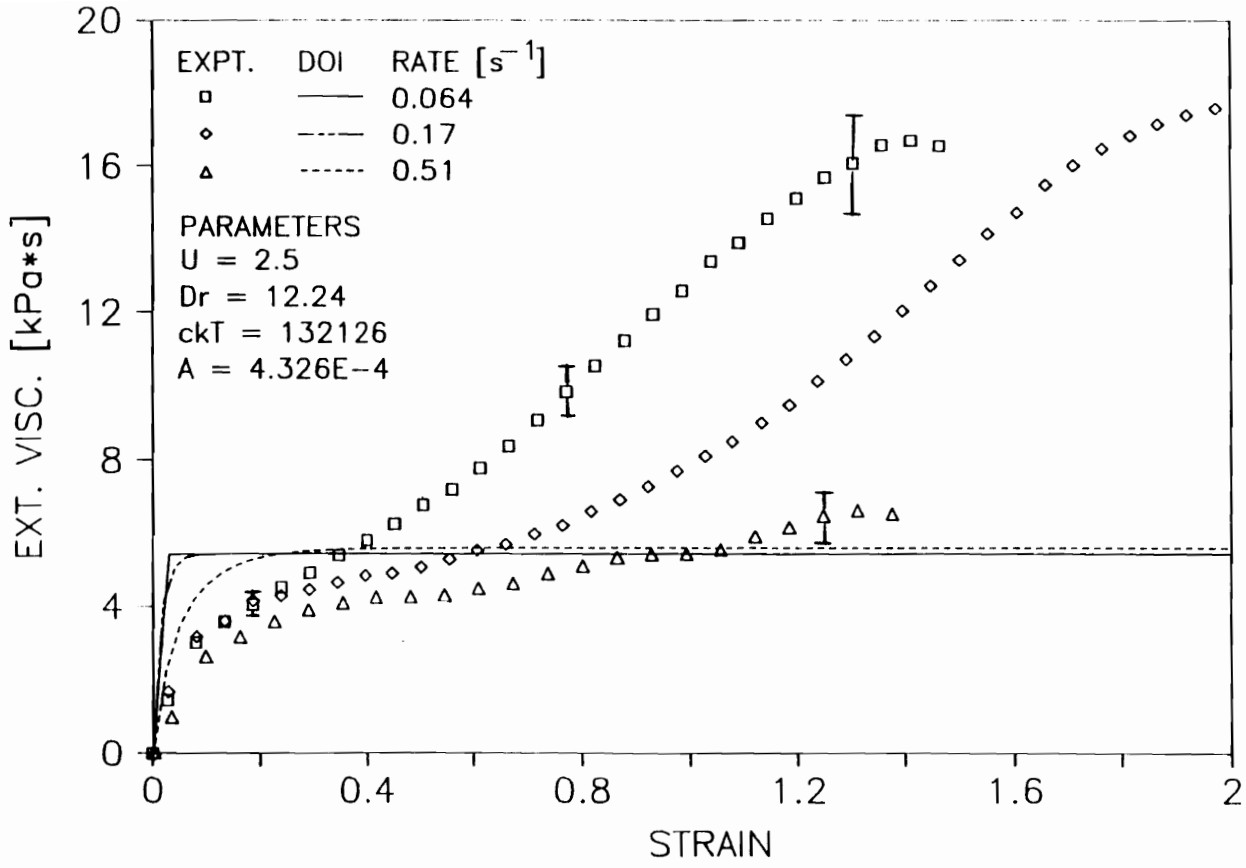

Figure 81. Predictions of the Doi theory for transient elongational viscosity growth of an isotropic HPC EF melt: U=2.5, D_r=12.2, ckT=1.32E5, A=4.3E-4. Theory given by lines and experimental data by symbols.

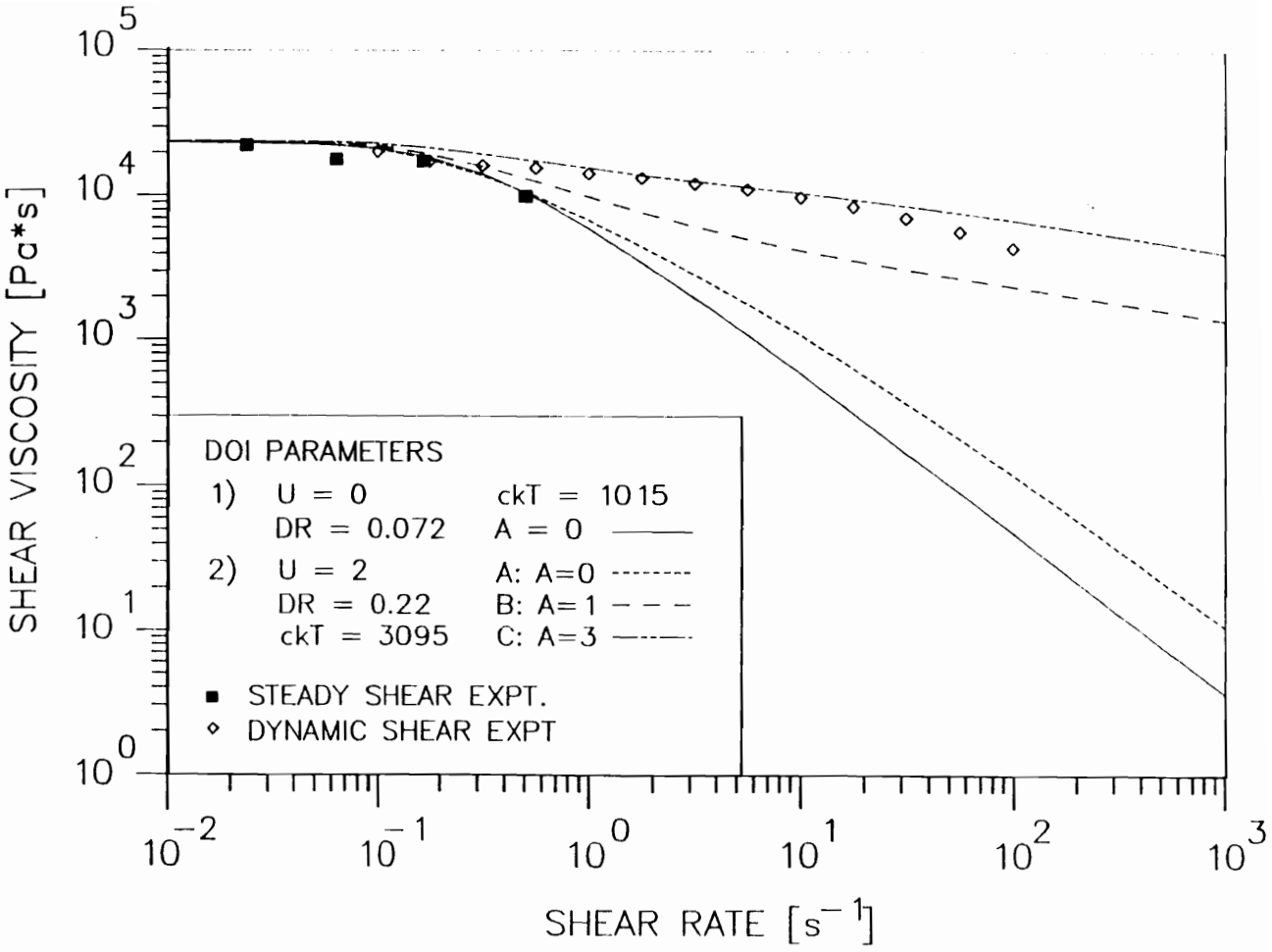

Figure 82. Prediction of the Doi theory for steady shear viscosity of an isotropic HPC EF melt: Parameters fit to steady shear viscosity and given in figure. Theory given by lines and experimental data by symbols.

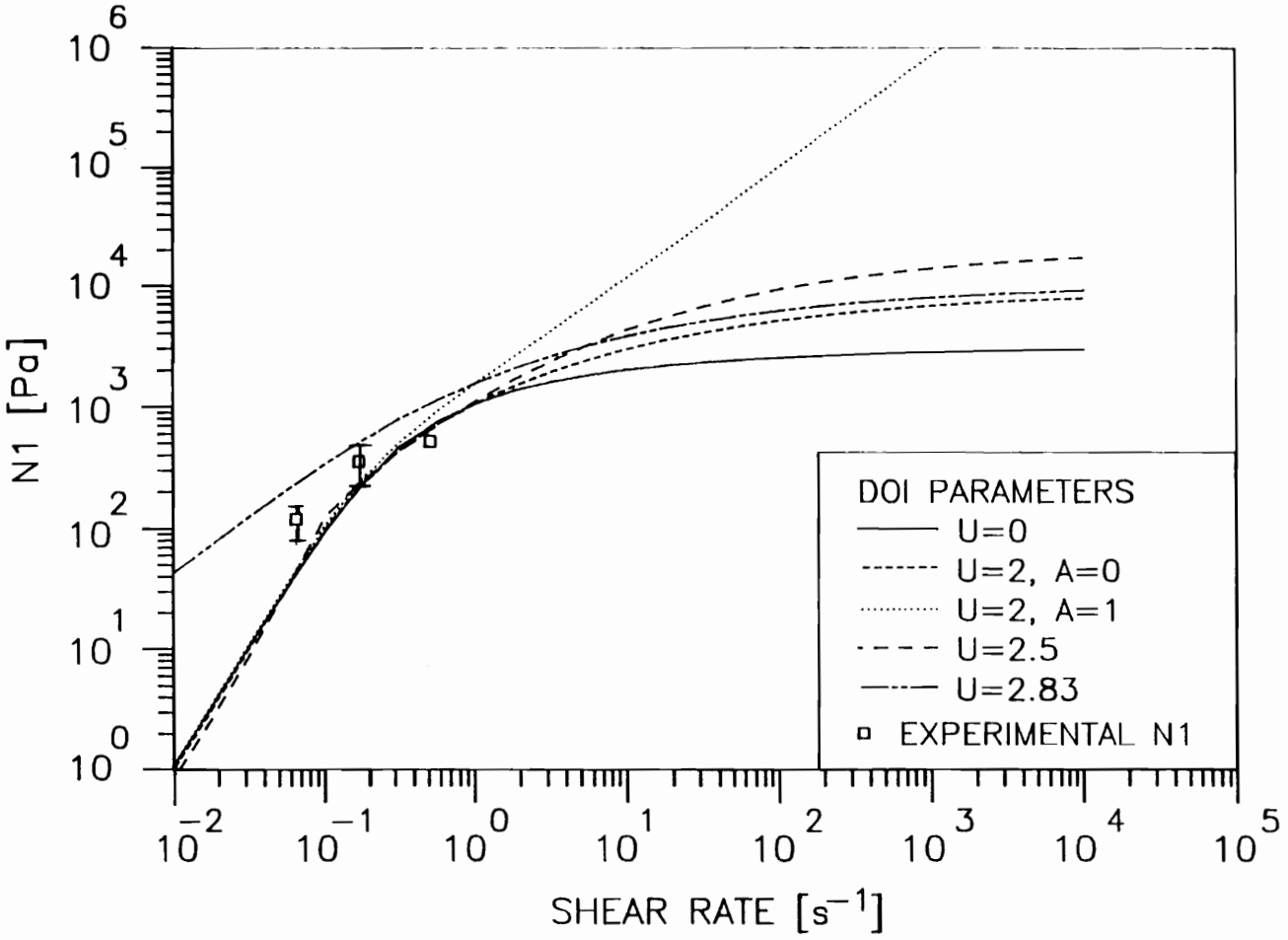

Figure 83. Predictions of the Doi theory for the steady state N1 of an isotropic HPC EF melt: Parameters fit to steady shear viscosity and given in figure. Theory given by lines and experimental data by symbols.

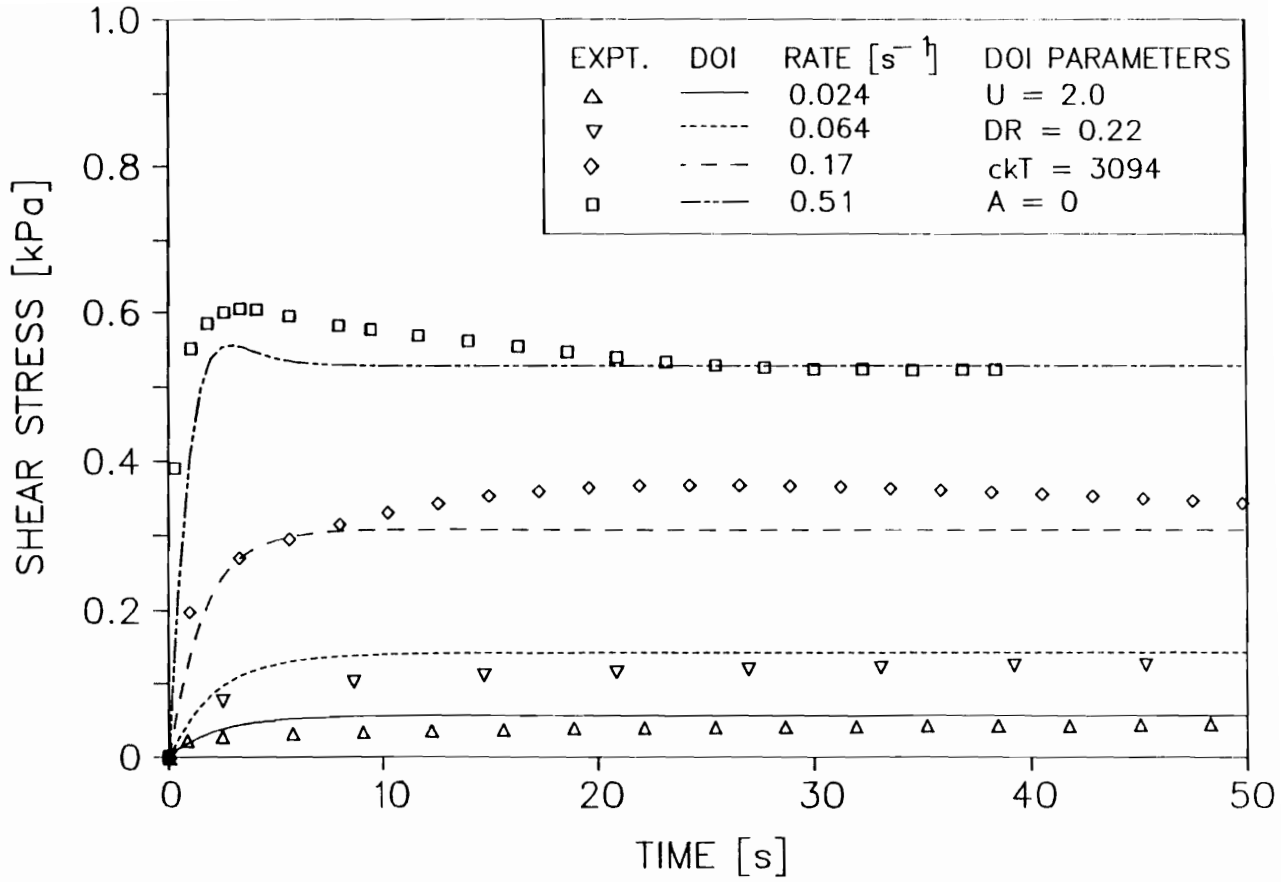

Figure 84. **Predictions of the Doi theory for transient shear stress growth of an isotropic HPC EF melt using fitted parameters: U=2, D_r=0.22, ckT=3090, and A=0. Theory given by lines and experimental data by symbols.**

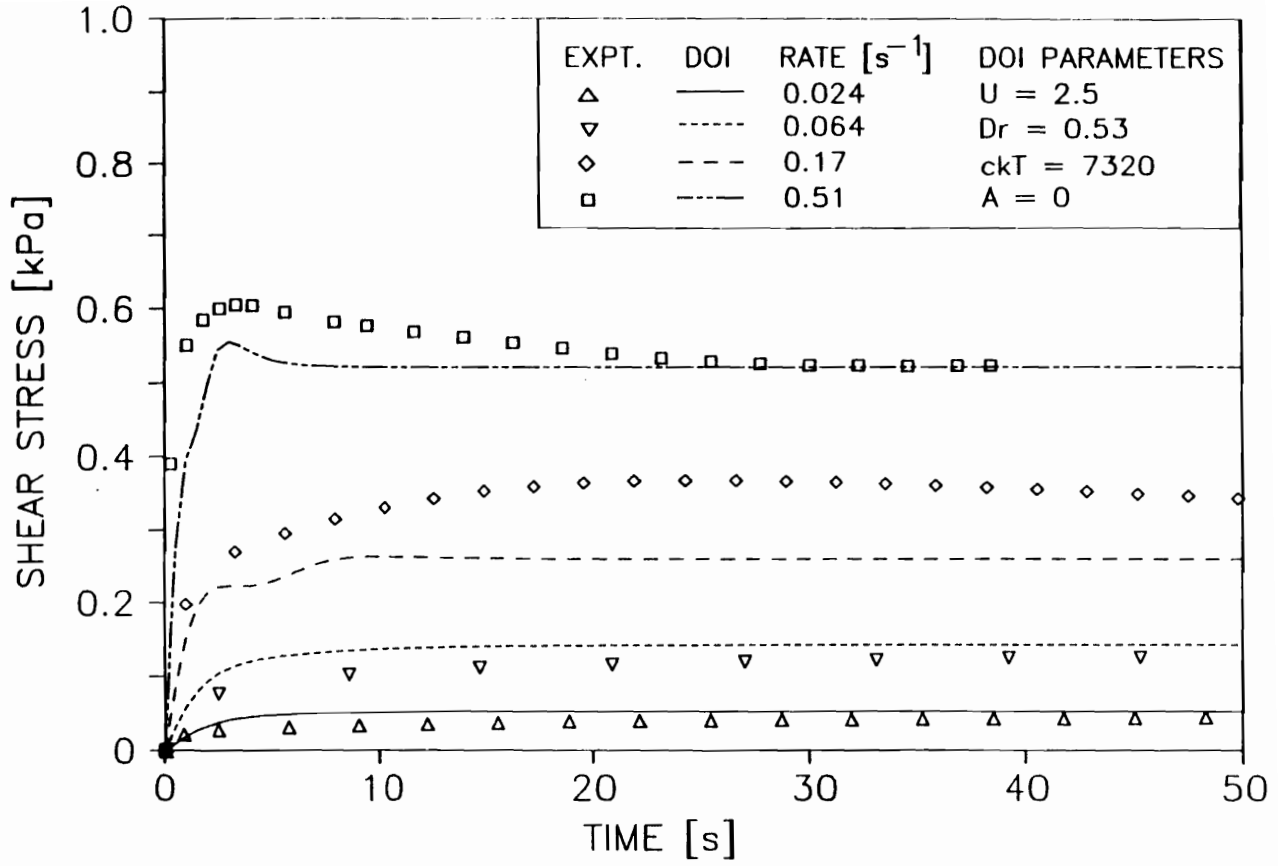

Figure 85. **Predictions of the Doi theory for transient shear stress growth of an isotropic HPC EF melt using fitted parameters: U=2.5, D_r=0.53, ckT=7320, and A=0. Theory given by lines and experimental data by symbols.**

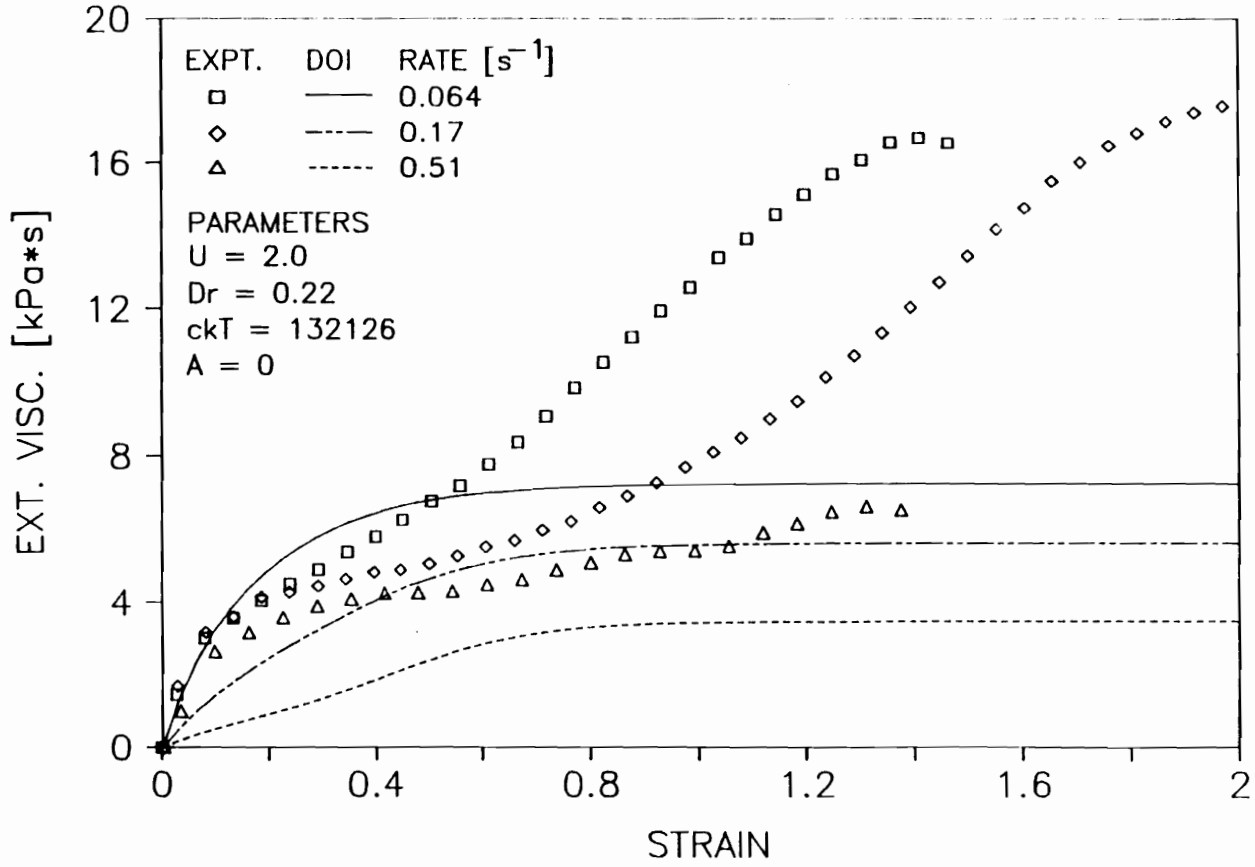

Figure 86. Predictions of the Doi theory for transient elongational viscosity growth of an HPC EF melt using fitted parameters: U=2, D_r=0.22, ckT=3090, and A=0. Theory given by lines and experimental data by symbols.

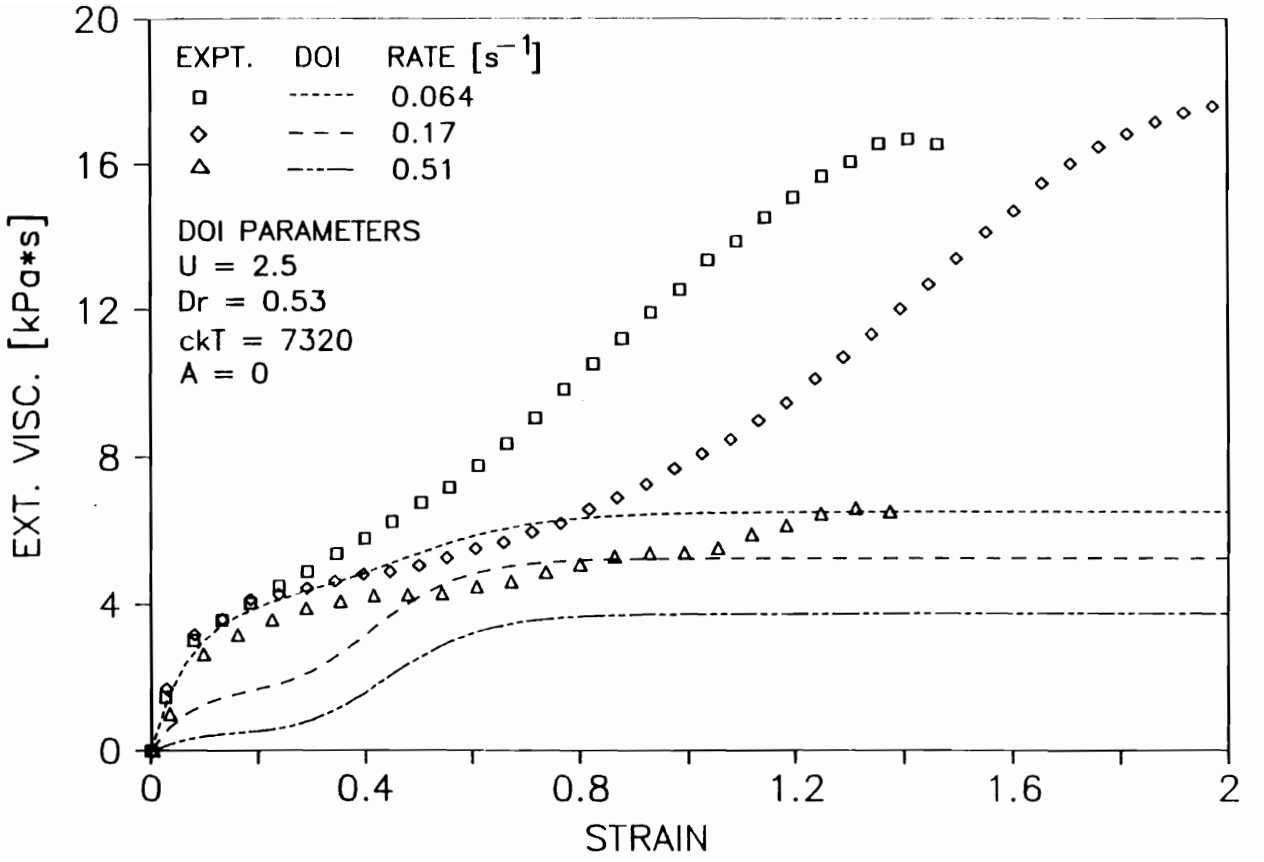

Figure 87. Predictions of the Doi theory for transient elongational viscosity growth of an HPC EF melt using fitted parameters: U=2.5, D_r=0.53, ckT=7320, and A=0. Theory given by lines and experimental data by symbols.

Results of the Doi theory were obtained for steady flow using parameters based on molecular characteristics in order to determine whether the Doi theory can *predict* the the rheological behavior of LCPs. The solutions for the steady shear viscosity obtained in this way for the HPC EF and HBA/HNA systems were orders of magnitude (3 to 4) different than the experimental behavior and do not even appear in the corresponding figures for the fitted parameters, given by Figures 88 and 89. The predictions of the steady state first normal stress difference are shown in Figure 89, where the predictions based on the theoretical parameters are shown in the curve for U=31. While no reliable experimental values of N1 are available for comparison, the measured values of N1 for other LCP systems with comparable shear viscosities are orders of magnitude higher than the predicted values [15,53,62,71,80,89,117]. No determination of the predictions for steady elongational flow was necessary as the predicted Trouton ratios for values of U of 31.4 and 161 were 497 and 2860, respectively [45]. These values are orders of magnitude too large as indicated by the experimentally determined ratio of $\bar{\eta}_e^+(t, \dot{\varepsilon})/\eta^+(t, \dot{\gamma})$ at the point where the samples tested in the ER fractured. Since the steady flow behavior could not be predicted, no calculations were made for the transient flow behavior. The Doi theory then appears to be incapable of predicting the shear or elongational flow behavior of the anisotropic HPC EF melt or the HBA/HNA melt when parameters are determined from the theoretical relations.

Next, solutions to the Doi equations using experimentally fitted parameters were obtained for steady flows in order to determine whether the equations can be used to *model* the flow behavior of the anisotropic HPC EF and HBA/HNA melts. Again, several values of U were chosen for each material and the remaining parameters (D_r, ckT, and A) were fit to experimental steady shear viscosity data as described in Appendix C. The resulting sets of parameters are given in Table 9. Solutions for the steady shear viscosity of HPC EF and HBA/HNA are shown in Figures 88 and 89, respectively. It was found that several sets of the parameters (U,D_r,ckT) could model the steady shear viscosity equally well, while the value of A remained relatively constant since it alone describes the magnitude of the viscosity in the high rate region of the viscosity curve. It can be seen in Figures 88 and 89 that there is semi-quantitative

agreement between the experimental and predicted behavior. Also, the slope of the curve in the high rate or power-law region is found to be equal to -1/3, which is within the range of values observed in LCP systems [18].

The predictions of the steady first normal stress difference were calculated for each material using the same sets of parameters as were used for calculating the viscosity. Representative results of these calculations are shown in Figure 89

for HPC EF. While no direct comparison of the theory with experimental values for HPC EF is possible it is worthwhile to briefly examine the predicted behavior. The magnitude of N1 is seen to depend on the value of U, but the shape of the curve is unchanged. At low rates, the value of the N1 is seen to depend linearly on $\dot{\gamma}$. On the other hand, the shape of the curve in the high rate region is seen to depend tremendously on whether the term for rod-solvent interactions is retained (i.e. $A \neq 0$). Without the term the value of N1 approaches a high rate limit while the value of N1 is seen to increase indefinitely when the term is retained. Additionally, the value of N1 is again predicted to depend linearly on $\dot{\gamma}$ at very high shear rates.

The predictions for the steady elongational flow behavior of the HBA/HNA copolyester were calculated in order to determine the steady elongational flow behavior predicted by the Doi theory. The parameters used were those determined from shear flow data and the resulting predictions are shown in Figure 91 for one set of parameters (U, D_r, ckT) and with varying values of A. The steady elongational viscosity ($\bar{\eta}_e$) is predicted to be Newtonian at low elongation rates and go through a region of rate thinning at moderate rates. At high elongation rates, the behavior is seen to depend on whether or not the rod-solvent term is retained. Without the term, $\bar{\eta}_e$ is seen to rate thin, with a slope of -1 which indicates saturation of the extensional stress. On the other hand $\bar{\eta}_e$ is seen to exhibit a second plateau at high rates if the rod-solvent term is retained. Of particular note is the curve for $A = 0.01$, which is the value of A which gave the best fit for the steady and dynamic shear viscosity data. According to that curve, the elongational viscosity of HBA/HNA would be rate thinning at the rates used for transient elongational viscosity growth tests. This is at least consistent with the experimental transient flow results.

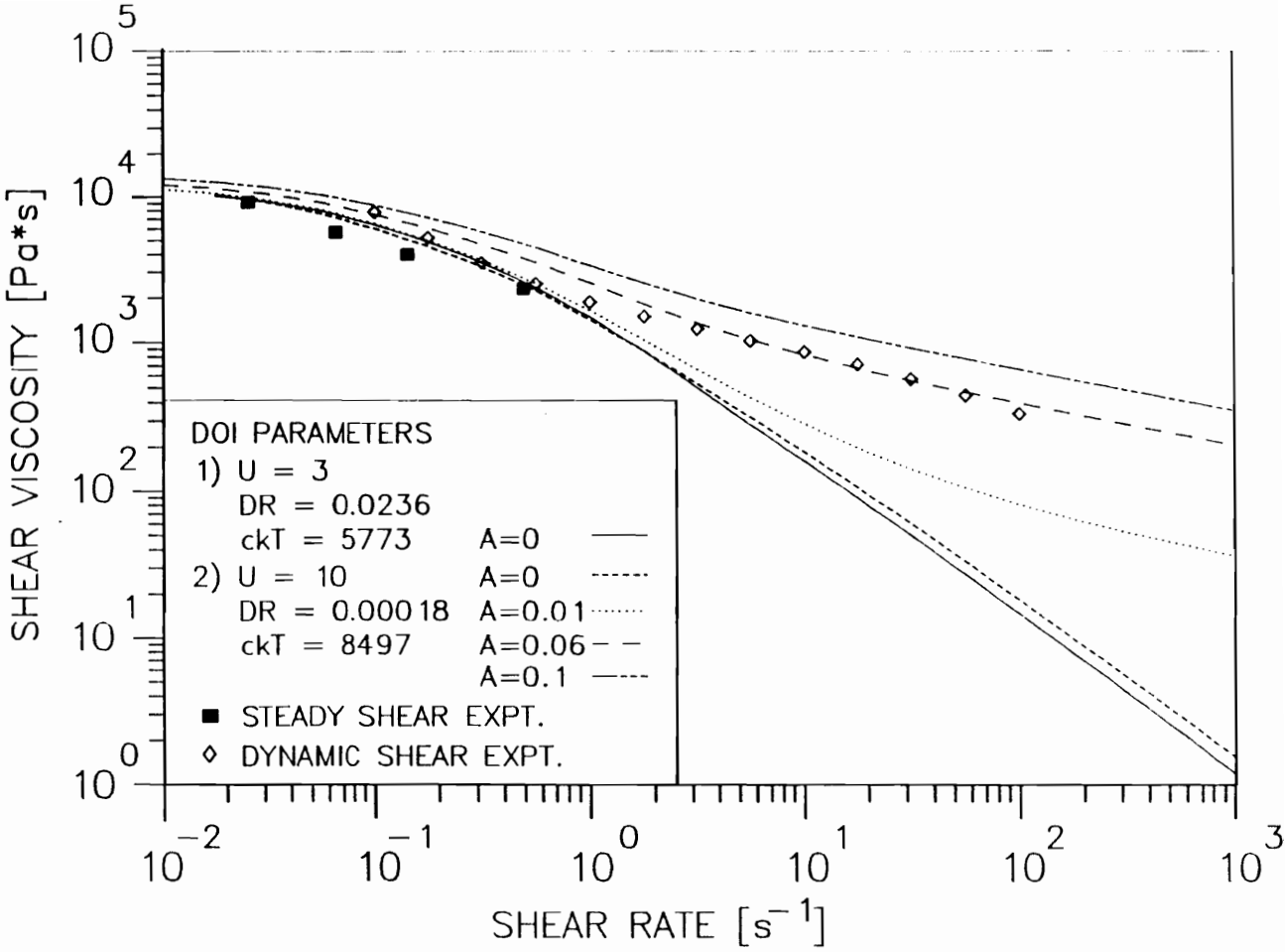

Figure 88. Predictions of the Doi theory for the steady shear viscosity of anisotropic HPC EF melt: Parameters fit to steady shear viscosity and given in figure. Theory given by lines and experimental data symbols.

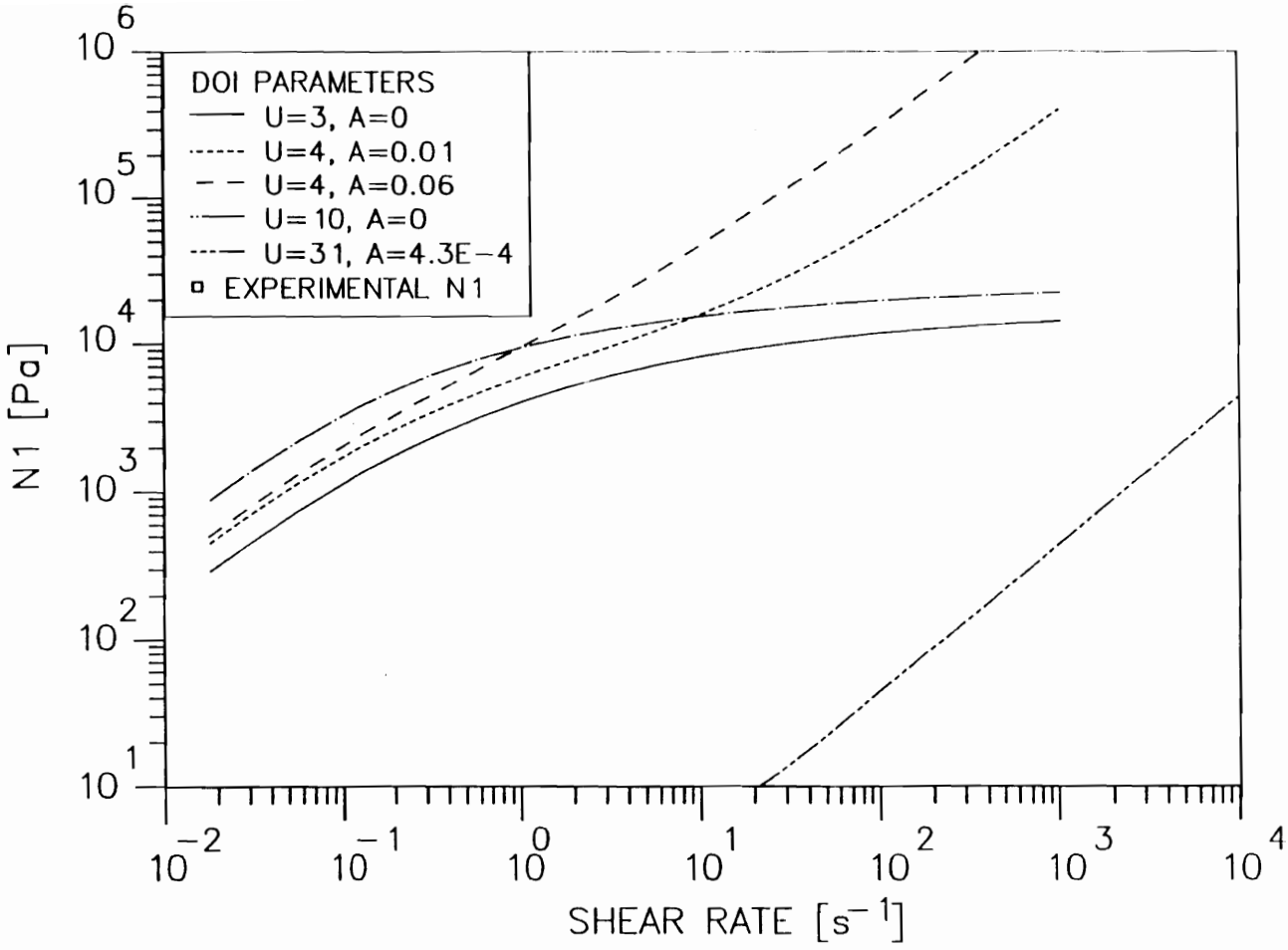

Figure 89. Predictions of the Doi theory for the steady N1 of anisotropic HPC EF melt: Parameters fit to steady shear viscosity and given in figure. Theory given by lines and experimental data symbols.

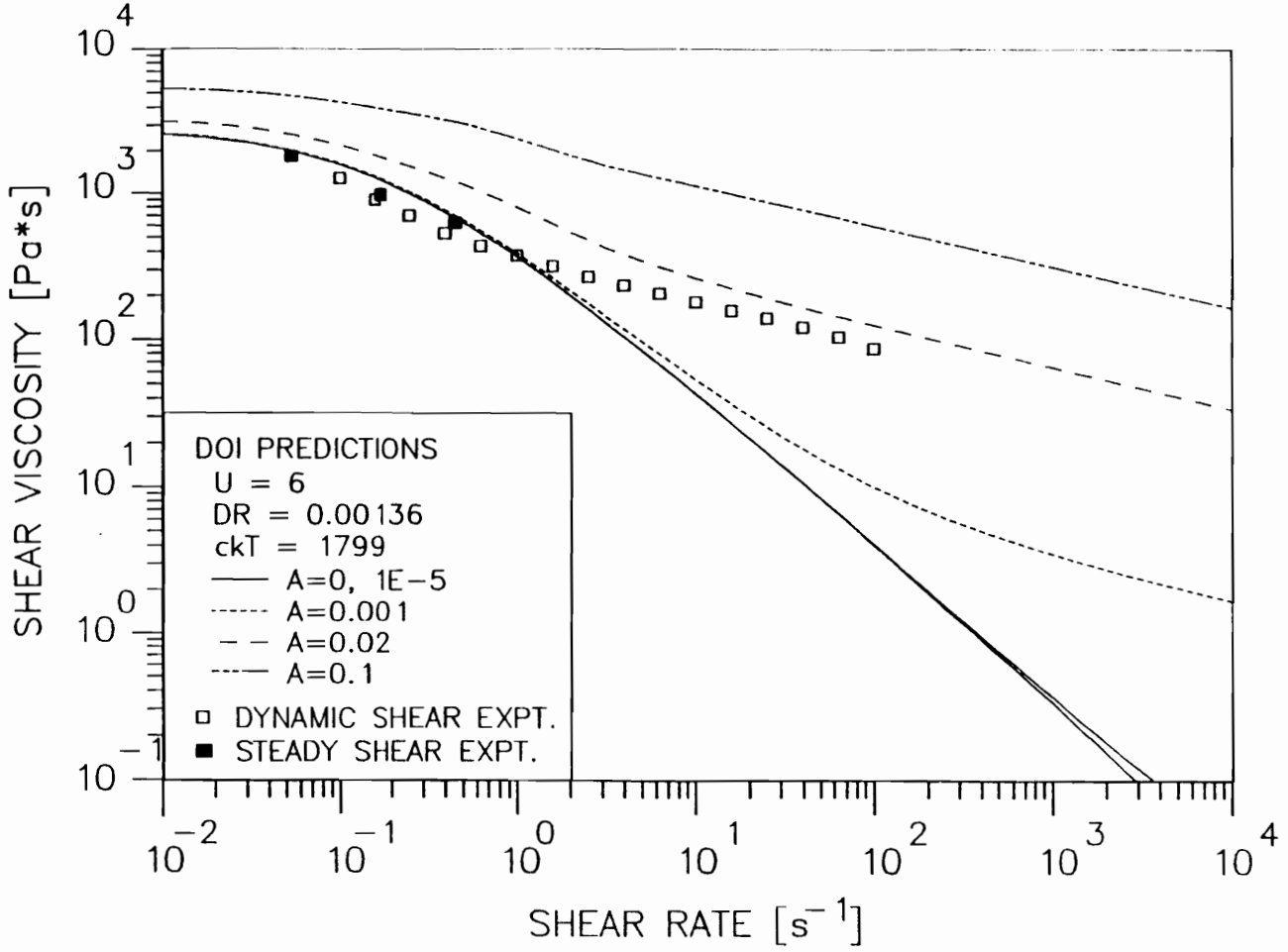

Figure 90. Predictions of the Doi theory for the steady shear viscosity of HBA/HNA: Parameters fit to steady shear viscosity and given in figure. Theory given by lines and experimental data symbols.

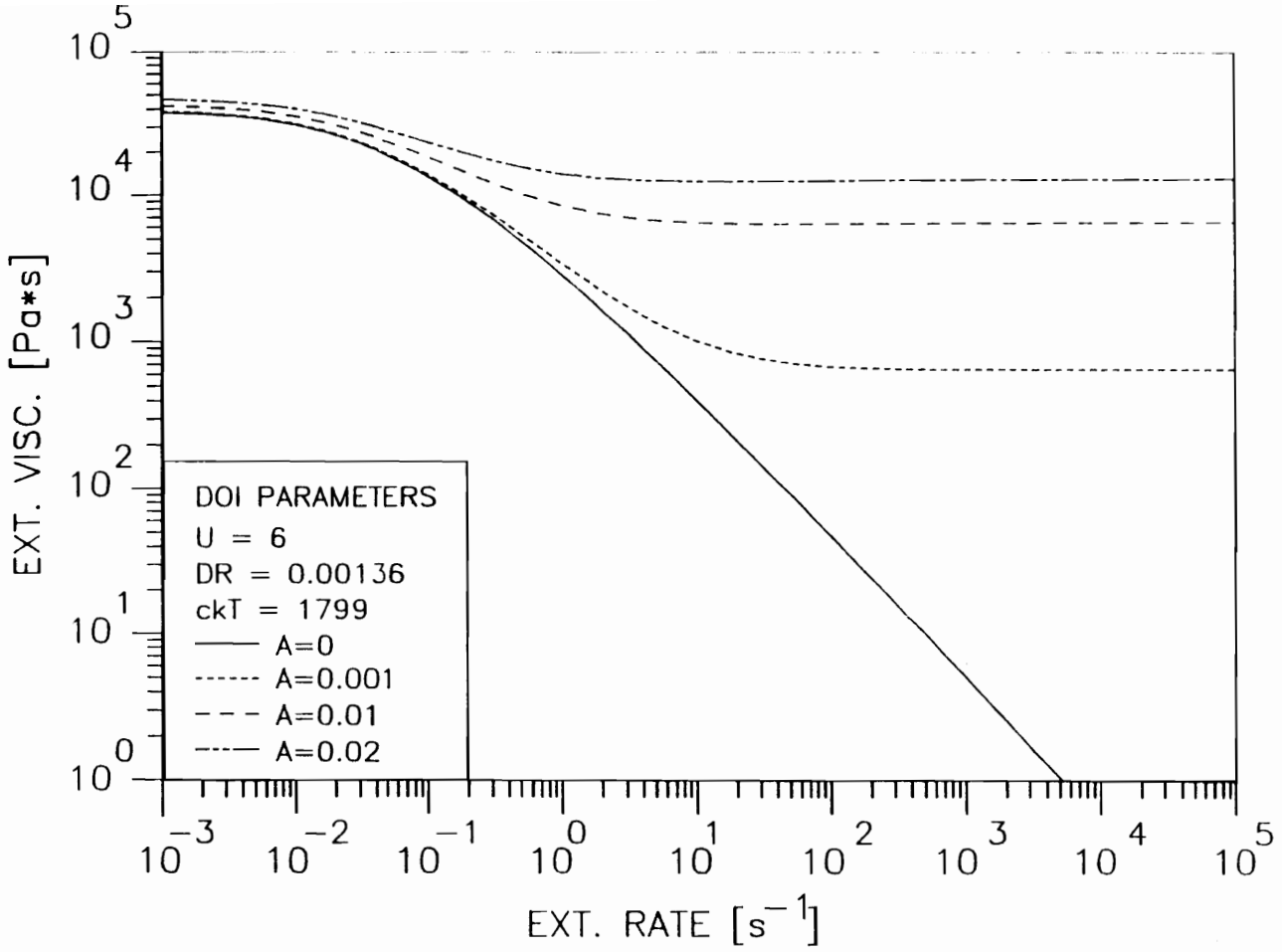

Figure 91. Predictions of the Doi theory for the steady elongational viscosity of HBA/HNA: Parameters fit to steady shear viscosity and given in figure. Theory given by lines.

The numerical solutions to the Doi theory were also obtained for the transient shear and elongational flow of the anisotropic HPC EF melt and HBA/HNA using parameters fitted to their respective steady shear flow data. Both the effect of varying parameters sets, i.e. (U,D_r,ckT), and of varying initial conditions were investigated. The parameter A was previously shown to have no qualitative effect on the transient flow results for the isotropic system (also confirmed for the anisotropic materials) and was set to zero to simplify the calculations. The parameter sets investigated are given in Table 9, while the the initial conditions investigated were those given in Table 5 on page 122. Additionally the use of a Voigt average to simulate a multidomain system is considered at the end of this section. Finally, only results for the HPC EF melt are presented here due to the large number of solutions and behavior similarities between the anisotropic HPC EF and HBA/HNA melts. The results for the HBA/HNA were found to be nearly identical.

An important first point in the investigation of the transient flow predictions using the Doi theory is to stipulate that the initial orientation be physically realistic according to the equations for the theory. This means that the value of S, the scalar order parameter, must initially be equal to the equilibrium value for the fluid at rest, given by equation 3.5.7. The consequences of not using this condition are illustrated in Figures 92 and 93 for transient shear stress and elongational viscosity growth. In both figures negative undershoots are seen, which is physically impossible. Therefore, in order to prevent spurious transients in the solutions, subsequent transient flow calculations were made with initial conditions which satisfy the equilibrium relations in the Doi theory, i.e. equations 2.1.1 and 3.5.7.

The effect of changing the set of parameters (U,D_r,ckT) was investigated next. As previously stated, a number of sets of (U,D_r,ckT) were found for each material which gave nearly exactly the same solution for the steady shear viscosity. While four such sets were determined for the anisotropic HPC EF melt (characterized by U values of 3, 4, 6, and 10), results are shown only for the sets characterized by $U=3$ and $U=10$ as similar behavior is seen for the intermediate sets. Also, the initial condition used to obtain the solutions were those determined from subjecting the materials to very low deformation rate flows as discussed in section

3.5, with the initial director orientations given in Table 5 on page 122. The transient shear stress and elongational viscosity growth predictions are shown in Figures 94 through 97 for parameter sets with U=3 and U=10. In the transient shear flow predictions, it can be seen that there is very little difference between the behavior predicted by the Doi theory using the two different parameter sets, with the transient slightly longer for higher U. Likewise, the shape of the curves are similar for the transient elongational flow behavior predicted using the two different parameter sets. However, there is a tremendous dependence of the steady elongational viscosity on the parameter U. For the HPC EF material, it can be seen that U must be in the range 3 to 10 to be able to model the elongational flow behavior. It turns out that of the parameters sets used in the calculations, the best agreement for both LCPs is for the sets with U=4.

One objective of this work was to determine whether the adjustable parameters determined from shear flow data could be used to obtain predictions for elongational flow behavior. In the transient flow data shown in Figures 94 through 97 it was demonstrated that a number of parameter sets can equally well describe the shear flow behavior of the LCPs, while only one particular set can even possibly be used to model the elongational flow behavior. It is apparent that there is no method which can be used to determine this set exclusively from the shear flow results. Therefore, it appears that the Doi theory in the present form is unable to predict the elongational flow behavior of LCPs when the adjustable parameters are determined exclusively from shear flow data.

The transient flow predictions presented in Figures 94 to 97 are now examined again to determine how the initial orientation effects the predicted behavior. As stated, the initial conditions used were those for the director orientation obtained in the limit of very slow flow. The predictions for shear stress growth are seen to reproduce the stress overshoot which occurs upon the inception flow. However, the theory under predicts the magnitude of the overshoot peak and also the time at which it occurs. For the case of elongational flow, it can be seen that the predicted values of $\bar{\eta}_e^+(t, \dot{\varepsilon})$ approach a steady state much too soon. While these results are discouraging, they can be explained somewhat when one considers the type of flow test which

is effectively simulated by the initial conditions used. The initial conditions were for slow flow and represent those for a test in which the flow rate is stepped up from a low deformation rate to a higher one. This is in contradiction to the experimental studies, in which the LCP was initially at rest. It should be noted that previous work [24,95] has shown that pre-shearing an LCP can reduce the overshoot peak obtained on the startup of steady flow. It also seems reasonable that such pre-shearing would reduce the time it takes for the flow to reach steady state. The use of the slow-flow initial condition then appears to be inappropriate for the modelling of transient flow in the case where an LCP is initially at rest.

Since the director orientation in a liquid crystal domain at rest is undetermined, calculations were made to determine the effect of the initial director orientation on the transient flow predictions of the Doi theory. Several different initial director orientations were investigated and these were given by the last 6 initial conditions in Table 5 on page 122, along with the result for the slow-flow initial condition previously described. The set of adjustable parameters used was ($U=4$, $D_r=0.0064$, $ckt=6030$, $A=0$) and was chosen because this set best fits the experimental peak values of $\bar{\eta}^+_{\bullet}(t, \dot{\varepsilon})$. The solutions for the transient shear stress and first normal stress difference are shown in figures 98 and 99 for a rate of 0.049 s^{-1}. It can be seen in Figure 98 that the initial director orientation has a tremendous effect on the transient shear flow behavior predicted by the theory. When the initial director is close to the final value, no overshoot is predicted while if the director must travel through a large angle upon the inception of flow, a large overshoot is predicted. It is noteworthy that the response for the initial condition ($n_1(0)=-0.41$, $n_2(0)=0.71$) is very similar to the experimental behavior. The transient first normal stress difference also depends tremendously on the initial director orientation as shown in Figure 99. It is noteworthy that certain initial conditions result in a negative undershoot in $N1_{\bullet}$ since such behavior has been seen in 60HBA/PET and 80HBA/PET at certain temperatures [60,87,89].

One feature which can be used to characterized the behavior of a polymer system is the ratio of the time for the shear and first normal stress difference to reach steady state upon the inception of steady shear flow. For example, in flexible-chain polymers the overshoot peak in

the first normal stress difference is observed to occur at about twice the time as that for the shear stress [105]. A comparison of the predictions for the transient shear stress and first normal stress difference can be made between Figures 98 and 99, and the predictions for one set of initial conditions is replotted together in Figure 100 for additional clarity. It can be seen that the predicted time for the evolution of N_1 is just slightly longer than that for $\eta^+(t, \dot{\gamma})$. This can be compared to the experimental behavior of the HBA/HNA copolyester as shown in Figures 45 and 55. This comparison is valid since the transient experimental N1 behavior was found to be reproducible. It can be seen that the N1 transients occur over roughly the same time scale as the viscosity transients at each rate. Similar observations can be made for HPC EF at 190 °C. Furthermore, this observation has been confirmed by Guskey [214] for HBA/HNA and by Wissbrun [86] for a thermotropic copolyester. While it is not clear whether this type of behavior is general for LCP systems, the Doi theory predictions are consistent with experimental behavior determined here.

The effect of initial orientation on the elongational viscosity growth behavior was also investigated, using the same initial conditions as for the transient shear flow and at an extension rate of 0.49 s^{-1}. The predictions are shown in Figure 101, where it is seen that initial director orientation has a tremendous effect on the predicted behavior. Elongational viscosity overshoot is even predicted for certain initial director orientations, which would result in an unstable flow. It is also noteworthy that none of the solutions shown provide for more than qualitative agreement with the the experimental behavior and many show no agreement whatsoever. On the other hand few initial conditions were tried an it is encouraging that the transient response occurs over approximately the range of strain that experimental data are available.

In view of the transient flow results presented to this point, it is apparent that the Doi theory cannot predict the transient flow behavior of LCPs when the initial conditions are based on a single director orientation. For example, while the transient shear stress growth of HPC EF was modelled in a semi-quantitative manner, the discovery of an initial condition affording such a solution was likely fortuitous. At the same time the Doi theory would be impractical for

use in flow modelling if an initial condition had to be found to model each set of data. It was also noted that the elongational viscosity growth could not be predicted with any of the initial conditions tried. Furthermore, LCP melts are known to exhibit a polydomain texture in the quiescent state and therefore a single initial orientation is physically unrealistic. These arguments point to the use of a multidomain model for prediction of transient flow behavior.

The averaging of the components of the stress tensor over a number of domains was then investigated for the modelling of transient flow using the Voigt averaging method as described in section 3.5. The use of such an averaging scheme represents a realistic initial condition, i.e. no net molecular orientation at the start of flow, and eliminates the need to determine a specific initial director orientation at the test start. Predictions of the shear stress growth calculated using a multidomain average are shown in Figure 102, with either 3 or 6 domains used in the averaging of the stress tensor. While this is a very low number of domains and does not represent a continuum by any means, it can be seen that dramatic improvement is obtained in the theoretical predictions over those obtained for a single domain. Also, it is seen that the 6 domain average more accurately models the experimental behavior than the 3 domain average. Although this might be fortuitous, the improvement of the predictions with an increasing number of domains is expected assuming the validity of the averaging method used. In contrast to the results for shear, the predictions for the transient elongational viscosity growth obtained with a 6 domain average do not even qualitatively agree with experiment, as shown in Figure 103. At the same time it is possible that increasing the number of domains to represent a more continuous distribution of initial director orientations could give significant improvement in the predictions.

In summary, it was shown that the Doi theory cannot predict the shear or elongational flow behavior of both isotropic and anisotropic HPC EF melts when parameters are determined from the theoretical relations which depend only on molecular characteristics. Similar results were found for HBA/HNA melts. On the other hand, the Doi equations were able to model the steady shear behavior of the isotropic HPC EF melt at least semi-quantitatively with the retention of the rod-solvent interaction contribution to the stress tensor. Additionally, the steady

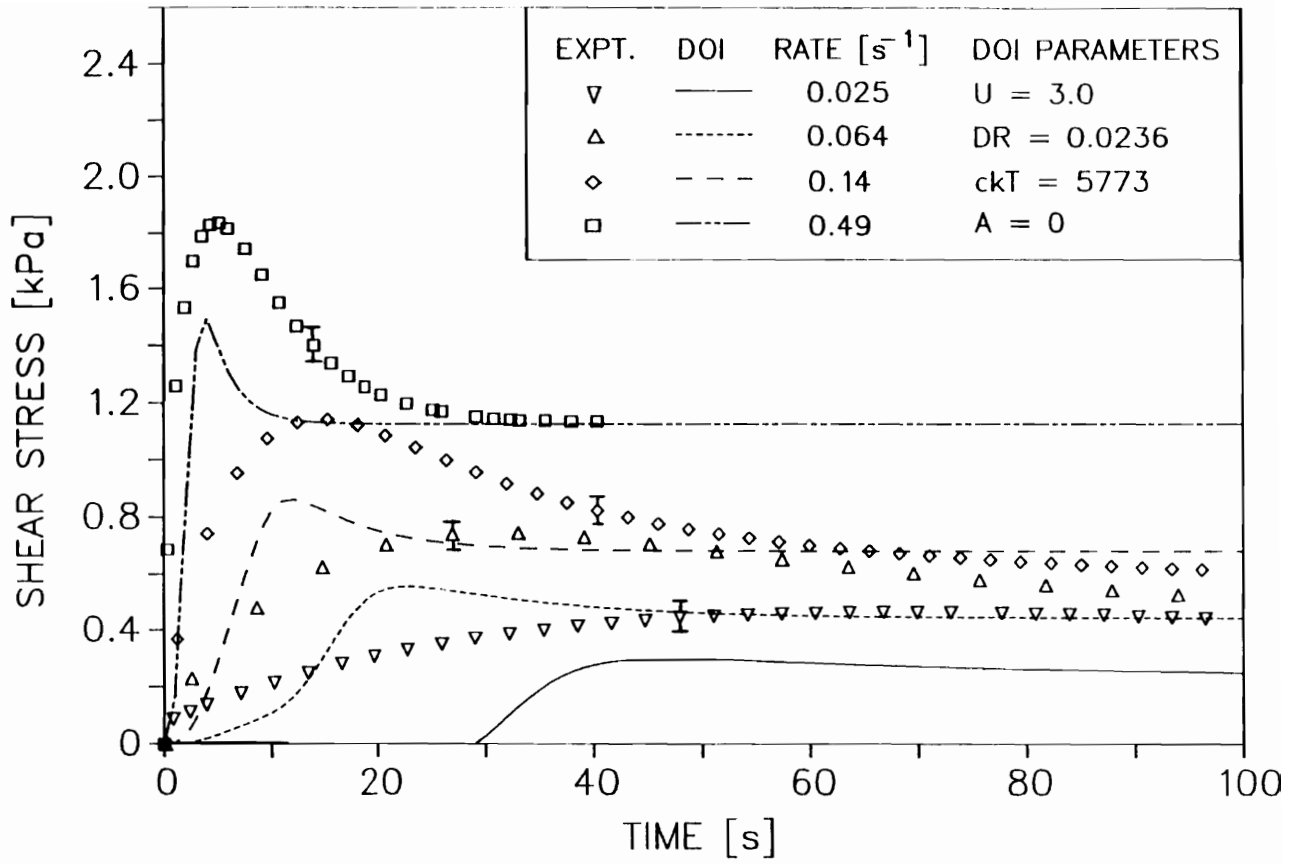

Figure 92. **Shear stress growth predictions for anisotropic HPC EF melt. The initial conditions was $S_{\alpha\beta}(0)=0$ for all $\alpha\beta$: Parameters are U=3, D_r=0.0236, ckT=5770, and A=0. Theory given by lines and experimental data by symbols.**

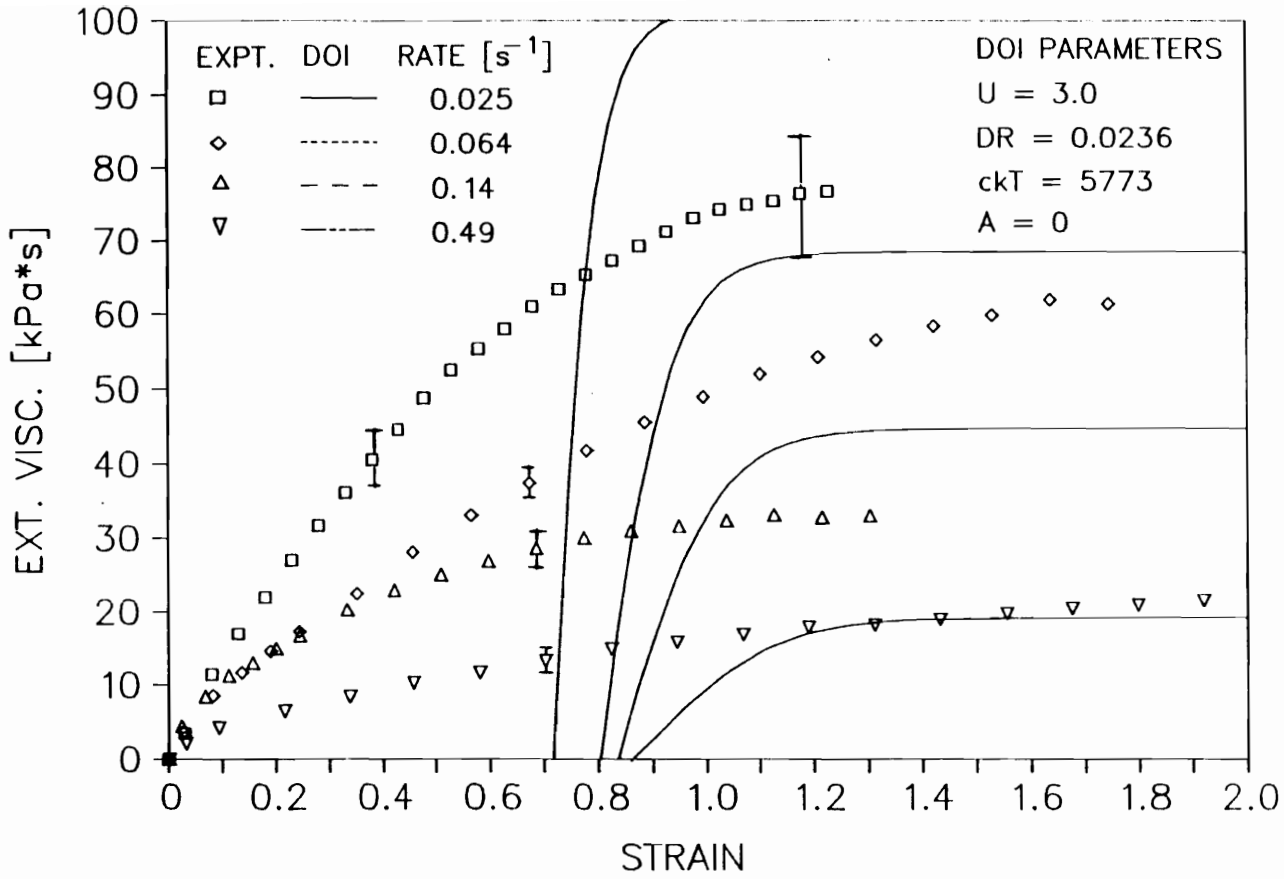

Figure 93. **Elongational viscosity growth predictions for anisotropic HPC EF melt. The initial condition was $S_{\alpha\beta}(0)=0$ for all $\alpha\beta$: Parameters are U=3, $D_r=0.0236$, ckT=5770, and A=0. Theory given by lines and experimental data by symbols.**

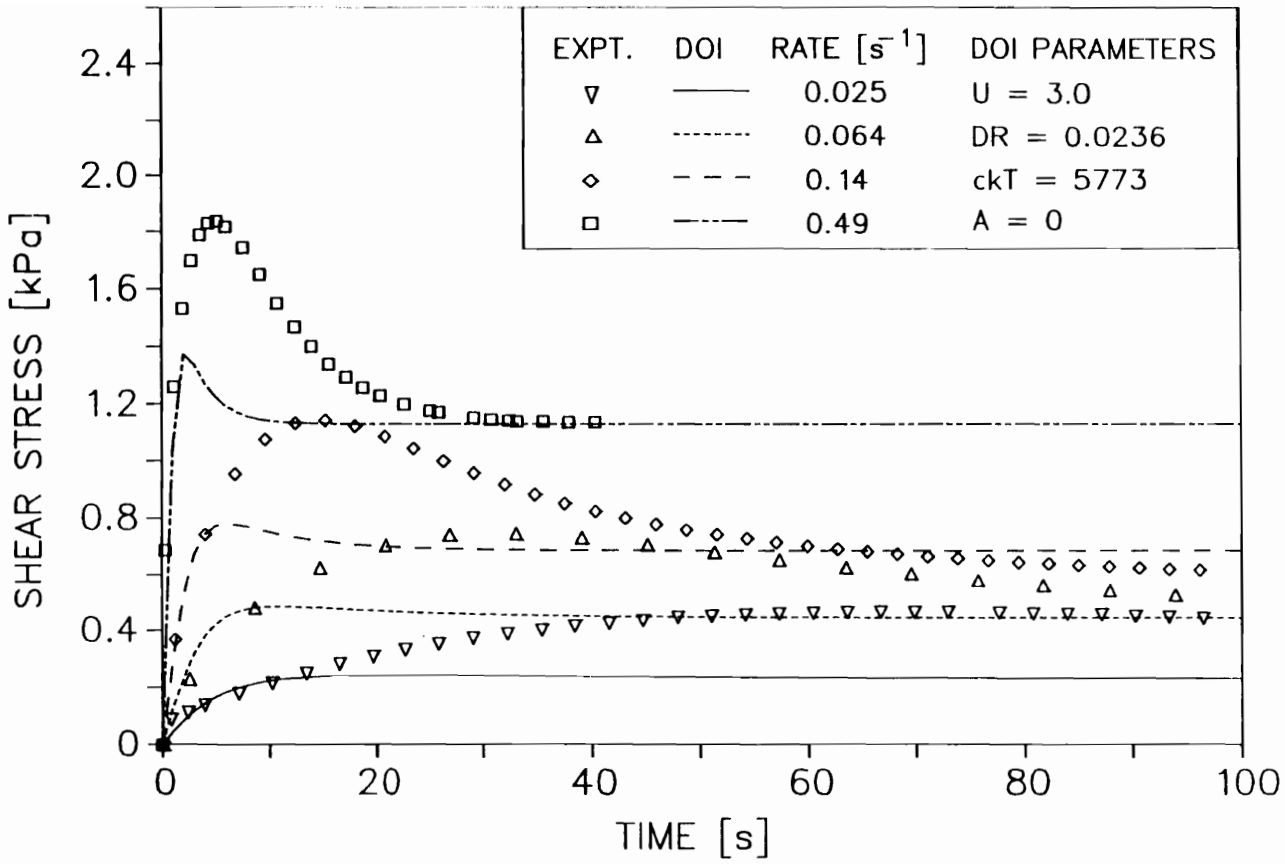

Figure 94. Shear stress growth predictions for anisotropic HPC EF melt. The initial condition was that for slow flow: Parameters are U=3, D_r=0.0236, ckT=5770, and A=0. Theory given by lines and data by symbols.

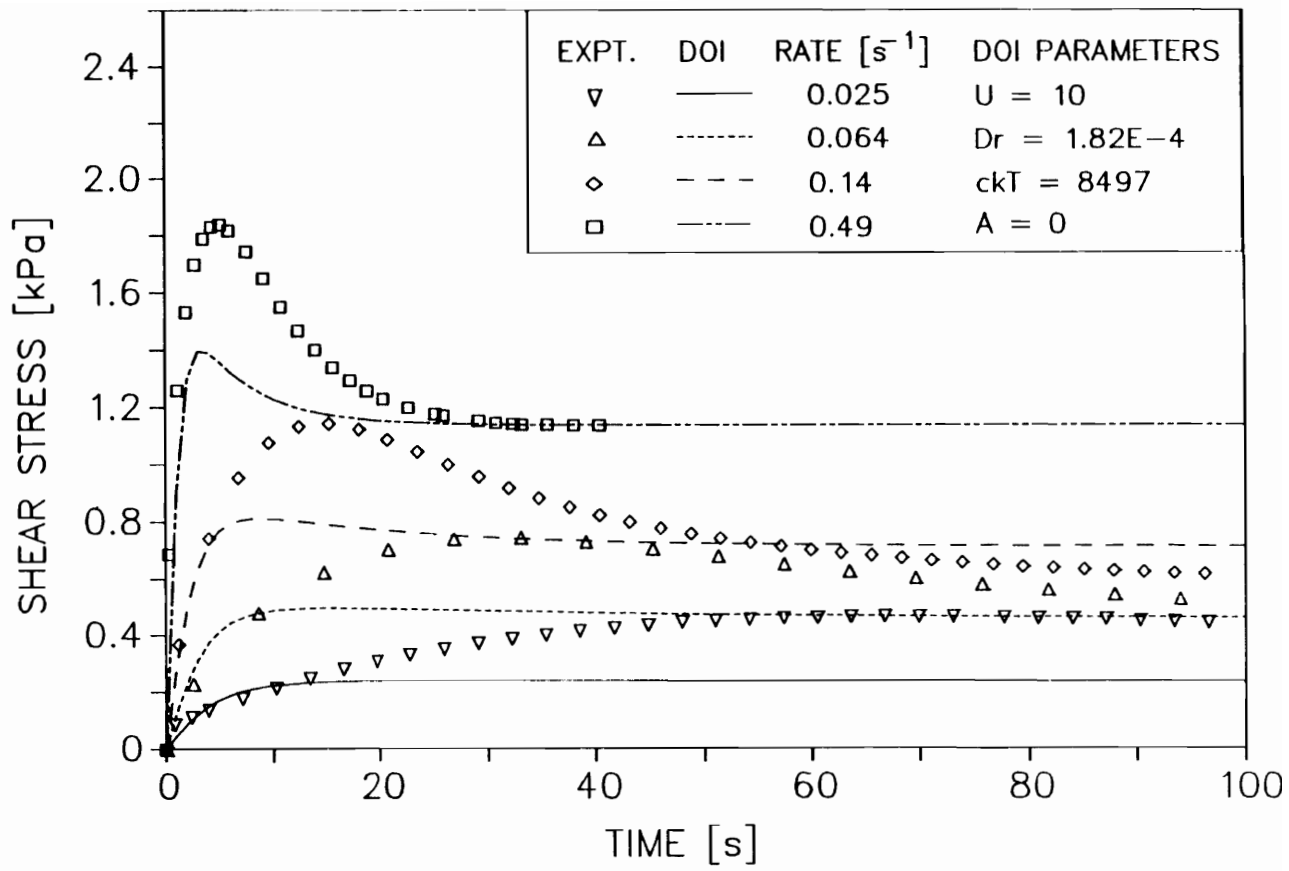

Figure 95. Shear stress growth prediction for anisotropic HPC EF melt. The initial condition was that for slow flow: Parameters are U=10, D_r=1.82E-4, ckT=8500, and A=0. Theory given by lines and data by symbols.

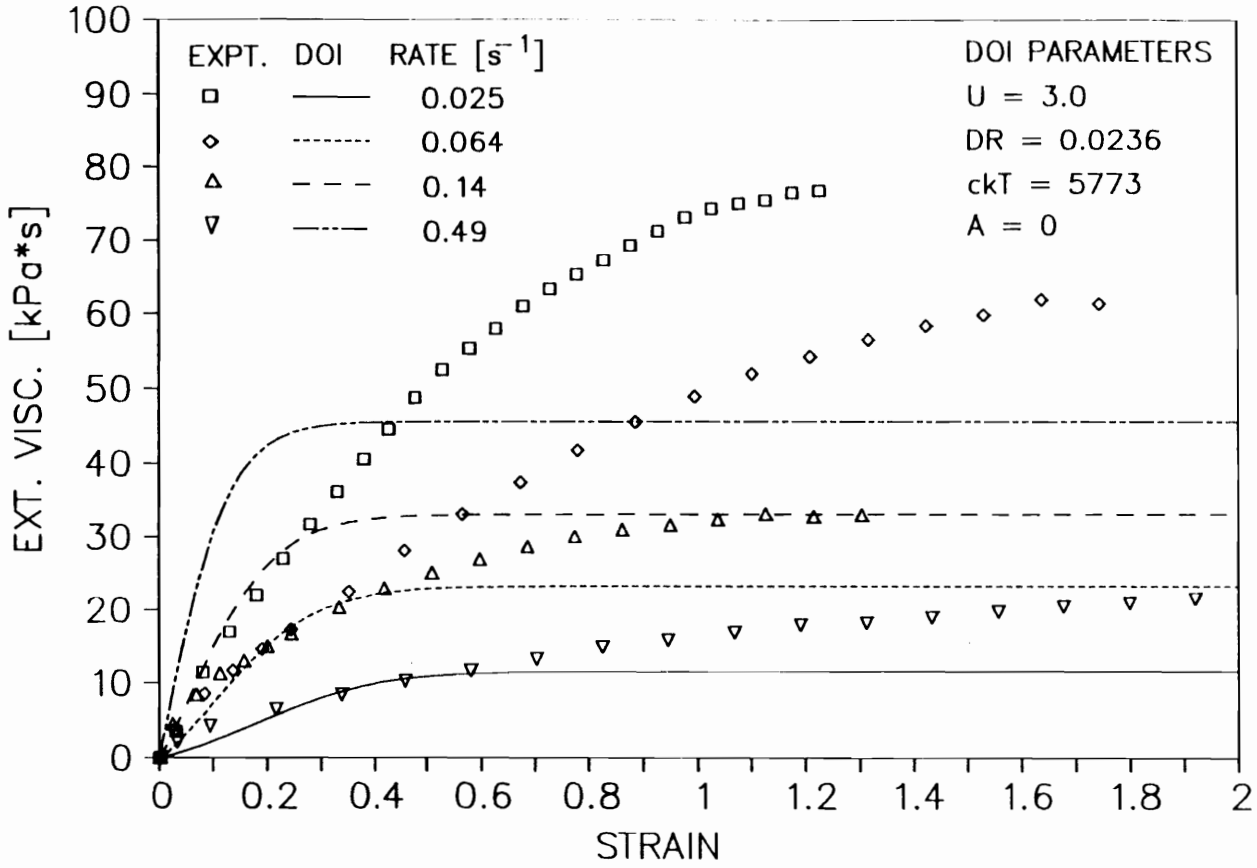

Figure 96. Elongational viscosity growth predictions for anisotropic HPC EF melt. The initial condition was $n_1(0)=1$: Parameters are $U=3$, $D_r=0.0236$, $ckT=5770$, and $A=0$. Theory given by lines and data by symbols.

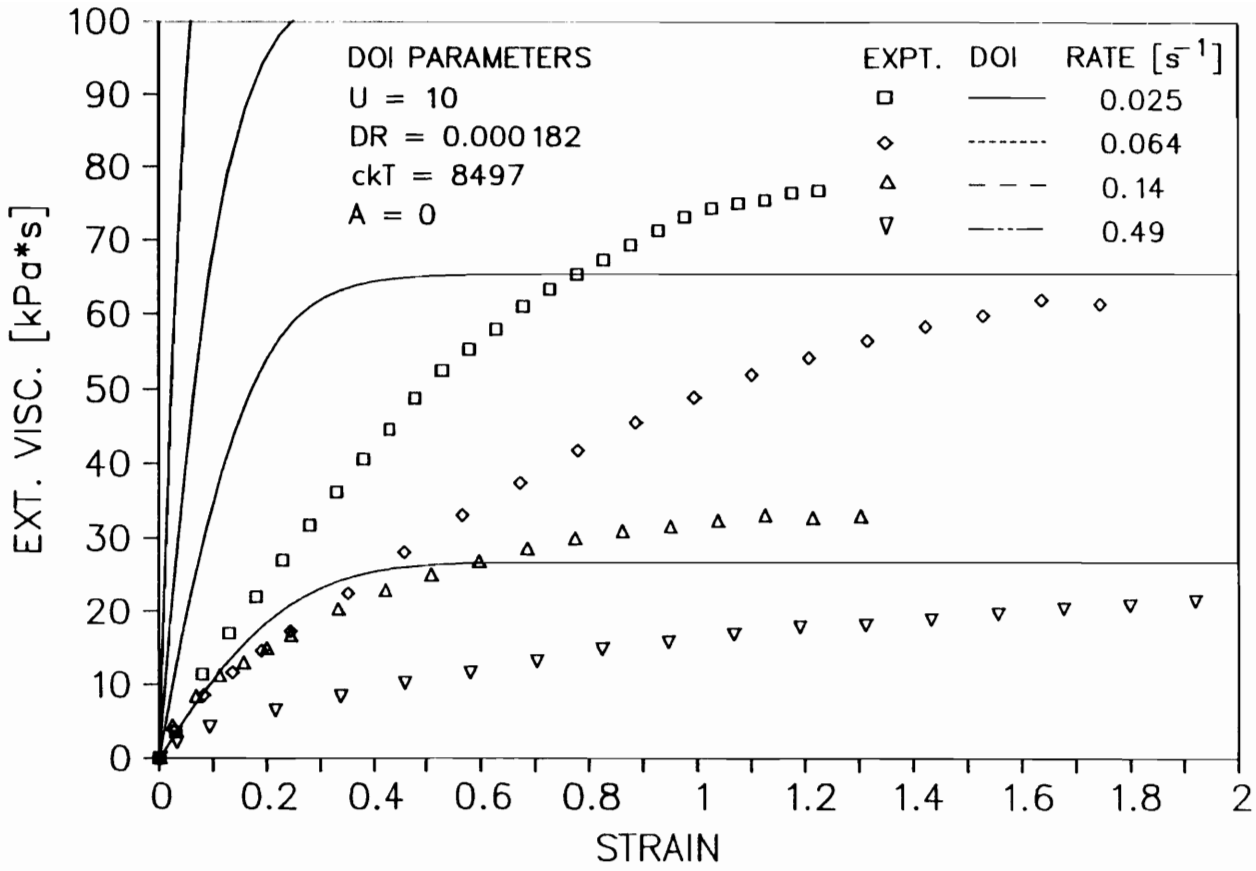

Figure 97. **Elongational viscosity growth predictions for anisotropic HPC EF melt. The initial condition was $n_1(0)=1$: Parameters are U=10, D_r=1.82E-4, ckT=8500, and A=0. Theory given by lines and data by symbols.**

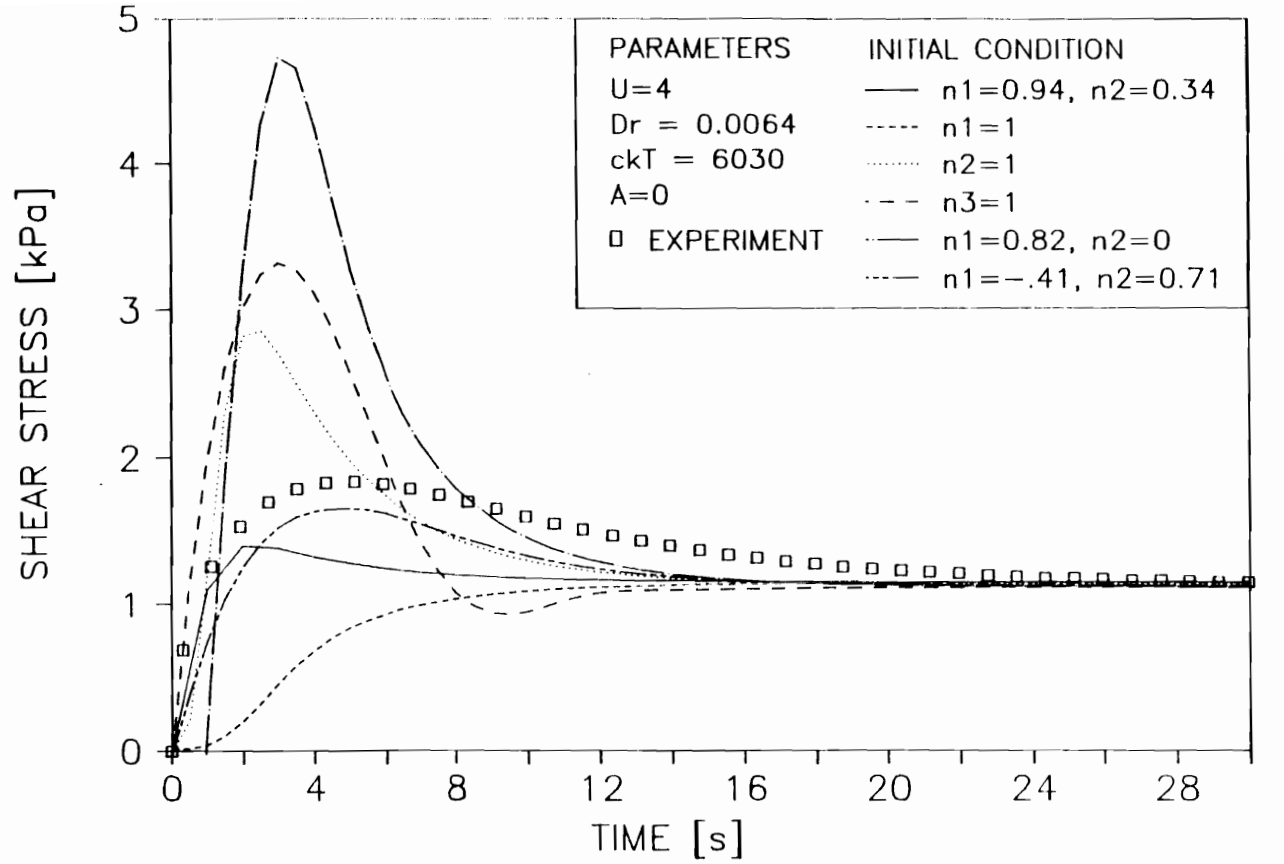

Figure 98. **Shear stress growth predictions for anisotropic HPC EF melt. Varying initial conditions were used as described in figure: Parameters are U=4, D_r=0.0064, ckT=6030, and A=0. Shear rate is 0.49 s^{-1}. Theory given by lines and data by symbols.**

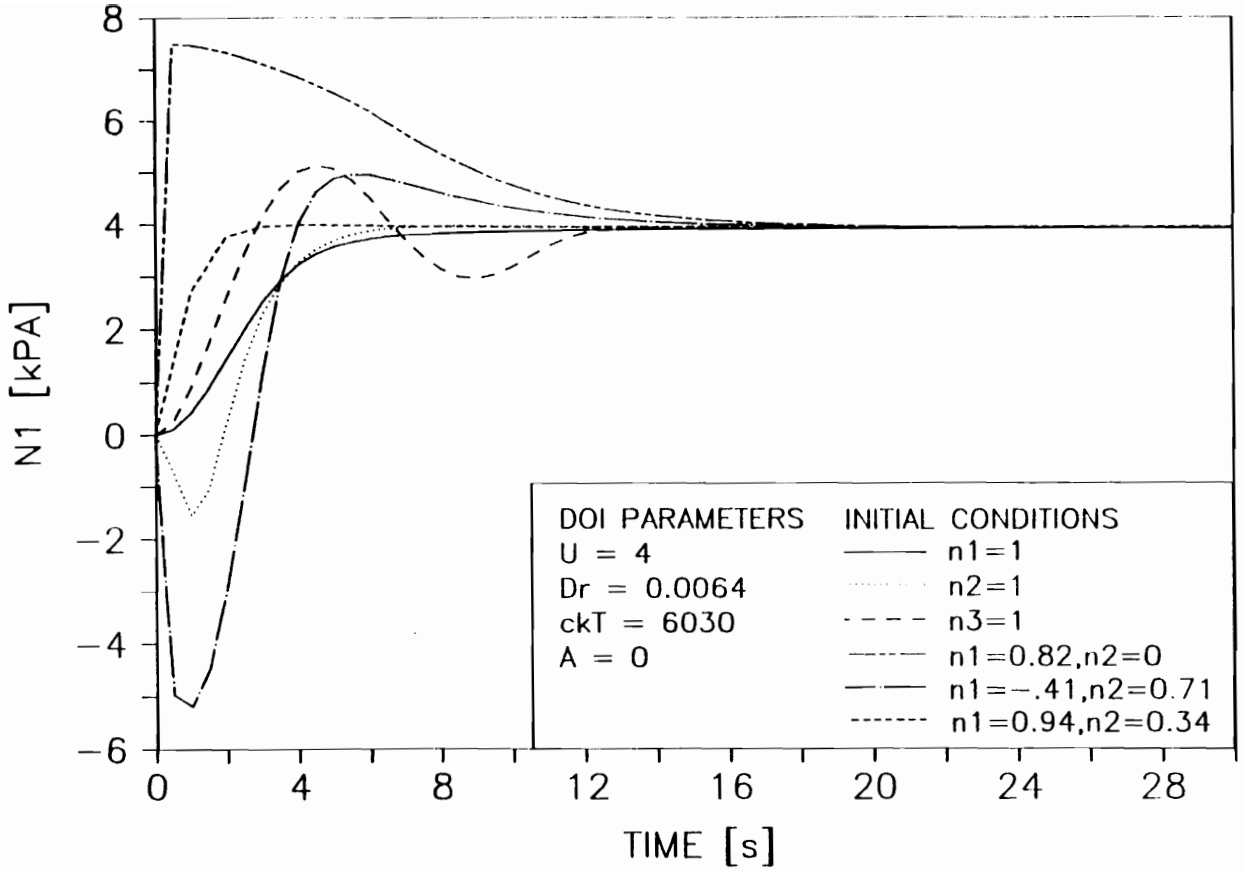

Figure 99. **Transient N1 predictions for anisotropic HPC EF melt. Varying initial conditions were used as described in figure: Parameters are U=4, D_r=0.0064, ckT=6030, and A=0. Shear rate is 0.49 s^{-1}. Theory given by lines and data by symbols.**

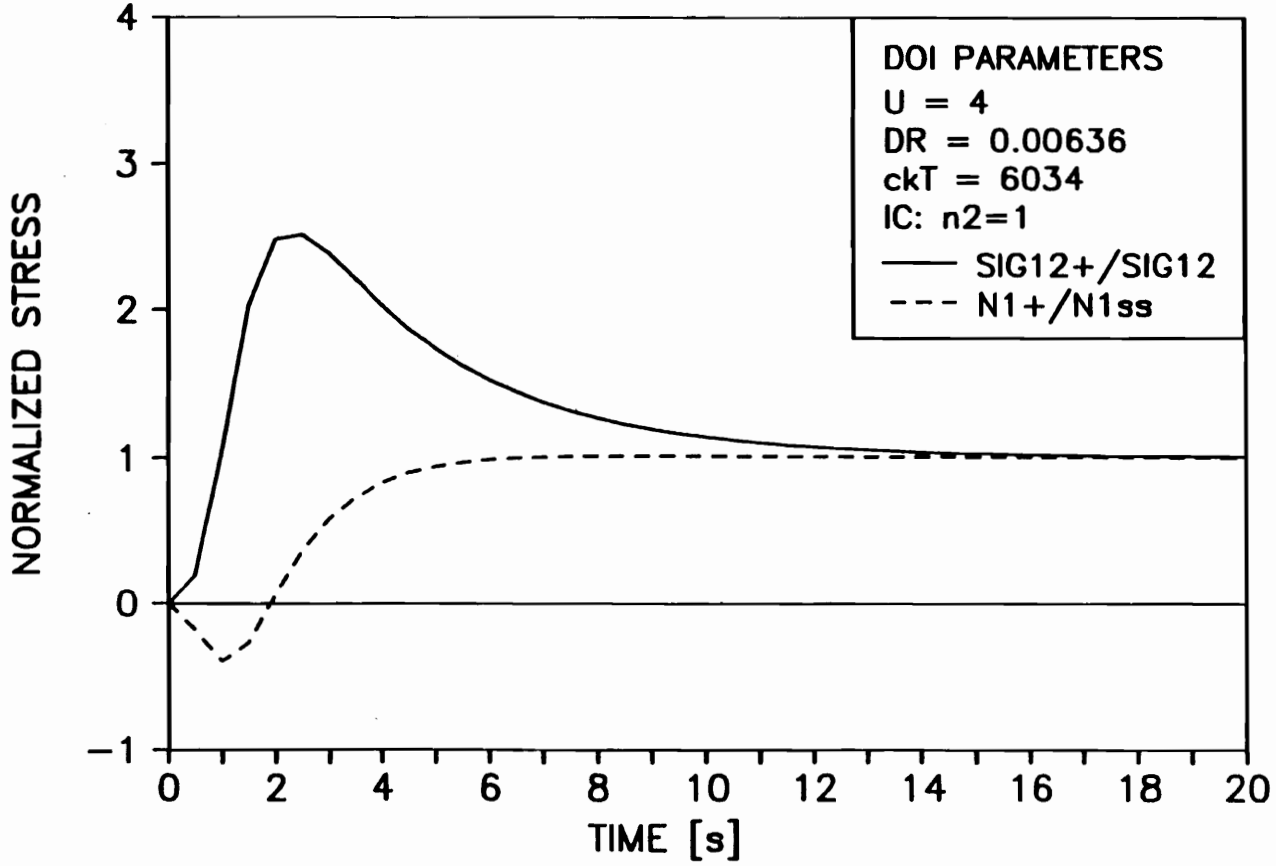

Figure 100. Comparison of Doi predictions of $\bar{N}_1^+$ and transient shear stress at 0.49 s^{-1} and an initial conditon of $n_2(0)=1$: Parameters are U=4, D_r=0.0064, ckT=6030, and A=0. Stress values normalized by steady state values.

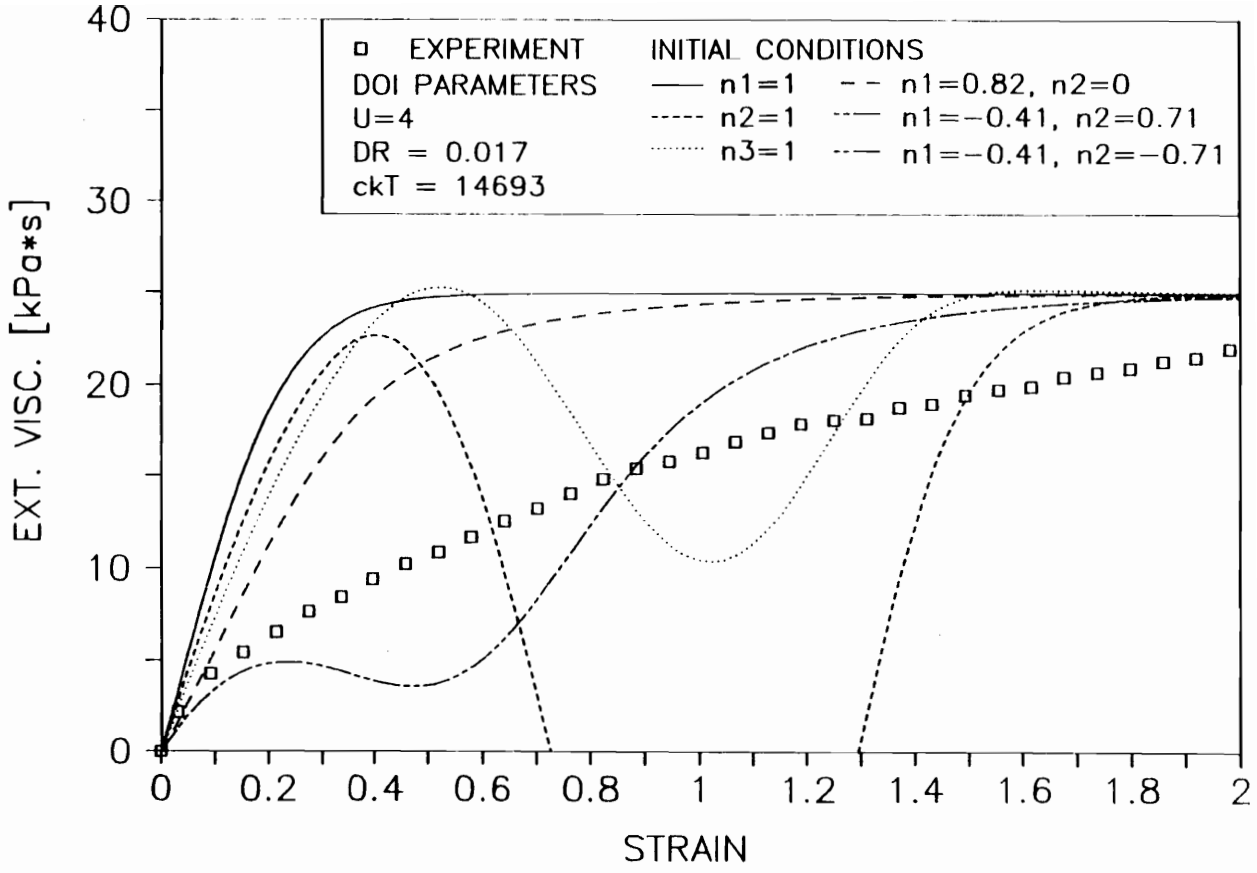

Figure 101. **Elongational viscosity growth for anisotropic HPC EF melt. Varying initial conditions used as described in figure: Parameters are U=4, D_r=0.017, ckT=14960, and A=0. Shear rate is 0.49 s^{-1}. Theory given by lines and data by symbols.**

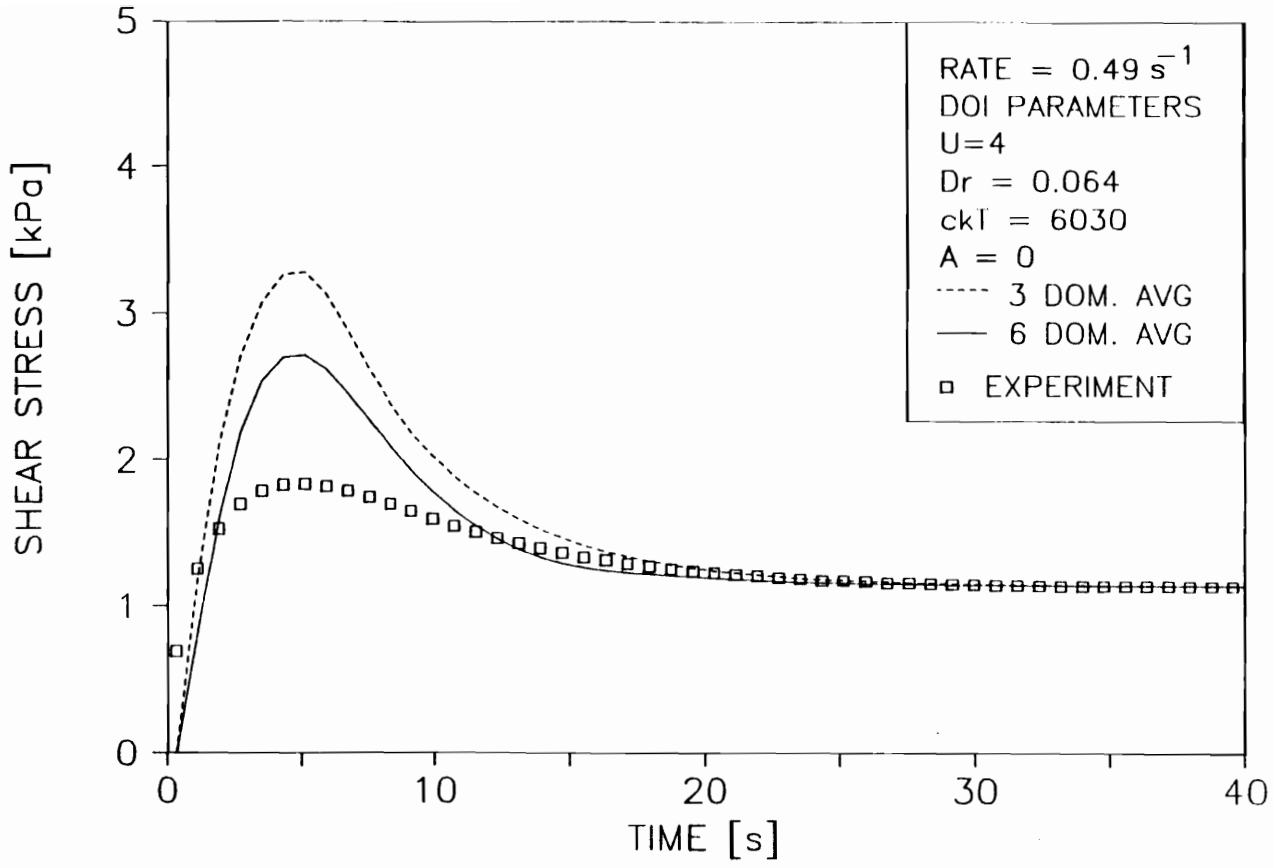

Figure 102. Shear stress growth prediction for anisotropic HPC EF melt using multidomain averages. $\dot{\gamma}=0.49$ s^{-1}.: Parameters are U=4, $D_r=0.0064$, ckT=6030, and A=0. Shear rate is 0.49 s^{-1}. Theory given by lines and data by symbols.

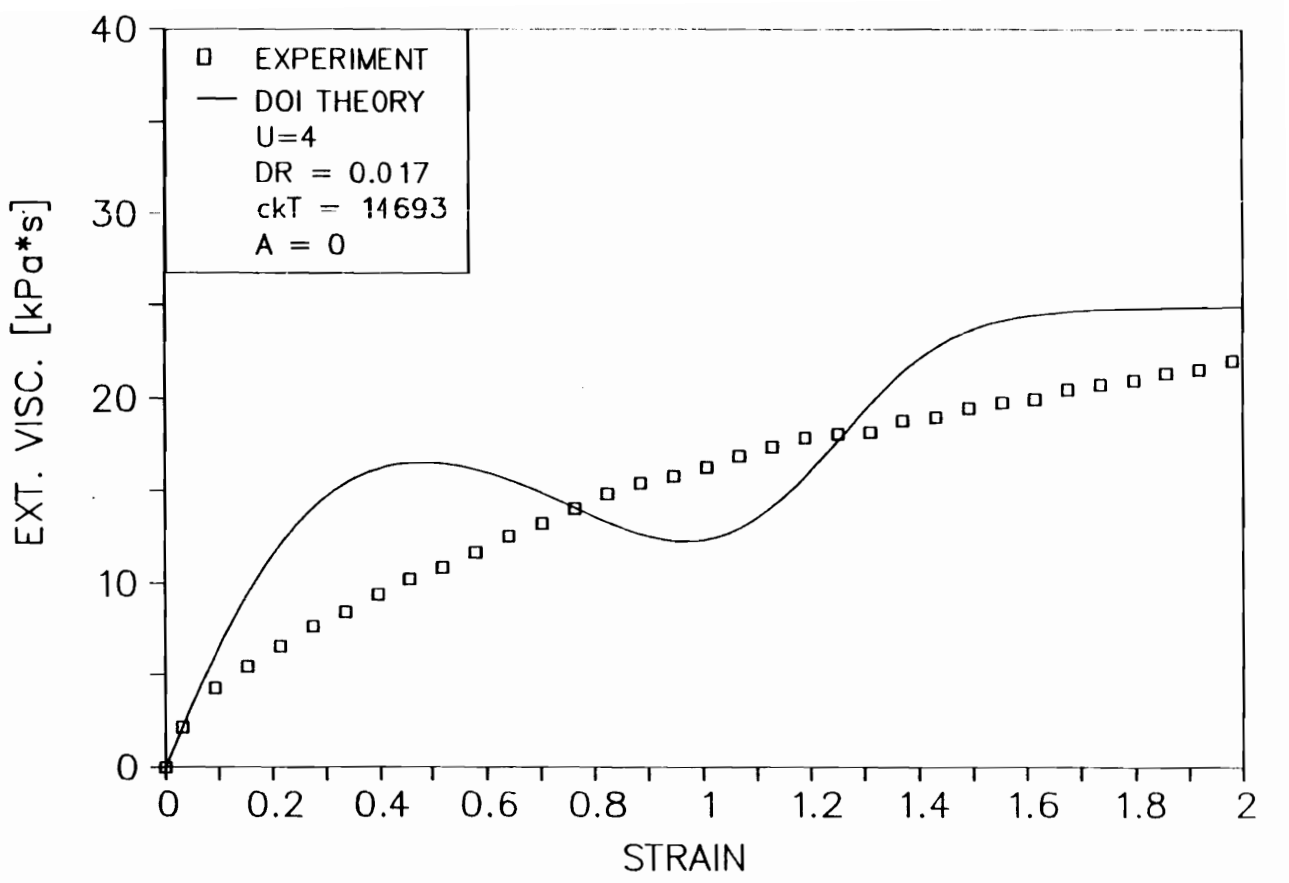

Figure 103. Elongational viscosity growth prediction for anisotropic HPC EF melt. using multidomain averages.: Parameters are U=4, D_r=0.17, ckT=14960, and A=0. $\dot{\varepsilon}$=0.49 s^{-1}. Theory given by lines and data by symbols.

shear viscosity behavior of the liquid crystalline melts could also be modelled semi-quantitatively while no evaluation was possible for the prediction of the steady first normal stress difference. The Doi theory was shown to be able to qualitatively model the transient shear stress behavior of the LCPs when a multidomain average was used to simulate the initial condition of a globally unoriented melt. While no evaluation could be made of the ability of the Doi theory to model the steady elongational flow behavior of the LCPs, the predictions of the theory were consistent with the experimental transient elongational flow behavior of the LCPs. Also, the Doi theory was found to be capable of qualitativlly modelling the transient elongational flow behavior of the TLCPs only at very short times, with no improvement obtained through the use of a multidomain average. At the same time it is thought that some improvement could be obtained through the use of a much larger number of domains. Finally it was found that the elongational flow behavior of the LCPs could not be predicted by the Doi theory with parameters determined solely from shear flow.

5.3 Discussion of Doi Theory

In choosing a constitutive equation for the modelling of a polymeric system a primary question is whether the equations effectively describe the physics governing the behavior of the system. In the work just presented, two primary questions are whether the Doi theory describes: (1) the steady flow behavior and structure of LCPs and (2) the transient flow behavior and evolution of structure in LCPs. The discussion to follow focuses mainly on these two questions.

The steady flow predictions of the Doi theory are considered first. The Doi theory, with parameters determined from their theoretical relations, was shown to be incapable of predicting the steady flow behavior of the LCP systems investigated. This discrepancy could be

indicative that the Doi theory is based on a physically incorrect model, that there is error in the determination of the adjustable parameters, or both. Each of these is discussed next.

The Doi theory is based on the model of a system of rod-like molecules existing in a homogeneous phase. During steady flow, the director is predicted to take on a fixed orientation, which depends on the type of deformation and rate (It should be noted that recent work by Marrucci [217] and Larson [218] predict director tumbling at low rates and for large intermolecular interactions). This compares to the observations presented in section 2.2 of the literature review, where it was shown that at low deformation rates there is still a polydomain texture present in the material [34,109,140,141], which is eventually broken up under flow to form a highly oriented monodomain texture at high rates (it should be noted that the existence of a polydomain texture during steady elongational flow has not been shown). At the same time the exact structure of LCPs under flow conditions has been well characterized at low rates and it is possible that the domains merely float is a nematic matrix which could be described by the Doi equations. In any case, until such knowledge is available the physical basis for the use of the Doi theory to model the flow behavior of LCPs at low rates remains uncertain.

Next, the possibility of error in the calculation of the adjustable parameters is considered. In the calculation of the parameters (U, D_r, ckT, and A) there is uncertainty in many of the constants and molecular parameters (see Appendix C). The constants ν_1 and ν_2 appear in the theoretical relations and basically represent fudge factors. Neither one is known precisely and experimental values of ν_1, have been found to vary from 10^3 to 10^4 [182], introducing an order of magnitude uncertainty in the calculations where it is used. Other constants or molecular quantities which carry significant uncertainty are $\overline{M}_N$, the length of the molecules (L), the diameter of the molecules (d), and the composition of the material. Also, the assumption that the molecules have a rod-like conformation is likely in error and the aspect of polydispersity further complicates the issue. Therefore, it appears that the adjustable parameters calculated from the theoretical relations carry with them great uncertainty.

It was shown that errors are possible in both the physical basis for the Doi theory and in the determination of the parameters. Some insight into which one causes the discrepancy between the Doi predictions and experimental behavior can be obtained by considering the results for the case where the parameters where experimentally fit to the data. It was shown that the Doi theory could predict the experimental steady and dynamic shear viscosity behavior of the LCPs investigated when the parameters were fit to the data. While no evaluation was possible for the steady first normal stress difference and the steady elongational viscosity predictions, the predictions were not inconsistent with the experimental behavior observed in other LCP systems. While it was shown here that no negative values of N1 were predicted by the Doi theory, as were observed for the HBA/HNA system at low rates, Marrucci [217] and Larson [218] have shown that they can be predicted when the decoupling approximation (equation 2.3.12) is replaced by a more accurate expression. The discrepancies between the predictions of the Doi theory and the experimental of the LCPs under investigation for steady flows then appears to be due mainly to errors in the parameters.

Before going to the transient flow predictions, the addition of the rod-solvent interaction term to the stress tensor should be considered. Since the systems under investigation were thermotropic, and thus had no solvent, the question arises as to whether there is a physical basis for the term. Such a basis can be found after examination of its derivation from the kinematic equation for rod-like molecules in dilute solution [219]. While Doraiswamy and Metzner [186] attribute the term to rod-solvent friction, the term was originally derived to account for all hydrodynamic drag acting on the polymer molecules as a result of flow. In the bulk material then, the term accounts for forms of rod-rod friction resulting from the macroscopic flow field and heretofore unaccounted for.

One such interaction unaccounted for previously in the Doi theory was friction due to translational motion of the rod-like molecules. In Doi's derivation [39], the movement of the rod-like molecules is restricted mainly by the restrictions to rotational motion from neighboring molecules and other types of restrictions are then neglected in comparison. However, as the orientation distribution of the molecules sharpens, as would occur at high flow rates, the

restriction to rotational motion decreases more and more. The flow of the material is expected to occur more and more by the motion of rods past one another than by the reptation type motion proposed by Doi [39]. As rate increases, the force associated with rod-rod friction should then become increasingly significant in comparison to the forces arising from rod-rod impingement. Eventually, the rod-rod friction forces will be the predominant contributions to the stress tensor and are likely to be the ones represented by the so-called rod-solvent term.

One limitation to the term representing rod-rod friction should be noted. Even with the term, the Doi theory is still unable to vary the predicted slope of the shear viscosity versus shear rate curve at high rates (i.e. in the power-law region). At the same time the slope of the shear viscosity curve in the power-law region has been observed to vary for different LCP systems with typical values in the range -0.3 to -0.7 [18]. Modifications to the term to allow for variations in the power-law slope have not been made and none are apparent at this time. Therefore, the ability of the Doi theory to model the steady flow behavior of some LCP systems appears to be limited in this respect.

At this point the use of the proposed averaging scheme for the modelling of the transient flow behavior of multidomain systems is considered. In using the model proposed here a number of simplifying assumptions were used. The Voigt average used to calculate the stress tensor relies upon two assumptions which could be in error. These are that the individual domains are each subjected to the same deformation field and that the effects of interdomain interactions, such as the effect due to Frank elasticity [220], are negligible. In a real LCP system, it is unlikely that the domains will each be subjected to a similar deformation field unless the size scale of the liquid crystal domains is similar to that of the test dimensions and, which is not the case since domain size scales are usually on the order of microns in size [4,7]. The system is then more likely to be described by a Reuss type average [209], where elements are in series and subjected to a constant stress state but with varying local deformation rates. The calculations made with a Voigt average then would be expected to overpredict the stress overshoot upon inception of flow. It is then encouraging that this was actually observed as

was shown in Figure 102, but also indicates that a better averaging method for the stress tensor could be found.

The assumption that interdomain interactions can be neglected is considered next. Such interactions have been associated with Frank elasticity [220] arising from bend, twist, and splay defects. According to Marrucci [220], the stress associated with such defects can be estimated from the formula:

$$\sigma = \frac{K}{A^2} \tag{5.2.1}$$

where K is an average Frank distortion modulus and A is the radius of curvature of the local director. An order of magnitude estimation of this stress can be easily calculated. For low molecular weight liquid crystals, K is on the order of 10^{-12} Pa [217]. Additionally, from the optical micrographs shown in section 4.4, the domain size can be estimated to be of the order of 2 μm, giving a value of A of 1 μm. The resulting stress associated with Frank elasticity in the equilibrium material is then approximately 1 Pa. While this is negligible compared to the viscous stress in the materials investigated, it should be noted that there is considerable uncertainty in the domain size of LCPs during flow and that the size of the domain can be reduced by flow [221]. Any significant decrease in the value of A would make such elastic stresses significant at low flow rates. Therefore, further consideration of this feature of LCPs is warranted.

In order to determine whether Frank elasticity is important in the transient flow behavior, some very recent work by Burghardt and Fuller [222] and by Larson and Doi [223] on the predictions of transient flow properties is considered. In the work of Burghardt and Fuller [222] the predictions of the Leslie-Ericksen theory were examined for the case where the director is allowed to tumble. They considered of shear flow between two plates, with one plate stationary and one plate moving. Upon the inception of steady shear flow, multiple overshoot peaks were predicted in the shear stress and they were predicted to occur at strain values which were independent of shear rate. The overshoot peaks were found to result from the

viscous forces acting on the director instead of the elastic forces associated with the defect structure of the material. Additionally, calculations were made for the case where no tumbling of domains occurred and it was again found that the initial overshoot peak occurred at a constant strain. The predictions of the model for strain recovery were also examined and it was also found that the recovery time scaled with the prior shear rate. Again, it was indicated that the elastic stresses associated with the polydomain texture of the materials had no influence on the recovery behavior [222].

In other very recent work Larson and Doi [223] have proposed a model to predict the behavior of a multidomain LCP system. The the Leslie-Ericksen theory was used to model each individual domain and the stress tensor was calculated by averaging the stress over all possible domain orientations in a manner which is effectively the same as the Voigt average used here. However, differences exist in the two models since that of Larson and Doi [223] includes the effect of Frank elasticity and their model also assumes that the molecules within any one domain are perfectly aligned. Additionally, the term for Frank elasticity enables the prediction of changes in domain size during flow. In their predictions of shear stress growth upon the inception of flow, stress oscillations are again observed and they are found to occur at a constant strain, independent of shear rate. The shear stress oscillations were found to result from the tumbling of domains, in agreement with the work of Burghardt and Fuller [222]. However, in this work Frank elasticity is shown to be necessary for the damping of these oscillations. Also, it is indicated that Frank elasticity might be the driving force for strain recovery through its indirect influence on the viscous stress. According to the work work of Larson and Doi [223] then, the elastic forces describing interdomain interactions are an important feature of LCPs.

From the discussion of the work above, it becomes apparent that Frank elasticity is not responsible for the scaling of shear stress with strain during transient testing. In fact, from the work discussed above it seems that they mainly act as an effective diffusivity. Since director tumbling is not possible in the equations used with the multidomain proposed in this work

such dissipative effects might not be necessary. It then appears that as a first approximation, the assumption of that interdomain interactions are negligible is valid.

Finally, some weaknesses of the multidomain model proposed weakness of the multidomain model proposed here should be discussed. While a polydomain system can be modelled for transient flow from the rest state, the model predicts that a monodomain texture is achieved at steady state flow and this might not be correct. Additionally there is no provision in the model for the recovery of an unoriented texture in the system following the cessation of flow. Upon the cessation of flow relaxation is driven only by the recovery of the orientation distribution to its equilibrium value and the director orientation remains unchanged. Therefore, the Doi theory, used with the proposed multidomain model, might not adequately describe the physical state of the material under some transient flow situations. The use of the proposed multidomain averaging scheme for the modelling of transient flow might only be useful for the modelling of fluids initially at rest.

6.0 Conclusions and Recommendations

An investigation of the transient flow behavior of several thermotropic liquid crystalline polymers has been conducted. First, the state of the materials at the test conditions was studied by a number of test methods. Next, the transient shear and elongational flow behavior of the TLCPs were determined in order to establish whether the behavior of LCP systems is fundamentally different from that for polymer systems which display an isotropic state at equilibrium. These results were then used to establish whether the Doi theory, in its original or modified form, can be used to either predict or model the shear and elongational flow behavior of LCPs. The following conclusions and recommendations are made pertaining to this work.

6.1 Conclusions

6.1.1 State of Materials

1. The combination of several test techniques including dynamic shear tests, DSC, WAXS, and optical microscopy has provided valuable insight into the nature of the materials investigated (in transient flow tests), indicating whether the materials are purely liquid crystalline or whether they might contain other phases such as isotropic melt or residual crystallinity. The test methods listed above were used to characterize thermal transitions and the physical state of the materials. Some conclusions on the nature of the melts at the temperatures used for transient flow testing are:

2. The HPC EF melt at 190 °C and HPC G melt at 200 °C exist in a complex multiphase state. This state consists mainly of an anisotropic phase, but also contains both an isotropic phase and a small amount of residual crystallites. Evidence for the anisotropic nature of the melt comes from birefringence observed by means of optical microscopy, shear thinning dynamic viscosity over the range of 0.1 to 100 rad/s, and a minimum in the viscosity versus temperature curve. Evidence for the existence of some isotropic phase comes from DSC measurements and from the viscosity versus temperature curve, where it is seen that the slope is positive at 190 °C, indicating a 2 phase region. Also, the WAXS patterns of HPC EF annealed at 190 are somewhat more diffuse than would be expected for a purely anisotropic material. Finally, evidence for the existence of residual crystallinity comes from WAXS patterns and the observation that G′ is higher than G″ at low frequencies in a frequency sweep test. This indicates elasticity resulting from residual crystallinity. Analogous results were seen for the HPC G material at 200 °C.

3. The HPC EF melt at 210 °C and the HPC G melt at 240 °C exist in an isotropic state with the possibility that minute amounts of residual crystallinity are present. Evidence for the

isotropic nature of the material comes from the observation of zero birefringence by optical microscopy, the appearance of a zero shear viscosity as indicated in a frequency sweep test, and values of tanδ much higher than those for the same materials in the liquid crystal state. Additionally, the position of the viscosity is the viscosity versus temperature curve indicates an isotropic melt state. The lack of solid evidence for residual crystallinity for HPC EF comes from the observation that the dependence of G′ on ω increases as ω decreases, showing lack of an elastic structure. Also, WAXS and optical microscopy show no solid evidence of residual crystallinity. At the same time, for the case of HPC EF the temperature is less than T_m^0, the equilibrium melting temperature of the material, and thus residual crystallinity can't be ruled out.

4. The HBA/HNA melts at 301 and 320 °C exist in a nematic liquid crystalline state with a small but stable amount of residual crystallinity present. In relative terms, the amount of residual crystallinity in the melt at 320 °C is less than at 300 °C. A comparison of G′ and G″ at low frequencies indicates some elasticity in the material at a level which is too large to be due to the domain texture. A negative normal force was measured at low shear rates and this has previously been seen to correspond to the existence of residual crystallinity in other copolyesters containing HBA. At the same time it has been shown in previous work that residual crystallinity can exist up to 320 °C and T_m^0 for HBA/HNA has been reported to be 372 °C. From thermodynamic arguments the amount of residual crystallinity at 320 °C would be lower than at 301 °C.

6.1.2 Transient Shear Flow Behavior

1. While much of the transient shear flow behavior of the LCPs investigated is similar to that for isotropic melts of both flexible-chain polymers and rodlike polymers, the observation that the magnitude of the reduced stress is independent of deformation rate at low rates appears to be unique to liquid crystalline systems. While stress overshoot upon the inception of

shear flow has been observed to occur at constant strain values in flexible-chain polymer melts, the magnitude of the overshoot peak is found to be rate dependent. Behavior similar to that of flexible-chain materials was also found for the isotropic HPC EF melt. On the other hand, all of these materials show relaxation behavior in which the rate of relaxation increases with prior shear rate.

2. Many of the features of the transient flow behavior determined for the LCPs investigated appear to be general for all LCP systems. At the same time, the occurrence of negative first normal stress differences is not a general feature of LCPs and this, coupled with the presence of residual crystallinity, indicates that the transient shear flow behavior determined for these materials might representative of the liquid crystalline state of the materials. In the transient shear stress growth/relaxation experiments some features were commonly seen in all of the materials for temperatures where they were known to be in an anisotropic state. These features include large stress overshoots on the inception of steady shear (larger than would be expected for an isotropic material), the overshoot peak occurring at a relatively constant value of strain of about 2, and stress relaxation which occurs faster as prior shear rate increases. These observations have been seen in many other LCPs too. However, in HBA/HNA at 301 and 320 °C, a negative first normal stress difference was measured at rates below approximately 0.5 s^{-1}. This behavior is not believed to be common for LCPs but is sometimes seen in systems which contain both liquid crystal and solid phase (residual crystallinity or insoluble polymer). Also, the presence of residual crystallinity in the HBA/HNA and HPC systems raises questions about the generality of their behavior.

6.1.3 Elongational Flow Behavior

1. A rotary clamp type rheometer has been constructed which is capable of of quantitatively measuring the extensional stress growth behavior of polymeric melts with viscosities in the range 10^3 to 10^7 Pa*s when used in a single rotary clamp and fixed end mode.

A rotary clamp type rheometer was built based on the designs of Meissner, Laun, and Munstedt. The utility of the rheometer was determined by running extensional stress growth tests on NTA 101 (LLDPE) at 170 °C. The results were compared to results from tests conducted on a Rheometrics Extensional Rheometer at rates from 0.02 to 0.2 s^{-1}, with good to excellent agreement seen at all rates and for Hencky strains up to 2. The results also quantitatively agreed with $3\eta^+(\dot{\gamma} = 0.02)$, which has been previously reported for LLDPE at low rates.

2. The extensional viscosity growth behavior of two thermotropic LCPs has been determined under isothermal conditions. While some differences are seen in the behavior of the TLCPs from the behavior known for flexible-chain polymers, there is no evidence that the behavior is fundamentally different.

A. The extensional viscosity growth function ($\bar{\eta}_e^+(t, \varepsilon)$) of TLCPs, which are thought to be uninfluenced by the presence of residual crystallinity, seems to follow the value of three time the shear viscosity growth function ($3\eta^+(t, \dot{\gamma})$) at small strain values as is typically seen for isotropic flexible-chain polymer melts.

B. For the case of TLCPs which show evidence of residual crystallinity, the value of $\bar{\eta}_e^+(t, \dot{\varepsilon})$ deviates positively from the value of $3\eta^+(t, \dot{\gamma})$ as strain is increased, starting either at very low strains or in some cases, throughout the entire strain range. This contrasts with the behavior of isotropic flexible-chain melts, where $\bar{\eta}_e^+(t, \dot{\varepsilon}) = 3\eta_0^+(t)$ at low strains regardless of rate. Differences in behavior therefore cannot be attributed unequivocally to the liquid crystalline state of the TLCPs.

C. TLCPs, whether purely liquid crystalline or multiphase, always show a positive deviation of $\bar{\eta}_e^+(t, \dot{\varepsilon})$ from $3\eta^+(t, \dot{\gamma})$ at low strains, regardless of extension rate. This strain at which a positive deviation or "strain hardening" effect is seen is typically on the order of 0.1 to 0.5, which is lower than the the strain at which strain hardening has been seen to occur in flexible-chain polymer melts such as LDPE. As above, this might be partially due to the presence of residual crystallinity.

D. No evidence was found for the existence of a steady state elongational viscosity in the TLCPs investigated (possibly because of limited levels of strain achieved in the tests). At the same time isotropic flexible-chain polymer melts are generally acknowledged to exhibit a steady state extensional viscosity at low enough strain rates.

E. When the values of $\bar{\eta}_{\bullet}^{+}(t, \dot{\varepsilon})$, measured at different rates, are compared at the same strain the function $\bar{\eta}_{\bullet}^{+}(t, \dot{\varepsilon})$ is seen to be rate thinning over the entire range of rate and strain investigated for the TLCPs. Such "strain rate thinning" behavior is predicted for a linearly viscoelastic material at low strains but not at steady state. Behavior similar to that described above for the LCPs has been observed in flexible-chain polymers which strain harden within a certain range of extension rates.

3. The extensional viscosity growth behavior of LCPs appears to be attributable not only to their rigid chain conformations, but also to their anisotropic nature and/or polydomain texture. The extensional viscosity growth behavior of the HPC EF material was determined in both the anisotropic and isotropic melt states. The shapes of the $\bar{\eta}_{\bullet}^{+}(t, \dot{\varepsilon})$ curves for the HPC in the two different states were markedly different. While the anisotropic HPC EF melt showed behavior similar to the HBA/HNA copolyester (liquid crystal), the isotropic HPC EF melt showed behavior somewhat similar to that for a material such as LDPE. The anisotropic HPC EF melt showed deviation of $\bar{\eta}_{\bullet}^{+}(t, \dot{\varepsilon})$ from $3\eta^{+}(t, \dot{\gamma})$ at lower strains than the isotropic melt. Additionally the anisotropic HPC EF melt showed no constant extensional viscosity value while the isotropic HPC EF melt showed a plateau in the $\bar{\eta}_{\bullet}^{+}(t, \dot{\varepsilon})$ versus time curve which corresponded to the relation $\bar{\eta}_{\bullet}^{+}(t, \dot{\varepsilon}) = 3\eta^{+}(t, \dot{\gamma})$ However, the generality of this conclusion is uncertain because of the possible influence of residual crystallinity on the results.

6.4 Morphology of Drawn Films

1 A high degree of molecular orientation can be obtained in TLCPs having undergone uniaxial elongation and having Hencky strains as low as 1.6. The degree of molecular orientatation increases with increasing extensional strain. Wide angle x-ray scattering (WAXS) patterns of both HBA/HNA and 60HBA/PET drawn films, with Hencky strains in the range of 1.6 to 4.7 (draw ratios from 5 to 110) show a high degree of molecular orientation at the lower strain values and an increase in molecular orientation with increasing strain.

2 The liquid crystalline domains become elongated during uniaxial extensional deformation and the degree of elongation, i.e. geometric aspect ratio, increases with increasing extensional strain. Scanning electron microscopy (SEM), polarized optical microscopy (POM), and small angle light scattering (SALS) were used to probe the structure of the HBA/HNA and 60HBA/PET drawn films. The combination of the three techniques gave clear evidence that the supermolecular structures present in the LCPs became highly elongated during uniaxial extensional flow and the aspect ratio of the domains increased with increasing extensional strain.

3. The technique of small-angle light scattering shows promise for use in following the geometric changes occurring in the domain structure of LCPs resulting from flow. A good correlation was seen between changes in the anisotropy of SALS patterns taken of drawn LCP films and changes in the anisotropy of the microstructure of the films as determined by optical microscopy and SEM.

6.1.5 Doi Theory

1. The Doi theory, in both the original and modified form, is unable to predict the shear and elongational flow behavior of either the isotropic or anisotropic HPC EF material when parameters are determined from the theoretical relations.

2. The Doi theory, with the retention of the rod-solvent interaction term in the stress tensor, is able to semi-quantitatively model the steady shear viscosity and qualitatively model the transient shear viscosity behavior of the isotropic HPC EF melt when the adjustable parameters are fit to experimental data.

3.The Doi theory can predict the steady state first normal stress difference of the isotropic HPC EF melt (within the limited range investigated) with parameters determined from steady shear viscosity data.

4. The Doi theory was not able to predict or model the transient elongational flow behavior of the HPC EF melt. This also implies that the Doi theory is unable to predict the elongational flow behavior of isotropic HPC EF melts when adjustable parameters are determined from shear flow data.

5. The Doi theory, with the retention of a rod-solvent interaction term in the stress tensor, can semi-quantitatively model the steady shear viscosity behavior of the anisotropic HPC EF melt and HBA/HNA melts when parameters are fit using experimental data.

6. The Doi theory can qualitatively predict the transient shear stress growth behavior of liquid crystalline polymers when both the multidomain averaging of the stress tensor and parameters, fit to steady shear viscosity data, are used. The use of a multidomain average in the calculation of the stress tensor was seen to tremendously improve the theoretical predictions. With the use of a multidomain average, the theory predicted the correct strain at which the overshoot peak occurred. While the magnitude of the overshoot peak was not correct, it was shown that this could be at least partially explained as being due to the use of the Voigt average.

7. The Doi theory cannot predict the elongational flow behavior of liquid crystalline polymers when the adjustable parameters are determined only from shear flow data. Several equivalent sets of parameters were found to be capable of describing the steady shear flow behavior of the LCP melts. Since the Trouton ratio ($\bar{\eta}_{\bullet}(\dot{\varepsilon})/\eta(\dot{\gamma})$) of the material at low rates is fixed by the value of U, the correct value of U for a thermotropic system can only be determined once the Trouton ratio is known, requiring experimental values of the elongational viscosity.

8. The Doi theory was unable to even qualitatively model the elongational viscosity growth behavior of the liquid crystalline polymers investigated. While some qualitative agreement was found for the predictions of the theory when certain initial conditions were used, predictions arrived at through the use of a realistic initial condition (i.e. the multidomain average) did not even show qualitative agreement with the $\bar{\eta}_{\bullet}^{+}(t, \dot{\varepsilon})$ behavior determined experimentally.

6.2 Recommendations

Although some questions about the behavior of the liquid crystalline polymers studied have been answered, certain questions specific to these materials and to all liquid crystalline polymers remain. Recommendations are given below for further work in this area.

1. Examine the HPC EF material with solid state NMR at elevated temperatures in order to better establish the state of the material. The HPC materials are known to exist in a complex state at the temperatures used for rheological measurements. At 190 °C HPC EF was found to consist of anisotropic melt, isotropic melt, and residual crystallinity. However, no quantitative value was placed on the relative amounts of material in the different phases and there is still some uncertainty about the mesophase type exhibited by HPC.

2. Examine the transient shear flow behavior of other liquid crystalline materials in order to establish what behavior is characteristic of the liquid crystalline state, especially in regard to the N1 behavior. Relatively little work has been reported on the transient flow behavior of LCPs. Additionally, the materials investigated in these studies have often been complex or multiphase systems and might not display behavior characteristic of a pure liquid crystalline state. Work should therefore focus on systems known to exhibit a specific mesophase type and free of residual crystallinity or isotropic material.

3. Further modify the ER to increase its sensitivity and thus increase the number of LCPs which can be investigated. By pursuing other leaf spring designs and working with the fixed end configuration of the ER, it should be possible to increase the force sensitivity. Doing so might permit the study of lower viscosity LCP systems or increase the range of Hencky strain over which force measurement is possible. Some additional increase in the range of force resolution could also be achieved through the use of a better data acquisition system.

4. Examine the transient elongational flow behavior of other TLCPs in the ER. Again, TLCPs should be chosen which are known to exhibit a purely liquid crystalline state (free of residual crystallinity!). A number of semi-flexible thermotropic copolyesters have recently been produced which would be ideal for this purpose, especially since they have low nematic-isotropic transitions and could be studied in both states. At the same time none have been available in sufficient quantity to test in the ER to date.

5. Rheo-optical studies should be carried out on LCPs subjected to steady shear flow in order to determine the effect of flow on the domain size and also to answer the question of whether there is tumbling of domains during flow. The effect of shear flow on domain size at low shear rates is still not well known and a knowledge of this would be valuable for the modelling of the flow behavior. At the same time, a knowledge of whether domains tumble during flow would provide an additional criteria for the evaluation of constitutive models for LCPs.

6. Studies should be made to determine what types of structural changes take place in LCPs during transient shear and elongational flows. While some structural studies have been

carried out on LCPs during shear flow, there is still some uncertainty as to evolution of structure on the startup and cessation of flow. In the case of elongational flow, it is still uncertain whether an oriented microstructure can be obtained during isothermal flow or whether it is necessary to elongate the material while it cools. Also, the question of whether a certain level of stress is necessary to break up the domain structure has not been completely answered and such results would provide additional evidence for settling this issue.

7. Further work should be carried out in evaluating the predictions of the Doi theory using a larger number of domains for the Voigt average and also other domain averaging schemes should be tried. The Doi theory was found to be able to qualitatively predict the transient shear stress growth behavior of the TLCPs when a multidomain average was used. However, only a small number of domains were used and they did not represent very well a continuum of initial orientations. The work should also be extended to other shear rates in order to determine whether the scaling relations observed in some LCPs can be predicted by the theory. This should be the case as indicated by the work of Burghardt and Fuller [223] and Larson and Doi [224], but it has yet to be confirmed.

8. The effect of molecular polydispersity on the predictions of the Doi theory should be carried out for both steady and transient flows. This modification to the Doi theory is warranted since the industrially important LCP systems most studied to date are polydisperse and this should effectively increase the number of relaxation times possible for the system. Also, in previous studies on the elongational flow behavior of flexible-chain polymer systems it was shown that a small amount ($\simeq$ 1% by weight) of high molecular weight material can significantly effect the material behavior.

References

1. Chung, T. S., **Polym. Eng. Sci.**, 26, 901, 1986.
2. Chiou, J. S., and Paul, D. R., **J. Pol. Sci., Part B: Pol. Phys.**, 25, 1699, 1987.
3. Brostow, W., Dziemianowicz, T. S., Romanski, J. and Werber, W., **Polym. Eng. Sci.**, 28(12), 785, 1988.
4. DeGennes, P. G., "The Physics of Liquid Crystals," Oxford University Press (Clarendon), London and New York, 1974.
5. Miesowicz, M., **Nature**, 158, 27, 1946.
6. Reinitzer, F., **Monatsheft fur Chemie**, Vol. 9, 421, 1888.
7. Calundann, G. W. and Jaffe, M., Proc. Robert A. Welch Found. Conf. Chem. Res., Res. Conf. XXVI, Synthetic Polymers, 1982.
8. Viola, G. G, PhD Dissertation, Virginia Polytechnic Institute and State University, Blacksburg, VA, 1985.
9. Luckhurst, G. R. and Gray, G. W., "The Molecular Physics of Liquid Crystals," Academic Press, London, 1979.
10. Flory, P. J., **Proc. R. Soc. London, Ser. A.**, 234, 73, 1956.
11. Ober, Ch. K., Jin, J. I. and Lenz, R. W., **Advances in Pol. Sci.**, 59, 103, 1984.
12. Noel, C., **Makromol. Chem. Makromol. Symp.**, 22, 95, 1988.
13. Asada, T., Onogi, S. and Yanase, H., **Pol. Eng. Sci.**, 24(5), 355, 1984.
14. Oster, G., **J. Gen. Physiololgy**, 33, 445, 1950.
15. Aoki, H, White, J. L., and Fellers, J. F., **J. Appl. Pol. Sci.**, 23, 2293, 1979.
16. Bouligand, Y, Cladis, P. E., Liebert, L and Strzelecki, L., **Mol. Cryst. Liq. Cryst.**, 25, 233, 1974.
17. Onogi, S. and Asada, T., "Rheology", Vol. 1, G. Astarita, G. Marrucci, and L. Nicolais, eds., Plenum Press, New York, 1980.
18. Wissbrun, K. F., **J. Rheol.**, 25(6), 619, 1981.
19. Mishra, R. K., **Mol. Cryst. Liq. Cryst.**, 29, 201, 1975.
20. Done, D. D., PhD Dissertation, Virginia Polytechnic Institute and State University, Blacksburg, VA, 1987.
21. Kwolek, S. L., Mogan, P. W., Schaefgen, J. R., and Gulrich, L. W., **Macromolecules**, 10, 1390, 1977.
22. Troughton, M. J., Unwin, A. P., Davies, G. R. and Ward, I. M., **Polymer**, 29, 1389, 1988.
23. Zachariades, A. E. and Kanamoto, T., in "High Modulus Polymers Approaches to Design and Development," ed. by A. E. Zachariades and R. S. Porter, Marcel Dekker, Inc., New York and Basel, 1988.
24. Cogswell, F. N., in "Recent Advances in Liquid Crystal Polymers", ed. by L. L. Chapoy, Elsevier, London, 1985.
25. Ophir, Z. and Ide, Y., **Pol. Eng. Sci.**, 23(14), 792, 1983.
26. Jackson, W. J. Jr. and Kuhfuss, H. F., **J. Pol. Sci. Pol. Chem. Ed.**, 14, 2043, 1976.
27. Ide, Y. and Ophir, Z., **Pol. Eng. Sci.**, 23(5), 261, 1983.
28. Viola, G. G., Baird, D. G. and Wilkes, G. L., **Pol. Eng. Sci.**, 25(14), 888, 1985.
29. Done, D. and Baird, D. G., **Pol. Eng. Sci.**, 27(11), 816, 1987.

30. Lewis, D. N. and Fellers, J. F., PATRA Report No. 233, April, 1986.
31. Blizard, K. G., PhD Dissertation, Virginia Polytechnic Institute and State University, 1987.
32. Blizard, K. G, Wilson, T. S. and Baird, D. G., **Int. Pol. Proc.**, 5, 53, 1990.
33. Baird, D. G., in "Liquid Crystalline Order in Polymers," A. Blumstein ed., Academic Press, 1978.
34. Onogi, Y., White, J. L., and Fellers, J. F., **J. Non Newt. Fl. Mech.**, 7, 121, 1980.
35. Erickson, J. L., "The Mechanics of Viscoelastic Fluids," Ed. by R. S. Rivlin, (AMD Vol. 22), ASME, New York, 1977.
36. Leslie, F. M., Advances in Liquid Crystals, Vol. 4, Ed. by G. H. Brown, Academic Press, New York, 1979.
37. Duffy, B. R., **J. Non. Newt. Fl. Mech.**, 4, 177, 1978.
38. Hand, G. L., **J. Fluid Mech.**, 13, 33, 1962.
39. Doi, M., **J. Pol. Sci. Pol. Phys. Ed.**, 19,229, 1981.
40. Meissner, J., Raible, T. and Stephenson, S. E., **J. Rheol.**, 25(1), 1, 1981.
41. Laun, H. M. and Müntedt, H., **Rheol. Acta**, 26, 208, 1976.
42. Metzner, A. B. and Prilutski, G. M., **J. Rheol.**, 30(3), 661, 1986.
43. Porter, R. S. and Johnson, J. F., "Rheology," Erich ed., vol. 4, Ch. 5, Academic Press, New York, 1967.
44. Baird, D. G., in "Polymeric Liquid Crystals," A. Blumstein ed., Plenum Press, New York, 1985.
45. Prilutski, G. M., Ph.D. Dissertation, University of Delaware, 1984.
46. Marrucci, **Pure & Appl. Chem.**, 57(11), 1545, 1985.
47. Fukada, E., and Date, M., **Biorheology**, 1, 101, 1963.
48. Marchessault, R. H., Moorehead, F. F. and Walters, N. M., **Nature**, 184, 632, 1959.
49. Hermans, J. Jr., **J. Polym. Sci., Part C2**, 129, 1963.
50. Baird, D. G., **J. Appl. Pol. Sci.**, 13, 755, 1978.
51. Baird, D. G. and Ballman, R. L., **J. Rheol.**, 23(4), 505, 1979.
52. Papkov, S. P., Kulichikhin, V. G., Kalmykova, V. D. and Malkin, A. Y., **J. Polym. Sci. Polym. Phys. Ed.**, 12, 1753, 1974.
53. Kiss, G. and Porter, R. S., **J. Polym. Sci.: Polym. Symp.**, 65, 193, 1978.
54. Mewis, J. and Moldenaers, P., **Chem. Eng. Commun.**, 53, 33, 1987.
55. Yanase, H. and Asada, T., **Mol. Cryst. Liq. Cryst.**, 153, 281, 1987.
56. Elliot, H. H., **J. Appl. Pol. Sci.**, 13, 755, 1969.
57. Shimamura, K., White, J. L. and Fellers, J. F., **J. Appl. Pol. Sci.**, 26, 2165, 1981.
58. Suto, S., White, J. L., and Fellers, J. F., **Rheol. Acta**, 21, 62, 1982.
59. Sugiyama, H., Lewis, D. N., White, J. L., and Fellers, J. F., **J. Appl. Pol. Sci.**, 30, 2329, 1985.
60. Gotsis, A. D. and Baird, D. G., **J. Rheol.**, 29(5), 539, 1985.
61. Kulichikhin, V. G., Kudryavtsev, G. I., and Papkov, S. P., **Intern. J. Polymeric Mater.**, 9, 239, 1982.
62. Baird, D. G., **J. Rheol.**, 24(4), 465, 1980.
63. Aharoni, S. M., **Polymer**, 21, 1413, 1980.
64. Bahar, I. and Erman, B., **J. Pol. Sci.: Part B: Pol. Phys.**, 24, 1361, 1986.
65. Flory, P. J. and Ronca, G., **Mol. Cryst. Liq. Cryst.**, 54, 289, 1979.
66. Kiss, G., **J. Rheol.**, 30(3), 585, 1986.
67. Wissbrun, K. F. and Griffin, A. C., **J. Polym. Sci.: Polym. Phys. Ed.**, 20, 1835, 1982.
68. Acierno, D. La Mantia, F. P., Polizzotti, G., Ciferri, A., Krigbaum, W. R. and Kotek, R., **J. Pol. Sci. Pol. Phys. Ed.**, 21, 2027, 1983.
69. Blumstein, A., Thomas, O. and Kumar, S., **J. Pol. Sci. Pol. Phys. Ed.**, 24, 27, 1986.
70. Tuttle, J. R., Bartony, H. E., and Lenz, R. W., **Polym. Eng. Sci.**, 27(15), 1156, 1987.
71. Bickel, A., Shaw, M. T., and Samulski, E. T., **J. Rheol.**, 28, 647, 1984.
72. Bird, R. B., Armstrong, R. C., Hassager, O., "Dynamics of Polymeric Liquids," Vol. 1, John Wiley Pub., New York, 1977. Vol. 1, 2nd ed., 1987.
73. Yang, J. T., **J. Am. Chem. Soc.**, 80, 1783, 1958.
74. Yang, J. T., **J. Am. Chem. Soc.**, 81, 3902, 1959.
75. Wong, C. P. and Berry, G. C., **Polymer**, 20, 229, 1979.
76. Jerman, R. and Baird, D. G., **J. Rheol.**, 25(2), 275, 1981.

77. Jackson, W. J. Jr., **Br. Polym. J.**, 12(4), 154, 1980.
78. Metzner, A. B., **J. Rheol.**, 29(6), 739, 1985.
79. Baird, D. G., private communication.
80. Kiss, G. and Porter, R. S., **Mol. Cryst. Liq. Cryst.**, 60, 267, 1980.
81. Iizuka, E., **Mol. Cryst. Liq. Cryst.**, 25, 287, 1974.
82. Duke, R. W., and Chapoy, L. L., **Rheol. Acta**, 15, 548, 1976.
83. Hutton, J. F., **Rheol. Acta**, 14, 979, 1975.
84. Hwang, T. A., PhD Dissertation, University of Wisconsin, Madison, WI, 1976.
85. Lem, K.-W. and Han, C. D., **J. Rheol.**, 27(3), 263, 1982.
86. Wissbrun, K. F., **Br. Polym. J.**, 12(4), 163, 1980.
87. Gotsis, A. D., M.S. Thesis, Virginia Polytechnic Institute and State University, Blacksburg, VA, 1984.
88. Baird, D. G., Gotsis, A. D. and Viola, G. G., **Polym. Prepr. Am. Chem. Soc. Div. Polym. Chem.**, 24(2), 292, 1983.
89. Gotsis, A. D., **Rheol. Acta**, 25, 275, 1986.
90. Ogagawa, A. Cox, R. G. and Mason, S. G., **J. Colloid Interface Sci.**, 45, 303, 1973.
91. Currie, P. K., **Mol. Cryst. Liq. Cryst.**, 73, 1, 1981.
92. Chaffey, E. and Porter, R. S., **J. Rheol.**, 29(3), 281, 1985.
93. Cogswell, F. N., **Br. Polym. J.**, December, 170, 1980.
94. Moldenaers, P. and Mewis, J., **J. Rheol.**, 30(3), 567, 1986.
95. Viola, G. G. and Baird, D. G., **J. Rheol.**, 30(3), 601, 1986.
96. Mewis, J. and Moldenaers, P., **Mol. Cryst. Liq. Cryst.**, 153, 291, 1987.
97. Griffin, A. C. and Haven, S. J., **J. Pol. Sci. Pol. Phys. Ed.**, 19, 951, 1981.
98. Mandelkern, L., "Crystallization of Polymers," McGraw-Hill, New York, 1964.
99. Gochanour, C. R. and Weinberg, M., **J. Rheol.**, 30(1), 101, 1986.
100. Lin, Y. G. and Winter, H. H., **Macromolecules**, 21, 2439, 1988.
101. Mewis, J. and Metzner, A. B, **J. Fluid Mech.**, 62, 593, 1974.
102. Batchelor, G. K., **J. Fluid Mech.**, 44, 419, 1970.
103. Noel, C., in "Recent Advances in Liquid Crystalline Polymers," ed. by L. L. Chapoy, Elsevier, London, 1985.
104. Shiwaku, T., Nakai, A., Hasegawa, H., and Hashimoto, T., **Polymer Commun.**, 28, 174, 1987.
105. Tanner, R. I., "Engineering Rheology," Oxford University Press, New York, 1985.
106. Kalika, D. S., Giles, D. W., and Denn, M. M., **J. Rheol.**, 34(2), 139, 1990.
107. Mackley, M. R., **Mol. Cryst. Liq. Cryst.**, 153, 249, 1987.
108. Bhattarcharya, S. K. and Misra, A., **Pol. Eng. Sci.**, 30(2), 124, 1990.
109. Kiss, G., Orrel, T. S. and Porter, R. S., **Rheol. Acta**, 18, 657, 1979.
110. Kalika, D. S., Nuel, L. and Denn, M. M., **J. Rheol.**, 33(7), 1059, 1989.
111. Larson, R. G., and Mead, D. W., **J. Rheol.**, 33(8), 1251, 1989.
112. Wunder, S. L., Ramachandran, S., Gochanour, C. R. and Weinberg, M., **Macromolecules**, 19, 1696, 1986.
113. Amundson, K. R., Kalika, D. S., Shen, M.-R., Yu, X.-M., Denn, M. M and Reimer, J. A., **Mol. Cryst. Liq. Cryst.**, 153, 271, 1987.
114. Chen, J., White, J. L. and Kyu, T., **SPE ANTEC**, 723, 1986.
115. Fujiyama, M., **J. Appl. Pol. Sci.**, 40, 67, 1990.
116. Horio, M., Kamei, E., and Matsumobu, K., **J. Soc. Rheol., Japan**, 36, 27, 1988.
117. Prasadarao, M., Pearce, E. M. and Han, C. D., **J. Appl. Pol. Sci.**, 27, 1343, 1982.
118. Doppert, H. L. and Picken, S. J., **Mol. Cryst. Liq. Cryst.**, 153, 109, 1987.
119. Marrucci, G. and Maffettone, P. L., **Macromolecules**, 22, 4076, 1989.
120. Carter, B., PhD Dissertation, Virginia Polytechnic Institute and State University, Blacksburg, VA, 1986.
121. Ide, Y. and White, J. L., **J. Appl. Pol. Sci.**, 22, 1061, 1978.
122. Acierno, D., La Mantia, F. P., Polizzotti, G., Ciferri, A. and Valenti, B., **Macromolecules**, 15(6), 1455, 1982.
123. Tealdi, A., Ciferri, A. and Conio, G., **Pol. Commun.**, 24, 145, 1983.
124. Muramatsu, H. and Krigbaum, W. R., **J. Pol. Sci: Part B: Pol. Phys.**, 25, 2303, 1987; 24, 1695, 1986.

125. Cuculo, J. A. and Chen, G.-Y., **J. Pol. Sci.: Part B: Pol. Phys.**, 26, 179, 1988.
126. Kenig, S., **Pol. Eng. Sci.**, 27(12), 887, 1987.
127. Amano, M. and Nakagawa, K., **Polymer**, 28, 263, 1987.
128. Zhou, Z., Wu, X. and Wang, M., **Pol. Eng. Sci.**, 28(3), 1988.
129. Itoyama, K., **J. Pol. Sci.: Part C: Pol. Lett.**, 27, 369, 1989.
130. Sarlin, J. and Törmälä, P., **J. Appl. Pol. Sci.**, 40, 453, 1990.
131. Larson, R. G., **J. Non Newt. Fl. Mech.**, 23, 249, 1987.
132. Zachariades, A. E. and Logan, J. A., **Pol. Eng. Sci.**, 23(15), 797, 1983.
133. Sukhadia, A. M., PhD Dissertation, Virginia Polytechnic Institute and State University, Blacksburg, VA, 24061, 1991.
134. Sawyer, L. C. and Jaffe, M., **J. Mater. Sci.**, 21, 1897, 1986.
135. Joseph, E., Wilkes, G. L. and Baird, D. G., **Pol. Eng. Sci.**, 25(7), 377, 1985.
136. Suokas, E., Sarlin, J. and Törmälä, P., **Mol. Cryst. Liq. Cryst.**, 153, 515, 1987.
137. Pirnia, A. and Sung, C. S. P., **Macromolecules**, 21, 2669, 1988.
138. Hedmark, P. G., Lopez, J. M. R., Westdahl, M., Werner, P.-E., Jansson, J.-F. and Gedde, U. W., **Pol. Eng. Sci.**, 28(19), 1248, 1988.
139. Baird, D. G., Joseph, E., Pisipati, R., Viola, G. and Wilkes, G. L., **SPE ANTEC**, 508, 1984.
140. Asada, T., Muramatsu, H., Watanabe, R. and Onogi, S., **Macromolecules**, 13, 867, 1980.
141. Graziano, D. J. and Mackley, M. R., **Mol. Cryst. Liq. Cryst.**, 106, 73, 1984.
142. Donald, A. M., Viney, C. and Windle, A. H., **Polymer**, 24, 155, 1983.
143. Viney, C., Donald, A. M. and Windle, A. H., **Polymer**, 26, 870, 1985.
144. Nishio, Y., Yamane, Y, and Takahashi, T., **J. Pol. Sci.: Pol. Phys. Ed.**, 23, 1053, 1985.
145. Viney, C. and Windle, A. H., **Polymer**, 27, 1325, 1986.
146. Kyotani, M. and Kanetsuna, H., **J. Macromol. Sci.-Phys.**, B26(3), 325, 1987.
147. Hudson, S. D., Thomas, E. L. and Lenz, R. W., **Mol. Cryst. Liq. Cryst.**, 153, 63, 1987.
148. Chen, S., Jin, Y., Hu, S. and Xu, M., **Pol. Commun.**, 28, 208, 1987.
149. Hashimoto, T., Nakai, A., Shiwaku, T, Hasegawa, H., Rojstaczer, S. and Stein, R. S., **Macromolecules**, 22, 422, 1989.
150. Hashimoto, T., Takebe, T. and Suehiro, S., **Polymer J.**, 18(2), 123, 1986.
151. Navard, P., **J. Pol. Sci.: Pol. Phys. Ed.**, 24, 435, 1986.
152. Fincher, C. R. Jr., **Mol. Cryst. Liq. Cryst.**, 155, 559, 1988.
153. Ernst, B. and Navard, P., **Macromolecules**, 22, 1419, 1989.
154. Ernst, B, Navard. P., Hashimoto, T. and Takebe, T., **Macromolecules**, 23, 1370. 1990.
155. Wilkes, G. L., **J. Macromol. Sci. Revs. Macromol. Chem.**, C10(2), 149, 1974.
156. Tabar, R. J., Stein, R. S. and Long, M. B., **J. Pol. Sci. Pol. Phys. Ed.**, 20, 2041, 1982.
157. Wasiak, A. Peiffer, D and Stein, R. S., **J. Pol. Sci. Pol. Lett Ed.**, 14, 381, 1976.
158. Tabar, R. J., PhD Dissertation, University of Massachusetts, Amherst, MA, 1983.
159. Tabar, R. J., Leite-James, P. and Stein, R. S., **J. Pol. Sci. Pol. Phys. Ed.**, 23, 2085, 1985.
160. Stein, R. S., **Polymer J.**, 17, 289, 1985.
161. Effler, L. J., Lewis, D. N. and Fellers, J. F., submitted for publication.
162. Effler, L. J., MS Thesis, University of Tennessee, 1987.
163. Hashimoto, T., Ebisu, S., Inaba, N. and Kawai, H., **Polymer J.**, 13(7), 701, 1981.
164. Stein, R. S., Erhardt, R. van Aartsen, J. J., Coough, S. and Rhodes, M. B., **J. Pol. Sci., C**, 13, 1, 1966.
165. Rhodes, M. B. and Stein, R. S., **J. Pol. Sci. Part A-2**, 7, 1539, 1969.
166. van Aartsen, J. J., **Eur. Pol. J.**, 6, 1095, 1970.
167. Moritani, M., Hayashi, N., Utsuo, A., and Kawai, H., **Polymer J.**, 2, 74, 1971.
168. Hayashi, N. and Kawai, H., **Polymer J.**, 3, 140, 1972.
169. Murakami, T., Hayashi, N., Hashimoto, T. and Kawai, H., **Polymer J.**, 4, 452, 1973.
170. Prud'homme, R. E. and Stein, R. S., **J. Pol. Sci. Pol. Phys. Ed.**, 12, 1805, 1974.
171. Samuels, R. J., **J. Pol. Sci. Part A-2**, 7, 1197, 1969.
172. Kyu, Y., Mukherjee, P., and Park, H.-S., **Macromolecules**, 18, 2331, 1985.
173. Wilkes, G. L., **Mol. Cryst. Liq. Cryst.**, 18, 165, 1972.
174. Chien, J. C. W. and Chang, E. P., **Macromolecules**, 5, 610, 1972.
175. Lim, Y. W., Sarko, A. and Marchessault, R. H., **Tappi**, 53, 2314, 1970.
176. Borch, J. and Marchessault, R. H., **J. Pol. Sci. Part C**, 28, 153, 1969.

177. Rojstaczer, S. and Stein, R. S., **Mol. Cryst. Liq. Cryst.**, 157, 293, 1988.
178. Wissbrun, K. F., Kiss, G. and Cogswell, F. N., **Chem. Eng. Comm.**, 53, 149, 1987.
179. Lenz, R. W., Jin, J. I. and Feichtinger, K. A., **Polymer**, 24, 327, 1983.
180. Doi, M. and Edwards, S. F., Chs. 8-10 in "The Theory of Polymer Dynamics," Clarendon Press, Oxford, 1986.
181. Doi, M., **J. Phys.** (Paris), 36, 607, 1986.
182. Doi, M. and Edwards, S. F., **J. Chem. Soc. Faraday. Trans. II**, 74, 568, 1978; 74, 568, 1978.
183. Kirkwood, J. G. and Auer, P.L., **J. Chem. Phys.**, 19, 281, 1951.
184. Onsager, L., **Ann. N. Y. Acad. Sci.**, 51, 627, 1949.
185. Kuzuu, N. and Doi, M., **J. Phys. Soc. Japan**, 52(10), 3486, 1983.
186. Doraiswamy, D. and Metzner, A. B., **Rheol. Acta**, 25, 580, 1986.
187. Grizzuti, N. and Marrucci, G., **J. Pol. Sci. Pol. Lett. Ed.**, 21, 83, 1983.
188. Marrucci, G. and Grizzuti, N., **J. Non Newt. Fl. Mech.**, 14, 103, 1984.
189. Chow, A. W. and Fuller, G. G., **Macromolecules**, 18, 786, 1985.
190. Chow, A. W., Fuller, G. G., Wallace, D. G., and Madri, J. A., **Macromolecules**, 18, 793, 1985.
191. Chow, A. W., Fuller, G. G., Wallace, D. G., and Madri, J. A., **Macromolecules**, 18, 805, 1985.
192. Chu, S.-C., Venkatramen, S., Berry, G. C., and Einaga, Y., **Macromolecules**, 14, 939, 1981.
193. Berry, G. C., Hager, B. L. and Wong, C. P., **Macromolecules**, 10, 361, 1977.
194. McFarlane, F. E., Nicely, V. A., and Davis, T. G., in "Contemporary Topics in Polymer Science," Vol. 2, Plenum Press, New York, 109-138, 1977.
195. Sun, T. and Porter, R. S., **Pol. Commun.**, 31, 70, 1990.
196. Klug, E. D. in "Methods in Carbohydrate Chemistry," R. L. Whistler Ed., Vol. III, Academic Press, New York, 1963, p.315.
197. Strunk, D. L., Aqualon Company, private communication, 1989.
198. "Klucel Hydroxypropylcellulose A Nonionic Water-Soluble Polymer," Aqualon Company, Wilmington, DE, 1987.
199. Blackwell, J., Chivers, R. A., Gutierrez, G. A. and Biswas, A., **J. Macromol. Sci.-Phys.**, B24(1-4), 39, 1985-86.
200. Wirick, M. G. and Waldman, M. H., **J. Appl. Pol. Sci.**, 14, 579, 1970.
201. Rodriquez, F., "Principles of Polymer Systems," 2nd Ed., McGraw-Hill Book Company, New York, 1982.
202. "Rheometrics Mechanical Spectrometer Operations Manual," Rheometrics Inc., Union, New Jersey, 1989.
203. Meissner, J., **Trans. Soc. Rheol.**, 16, 405, 1972.
204. Moynihan, R. H., Baird, D. G. and Ramanathan, R., **J. Non. Newt. Fl. Mech.**, 36, 255, 1990.
205. "Rheometrics Extensional Rheometer Operations Manual," Rheometrics Inc., Piscataway, New Jersey.
206. Mitchell, G. R. and Windle, A. H., **Polymer**, 24, 513, 1983.
207. Laun, H. M. and Schuch, H., **J. Rheol.**, 33(1), 119, 1989.
208. Jensen, A. and Chenoweth, H. H., "Statics and Strength of Materials," McGraw Hill, New York, 1983.
209. Larson, R. G. and Mead, D. W., **J. Rheol.**, 32(3), 185, 1989.
210. Burghardt, W. R., **J. Rheol.**, 35(1), 49, 1985.
211. Wang, Y., Hu, S., Xu, M., and Zhou, Q., **Pol. Commun.**, 29, 103, 1988.
212. Kamal, M. R., Khennache, O. and Wilson, D. R., **Pol. Eng. Sci.**, 29(15), 984, 1989.
213. Moldenaers, P. and Mewis, J., **J. Non Newt. Fl. Mech.**, 34, 359, 1990.
214. Guskey, S. and Winter, H. H., submitted for publication.
215. Petrie, C. J. S., "Elongational Flows," Pitman Publishers, Ltd., London, 1979.
216. Larson, R. G. and Mead, D. W., **Macromolecules**, 23, 2524, 1990.
217. Marrucci, G. and Maffettone, **Macromolecules**, 22, 4076, 1989.
218. Larson, R. G., **Macromolecules**, 23, 3983, 1990.
219. Bird, R. B., Curtiss, C. F. Armstrong, R. C., and Hassager, O.,"Dynamics of Polymeric Liquids," Vol. 2, 2nd Ed., John Wiley Pub., New York, 1987.
220. Marrucci, G., **Proc. IX Int. Congr. Rheol.**, Acapulco, Mexico, October, 1984.
221. Alderman, N. J. and Mackley, M. R., **Far. Disc. Chem. Soc.**, 79, 149, 1985.
222. Burghardt, W. R. and Fuller, G. G., **J. Rheol.**, 34(6), 959, 1990.

223. Larson, R. G. and Doi., M., **J. Rheol.**, 35(4), 539, 1991.
224. Onogi, Y., White, J. L. and Fellers, J. F., **J. Pol. Sci. Pol. Phys. Ed.**, 18, 663, 1980.
225. Baird, D. G., **ACS Polymer Prepr.**, 23(2), 10, 1982.

Abbreviations

DCPE	bis(4-carboxyphenoxy)ethane
DHN	2.6-dihydroxynaphthoic acid
DR	Draw ratio
DSC	differential scanning calorimetry
ER	extensional rheometer (built at VPI)
HBA	para-hydroxybenzoic acid
HBA/HNA	HBA/2-hydroxy-6-naphthoic acid copolyester with mole ratio (73/27)
HNA	2-hydroxy-6-naphthoic acid
HPC	hydroxypropylcellulose
HQ	hydroquinone
LCP	liquid crystalline polymer
LCP60	60 mole % HBA/40 mole % PET copolyester
LCP80	80 mole % HBA/20 mole % PET copolyester
LLDPE	linear low density polyethylene
MHQ	methyl hydroxquinone
NDA	Naphthalene dicarboxylic acid
PBA	poly(para-benzamide)
PBDG	poly(γ-benzyl-D-glutamate)
PBG	poly(γ-benzylglutamate)
PBLG.	poly(γ-benzyl-L-glutamate)
POM	polarized optical microscopy
PPTA	poly(para-phenylene terephthalamide) "Kevlar"
RER	Rheometrics Extensional Rheometer
RMS	Rheometrics Mechanical Spectrometer
SALS	small angle light scattering
TA	terephthalic acid
TGA	thermogravimetric analysis
TLCP	thermotropic liquid crystalline polymer
WAXS	wide angle light scattering
60HBA/PET	60 mole % HBA/40 mole % PET copolyester

Nomenclature

a	defined as **r** •**s**/r [165] (SALS) or tube radius containing rod in Doi Theory.
A	Free energy of the solution of rigid rods
b	polarizability tensor, with magnitude b.
c	concentration number of rods per unit volume
C,U	dimensionless interaction potential $=\nu_1 c d L^2$
d	rod diameter in Doi theory
D_{ro}	diffusion constant for rigid rods with no inter-rod interactions.
D_r	rotational diffusion constant for a rod in a
D_r	rotational diffusion constant for a rod with orientation **u** in concentrated solution ($D_r = fcn(t,\mathbf{u})$). semi-concentrated isotropic solution
$\bar{D}_r$	averaged rotational diffusion coefficient in in concentrated solution ($\bar{D}_r = fcn(f)$).
E	electric field vector, with magnitude E
f	orientation distribution function ($f = fcn(\mathbf{u},t)$).
F(S)	term in Doi theory for Brownian motion contribution to orientation derivative
G(S)	term in Doi theory for Kinematic contribution to orientation derivative.
G*	dynamic shear modulus
G',G"	dynamic storage and loss moduli
h	$4\pi/\lambda \sin(\theta/2)$
Hv	SALS with vertical polarizer and horizontal analyzer

i,j,k	unit direction vectors for a x, y, z cartesian coordinate system.
I	Intensity of scattered light
I_E, I_{II}, I_X	Intensity of scattered light with polarizers situated as described in Figure 22.
k	$2\pi/\lambda$ (SALS) or Boltzmanns constant (Doi)
k_B	Boltzmanns constant
$K_{\alpha\beta}$	velocity gradient tensor, $K_{\alpha\beta} = v_{i,j} = \partial v_i/\partial x_j$
L	length of a rod (SALS) or molecule (Doi theory)
M	induced dipole moment in a scattering element
$N(\alpha,\phi)$	orientation distribution of rodlike particles (SALS)
$O.$	direction of analyzer polarization
r	position vector whose magnitude equals the distance to the origin
s	scattering vector, equals s_0-s′
s_o	the direction vector for the incident light
s'	the direction vector of the scattered light
S	scalar order parameter, $= 3/2S^2_{\nu\mu}$
$S^2_{\nu\mu}$	defined as **S**:**S**
$T^o(R)$	correlation function for SALS theory
V	mean field potential in Doi theory
$v_{i,j}$	the velocity gradient tensor $= \partial v_i/\partial x_j$
Vv	SALS pattern taken with both analyzer and polarizer in the vertical position
α_l, α_t	longitudinal and tangential polarizabilities of a rodlike particle
α,β,γ	used sometimes as indices
α	polarizability tensor
ε	parameter describing degree of rod orientation in SALS theory for rodlike particles
$\dot{\varepsilon}$	the extension rate
εt	Hencky strain for elongational deformation
$\eta, \eta(\dot{\gamma})$	steady shear viscosity
η^*	dynamic shear viscosity
η', η''	dynamic storage and loss viscosity
η_s	solution viscosity
η^+	transient shear viscosity growth function
η_G^+	transient shear viscosity of linearly viscoelastic material
$\bar{\eta}_e^+$	transient extensional viscosity growth function
$\dot{\gamma}$	steady shear rate
$\dot{\gamma}t$	Hencky strain for shear deformation
λ	wavelength of radiation
μ	azimuthal angle (SALS)
ν_1, ν_2	undetermined constants in the Doi theory
ω	the angle between the rod axis and direction of maximum polarizability
Ω	90 - μ
ϕ	angle made by projection of a rodlike particle in the x-y plane with the x axis.
ρ	scattering power
$\tau_{\alpha\beta}$	the total stress tensor
θ	radial scattering angle (SALS)

Appendix A. SALS in LCPs

The technique of small angle light scattering was shown in section 2.2.3 to be important for the determination of structure in LCP systems undergoing flow. However, interpretation of SALS patterns is not entirely straight forward, and depends heavily on theoretical considerations. For this reason and since the method of SALS is a part of the proposed research objective of this work, the technique of SALS and its use for determining structure in LCP systems is reviewed here in some detail.

A.1 Introduction to SALS

Small-angle light scattering has become a standard technique for the characterization of superstructure on the order of 0.1 to 50 μm's in solid polymers. For example, SALS has been used extensively to characterize the spherullitic texture of semi-crystalline polymers. In this section, the experimental technique of SALS is reviewed for its application in the characterization of superstructure in liquid crystalline polymers, especially in regard to the polydomain texture. First, the experimental technique is demonstrated. The interpretation of SALS patterns based on both structure models and statistics is then demonstrated. The two

dimensional model for a rigid rod is developed. Finally, experimental studies on liquid crystalline materials are reviewed and compared to theory. For more information on the general method of SALS the reader is referred to the review by Wilkes [155].

A.2 Experimental

The experimental method is illustrated in Figure 104 for a photographic setup. Linearly polarized light from a gas laser passes through, in secession, a polarizer (if the laser light is not previously polarized from the laser), the sample, and a second polarizer (called the analyzer). The scattered light is projected onto a screen, a ground glass plate, or is directly recorded by an open back polaroid camera [155]. The sample consists of a flat film, which is mounted so that the plane of the film is perpendicular to the incident light and so that the deformation direction is in the vertical direction. The electric vector of the incident light is usually vertical, while the analyzer can be either vertical or horizontal. The directions of polarization of the analyzer and of the incident light are specified by a two letter combination X_Y, where X specifies the analyzer direction and Y the incident beam or polarizer direction. For example, an H_V pattern has the analyzer horizontal and the incident beam polarized vertically.

Although simple to use, the method above only yields qualitative results. Quantitative results were obtained by using photomultipliers as detectors and scanning the image in either the radial or azimuthal directions, depicted in Figure 17 by the angles θ and μ, respectively.. More recently, the development of video and computer technology have made it possible to digitize the entire SALS pattern. This method was developed by Stein and coworkers [156-160]. The apparatus consists of a vidicon detector or video camera tube, an Optical Multichannel Analyzer (OMA2) to control the hardware and digitize the signal, and a Digital Equipment Corporation LS 11/2 microprocessor with 64 kilobytes of RAM to store the image. The resolution was a 50 by 50 grid and the intensity range at each point was 0 to 16384, or 14 bits. An

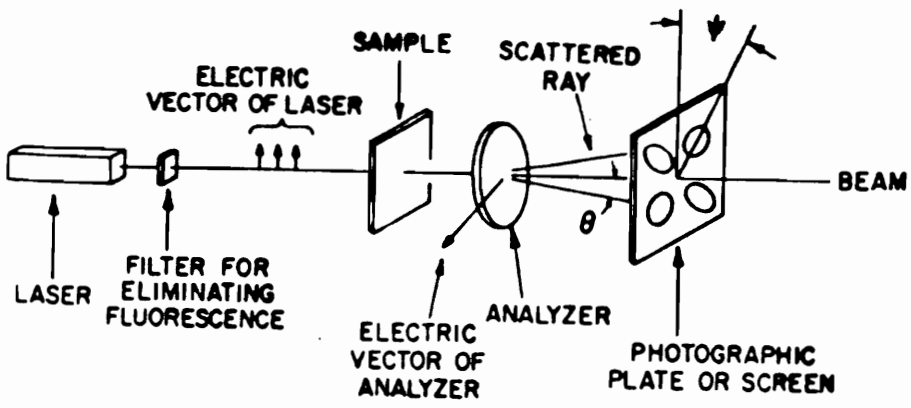

Figure 104. Photographic small-angle light scattering apparatus [155].

entire image could be digitized and stored in 4 seconds. Subsequent improvements were expected to increase the grid to 100 x 100 points and decrease the time to collect an image to 100 milliseconds. A similar apparatus was later developed by Fellers and coworkers [161,162]. This apparatus is capable of recording a 249 x 236 grid and can distinguish 256 intensity levels (8 bits). Effler and coworkers [161] have reviewed the state of the art and indicate that the largest limitation with current equipment is the limited intensity resolution.

A.3 Interpretation of SALS for LCPs

The scattering of electromagnetic radiation of visible wavelengths, when passing through a specific medium, is due to its interaction with electrons (especially valence electrons) [155]. The electrons are forced to oscillate in phase with the light, creating oscillating dipoles which emit electromagnetic radiation of the same frequency. If the dipoles are arranged in a uniform manner in the medium, the phase relationships between the scattered rays are such that in all directions except the incident beam direction the intensities will add to zero. On the other hand, if heterogeneities exist in the material, the net scattered intensity will be nonzero. As in small-angle x-ray scattering (SAXS), in small-angle light scattering there exists a reciprocal relationship between the size of the scattering element and the radial scattering angle θ as is given by Braggs law. However, in SALS the size of the structure probed is different because of the different wavelength range and also the aspect of polarizability (α) is important, unlike x-ray scattering [155].

The types of heterogeneities leading to light scattering include (1) density fluctuations, (2) correlations in the orientation of the optic axis of anisotropic elements or regions, (3) fluctuations in the local anisotropy of elements, and (4) optical rotation [155]. The first type gives rise to isotropic scattering, e.g. V_V while the last three give rise to anisotropic scattering, which is seen in both V_V and H_V scattering. The Schlieren texture of nematic LCPs was previously described as being due to the variation in the orientation of the director field **n**, which is

caused by a spatial distribution of disclinations. It is the spatial correlation of the fluctuations of the director field which are responsible for the depolarized (H_v) and polarized (V_v) components of small-angle light scattering in nematic LCPs [149]. For cholesteric LCPs, form optical rotation results from their twisted structure (see Fig. 2) and has a significant effect on the small-angle light scattering from such systems. Although the SALS from cholesteric liquid crystals will not be treated here, a theoretical interpretation can be found in the work of Hashimoto and coworkers [163].

The interpretation of SALS patterns involves either a comparison with the pattern calculated using a specific scattering model (model approach) or is made by a statistical analysis of the experimental pattern. In the model approach, a structural model of the system of interest must be specified, the SALS pattern calculated, and the calculation then compared to the experimentally observed pattern. In the statistical approach, the scattering system is described in terms of anisotropic or isotropic optical density fluctuations, persistence lengths, or radial distribution correlation functions [155]. Both approaches have been applied to the interpretation of the SALS of LCPs and each will be developed here.

Model Approach. The most common structural model for the interpretation of LCP systems has been that for the scattering from anisotropic rods, a case which has been extensively studied [164-170]. The scattering from a single anisotropic rod of length, L, and infinitesimal thickness is considered first, with the geometry of the system shown in Figure 105. The rod is made up of anisotropic scattering elements whose maximum polarizability is at a fixed angle ω with the rod axis. The scattering amplitude from a volume element in the rod is then [165]

$$dE = \rho e^{ikr \cdot s} dr \tag{A.1}$$

where ρ is the scattering power, $k = 2\pi/\lambda$, λ is the wavelength of the incident light, $\mathbf{r}$ is the position of the scattering element (where the origin is at the rod center), and $\mathbf{s} = \mathbf{s}_0 - \mathbf{s}'$. The unit vectors $\mathbf{s}_0$ and $\mathbf{s}'$ are the directions of the incident and scattered light. In the coordinate system shown $\mathbf{s}_0$, $\mathbf{s}'$, and $\mathbf{r}$ will be

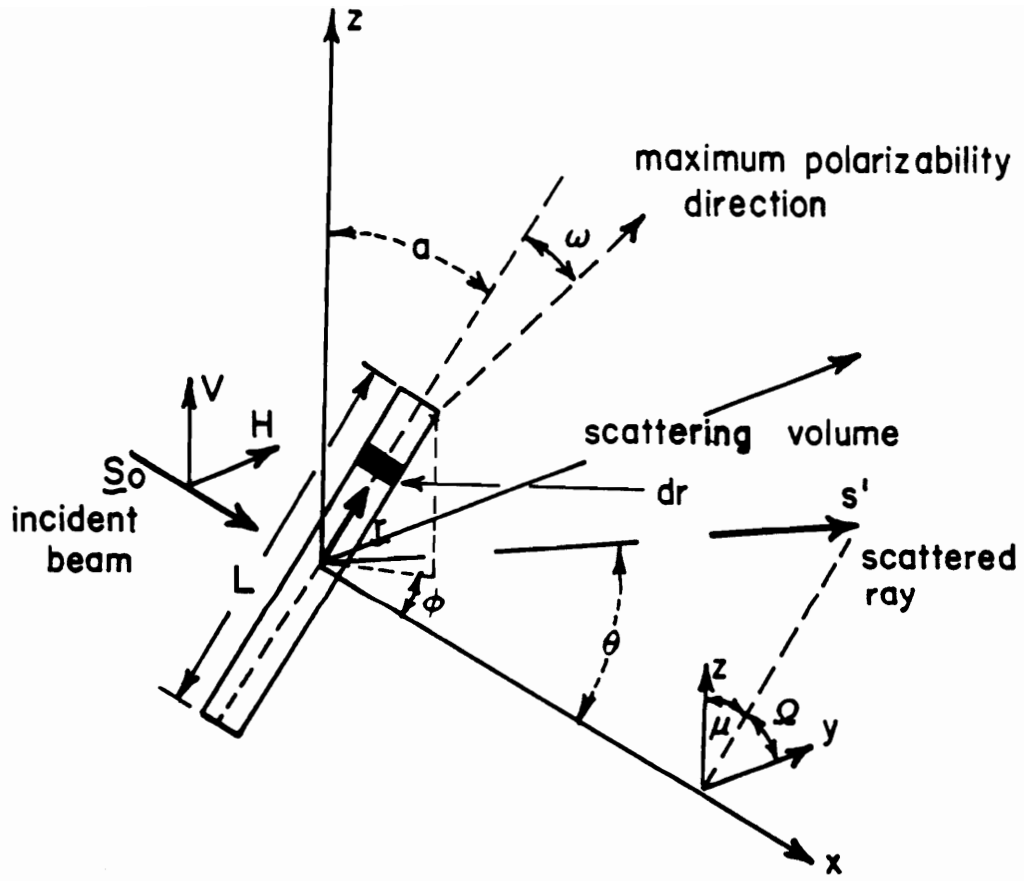

Figure 105. Definition of the geometry for the scattering from a single anisotropic rod [165].

$$\mathbf{s}_0 = \mathbf{i} \tag{A.2a}$$

$$\mathbf{s}' = \cos\theta\mathbf{i} + \sin\theta\cos\Omega\mathbf{j} + \sin\theta\sin\Omega\mathbf{k} \tag{A.2b}$$

$$\mathbf{r} = r[(\sin\alpha\cos\phi)\mathbf{i} + (\sin\alpha\sin\phi)\mathbf{j} + (\cos\alpha)\mathbf{k}] \tag{A.2c}$$

where $\Omega = 90\text{-}\mu$, μ being the azimuthal angle. In order to determine the scattering amplitude from the entire rod, E, the amplitudes dE are added up or equivalently, dE is integrated over the entire rod volume to obtain [165]

$$E = \int_{+L/2}^{-L/2} \rho e^{ikar} dr \tag{A.3}$$

where *a* is given as

$$a = -\sin(\alpha + \Omega)\sin\theta \tag{A.4}$$

for the case where the rod is oriented within the plane of the film, i.e. $\phi = 90^0$. Since the scattering power ρ is independent of **r**, equation A.3 can be integrated to obtain

$$E = \rho L \frac{[\sin(kaL/2)]}{(kaL/2)} \tag{A.5}$$

The next step is to obtain an expression for ρ. This parameter depends upon the direction of the dipole moment, which in turn depends upon the relative orientation of the rod and the electric vector of the incident light. A general expression for ρ is

$$\rho = \rho_0(\mathbf{M}\bullet\mathbf{O}) \tag{A.6}$$

where ρ_0 is the scattering power of a rod per unit length per unit incident field strength when the rod is oriented in the z direction, **O** is the direction of the analyzer (e.g. **O** = **j** for H_v scattering) and **M** is the induced dipole moment.

It has been shown [165] that

$$\mathbf{M} = \delta[(\mathbf{E}\bullet\mathbf{r})/r]\mathbf{r} + \alpha_t\mathbf{E} \tag{A.7}$$

where $\delta = \alpha_l - \alpha_t$ and represents the optical anisotropy of the rod. The parameters α_l and α_t represent the difference in polarizability between the rod in the longitudinal direction and its surroundings and between the rod in the tangential direction and its surrounding, respectively. Also, in order for the anisotropy of the rod to be completely described by α_l and α_t, cylindrical symmetry must exist in the polarizability.

Noting that $\mathbf{E} = E\mathbf{k}$ and going through the necessary algebra, ρ for both H_v and V_v scattering become [165]

$$\rho(H_V) = \rho_0[\delta \sin\alpha \cos\alpha \sin\phi] \tag{A.8a}$$

$$\rho(V_V) = \rho_0(\delta \cos^2\alpha + \alpha_t) \tag{A.8b}$$

For H_v scattering it is seen that scattering is due entirely to the anisotropy of the rod, while for V_v scattering there is also an isotropic component, which results from density fluctuations.

The scattered intensity can now be calculated and is proportional to the square of the amplitude. For an assembly of rods, neglecting the interparticle effects, the total scattered intensity is simply the sum of the scattered intensity of the individual rods. Since the maximum polarizability can be in a direction other than along the rod axis, it is necessary to adjust the values of α that are used in the equation for ρ. For the case where the rods lie within the plane of the sample (i.e. two dimensional case), this is done by substituting $\alpha' = \alpha + \omega$, where ω is the direction the maximum polarizability makes with the rod axis. To include the effect of a nonrandom distribution of rods, a distribution function $N(\alpha,\phi)$ is used. The intensity is now [165]

$$I = \int\int N(\alpha,\phi)E^2 d\alpha d\phi \tag{A.9a}$$

$$E_{H_v} = \rho_0 L\delta \sin\alpha' \cos\alpha' \sin\phi[\sin(kaL/2)/(kaL/s)] \quad (A.9b)$$

$$E_{V_v} = \rho_0 L(\delta \cos^2\alpha' + \alpha_t)[\sin(kaL/2)/(kaL/s)] \quad (A.11c)$$

The choice of a suitable distribution function is usually made with some prior knowledge about the structure of the system. An elliptical distribution function was suggested by Rhodes and Stein for the case where $\phi = 90^0$ and was given as

$$N(\alpha) = N_0(\varepsilon^{-2}\cos^2\alpha + \varepsilon^2 \sin^2\alpha)^{-1/2} \quad (A.10)$$

The degree of orientation is essentially specified by the parameter ε. When $\varepsilon = 1$, the rods are randomly distributed within the plane of the sample. As ε increases above one, more rods become oriented in the vertical direction than the horizontal direction, on the average.

The scattering patterns calculated from the analysis above are shown in Figure 106 and Figure 107 and have a few noticeable characteristics. In all the patterns shown, both H_v and V_v, the intensity decreases monotonically with the radial angle θ and shows four maxima as a function of azimuthal angle μ. The azimuthal angles at which these maxima occur is either at odd multiples of 45^0 (± 45 type) or at 0 and multiples of 90^0 (0-90 type), and depend upon the angle ω.

A number of experimental SALS studies on LCPs have been made and interpreted in terms of the theory for anisotropic rods just presented. Samuels [171] and Kyu and coworkers [172] studied HPC; Wilkes [173] studied PBLG and poly(γ-methyl-L-glutamate) (PMG); Chien [174] studied collagen; Marchessault and coworkers [175-176] studied cellulose based systems; and Effler [161,162], Rojstaczer [177], and Hashimoto and coworkers [149] studied the 60HBA/PET copolyester; and Wang [211] and Rojstaczer and Stein [212] studied semi-flexible copolyesters. Samuels found that the SALS patterns of water-cast HPC films were in good agreement with the theory (for $\omega = 45^0$) provided the appropriate distribution function $N(\alpha)$ was used [172]. Chien and Chang [174] also observed the 0-90 H_v patterns and found that the theory was useful for the interpretation of structural changes occurring in uniaxially deformed

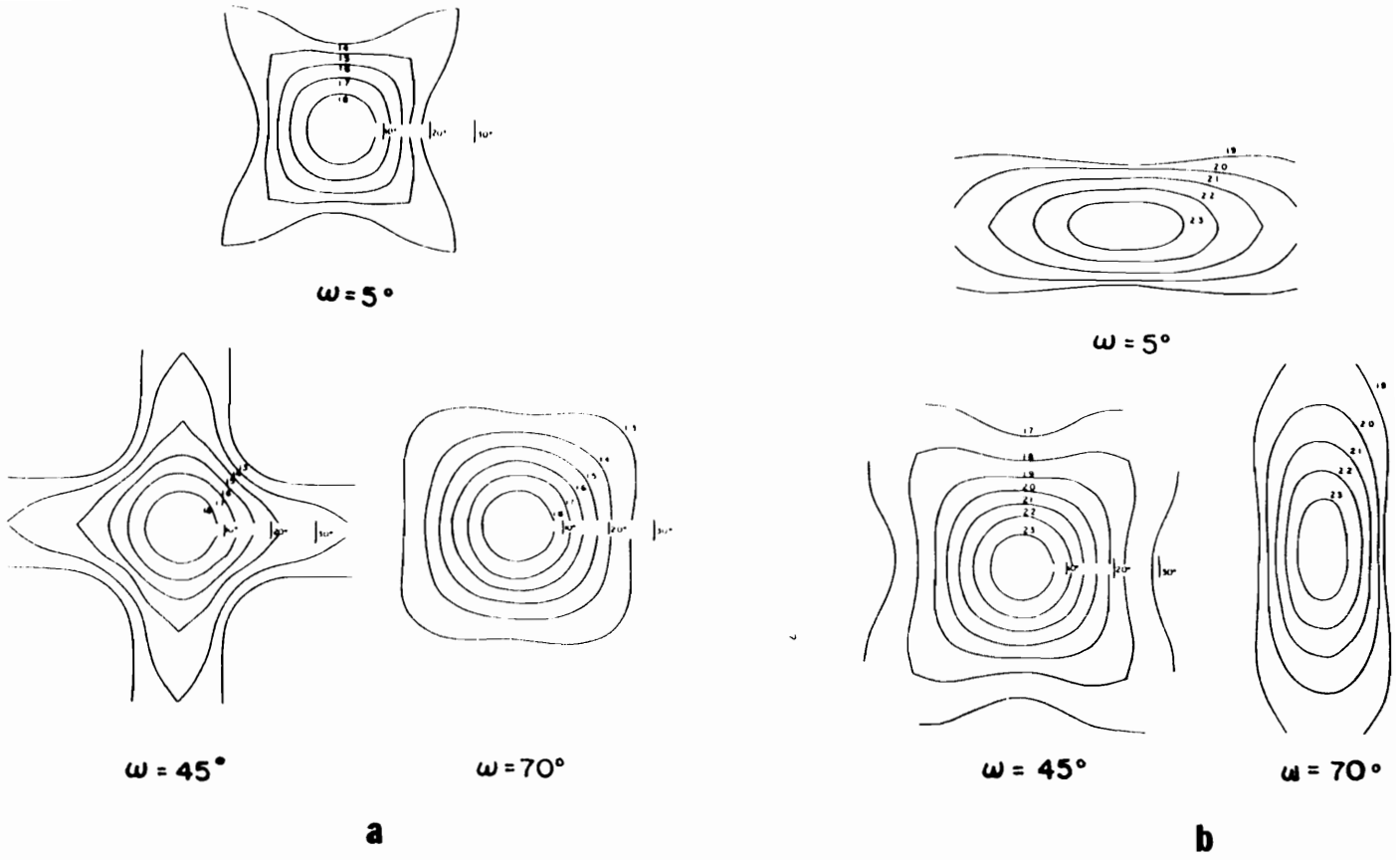

Figure 106. Intensity contour plots of (a) H_V and (b) V_V scattering for a random assembly of anisotropic rods [165].

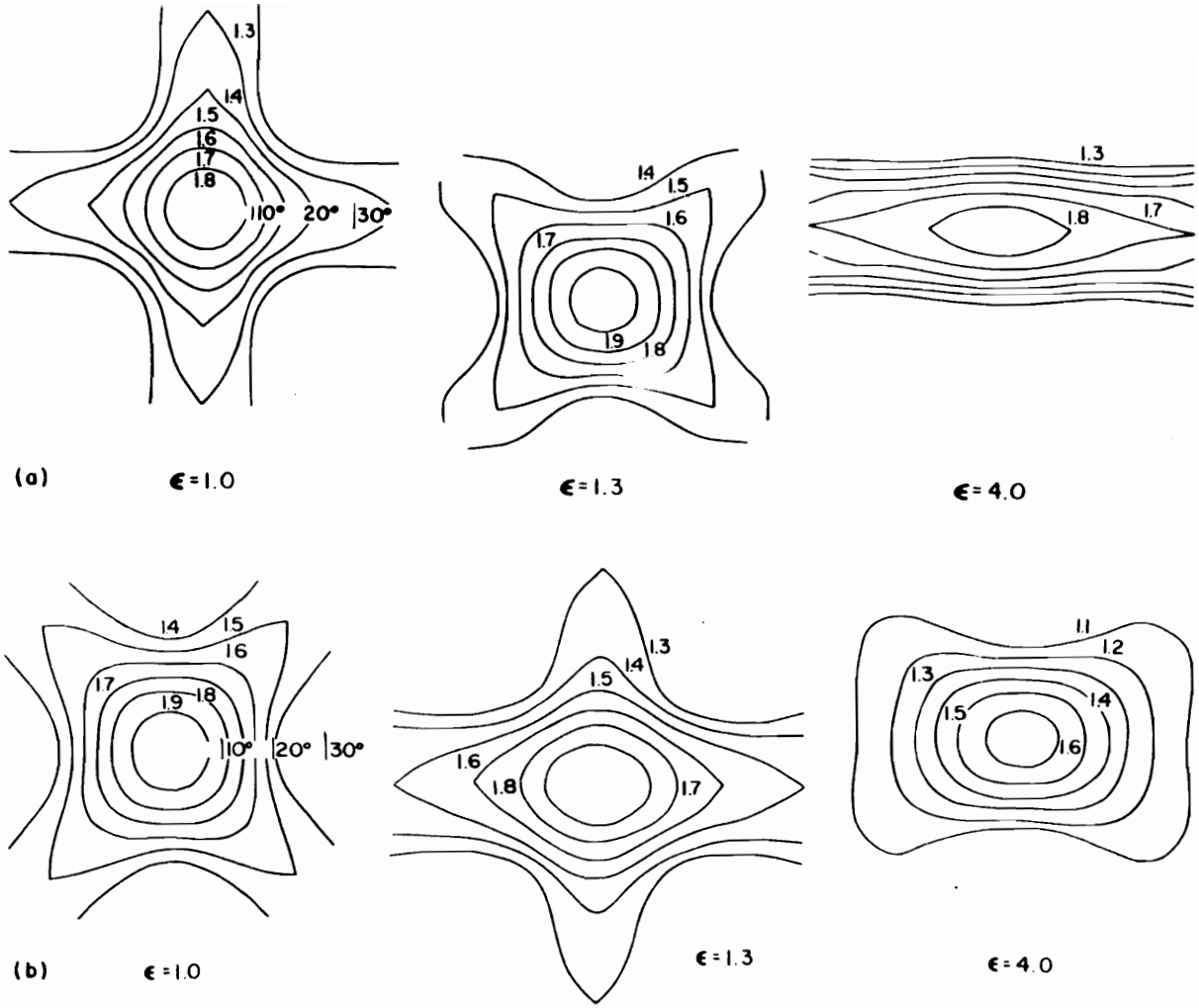

Figure 107. Intensity contour plots of (a) H_V and (b) V_V scattering from nonrandom distributions of anisotropic rods [165].

films. Wilkes [173] found that solution cast films of PBLG and PMG had 0-90 H_v patterns, in agreement with the theory for $\omega = 45^0$. However, it was noted that the scattering from films with solution present gave a $\pm 45^0$ H_v pattern, which could either be due to rodlike or spherullitic scattering [173].

In contrast to the studies cited above, no general agreement with the theory has been observed for thermotropic systems. Kyu [172] studied the SALS from compression molded films of HPC. A 0-90 H_v pattern and a circularly symmetric V_v pattern was observed, which do not have a theoretical match but do not necessarily show disagreement since density flucuations could have obscurred the V_v pattern. Effler [161,162] studied the SALS of compression molded films of the 60HBA/PET copolyester which had been well annealed and then quenched. The H_v patterns had circularly symmetric intensity patterns which dropped off nearly monotonically with the square of the scattering vector h, where $h = (4\pi/\lambda)\sin(\theta/2)$.

Perhaps the most striking disagreement with theory is in the data of Rojstaczer [177,212] and Hashimoto [149]. They studied the changes in texture of thermotropic copyesters which had been rapidly brought from the isotropic state to a temperature at which the nematic Schlieren texture would form, as seem by optical microscopy. Both copolyesters, one of which was the 60HBA/PET copolyester, showed not only well defined H_v 0-90 and V_v $\pm 45^0$ patterns, but also maxima as a function of θ for the H_v patterns as shown in Figure 108. Also, the maxima were seen to move to smaller values of θ with increasing time indicating an increase in the size of the structure. Hashimoto and coworkers correlated this with a decrease in the number of disclinations or an increase in domain size.

In an effort to understand the behavior seen, Hashimoto and coworkers [149] developed a new theoretical model, based on the light scattering from isolated disk-shaped disclinations. Although the model could generate SALS patterns similar to those observed, the structural basis for this was inconsistent with the known structure from polarized optical microscopy (POM) [149]. However, it was qualitatively shown that the observed scattering could arise from the interference between rodlike regions thought to exist in the interstitial regions between disclinations.

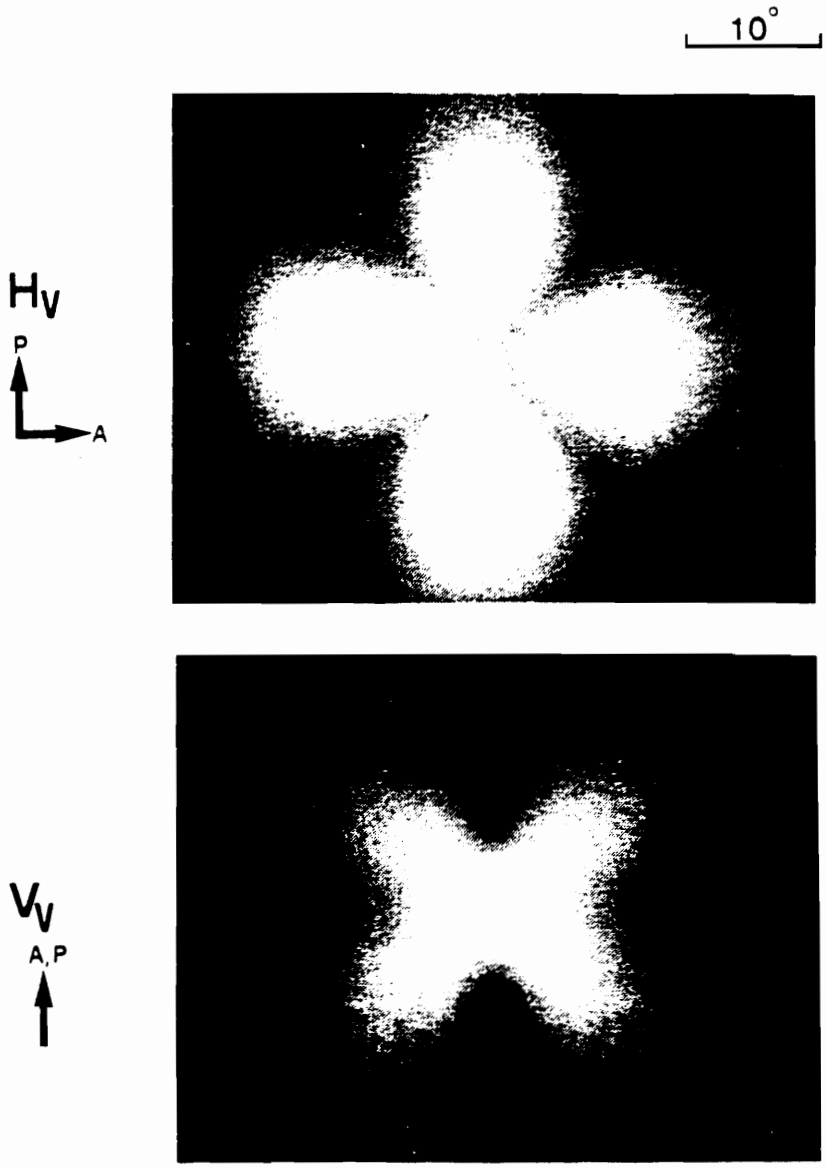

Figure 108. The SALS H_V and V_V patterns for films of 60HBA/PET [149].

In this section the theory of scattering from anisotropic rods was presented and compared with experimental results. It was shown that the scattering behavior of many liquid crystalline systems can be interpreted in this way. However, the SALS from thermotropic systems are not always interpretable in terms of rodlike scattering, this possibly due the non-equilibrium textures which are formed. Therefore, in some LCP systems another approach for interpreting data is necessary.

Statistical Approach. The statistical approach is often used to interpret data when no reasonable model can be formulated and is often necessary when a system is highly disordered [155]. The system is then described in terms of anisotropic or isotropic "fluctuations", persistence lengths, and/or radial correlation functions. The theoretical basis for the statistical approach is described by Wilkes [155] and will not be given here. However, Prud'homme and Stein derived an expression for the scattering of light by anisotropic rods which is equivalent to a statistical development. In their dervivation they used a Gaussian function $T_0(R)$ to specify the relative orientation between scattering elements as a function of inter-rod distance, R. This function was

$$T_0(R) = e^{R^2/a_0^2} \tag{A.11}$$

where a_0 is a correlation distance. The resulting H_v scattering intensity then is [170]

$$I_{H_v} = \frac{KL^2\delta^2}{2} a_0^2 \exp[-k^2 a_0^2 \sin^2\theta/4] \tag{A.12}$$

This approach was used by Effler [161,162] to interpret SALS H_v patterns obtained from 60HBA/PET compression molded films. Characteristic dimensions were calculated from the slope of a plot of ln(I) versus h^2, with typical values calculated to be in the range of 1.1 to 1.5 μm. These results were supported by polarized optical microscopy and scanning electron microscopy (SEM). Although the patterns observed here were circularly symmetric, Effler [162] noted that a characteristic dimension could be calculated for any particular azimuthal direction using this method.

Although few studies have used the statistical approach to interpret the small-angle light scattering of LCPs, it is seen to be useful in the case of the compression molded films of 60HBA/PET. Using this technique, an average correlation size of the scattering elements can be determined in any given direction within the plane of the sample. For nematic LCPs, the lengths measured are expected be directly related to the size of the domains.

Appendix B. Extensional Rheometer (ER)

In this appendix the principles behind the design of the dual rotary clamp extensional rheometer, procedures for its use, and programs used in data evaluation are detailed. Some schematics showing the general design are presented but intricate details of the extensional rheometer construction are not shown.

B.1 Construction of Extensional Rheometer

Most of the parts to the extensional rheometer were constructed at VPI in the chemical engineering shop by Wendell Brown based on the designs drafted by the author. This includes the rheometer tank, rotary gears, motor and gear supports, sample fixtures, tank top, etc.. The rheometer tank was constructed from copper plates, with copper used because of its high thermal conductivity. The size of the tank was minimized because of the high cost of the oil used. Quartz windows were installed to enable optical studies to be carried out during flow. The heating control of the rheometer was accomplished by electric plate heaters mounted on the sides and bottom of the tank, with thermocouples located at two locations along the centerline of the tank and about 1/3 of a tank length from each end. Finally, copper coils were

build into the bottom plate of the rheometer to allow for a second heating/cooling system using a external thermal bath as the heating/cooling source.

The materials used in the rheometer parts depended on the location and purpose of that part. Most of the parts located inside the tank were constructed with stainless steel to minimize corrosion and because of increased thermal stability over aluminum. However, when possible, aluminum was used for parts supporting the motors in order to minimize the weight of the motor assembly and thus increase accuracy of force measurement when the dual rotary clamp configuration was necessary.

When possible, parts were purchased and these include the electric motors, linear voltage displacement transducer (LVDT), LVDT signal conditioner, quartz windows, motor and heater controllers, force calibration arm, data acquisition board, heaters, and insulation. While a list of sources is not given here, it is noted that the LVDTs were specially constructed by Schaevitz Engineering for temperatures up to 230 °C. When the test temperature was above 230 °C, the LVDT was attached to a fixture outside the tank and connected to the leaf spring through a 3/8" hole drilled in the tank wall.

A diagram for the electrical connections of the extensional rheometer (ER) is shown in Figure 109 in order to demonstrate the control of different aspects of operation. The temperature of the rheometer was controlled on each side of the tank by separate heating controllers (Omega 2000 series), using a platinum RTD on one side and J thermocouple (TC) on the other. The motors driving each set of rotary clamps were each powered and controlled by their own external controller (Electrocraft BM 352). Finally, the LVDT used for measuring the leaf spring displacement was connected to a signal conditioner (to eliminate noise and amplify the signal), which was then connected to the A/D converter/data acquisition card (Data Translation DT2801) installed in an IBM PC.

The specifications and range of operating conditions of the extensional rheometer were determined both from design considerations and from experimental work, a summary of which is given in Table 10. The temperature range of operation is from room temperature to approximately 320 °C, limited on the upper end by the immersion oil used and the silicon rubber

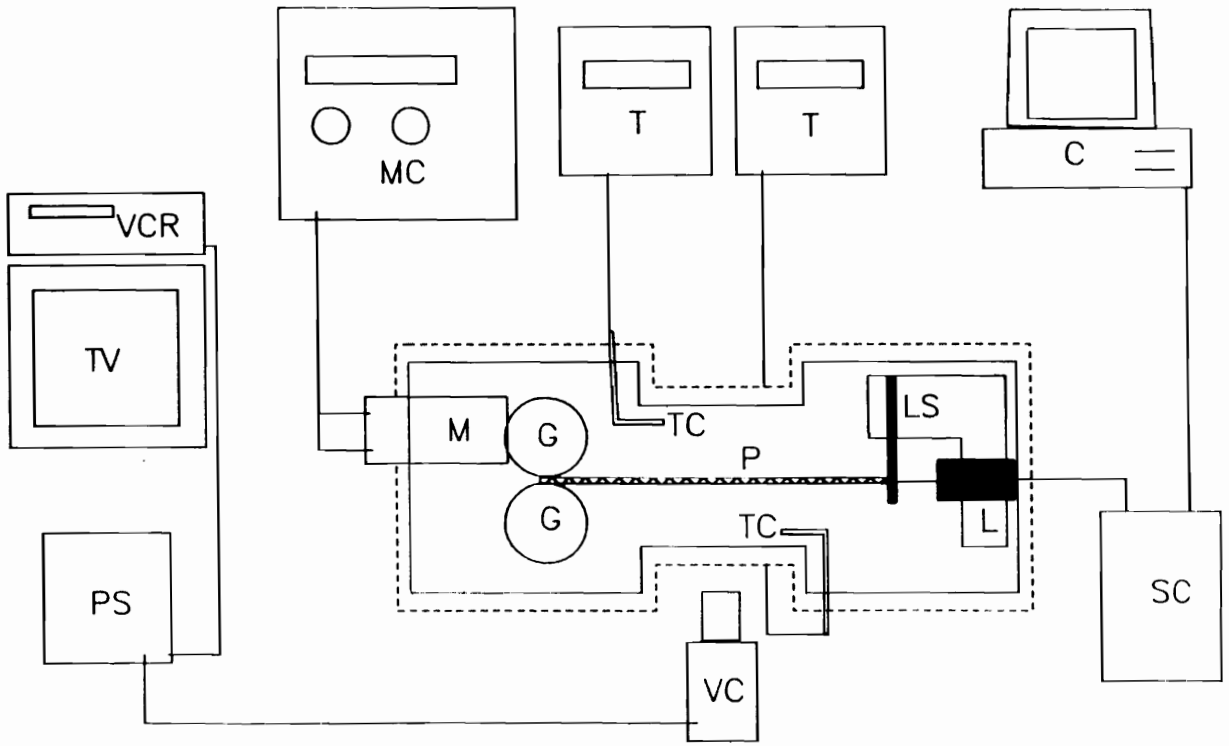

Figure 109. Overall Schematic of Electrical Connections for the ER.

gaskets in the quartz windows. The range of obtainable elongation rates in the rheometer is approximately 0.0005 to 0.5 and could be further modified to increase that range by a factor of 15. Finally, the force resolution with the current leaf spring is approximately 0.001 to 1 Newton (or 0.1 to 100 g), allowing for measurement of elongational viscosities greater than 1000 Pa*s for rate of 0.01 to 0.5 s^{-1} with better than 10 % accuracy (determined by force calibration). Since the force range can be shifted by the use of a different leaf spring and the force measured also depends on the sample cross section, the actual range of sample viscosity which can be measured has not been determined.

B.2 Sample Preparation

As indicated in Chapter 3, samples used for testing in the ER were cylindrically shaped with a diameter of about 0.394" (1 cm) and 9" in length. When possible, samples were made in an Instron Capillary Rheometer (Model 3211) because of the uniform cross section and correct length obtained in the molded samples. Samples of the HBA/HNA copolyester and LLDPE were made in this way. Samples were loaded into the capillary rheometer barrel with frequent tamping, and let melt for 10 minutes at the molding temperature (300 °C for HBA/HNA and 170 °C for LLDPE). After that the samples were slowly cooled in the capillary rheometer barrel over a period of about 1.5 hours, then removed.

Samples of the HPC could not be molded in the capillary rheometer barrel because it was received in powder form. Therefore, samples of HPC E and HPC G were extruded through a 1/4" diameter and 15.4 L/D ratio cylindrical die attached to a Killion Laboratory extruder with a 1"x20" barrel. The material was extruded with die and barrel temperatures in the range 160 to 170 °C for best results. Also, the HPC samples had to be dried and stored under vacuum prior to extrusion to eliminate the formation of gas bubbles in the extruded rods.

After the samples were formed they were then glued to aluminum clips. Both the polymer and aluminum clip surfaces were prepared by prior roughening with a fine grade of

Table 10. Specifications of the Extensional Rheometer (ER).

Property	Specification
Temperature range	Approximately 25 to 320 °C. with uniformity of ±1 °C over the length of the tank.
Extension Rates	0.005 to 0.5 s^{-1} in fixed end configuration. 0.001 to 1 s^{-1} in dual rotary clamp configuration.
Force Measurement	Force measured by the deflection of a leaf spring. Measurement range of 0.001 to 1 Newton (0.1 to 100 grams) in fixed end configuration and with current leaf spring.
Digitization of Output	Data Translation DT2801 ADC with 12 bits of resolution at speeds up to 13000 Hz.
Optical Capability	Two 1"x2" quartz windows in side of tank at the center of the sample.

sandpaper. No chemical etching was needed for the LCPs but a chromic/sulfuric acid etch is generally used to oxidize the surface of polyolefins and was used for the LLDPE. Also, a high temperature epoxy adhesive was used for HPC materials and LLDPE, while a bismaleimide adhesive (Crest # 4446) was used for HBA/HNA.

B.3 Principle of Operation.

The basic principles behind the design of the rheometer was shown in Figure 29 on page 110. A polymer sample floats on top of an oil bath and is held at the test temperature by heat transfer from the oil. For the single rotary clamp configuration, one end of the sample is glued to an aluminum clip (force measurement end) while the other is held by the rotary clamp. At the start of the test, the gears start to rotate at a constant rotation rate, thereby extending the sample at a constant rate of extension. The force is measured by the deflection of a leaf spring, which the aluminum clip at the fixed end is attached to. The deflection of the leaf spring is linearly related to the force on the leaf spring and this is recorded digitally by computer. The deflection of the leaf spring (LS) is measured using a linear voltage displacement transducer (LVDT) and is recorded digitally with a personal computer. Again, the overall system is shown in Figure 109.

In addition to force measurement, the cross sectional area of the sample being elongated is also measured during testing by means of a video camera focused in through the side quartz window. While the strain on the sample can be estimated from a knowledge of the motor speed, the direct measurement is necessary because of previous reports of slippage in the rotary gears [40].

B.4 Operating Procedure.

Equipment Setup. Prior to testing the electrical system for the components of the ER are connected as previously shown in Figure 109. The temperature controllers for the ER are set to the test temperature and the tank is allowed to heat up, which usually takes from 45 to 60 minutes, with a longer equilibration time needed for higher temperatures.

The oils used in the ER tank varied according to the polymer used. A polydimethylsiloxane oil (Dow 200-20) was used for LLDPE. Two oils were generally used for the LCPs as described earlier in Chapter 3. For HPC materials, the top oil was a PDMS oil (Dow 200-50) and the bottom oil was a polyfluoroether oil (Nye Fluoroether Oil 483). For HBA/HNA, the top oil was a polyphenylmethylsilicone oil (Dow 710) while the bottom oil was a polyfluoroether oil (DuPont Krytox 16256). The possibility of polymer miscibility in the oils used was ruled out for the LCPs by comparing the weight of polymer samples before and after annealing in the respective test oils for 15 minutes. No indications of polymer-oil interaction were observed.

Force Calibration. Prior to sample testing (and sometimes also performed after as well), the displacement of the leaf spring was calibrated at the test temperature. Calibration was performed by looping a very thin metal wire around the sample peg and the other end going horizontally sideways over a roller, then vertically downward with a weight hanging onto it as shown in Figure 110a. Usually, 4 or 5 weights were used in the range of 0.5 to 50 grams. A plot of the weight versus leaf spring displacement is given in Figure 110b, where it can be seen that there is a linear relationship between the two (as is also theoretically predicted [208]).

Procedure for testing. The test procedure is rather involved and is given here in a number of steps, assuming the rheometer is setup and the force has been calibrated. Also, the procedure given is that used with the rheometer in a single rotary clamp configuration, which was used for all work appearing in this dissertation.

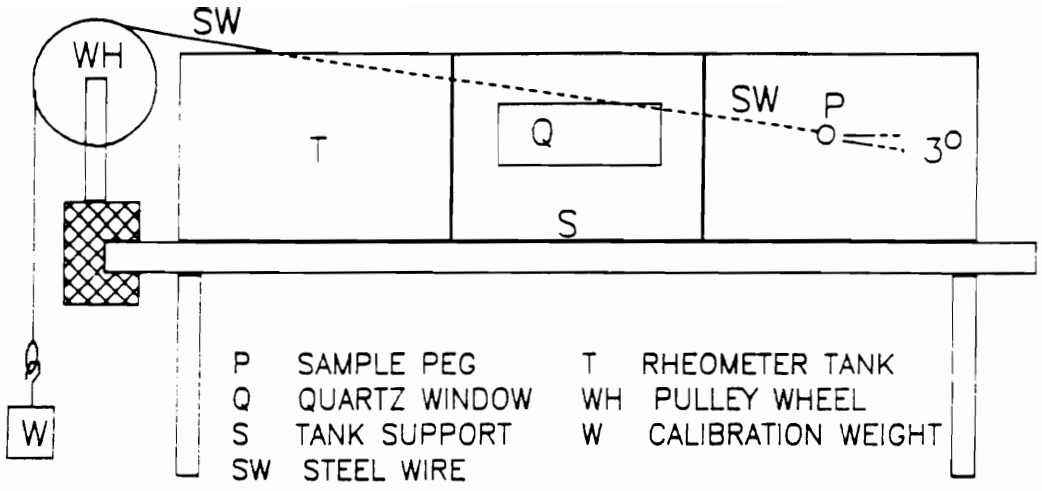

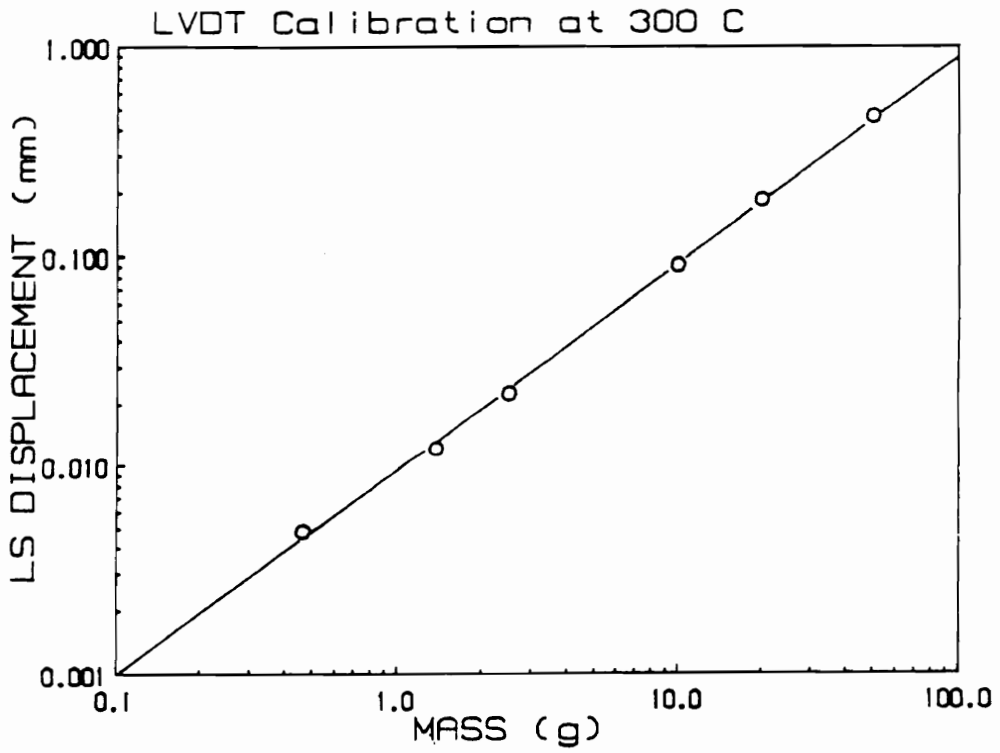

Figure 110. Schematic of (a) calibration technique and (b) representative calibration data for fixed end leaf spring.

1. The covers over the middle of the ER and on the LS end are removed and the sample is inserted into the oil bath with the fixed end connected to the sample peg. The covers are replaced and the time is noted.
2. The LVDT is zeroed as the polymer melts using the program CALIB.BAS, which is similar to the data collection program and therefore not given here.

   Next, the video camera is placed in front of the ER side and the camera is focused.
3. About 4 minutes after sample insertion, the now melted free end of the sample is drawn up into the rotary clamps approximately 3/4 inch. After that the motor is uncoupled and the appropriate motor speed is set for the desired elongation rate, based on the value computed from the velocity of the clamps.
4. The program which records the LVDT displacement (ERF.EXE) is started and parameters are set. These include number of points collected (10,000 used), LVDT gain (depends on material and rate but ranges from 1 to 8), and collection frequency (depends on elongation rate so that data is collected for a total strain of 5). The program waits for a keyboard signal before data recording begins.
5. Approximately 30 seconds before the start of the run or about 10 minutes after sample loading, the video recorder is started and the test number is given.
6. About 1 strain unit of time ($1/\dot{\varepsilon}$) before the sample begins deformation the computer data acquisition is started by hitting the return key. This provides for a baseline at the test start.
7. The elongation of the sample is started by hitting the start switch on the motor controller (or 2 switches in dual rotary clamp configuration).
8. The test proceeds and upon completion of data acquisition, the motor(s) are turned off, the video recording is stopped, and the camera is removed from the rheometer.
9. An set of output data files are created with the raw data (averaged over 5 points) in the form of LVDT displacement at time intervals equal to 5/(collection frequency). This is recorded to floppy disk.
10. The sample just run is removed from the rheometer and the whole procedure is repeated.

A couple of comments should be made about the program which is used to acquire data. The program (ERF.EXE) was written in basic and is used in compiled form. The program collects 10,000 points in a normal run but averages 5 points together and therefore outputs 2,000 points to disk. A copy of the program is reproduced in appendix B.6 with some initial proprietary parts eliminated for obvious reasons.

B.5 Data Treatment

In this section the details for the conversion of the raw data to final values of transient elongational viscosity are presented. The elongational viscosity is defined as:

$$\bar{\eta}_e^+ = \frac{\sigma_{11}^+ - \sigma_{22}^+}{\dot{\varepsilon}} \qquad \text{(B.1)}$$

where

$\sigma_{11}^+ - \sigma_{22}^+ = F(t)/A(t)$

F = force on sample = gKD(t)

K = calibrated spring constant

D(t) = displacement of leaf spring

A(t) = cross sectional area of test rod
= $A_0 \exp[-\varepsilon(t)]$

$\varepsilon(t)$ = Hencky strain = $\int_0^t \dot{\varepsilon}(t)\, dt$

Inserting all of the quantities above into equation B.1 the transient elongational viscosity is now:

$$\bar{\eta}_e^+(t) = \frac{gKD(t)e^{\varepsilon(t)}}{A_0\dot{\varepsilon}(t)} \tag{B.2}$$

The measured elongational viscosity is therefore calculated in terms of the measured quantities A_0, K, D(t), and $\varepsilon(t)$.

Before the final values of $\bar{\eta}_e^+(t)$ are obtained from the measured quantities above, the data is treated for noise reduction and a number of corrections are made. For the measured value of D(t), the first step is to use a Fourier Transform Filter to remove high frequency noise. Generally, the part of the signal with a frequency higher than 50 times the elongation rate is removed, though at very low rates no noise with a frequency lower than 2 Hz has been removed. This is accomplished using a program written in FORTRAN and using the IMSL subroutines FFTRF and FFTRB to calculate the forward and reverse transforms. The name of the program is BFFTF.FOR and a copy is included in Appendix B.6.

The elongational strain $\varepsilon(t)$ is measured via video recording as $\varepsilon(t) = 2\ln(D_0/D(t))$, where D_0 is the diameter of the sample measured on the screen at the start of the test and D(t) is the time dependent diameter. The data is then fit to a polynomial in the form:

$$\varepsilon(t) = A + Bt + Ct^2 + \ldots \tag{B.3}$$

using a least squares type of fit. For the case of the LCPs the data usually was linear and the polynomial was truncated after the second term. For the LLDPE data, at low rates it was found that a 2nd order fit was needed to accurately model the deformation history of the sample. While this sometimes meant that the elongation rate experienced by the polymer changed with time, the changes were usually no more than 25% and never more than 50%. In view of the Newtonian behavior of the LLDPE at the rates involved in this study, it was felt that this had a negligible effect on the results.

Two corrections were applied to the value of A_0 and are briefly described. First, the value of A_0 was corrected for density changes occurring in raising the temperature of the material from room temperature to melt temperature using the factor $(1 + 2\alpha\Delta T)$, where alpha is the thermal expansion coefficient either obtained from the literature or from a knowledge of the densities of the materials at room and melt temperatures (given in Table 3 on page 99). The other correction applied to A_0 is due to the need to initially draw the material into the rotary clamps so that they have a good grip at the start of the test. The correction for this is straightforward and results in approximately a 5.5 % reduction in the value of A_0.

B.6 Programs Used in Extensional Work

ERF.BAS (Data Acquisition During Test)

```
1000 'This program is specifically written to be used with the
1010 'rotary clamp rheometer and is based on PCLAB software,
1020 'example 02. This version is for the fixed end configuration.
1050 'The user of this program specifies the number of data points
1060 'read and the time between readings, which is the internal
1070 'clock period. Later in the program a choice for data output
1080 'is given as well as additional tests.
1120 '
1130 DIM ANALOG.ARRAY%(10001)
1140 INPUT "NUMBER OF VALUES";NUMBER.OF.VALUES%
1150 PRINT
1160 ERROR.VALUE% = 0
1170 CALL SET.ERROR.CONTROL.WORD(ERROR.VALUE%)
1180 HIGH.V! = +10!              'Highest Voltage in Range
1190 LOW.V! = -10!               'Lowest Voltage in Range
1200 RANGE! = HIGH.V!-LOW.V!     'Total Voltage Range
1210 NOC! = 4096!
1220 '
1230 LSB! = RANGE!/NOC!          'Voltage of least significant bit
1240 '
1250 'The next section sets up the A/D
1260 '
1270 TIMING.SOURCE% = 0          'Software trigger, int. clock
1280 '
1290 'Define Scan Channel
1300 '
1310 CLS
1320 INPUT "Enter the channel to be scan";START.CHAN%
1330 PRINT
1340 '
1350 PRINT "This will collect";NUMBER.OF.VALUES%;"data points."
1360 PRINT
1370 INPUT "DESIRED GAIN (1,2,4, or 8)";GAIN%
1380 END.CHAN% = START.CHAN%
1390 CALL SETUP.ADC(TIMING.SOURCE%,START.CHAN%,END.CHAN%,GAIN%)
1400 CALL GET.ERROR.CODE(ERROR.VALUE%)
1410 IF ERROR.VALUE% = 0 GOTO 1440
1420 PRINT "***Illegal channels or gain specified.": PRINT
1430 GOTO 1310
1440 SCALED.LSB! = LSB!/GAIN%    'Calculated scaled LSB
1450 SCALED.LOW! = LOW.V!/GAIN%  'Calculated scaled LOW voltage
1460 '
1470 'Next Set up the Internal Clock
1480 '
1490 INPUT "Enter the Clock Frequency (13 to 12000) ";REQUESTED.FREQ
1500 CLOCK.DIVIDER% = (400000!/REQUESTED.FREQ)-.5
```

```
1510 ACTUAL.FREQ=400000!/CLOCK.DIVIDER%
1520 PRINT "Actual Frequency is ";ACTUAL.FREQ;"Hertz"
1530 '
1540 CALL SET.CLOCK.DIVIDER (CLOCK.DIVIDER%)
1550 '
1560 'This part performs the actual data collection
1570 '
1580 PRINT
1590 INPUT "PRESS RETURN TO START, ENTER <N> TO ABORT TEST";TTST$
1600 IF TTST$="N" THEN GOTO 2210
1610 '
1620 CALL DISABLE.SYSTEM.CLOCK    'Turn off the PC's time of day clock
1630 CALL ADC.SERIES (NUMBER.OF.VALUES%,ANALOG.ARRAY%(0))
1640 CALL ENABLE.SYSTEM.CLOCK     'Turn on the PC's time of day clock
1650 CALL GET.ERROR.CODE(ERROR.VALUE%)  'Clear any error status
1660 IF ERROR.VALUE%<>0 THEN PRINT "Error during acquisition.",ERROR.VALUE%
1670 PRINT
1680 '
1690 'Next either send data to a specific data file and/or repeat
1700 'measurement of data experiment.
1710 '
1720 INPUT "Create Data File and Output Data (Y/N)";O$
1730 IF O$="N" THEN GOTO 2210
1740 INPUT "Name of Data File with NO Extension!";F$
1750 INPUT "ENTER TITLE LINE";T$
1752 INPUT "ENTER ROTATION RATE OF CLAMP 1";VEL1!
1754 INPUT "ENTER ROTATION RATE OF CLAMP 2";VEL2!
1756 RATE!=1.100658E-04*(VEL1!+VEL2!)
1760 '
1770 'The output is divided into two files. The first, xxxxx.DAT is for
1780 'the numerical data (later Fourier Transformed in FORTRAN). The
1784 'second (xxxxxx.INF) contains information about the test run such
1786 'as strain rate number of points, temperature, etc..
1790 '
1792 A$=F$ + ".DAT"
1794 B$=F$ + ".INF"
1796 OPEN A$ FOR OUTPUT AS #1
1800 OPEN B$ FOR OUTPUT AS #2
1810 PRINT #2,T$
1820 PRINT #2,"CLOCK PERIOD= ";1/ACTUAL.FREQ,"SECONDS"
1830 TTIME!=NUMBER.OF.VALUES%/ACTUAL.FREQ
1840 PRINT #2,"TEST PERIOD (SEC)";TTIME!,"EXT. RATE (1/S)";RATE!
1850 PRINT #2,"TIME","LVDT DISPLACEMENT"
1860 INUM% = NUMBER.OF.VALUES%/5!
1870 PERIOD= 5!/ACTUAL.FREQ
1875 STIME!=0!
1880 PRINT #1,INUM%, PERIOD,STIME!
1910 '
1920 'the next boxcar averages 5 points and prints out that average
1930 'value at 5 point intervals.
1932 'The multiplier on the DSPL! variable represents the gain and
1934 'sensitivity of the LVDT. The value of 0.140525 mm/V was calcu-
1936 'lated for an 050 HR LVDT with 6.025 mV/mil output at 3.0 V(rms)
1938 'excitation and gain of 10 in the signal conditioner.
1940 '
1950 FOR C%=0 TO NUMBER.OF.VALUES%-5 STEP 5
```

```
1960   AV! = ANALOG.ARRAY%(C%) + ANALOG.ARRAY%(C% + 1) + ANALOG.ARRAY%(C% + 2)
1970   AV! = (AV! + ANALOG.ARRAY%(C% + 3) + ANALOG.ARRAY%(C% + 4))/5!
1980   DSPL! = ((AV!*SCALED.LSB!) + SCALED.LOW!)*.140525
2000   PRINT #1,DSPL!
2010 NEXT C%
2190 CLOSE #1
2195 CLOSE #2
2200 '
2210 'At this point program asks if another data set is to be
2220 'gathered. If yes, starts again at 1360.
2230 '
2240 PRINT: INPUT "ALRIGHT TO PROCEED";PROC$
2250 IF PROC$ = "N" THEN 1710
2260 PRINT
2270 INPUT "Do you want to collect another data set";ANOT$
2280 PRINT
2290 IF ANOT$ = "Y" THEN GOTO 1310
2300 PRINT
2310 PRINT "***PROGRAM COMPLETED***"
2320 END
```

BFFTF.FOR (Fourier Transform Noise Filter)

```
C  Program BFFTF
C
C  This program calculates the Fast Fourier Transform of discrete
C  data, specifically to eliminate noise from the experimental
C  data from the dual rotary clamp extensional rheometer.
C
C  The data is read from an input file and then the Fourier Transform
C  is calculated. The data is input to the matrix SEQ and output to
C  the matrix COEF. This will then be output to a file.
C
C  This program is based of FFTF.FOR but allows a number of files to
C  be processed at once, being input from the file: BFFTF.DAT
C  The format for the file is L1: number files, L2-L(N+1): infile,
C  outfile.
C
C  PARAMETERS OR VARIABLES
C    INFILE   - matrix containing input file names (max. 20)
C    OUTFILE  - matrix containing output file names (max. 20)
C    NFILE    - number of files to be run
C    N        - number of points
C    I,J,K    - index variables
C    COEF(I)  - coefficient matrix for transformed variable
C    SEQ(I)   - input variable to be transformed
C    PERIOD   - time spacing between points
C    T        - total time period for data collection
C    W        - frequency (=index/T)
C    FCUT     - cutoff frequency
C    NCUT     - index for cutoff frequency
C    FFTRF    - subroutine which performs forward transform
C    FFTRB    - subroutine which performs backward transform
C
C  Start of program.
     CHARACTER*14 INFILE(20), OUTFILE(20)
     INTEGER NCUT, NFILE,I,J,K,L,N
     REAL COEF(2000), SEQ(2000), PERIOD, T, W, STIME, FCUT
     EXTERNAL FFTRF, FFTRB
C  Input file if opened and names of data files are read.
C
     OPEN(2,FILE='BFFTF.DAT')
     READ(2,*) NFILE
     DO 50 I=1, NFILE
       READ(2,*) INFILE(I), OUTFILE(I)
50   CONTINUE
     CLOSE(2)
C  This part of the program gives the choice of setting a cutoff
C  frequency. Same frequency used for entire batch.
     WRITE(*,*) 'Enter a 1 to set a cutoff frequency'
     READ(*,*) CUT
     IF (CUT.NE.1) GOTO 60
       WRITE(*,*) 'Input Cutoff Frequency'
       READ(*,*) FCUT
60   CONTINUE
C  Start the main function of Fourier Transform
```

```
      DO 900 II=1, NFILE
C
C  Read in data file
C
      OPEN(6,FILE=INFILE(II))
      READ(6,*) N, PERIOD, STIME
      DO 100 I = 1, N
        READ(6,*) SEQ(I)
100   CONTINUE
      CLOSE(6)
C
C  Now call Fourier Transform Routine
      CALL FFTRF(N,SEQ,COEF)
C
C  Now apply the cutoff frequency if one is to be set here.
      IF (FCUT.EQ.0.) GOTO 120
        NCUT=INT(FCUT*N*PERIOD+1.)
        DO 110 JJ=NCUT, N
          COEF(JJ)=0.
110     CONTINUE
120   CONTINUE
C
C  This part of the program takes the inverse Fast Fourier Transform
C  of the now 'cleaned' data.
      CALL FFTRB(N,COEF,SEQ)
C  Now print out the results. Output is the index, SEQ, and COEF.
C  Note: Frequency=index/(clock period.*#pts.)
C
      OPEN(8,FILE=OUTFILE(II),STATUS='NEW')
      WRITE(8,190) N,PERIOD,STIME
190   FORMAT(1X,I8,6X,2F14.8)
      DO 300 J=1,N
        WRITE(8,220) SEQ(J)/N
220   FORMAT(2X,F14.6)
300   CONTINUE
      CLOSE(8)
900   CONTINUE
      STOP
      END
```

Appendix C. Doi Theory Calculations

In this appendix some of the details for carrying out the calculations for the Doi theory are provided. This includes the method for the specification of the parameters and a listing of the computer programs used to carry out the calculations.

C.1 Determination of the adjustable parameters

Theoretical Evaluation. The parameters which had to be evaluated before calculations could be made using the Doi theory were ckT, U, D_r, and A (additional parameter for rod-solvent contribution to stress). Material properties used to calculate the parameters above were given in Table 3 and in Table 11 while a summary of the resulting parameter values is given in Table 9 on page 212.

The grouping of ckT is a kinetic factor and evaluation of this group depends on the determination of c, the concentration of rods per unit volume. This can be calculated with a knowledge of the LCP density ρ, number average molecular weight $\overline{M}_N$, and Avagadro's number N_0 with the formula:

Table 11. Properties of LCPs used in Doi Theory Calculations.

$$c = \frac{\rho N_0}{\overline{M}_N} \tag{C.1}$$

The dimensionless interaction potential U is defined by the Doi theory [39] as:

$$U = \nu_2 c d L^2 \tag{C.2}$$

where ν_2 is a constant approximately equal to 1, c is the concentration determined from above, d is the diameter of the rod, and L is the length of the rod. A value of 1 was used for ν_2 for lack of a better estimate, the rod diameters used were based on values estimated from WAXS [171,198], and the length of the molecules were calculated from a knowledge of $\overline{M}_R$, the average molecular weight of a repeat unit, and the average length of a repeat unit $\overline{L}_0$ as calculated from WAXS measurements for individual moities and a knowledge of composition.

The parameter D_r can be calculated according to the Doi theory in two ways. First, it can be calculated based on a knowledge of the the dilute solution rotational diffusion coefficient D_{ro} as follows:

$$D_r = \nu_1 (cL^3)^{-2} D_{ro} \tag{C.3}$$

where the quantity ν_1 is a constant on the order of 1300 [180] and the other constants have been defined. Alternately, at very low rates (within the Newtonian range) the value of D_r can be determined as:

$$D_r = \frac{ckT}{10\eta} \tag{C.4}$$

Because of uncertainty in such quantities as ν_1, d, D_{ro}, and L (due to chain flexibility and polydispersity), the second method was thought to be more valid and was used. Additionally, calculations were made using both methods for the HPC EF system at 210 °C, with values of 9.94 and 12.2 determined for the two methods, respectively.

The last parameter to be determined was the coefficient A, which describes the magnitude of the contribution to stress from rod-solvent interaction. The coefficient A is defined as

$$A = \frac{D_r}{D_{ro}} = \nu_1(cL^3)^{-2} \qquad (C.5)$$

and was determined from the molecular parameters on the right side of the equation.

Experimental Fitting. In order to fully investigate the potential of the Doi theory to model the flow behavior of LCPs, all four parameters described in the last section were treated as being experimentally adjustable. The procedure for determining these parameters using the experimental results from HPC EF and HBA/HNA is described here.

The parameter U describes the strength of molecular interactions and its specification determines the equilibrium state of the material. For experimental fitting of the isotropic HPC melt, U was therefore limited to the range $0 \leq U \leq 8/3$. One method of finding U is to use the ratio of first normal stress difference to the shear stress. However, this could not be done because the values of N1 were not thought to be adequately reliable. Instead, a few values of U were tried in order to evaluate the equations for a range of molecular interaction and these were 0, 2.0, and 2.5. For the materials in the liquid crystalline state, values of U were limited to the range $U \geq 3$. Again, several values were chosen to represent varying degrees of intermolecular potential. Values investigated were 3, 4, 6, and 10 for HPC EF (190 °C) and 4, 6, 10, and 25 for HBA/HNA.

Once the value of U was specified above, the steady state values of shear stress obtained from the transient stress growth tests were then used to detemine the values of D_r. The actual experimental quantity used to determine D_r was the ratio of shear stress at the highest rate measured to that at the lowest rate measured (rates are given in Table 4 on page 107). This method then treats the parameter D_r as the reciprocal of a relaxation time, which is consistent with the Doi theory [182].

After the values of U and D_r have been determined as described above, the value of ckT is determined next. This factor is found using the steady state value of the shear stress at the lowest rate tested for transient shear stress growth.

The last parameter to be experimentally fitted is A, which was done using dynamic rate sweep data since no steady shear values could be obtained at high rates in the RMS. One set of values of (U,D_r,ckT) were chosen for each material and held constant while values of A were tried, ranging from 10^{-5} to 1. Since the purpose of this modification was to see if the addition of rod solvent affects would provide for at least semi-quantitative agreement of the theory with experiment, no effort was made to find a best fit value of A at this time.

C.2 Doi Theory Computer Programs

The programs DOIT6.FOR (shear) and DOIE3B.FOR (elongation) were used for all of the calculations for the Doi theory. The programs were written in basic and compiled using MS FORTRAN 4.1 on an IBM AT compatible computer. The two programs appear in order on the next several pages.

DOIT6.FOR

```
      PROGRAM DOIT6
C-----------------------------------------------------------------------
C  Program name  : DOIT6
C  Written By    : Don Baird, Tom Wilson, and Carl Reed
C  Update (Carl) : 06-25-1989 Modified for data input from console
C  Purpose       : Calculate orientation order parameter and stress in
C                : Doi's theory for shear flow, including term for rod-
C                : solvent effects (3rd term). 6 COMPONENTS OF Sij
C-----------------------------------------------------------------------
C  Variables and Parameters
C   Y(i)        Orientation order parameter Y(1)=S11,Y(2)=S22,Y(3)=S33,
C              Y(4)=S12, Y(5)=S13, Y(6)=S23
C   YPRIME(i)   Derivatives of Y(i).
C   X           Variable denoting time
C   T           ckT (concentration, Boltsmanns const., Temperature)
C   SR           strain rate
C   D0           Rotational diffusion coefficient for concentrated,
C              unoriented solution.
C   U           Dimensionless interaction potential from Doi
C   SIGMA(i)    Stress tensor. Same assignments as for Sij.
C   A           D0=A*Dro, where Dro is the rotational diffusion
C              coefficient for dilute solutions. See Doi Theory.
C -----------------------------------------------------------------------
C
C   CALCULATES ORIENTATION ORDER PARAMETER AND STRESSES
C
      CHARACTER*14  OUTFILE
      INTEGER N,METH,MITER,INDEX,IWK(6),IER,K
      REAL Y(6), YPRIME(6),WK(103), X,TOL,XEND,H,U,S,T,SR,SIGMA(6),A
      COMMON D0, SR, U
      EXTERNAL FCN,FCNJ
      N=6
C  INPUT PARAMETERS REQUIRED BY DGEAR
      TOL = 0.0001
      H= 0.00001
      METH = 2
      MITER = 2
      INDEX = 1
C  INPUT INITIAL CONDITIONS
      X = 0.0
      Y(1) = 0.4843402
      Y(2) = -0.2146679
      Y(3) = -0.2696723
      Y(4) = 0.2036518
      Y(5) = 0.000
      Y(6) = 0.000
C  INPUT THE REMAINING PARAMETERS OF CKT, U, AND SR. U IS INITIALLY
C  CALCULATED FROM THE THEORY BUT MAY BE ADJUSTED TO MAKE THE THEORY FIT
C  THE EXPERIMENTAL RESULTS.
C
600   WRITE(*, 601)
601   FORMAT(/' Enter values for U, T, SR, D0, A and TMD')
      READ(*,*) U, T, SR, D0, A, TMD
```

```
      WRITE(*, 602) U, T, SR, D0, A
  602  FORMAT(' VALUES ARE: ', F8.3, F11.1, 2F10.5, E13.5/)
      WRITE(*, 603)
  603  FORMAT(' ENTER 0 TO CONTINUE; ENTER 1 TO RE-ENTER DATA'/)
      READ(*,*) JJ
      IF(JJ .NE. 0) GOTO 600
   50  WRITE(*, 604)
  604  FORMAT(' Enter filename for output data file, enclosed in quotes'/
     1/'       Example: ''OUTPUT.DAT'' '/)
      READ(*,*, ERR = 90) OUTFILE
      WRITE(*, 605)
  605  FORMAT(/'    Beginning calculation . . . '/)
C
      OPEN(6,FILE = OUTFILE, STATUS = 'NEW')
      WRITE(6,100) T,SR,D0,U,A
   100 FORMAT(1X,F11.3, F12.5, F12.6, F10.3, E13.5)
      WRITE(6,*) 'TIME    DR     S     S12    SIG12    N1'
C
C  THE SUBROUTINE DGEAR IS NOW CALLED.  IT RETURNS VALUES OF Y(I)
C
      DO 10 K = 1,100
      XEND = FLOAT(K)/TMD
      CALL DGEAR(N,FCN,FCNJ,X,H,Y,XEND,TOL,METH,MITER,INDEX,IWK,WK,IER)
      IF(IER.GT.128) GO TO 20
C  CALCULATE THE STRESSES
      S = Y(1)**2+Y(2)**2+Y(3)**2+2.*Y(4)**2+2*Y(5)**2+2*Y(6)**2
      DR = D0/(1.-1.5*S)**2
      E = A*T*SR*Y(4)/(2*D0)
      RN1=3.*T*((1.-U/3.)*Y(1)-U*(Y(1)**2+Y(4)**2 -S/3.)+U*Y(1)*S
     +-(1.-U/3.)*Y(2)+U*(Y(2)**2+Y(4)**2-S/3.-Y(2)*S))+E*(Y(1)-Y(2))
      RN2 = 3.*T*((1.-U/3.)*Y(2)-U*(Y(2)**2+Y(4)**2-S/3.-Y(2)*S)
     +-(1.-U/3.)*Y(3)+U*(Y(3)**2-S/3.-Y(3)*S))+E*(Y(2)-Y(3))
      SIGMA(4) = 3.*T*((1.-U/3.)*Y(4) - U*(Y(4)*Y(1)+Y(4)*Y(2)-
     +Y(4)*S))+E*Y(4)
C  PRINT OUT RESULTS FOR EACH TIME INCREMENT: t, DR, S, S12, SIG12, N1
C
      WRITE(6,110) X,DR,S,Y(4),SIGMA(4),RN1
   110 FORMAT(F8.2,1X,F11.5,1X,F10.5,1X,F10.5,2F11.2)
    10 CONTINUE
C  PRINT OUT THE FINAL VALUES OF Sij.
      WRITE(6,400) Y(1), Y(2), Y(3), Y(4), Y(5), Y(6)
  400  FORMAT(/,6F10.6,/)
      CLOSE(6)
      WRITE(*, 610)
  610  FORMAT('    Calculation complete. '/)
      STOP
   90  WRITE(*, 611)
  611  FORMAT(/' You forgot the quotes, redo from start . . .'/)
    20 CONTINUE
      goto 50
      STOP
      END
C
C  THE FUNCTION SUBROUTINE FNC CONTAINS THE RIGHT SIDE OF THE DIFFEREN-
C  TIAL EQUATIONS.
      SUBROUTINE FCN(N,X,Y,YPRIME)
```

```
      INTEGER N
      REAL X,Y(N),YPRIME(N),S,DR,D0,SR,U
      COMMON D0,SR,U
      S = Y(1)**2+Y(2)**2+Y(3)**2+2.*Y(4)**2+2*Y(5)**2+2*Y(6)**2
      DR = D0/(1.-1.5*S)**2
      YPRIME(1)=-6.*DR*((1.-U/3.)*Y(1)-U*(Y(1)**2+Y(4)**2+Y(5)**2
     +-S/3.) + U*Y(1)*S) +2.*SR*Y(4)*(2./3.-Y(1))
      YPRIME(2) = -6.*DR*((1.-U/3.)*Y(2)-U*(Y(2)**2+Y(4)**2+Y(6)**2
     +-S/3.-Y(2)*S))-SR*Y(4)*2./3.-2.*SR*Y(4)*Y(2)
      YPRIME(3)= -6.*DR*((1.-U/3.)*Y(3)-U*(Y(3)**2+Y(5)**2+Y(6)**2
     +-S/3.-Y(3)*S)) - SR*Y(4)*2./3.-2.*SR*Y(4)*Y(3)
      YPRIME(4) = -6.*DR*((1.-U/3.)*Y(4) - U*(Y(4)*Y(1)+Y(4)*Y(2)
     + +Y(5)*Y(6)-Y(4)*S))+SR/3.+SR*Y(2)-2.*SR*Y(4)**2
      YPRIME(5)= -6.*DR*((1-U/3.)*Y(5)-U*(Y(1)*Y(5)+Y(4)*Y(6)+
     +Y(5)*Y(3)-Y(5)*S))+SR*(Y(6)-2.*Y(4)*Y(5))
      YPRIME(6)= -6.*DR*((1-U/3.)*Y(6)-U*(Y(4)*Y(5)+Y(2)*Y(6)+
     +Y(3)*Y(6)-Y(6)*S))-2.*SR*Y(4)*Y(6)
      RETURN
      END
      SUBROUTINE FCNJ(N,X,Y,PD)
      INTEGER N
      REAL Y(N), PD(N,N),X
      RETURN
      END
```

DOIE3B.FOR

```
      PROGRAM DOIE3B
$DEBUG
C-----------------------------------------------------------------------
C  Program name: DOIE3B
C  Written By  : Tom Wilson, Don Baird, and Carl Reed
C  Date        : 04-01-1988 10:20:54 / last revision 10-07-90
C  Purpose     : Calculate stresses and orientation order parameter for
C              : extensional flow case, includes rod-solvent term for
C              : stress and six components of Sij
C-----------------------------------------------------------------------
C
C   THIS PROGRAM CALCULATES COMPONENTS OF THE STRESS AND ORIENTATION ORDER
C   PARAMETER TENSORS FROM DOI'S THEORY USING THE DIFFERENTIAL EQUATION
C   SOLVER,DGEAR.  THE INPUT VARIABLES ARE THE CONCENTRATION RELATED
C   PARAMETER, U, THE PRODUCT OF TEMPERATURE, CONCENTRATION, AND BOLTZ-
C   MAN CONSTANT, CKT, THE SHEAR RATE, SR, AND THE PRODUCT v1(cL¢3)¢-2
C   THE INITIAL VALUES OF THE ORDER PARAMETER TENSOR ARE ALSO INPUT.
C
C   PARAMETERS AND VARIABLES
C   ------------------------
C   THE CORRESPONDENCE BETWEEN THE COMPONENTS OF THE ORDER PARAMETER
C   S(I,J) PARAMETER TENSOR, S(I,J), AND THE STRESS TENSOR,SIGMA(I,J)
C   AND THE VARIABLES USED IN THE FORTRAM PROGRAM ARE LISTED AS FOLLOWS:
C   Y(1) = S(1,1), Y(2) = S(2,2), Y(3) = S(3,3), Y(4) = S(1,2), Y(5) =
C   S(1,3), AND Y(6) = S(2,3).  FOR THE STRESSES SIGMA(1,1) = SIG(1)
C   SIGMA(2,2) = SIG(2).....SIGMA(2,3) = SIG(6)
C
C   T      = ckT
C   D0     = Dr = rotary diffusion coefficient for a concentrated
C            isotropic solution.
C   DR     = rotary diff. coef. for concentrated anisotropic solution
C   U      = Dimensional interaction potential
C   SR     = Extensional strain rate
C   C      = v1*(cL¢3)¢(-2) = Dr/Dro
C   F(i)   = Component of dSij/dt due to Brownian motion
C   ETAi   = The two calculated extensional viscosities.
C   S      = defined as SijSij
C   SS     = scalar order parameter SS=(3/2*S)**1/2
C   TEND   = factor to change total time of calc., ttime=100/tend.
C
C   Other variables are generally those needed for the subroutine
C   DGEAR and can be found in a manual for IMSL Math subroutines.
C
      CHARACTER*14  OUTFILE
      INTEGER N,METH,MITER,INDEX,IWK(6),IER,K,I,J,JJ
      REAL Y(6),SIGMA(6),G(6),YPRIME(6),WK(103),X,TOL,XEND,H,S,F(6),
     &D0,SR,U,T,DR,ETA1,ETA2,C,SS
      COMMON D0,SR,U
      EXTERNAL FCN,FCNJ
      N=6
C  INPUT PARAMETERS REQUIRED BY DGEAR
      TOL = 0.00001
      H= 0.000001
      METH = 2
```

```
      MITER = 2
      INDEX = 1
C  INPUT INITIAL CONDITIONS
600   X = 0.0
      WRITE(*,190)
190   FORMAT(1X,' ENTER Sij FROM KEYBOARD? 0=YES, 1=NO',/)
      READ(*,*) NENT
      IF (NENT.EQ.1) GOTO 240
      WRITE(*.195)
195   FORMAT(' ENTER S11,S22,S33,S12,S13,S23',/)
      READ(*,*) (Y(J),J=1,6)
      GOTO 245
240   Y(1) = 0.5948411
      Y(2) = -0.2974205
      Y(3) = -0.2974205
      Y(4) = 0.0000
      Y(5) = 0.0000
      Y(6) = 0.0000
245   WRITE(*,250) X,(Y(I),I=1,6)
250   FORMAT(/,F6.2,1X,6F8.4)
C
C  INPUT THE REMAINING PARAMETERS OF CKT, U, SR, AND D0. U IS INITIALLY
C  CALCULATED FROM THE THEORY BUT MAY BE ADJUSTED TO MAKE THE THEORY FIT
C  THE EXPERIMENTAL RESULTS. PARAMETERS INPUT FROM KEYBOARD.
      WRITE(*, 601)
601   FORMAT(/,' Enter values for U, T, SR, D0, C, TEND'/)
      READ(*,*) U, T, SR, D0, C, TEND
      WRITE(*, 602) U, T, SR, D0, C, TEND
602   FORMAT(' VALUES ARE: ', F7.4, F10.1, 4F11.5 /)
      WRITE(*,603)
603   FORMAT(' ENTER 0 TO CONTINUE, ENTER 1 TO RE-ENTER DATA'/)
      READ(*,*) JJ
      IF (JJ.NE.0) GOTO 600
50    WRITE(*, 604)
604   FORMAT(' ENTER filename for output data file. enclosed in quotes'/
     &/'       Example:  ''OUTPUT.DAT''  '/)
      READ(*,*,ERR=90) OUTFILE
      WRITE(*,605)
605   FORMAT(/'   Beginning Calculation . . . '/)
C
      OPEN(6,FILE=OUTFILE, STATUS='NEW')
      WRITE(6,*) 'ckT   SR    D0    U    C'
      WRITE(6,100) T, SR, D0, U, C
100   FORMAT(1X, F11.1, F12.5, F10.5, F10.3, F15.5,/)
C
C  THE SUBROUTINE DGEAR IS NOW CALLED.  IT RETURNS VALUES OF Y(I) AND
C  F(I).  THE SIG(I)'S ARE THEN COMPUTED AT EACH TIME INTERVAL
C
      WRITE(6,*) 'Time   SIG11   ETA   S11    S   DR'
      WRITE(6,110) X, SIGMA(1), ETA1, Y(1), S, D0
      DO 10 K = 1,100
      XEND = FLOAT(K)/TEND
      S=Y(1)**2+Y(2)**2+Y(3)**2+2.*Y(4)**2+2.*Y(5)**2+2.*Y(6)**2
      DR = D0/(1.-1.5*S)**2
      CALL DGEAR(N,FCN,FCNJ,X,H,Y,XEND,TOL,METH,MITER,INDEX,IWK,WK,IER)
```

```
      IF(IER.GT.128) GO TO 20
C  VALUES OF STRESSES SIG(I) AND EXTENSIONAL VISCOSITIES ARE CALCULATED
C  FROM VALUES OF F(I) RETURNED FROM DEGEAR. ETA1 AND ETA2 ARE THE TWO
C  EXTENSIONAL VISCOSITIES, NOTING HERE ETA2 SHOULD BE ZERO AS A CHECK.
C
      S=Y(1)**2+Y(2)**2+Y(3)**2+2.*Y(4)**2+2.*Y(5)**2+2.*Y(6)**2
      DR=D0/(1.-1.5*S)**2
      F(1) = -6.*DR*((1.-U/3.)*Y(1)-U*(Y(1)**2+Y(4)**2+Y(5)**2-S/3.-
     &Y(1)*S))
      F(2) = -6.*DR*((1.-U/3.)*Y(2)-U*(Y(2)**2+Y(4)**2+Y(6)**2-S/3.-
     &Y(2)*S))
      F(3) = -6.*DR*((1.-U/3.)*Y(3)-U*(Y(3)**2+Y(5)**2+Y(6)**2-S/3.-
     &Y(3)*S))
      WRITE(*,500) S,DR,Y(1),D0
500   FORMAT(/,4F12.3)
      SIGMA(1)= -T*F(1)/(2.*DR)+0.75*T*SR*C/D0*Y(1)*(Y(1)+1./3.)
      SIGMA(2)= -T*F(2)/(2.*DR)+0.75*T*SR*C/D0*Y(1)*(Y(2)+1./3.)
      SIGMA(3)= -T*F(3)/(2.*DR)+0.75*T*SR*C/D0*Y(1)*(Y(2)+1./3.)
      ETA1 = (SIGMA(1) - SIGMA(2))/SR
      ETA2 = (SIGMA(2) - SIGMA(3))/SR
      SS = (1.5*S)**(.5)
C  PRINT OUT RESULTS FOR EACH TIME INCREMENT: SR, DR, Y(I), SIG(I)
C
      WRITE(6,110) X, SIGMA(1), ETA1, Y(1), SS, DR
110   FORMAT(F9.4, 1X, 2F11.3, 2F10.6, F12.5)
 10   CONTINUE
      CLOSE(6)
      WRITE(*,610)
610   FORMAT('   Calculation complete.   '/)
      GOTO 20
 90   WRITE(*,611)
611   FORMAT(/' You forgot the quotes, redo from start . . . '/)
      GOTO 50
 20   CONTINUE
      STOP
      END
C
C  THE FUNCTION SUBROUTINE FNC CONTAINS THE RIGHT SIDE OF THE DIFFEREN-
C  TIAL EQUATIONS.
      SUBROUTINE FCN(N,X,Y,YPRIME)
      INTEGER N,J
      REAL X,Y(6),YPRIME(6),S,T,G(6),F(6),DR,D0,SR,U
      COMMON D0,SR,U
      S = Y(1)**2+Y(2)**2+Y(3)**2+2.*Y(4)**2+2.*Y(5)**2+2.*Y(6)**2
      DR = D0/(1.-1.5*S)**2
      F(1) = -6.*DR*((1.-U/3.)*Y(1)-U*(Y(1)**2+Y(4)**2+Y(5)**2-S/3.-
     &Y(1)*S))
      F(2) = -6.*DR*((1.-U/3.)*Y(2)-U*(Y(2)**2+Y(4)**2+Y(6)**2-S/3.-Y(2)
     &*S))
      F(3) = -6.*DR*((1.-U/3.)*Y(3)-U*(Y(3)**2+Y(5)**2+Y(6)**2-S/3.-
     &Y(3)*S))
      F(4) = -6.*DR*((1.-U/3.)*Y(4) - U*(Y(4)*Y(1)+Y(4)*Y(2)+Y(5)*Y(6)-
     &Y(4)*S))
      F(5) = -6.*((1.-U/3.)*Y(5) - U*(Y(5)*(Y(1)+Y(3))+Y(4)*Y(6)-Y(5)*S
     &))*DR
      F(6) = -6.*((1.-U/3.)*Y(6) - U*(Y(4)*Y(5)+Y(6)*(Y(2)+Y(3))-Y(6)*
```

```
     &S))*DR
C SR is the extension rate here
      G(1) = SR*(2./3.+Y(1)-3.*Y(1)**2)
      G(2) = (-1./3.-Y(1)-Y(2)-3.*Y(2)*Y(1))*SR
      G(3) = (-1./3.-Y(1)-Y(3)-3.*Y(1)*Y(3))*SR
      G(4) = (1./2.-3.*Y(1))*SR*Y(4)
      G(5) = (1./2.-3.*Y(1))*SR*Y(5)
      G(6) = -SR*Y(6)*(1+3*Y(1))
C YPRIME IS NOW CALCULATED FROM F&G
      DO 200 J = 1,6
      YPRIME(J)=F(J)+G(J)
200   CONTINUE
      RETURN
      END
      SUBROUTINE FCNJ(N,X,Y,PD)
      INTEGER N
      REAL Y(N),PD(N,N),X
      RETURN
      END
```

Appendix D. Dynamic Shear Data

Table 12. Time Sweep of 60HBA/PET at 275 °C and 10Hz.

Time [s]	G′ [Pa]	G″ [Pa]	η^* [Pa*s]	tanδ
0.0	887	2060	224	2.323
1.0	846	1908	209	2.255
3.0	794	1722	190	2.169
5.0	749	1603	177	2.140
7.0	716	1531	169	2.138
9.0	703	1451	161	2.063
11.0	662	1440	158	2.175
13.0	663	1388	154	2.092
15.0	651	1364	151	2.095
17.0	643	1333	148	2.071
19.0	636	1322	147	2.079
21.0	630	1290	144	2.048
23.0	612	1267	141	2.070
25.0	602	1245	138	2.069
27.0	608	1237	138	2.036
29.0	603	1219	136	2.020
31.0	605	1218	136	2.012
33.0	590	1209	135	2.050
35.0	585	1180	132	2.017
37.0	584	1183	132	2.026
39.0	588	1170	131	1.988
41.0	587	1149	129	1.959
43.0	586	1139	128	1.943
45.0	600	1133	128	1.890
47.0	570	1139	127	2.000
49.0	570	1134	127	1.989
51.0	576	1112	125	1.932
53.0	568	1122	126	1.977
55.0	559	1121	125	2.004
57.0	590	1130	128	1.915
59.0	568	1119	126	1.970

Table 13. Time Sweep of HPC EF at 190 °C and 10Hz.

Time [s]	G′ [Pa]	G″ [Pa]	η^* [Pa*s]	tanδ
0.0	4547	6035	756	1.327
2.0	4581	6589	803	1.438
4.0	4718	7023	846	1.489
6.0	4847	7244	872	1.495
8.0	4942	7406	890	1.499
10.0	5019	7517	904	1.498
12.0	5107	7653	920	1.499
14.0	5176	7728	930	1.493
16.0	5238	7831	942	1.495
18.0	5314	7890	951	1.485
20.0	5370	7941	959	1.479
22.0	5418	8006	967	1.478
24.0	5482	8049	974	1.468
26.0	5530	8116	982	1.468
28.0	5564	8149	987	1.465
30.0	5597	8191	992	1.463
32.0	5646	8207	996	1.454
34.0	5719	8237	1003	1.440
36.0	5772	8297	1011	1.437
38.0	5803	8305	1013	1.431
40.0	5790	8328	1014	1.438
42.0	5859	8333	1019	1.422
44.0	5887	8363	1023	1.421

Table 14. Time Sweep of HPC EF at 210 °C and 10Hz.

Time [s]	G′ [Pa]	G″ [Pa]	η^* [Pa*s]	tanδ
0.0	3197	8169	877	2.555
2.0	2726	7410	790	2.718
4.0	2791	7381	789	2.645
6.0	2875	7350	789	2.557
8.0	2932	7159	774	2.442
10.0	2929	7031	762	2.400
12.0	2991	6934	755	2.318
14.0	3091	6805	748	2.202
16.0	3128	6726	742	2.150
18.0	3217	6705	744	2.084
20.0	3268	6703	746	2.051
22.0	3346	6705	749	2.004
24.0	3456	6670	751	1.930
26.0	3529	6704	758	1.900
28.0	3663	6742	767	1.841
30.0	3784	6784	777	1.793
32.0	3927	6854	790	1.745
34.0	4029	6894	799	1.711
36.0	4170	6910	807	1.657
38.0	4280	6956	817	1.625
40.0	4469	7072	837	1.582
42.0	4639	7093	848	1.529
44.0	4765	7173	861	1.505

Table 15. Time Sweep of HPC G at 200 °C and 10Hz.

Time [s]	G′ [Pa]	G″ [Pa]	η^* [Pa*s]	tanδ
0.0	47190	18570	5072	0.394
2.0	48020	18650	5152	0.388
4.0	48730	18830	5224	0.386
6.0	49390	18940	5289	0.383
8.0	49970	19060	5349	0.381
10.0	50570	19120	5406	0.378
12.0	51040	19280	5456	0.378
14.0	51570	19350	5508	0.375
16.0	51990	19440	5550	0.374
18.0	52490	19480	5599	0.371
20.0	52890	19560	5639	0.370
22.0	53290	19590	5677	0.368
24.0	53640	19660	5712	0.367
26.0	53980	19690	5746	0.365
28.0	54340	19700	5781	0.363
30.0	54690	19800	5816	0.362
32.0	54970	19810	5843	0.360
34.0	55240	19850	5870	0.359
36.0	55630	19930	5909	0.358
38.0	55920	20010	5939	0.358
40.0	56210	19990	5966	0.356
42.0	56480	19970	5990	0.354
44.0	56770	20050	6020	0.353

Table 16. Time Sweep of HPC G at 240 °C and 10Hz.

Time [s]	G′ [Pa]	G″ [Pa]	η^* [Pa*s]	tanδ
0.0	35150	20710	4080	0.589
1.0	34060	19800	3940	0.581
2.0	33090	18930	3812	0.572
3.0	32360	18280	3717	0.565
4.0	31680	17670	3627	0.558
5.0	31430	17230	3584	0.548
6.0	31280	16980	3559	0.543
7.0	31130	16630	3529	0.534
8.0	31130	16410	3519	0.527
9.0	31060	16180	3502	0.521
10.0	31010	15880	3484	0.512
11.0	31020	15780	3480	0.509
12.0	31030	15630	3475	0.504
13.0	31060	15480	3470	0.498
14.0	31090	15210	3461	0.489
15.0	31090	15130	3457	0.487
16.0	31350	15010	3476	0.479
17.0	31450	14880	3479	0.473
18.0	31460	14660	3471	0.466
19.0	31410	14530	3461	0.463
20.0	31450	14470	3462	0.460
21.0	31400	14310	3451	0.456
22.0	31330	14200	3439	0.453
23.0	31280	13990	3427	0.447
24.0	31180	13900	3414	0.446
25.0	31170	13660	3403	0.438
26.0	31160	13580	3400	0.436
27.0	31160	13460	3395	0.432
28.0	31120	13420	3389	0.431
29.0	31150	13250	3385	0.425
30.0	31140	13130	3380	0.422
31.0	31260	13010	3386	0.416
32.0	31210	12960	3380	0.415
33.0	31200	12960	3378	0.415
34.0	31150	12820	3369	0.412
35.0	31110	12730	3362	0.409

Table 17. Time Sweep of HBA/HNA at 301 °C and 10Hz.

Time [s]	G′ [Pa]	G″ [Pa]	η^* [Pa*s]	tanδ
0.0	631	1487	162	2.357
2.0	628	1429	156	2.277
4.0	603	1370	150	2.269
6.0	621	1335	147	2.149
8.0	591	1276	141	2.157
10.0	557	1264	138	2.268
12.0	545	1234	135	2.262
14.0	551	1182	130	2.146
16.0	535	1161	128	2.170
18.0	516	1187	129	2.301
20.0	542	1178	130	2.173
22.0	527	1173	129	2.226
24.0	544	1158	128	2.130
26.0	553	1164	129	2.104
28.0	545	1176	130	2.157
30.0	566	1198	133	2.117
32.0	586	1232	137	2.103
34.0	609	1231	137	2.022
36.0	595	1249	138	2.099
38.0	623	1246	139	2.001
40.0	648	1265	142	1.950
42.0	656	1269	143	1.934
44.0	687	1310	148	1.907
45.0	688	1270	145	1.847
48.0	580	1134	127	1.954
50.0	568	1132	127	1.995
52.0	573	1109	125	1.934
54.0	568	1127	126	1.985
56.0	577	1111	125	1.926
58.0	576	1108	125	1.924
60.0	571	1109	125	1.941

Table 18. Time sweep of HBA/HNA at 320 °C and 10Hz.

Time [s]	G′ [Pa]	G″ [Pa]	η^* [Pa*s]	tanδ
0.0	569	1211	133.8	2.130
1.0	563	1173	130.1	2.083
2.0	552	1109	123.8	2.011
3.0	552	1117	124.6	2.025
4.0	539	1101	122.6	2.042
5.0	543	1070	120.0	1.970
6.0	540	1053	118.3	1.951
7.0	519	1045	116.7	2.012
8.0	530	1042	116.9	1.965
9.0	512	1048	116.6	2.048
10.0	499	1018	113.3	2.040
11.0	520	1031	115.5	1.984
12.0	512	1035	115.4	2.023
13.0	506	1034	115.1	2.043
14.0	511	1025	114.6	2.007
15.0	522	1025	115.0	1.965
16.0	533	1034	116.3	1.941
17.0	519	1030	115.4	1.986
18.0	523	1041	116.4	1.992
19.0	539	1040	117.1	1.928
20.0	527	1041	116.7	1.974
21.0	535	1046	117.5	1.957
22.0	550	1044	118.0	1.899
23.0	525	1042	116.7	1.984
24.0	555	1049	118.7	1.890

Table 19. Frequency Sweep of 60HBA/PET at 275 °C and 10Hz.

Frequency [rad/s]	G′ [Pa]	G″ [Pa]	η^* [Pa*s]	Torque [g*cm]
0.018	0.0	16.3	914.4	0.042
0.032	8.6	13.4	501.6	0.030
0.056	13.4	18.6	407.6	0.043
0.100	14.1	39.4	417.9	0.078
0.178	15.4	61.1	353.9	0.118
0.317	27.1	90.5	298.4	0.177
0.563	36.0	154.3	281.6	0.297
1.001	60.4	256.3	263.1	0.493
1.780	113.9	414.5	241.5	0.805
3.165	210.0	666.9	220.9	1.311
5.628	382.3	1034.0	195.8	2.069
10.010	658.0	1535.0	166.9	3.141
17.800	1054.0	2241.0	139.1	4.667
31.650	1610.0	3195.0	113.0	6.741
56.280	2351.0	4504.0	90.3	9.449
100.000	3321.0	6179.0	70.2	12.330

Table 20. Frequency Sweep of HPC EF at 190 °C and 10Hz.

Frequency [rad/s]	G′ [Pa]	G″ [Pa]	η^* [Pa*s]	Torque [g*cm]
0.100	709	421	8246	1.54
0.178	841	487	5463	1.82
0.316	951	670	3679	2.18
0.562	1112	971	2625	2.76
1.000	1333	1442	1964	3.68
1.778	1682	2202	1558	5.19
3.162	2290	3364	1287	7.62
5.623	3286	5075	1075	11.33
9.999	4945	7509	899	16.86
17.780	7389	11020	746	24.90
31.620	11560	14860	595	35.23
56.230	17100	19620	463	48.07
100.000	24300	24820	347	61.24

Table 21. Frequency Sweep of HPC EF at 210 °C and 10Hz.

Frequency [rad/s]	G′ [Pa]	G″ [Pa]	η^* [Pa*s]	Torque [g*cm]
0.100	111	194	2236.0	0.28
0.178	99	296	1757.0	0.39
0.316	123	502	1635.0	0.65
0.562	210	842	1543.0	1.08
1.000	344	1421	1462.0	1.83
1.778	623	2327	1355.0	3.01
3.162	1123	3743	1236.0	4.89
5.623	2156	5894	1116.0	7.86
9.999	3995	9120	995.7	12.49
17.780	7096	13560	860.9	19.22
31.620	12050	19220	717.4	28.41
56.230	19440	25900	575.9	39.86
100.000	29520	32950	442.4	51.19

Table 22. Frequency Sweep of HPC G at 200 °C and 10Hz.

Frequency [rad/s]	G′ [Pa]	G″ [Pa]	η^* [Pa*s]	Torque [g*cm]
0.100	11670	6585	134000	8.30
0.159	13770	7809	99880	9.80
0.251	16330	9118	74470	11.56
0.398	19230	10250	54730	13.43
0.631	22470	11880	40270	15.64
1.000	26230	13370	29450	18.09
1.585	30560	14780	21420	20.81
2.512	35200	16260	15440	23.72
3.981	40270	17620	11040	26.84
6.310	45740	19050	7852	30.21
10.000	51620	20450	5551	33.82
15.850	57720	21860	3894	37.55
25.120	64080	23430	2716	41.40
39.810	70690	25280	1886	45.11
63.100	77560	27510	1304	47.90
100.000	84110	30010	893	48.54

Table 23. Frequency Sweep of HPC G at 240 °C and 10Hz.

Frequency [rad/s]	G′ [Pa]	G″ [Pa]	η^* [Pa*s]	Torque [g*cm]
0.100	5391	5246	75220	4.68
0.178	7271	6336	54240	5.99
0.316	9642	7748	39120	7.68
0.562	12700	9431	28130	9.80
1.000	16240	11490	19890	12.30
1.778	20730	13680	13970	15.32
3.162	26070	16190	9704	18.89
5.623	32410	18830	6666	23.02
9.999	39780	21520	4523	27.71
17.780	48200	24250	3034	32.97
31.620	57440	26710	2003	38.44
56.230	67500	28870	1306	43.39
100.000	77380	30400	831	45.68

Table 24. Frequency Sweep of HBA/HNA at 301 °C and 10Hz.

Frequency [rad/s]	G′ [Pa]	G″ [Pa]	η^* [Pa*s]	Torque [g*cm]
0.100	119	59	1323.0	0.330
0.159	124	75	914.9	0.360
0.251	127	100	644.2	0.400
0.398	153	133	509.4	0.510
0.631	171	177	390.7	0.620
1.000	201	251	321.6	0.800
1.585	238	353	268.4	1.060
2.512	296	537	244.0	1.530
3.981	372	719	203.3	2.030
6.310	456	1037	179.5	2.840
10.000	637	1517	164.5	4.130
15.850	869	2159	146.8	5.850
25.120	1252	3101	133.1	8.410
39.810	1830	4362	118.8	11.860
63.100	2692	6072	105.3	16.430
100.000	3880	8201	90.7	21.640

Table 25. Frequency Sweep of HBA/HNA at 320 °C and 10Hz.

Frequency [rad/s]	G′ [Pa]	G″ [Pa]	η^* [Pa*s]	Torque [g*cm]
0.100	223	101	2447.5	0.381
0.178	194	131	1326.5	0.369
0.316	228	171	899.8	0.445
0.562	258	249	638.6	0.559
1.000	314	383	494.7	0.774
1.778	398	599	404.7	1.126
3.162	504	897	325.5	1.610
5.623	747	1426	286.3	2.522
9.999	1035	2161	239.6	3.765
17.780	1585	3271	204.4	5.746
31.620	2534	5096	180.0	9.020
56.230	3992	7552	151.9	13.415
100.000	6211	10880	125.3	18.605

Table 26. Temperature Sweep of HPC EF, Frequency = 10Hz.

Temp [°C]	G′ [Pa]	G″ [Pa]	η^* [Pa*s]	tanδ
159.9	23840	18357	3009	0.770
160.8	23100	17826	2918	0.772
163.1	21180	16552	2689	0.782
165.3	18560	14963	2384	0.806
167.7	15780	13236	2060	0.839
169.9	13120	11615	1752	0.885
172.3	11000	10260	1504	0.933
174.7	9315	9175	1307	0.985
177.0	8110	8410	1168	1.037
179.4	6989	7646	1036	1.094
181.7	6121	7168	943	1.171
183.9	5491	6770	872	1.233
186.3	5060	6629	834	1.310
188.6	4864	6673	826	1.372
191.0	4807	6917	843	1.439
193.4	4853	7270	874	1.498
195.7	4876	7728	914	1.585
198.1	4886	8199	954	1.678
200.4	4767	8666	989	1.818
202.7	4560	8810	992	1.932
205.1	4275	8794	978	2.057
207.4	3830	8499	932	2.219
209.8	3335	7951	862	2.384
212.2	2866	7222	777	2.520
214.6	2405	6462	690	2.687
214.7	2055	5890	624	2.866
212.6	2022	5775	612	2.856
210.5	2121	5915	629	2.789
208.3	2349	6234	666	2.654
206.2	2652	6694	720	2.524
203.9	3064	7320	794	2.389
201.7	3618	8086	886	2.235
199.5	4220	8862	982	2.100
197.2	5002	9824	1102	1.964
194.9	5947	10835	1236	1.822
192.6	7009	11915	1382	1.700
190.3	8292	12944	1537	1.561
188.0	9260	13047	1600	1.409
185.7	8735	11382	1435	1.303
183.4	8187	10324	1318	1.261
181.0	7883	9696	1250	1.230
178.7	7721	9296	1209	1.204
176.3	7715	9081	1192	1.177
173.9	7777	9068	1195	1.166

Table 26. continued

Temp [°C]	G′ [Pa]	G″ [Pa]	η^* [Pa*s]	tanδ
171.5	8032	9165	1219	1.141
169.1	8427	9388	1262	1.114
166.7	8931	9824	1328	1.100
164.3	9774	10419	1429	1.066
161.9	10950	11268	1572	1.029

Table 27. Temperature Sweep of HPC G, Frequency = 10Hz.

Temp [°C]	G′ [Pa]	G″ [Pa]	η^* [Pa*s]	tanδ
159.2	64020	28300	7000	0.442
160.7	63040	27750	6888	0.440
163.0	60040	26200	6551	0.436
165.3	55220	23770	6012	0.431
167.6	50690	21630	5512	0.427
169.9	45800	19350	4972	0.423
172.3	41760	17570	4530	0.421
174.7	38440	16050	4166	0.418
177.1	35880	14940	3887	0.417
179.4	34140	14150	3696	0.415
181.7	32710	13590	3542	0.416
184.0	31980	13280	3463	0.415
186.4	31470	13100	3409	0.416
188.8	30870	12940	3348	0.419
191.1	30910	13030	3355	0.422
193.5	30830	13120	3351	0.426
195.7	31270	13420	3403	0.429
198.2	31110	13670	3398	0.440
200.5	32240	14150	3521	0.439
202.9	33830	15000	3701	0.443
205.3	36170	16130	3960	0.446
207.6	37500	16790	4109	0.448
210.0	40580	18200	4448	0.448
212.4	43900	19700	4812	0.449
214.7	44910	20150	4922	0.449
217.1	46810	21120	5135	0.451
219.5	45850	20830	5036	0.454
221.8	46360	21420	5107	0.462
224.3	46420	21920	5134	0.472
226.7	46240	22300	5134	0.482
229.1	44470	21870	4956	0.492
231.5	43750	22060	4899	0.504
233.9	43020	22160	4839	0.515
234.0	42620	22240	4808	0.522
231.9	42910	22320	4836	0.520
229.7	43720	22360	4911	0.512
227.6	44870	22420	5016	0.500
225.4	46200	22460	5137	0.486
223.2	47630	22410	5264	0.471
220.9	49070	22340	5392	0.455
218.7	50570	22250	5525	0.440
216.3	52950	22510	5753	0.425
214.1	54530	22290	5891	0.409
211.7	56100	22060	6028	0.393

Table 27. continued

Temp [°C]	G′ [Pa]	G″ [Pa]	η^* [Pa*s]	tanδ
209.5	57430	21700	6139	0.378
207.1	59590	21670	6341	0.364
204.8	61580	21510	6523	0.349
202.5	62520	20990	6595	0.336
200.1	62920	20260	6610	0.322
197.8	63960	19800	6696	0.310
195.5	64040	19110	6683	0.298
193.1	62780	18190	6536	0.290
190.7	60500	17120	6288	0.283
188.4	54950	16140	5728	0.294
186.1	49640	15210	5192	0.306
183.7	48030	14980	5031	0.312
181.4	47620	15050	4994	0.316
179.0	47240	15060	4959	0.319
176.6	47900	15490	5034	0.323
174.2	49040	16050	5160	0.327
171.7	50220	16600	5290	0.331
169.3	51770	17280	5458	0.334
166.9	53730	18270	5675	0.340
164.5	56230	19520	5952	0.347
162.1	59350	20860	6291	0.352

Appendix E. ER Data

Table 28. Transient extensional viscosity growth of NTA101 at 170 °C and 0.007 s^{-1}

Time [S]	$\bar{\eta}_e^+$ [Pa*s]
0.00	0
3.25	15661
9.50	34377
15.75	37387
22.00	40207
28.25	39378
34.50	38332
40.75	37990
47.00	38419
53.25	38480
59.50	37214
65.75	35363
72.00	36626
78.25	37154
84.50	37195
90.75	37706
97.00	38154
103.25	37202
109.50	39981
115.75	41116
122.00	38810
128.25	37315
134.50	37050
140.75	37032
147.00	36609
153.25	34109
159.50	34817
165.75	37270
172.00	34849
178.25	33247

Table 29. Transient extensional viscosity growth NTA 101 at 170 °C and 0.014 s^{-1}

Time [s]	$\bar{\eta}_e^+$ [Pa*s]	Time [s]	$\bar{\eta}_e^+$ [Pa*s]
0.000	0	123.500	41167
1.625	18236	126.625	41314
4.750	35222	129.750	41638
7.875	39137	132.875	42414
11.000	40966	136.000	42681
14.125	41922	139.125	43617
17.250	42475	142.250	45443
20.375	43107	145.375	45718
23.500	40897	148.500	46313
26.625	38064	151.625	46341
29.750	41158	154.750	46198
32.875	40959	157.875	46057
36.000	42055	161.000	45670
39.125	42339	164.125	47030
42.250	42654	167.250	48206
45.375	41900	170.375	49364
48.500	41977	173.500	49854
51.625	40134	176.625	50959
54.750	37833	179.750	52024
57.875	38085	182.875	52939
61.000	37543		
64.125	37672		
67.250	39634		
70.375	42274		
73.500	40047		
76.625	37658		
79.750	36347		
82.875	35643		
86.000	36512		
89.125	37403		
92.250	37387		
95.375	37973		
98.500	38313		
101.625	38866		
104.750	38445		
107.875	37535		
111.000	37727		
114.125	39442		
117.250	39961		
120.375	39967		

Table 30. Transient extensional viscosity growth of NTA101 at 170 °C and 0.053 s^{-1}

Time [S]	$\bar{\eta}_e^+$ [Pa*s]
0.000	0
0.433	9345
1.266	26799
2.099	30697
2.933	32163
3.766	34212
4.599	35547
5.432	34191
6.265	34149
7.098	32428
7.931	31887
8.764	32672
9.598	33114
10.431	33040
11.264	33031
12.097	35844
12.930	36910
13.763	37063
14.596	37076
15.429	36399
16.263	35311
17.096	33987
17.929	31905

Table 31. Transient extensional viscosity growth NTA 101 at 170 °C and 0.120 s^{-1}

Time [s]	$\bar{\eta}_e^+$ [Pa*s]	Time [s]	$\bar{\eta}_e^+$ [Pa*s]
0.000	0	12.350	38883
0.163	8926	12.663	36996
0.475	27404	12.975	37752
0.788	34307	13.288	39726
1.100	36763	13.600	39247
1.413	38620	13.913	37089
1.725	39634	14.225	37118
2.038	39814	14.538	37032
2.350	40067	14.850	34762
2.663	40130	15.163	32321
2.975	40330	15.475	29921
3.288	41451	15.788	28318
3.600	41756		
3.913	42223		
4.225	41444		
4.538	41429		
4.850	41294		
5.163	41341		
5.475	40694		
5.788	42080		
6.100	45485		
6.413	42860		
6.725	40753		
7.038	39420		
7.350	35248		
7.663	33179		
7.975	34716		
8.288	35225		
8.600	34733		
8.913	46510		
9.225	44590		
9.538	43873		
9.850	41892		
10.163	40086		
10.475	42620		
10.788	40512		
11.100	37435		
11.413	39244		
11.725	39005		
12.038	40476		

Table 32. Transient extensional viscosity growth of HPC EF at 190 °C and 0.0249 s^{-1}

Time [S]	$\bar{\eta}_e^+$ [Pa*s]
0	0
1.25	3620
3.25	11442
5.25	17034
7.25	22070
9.25	27063
11.25	31794
13.25	36251
15.25	40687
17.25	44711
19.25	48905
21.25	52642
23.25	55454
25.25	58075
27.25	61101
29.25	63454
31.25	65457
33.25	67419
35.25	69443
37.25	71387
39.25	73274
41.25	74452
43.25	75087
45.25	75546
47.25	76599
49.25	76858
51.25	76770

Table 33. Transient extensional viscosity growth of HPC EF at 190 °C and 0.0643 s^{-1}

Time [S]	$\bar{\eta}_e^+$ [Pa*s]
0.000	0
0.433	3821
1.266	8609
2.099	11678
2.933	14594
3.766	17279
4.599	19968
5.432	22547
6.265	25259
7.098	28130
7.931	30775
8.764	33144
9.598	35270
10.431	37495
11.264	39729
12.097	41843
12.930	43823
13.763	45656
14.596	47273
15.429	49045
16.263	50639
17.096	52102
17.929	53249
18.762	54300
19.595	55495
20.428	56596
21.261	57602
22.094	58428
22.928	59134
23.761	59873
24.594	60929
25.427	61976
26.260	61940
27.093	61383

Table 34. Transient extensional viscosity growth of HPC EF at 190 °C and 0.141 s^{-1}

Time [S]	$\bar{\eta}_e^+$ [Pa*s]
0.0000	0
0.1625	4462
0.4750	8370
0.7875	11207
1.1000	12908
1.4125	14896
1.7250	16651
2.0375	18519
2.3500	20303
2.6625	21950
2.9750	22893
3.2875	23962
3.6000	24979
3.9125	25914
4.2250	26851
4.5375	27782
4.8500	28602
5.1625	29444
5.4750	29975
5.7875	30561
6.1000	30971
6.4125	31282
6.7250	31579
7.0375	31847
7.3500	32358
7.6625	32805
7.9750	33082
8.2875	33054
8.6000	32756
8.9125	32866
9.2250	32958
9.5375	32761

Table 35. Transient extensional viscosity growth of HPC EF at 190 °C and 0.49 s^{-1}

Time [s]	$\bar{\eta}_e^+$ [Pa*s]	Time [s]	$\bar{\eta}_e^+$ [Pa*s]
0.000	0	4.940	24937
0.065	2211	5.065	24575
0.190	4319	5.190	23710
0.315	5476	5.315	22920
0.440	6580		
0.565	7679		
0.690	8475		
0.815	9445		
0.940	10260		
1.065	10896		
1.190	11699		
1.315	12575		
1.440	13265		
1.565	14059		
1.690	14860		
1.815	15440		
1.940	15818		
2.065	16320		
2.190	16915		
2.315	17416		
2.440	17912		
2.565	18117		
2.690	18213		
2.815	18822		
2.940	19011		
3.065	19503		
3.190	19794		
3.315	19978		
3.440	20489		
3.565	20738		
3.690	20958		
3.815	21345		
3.940	21554		
4.065	22029		
4.190	22028		
4.315	22186		
4.440	23152		
4.565	24047		
4.690	24741		
4.815	24980		

Table 36. Transient extensional viscosity growth of HPC EF at 210 °C and 0.0239 s^{-1}

Time [S]	$\bar{\eta}_e^+$ [Pa*s]
0.000	0
1.625	2188
4.750	3210
7.875	3921
11.000	4479
14.125	4830
17.250	5141
20.375	5521
23.500	5733
26.625	6008
29.750	6436
32.875	6879
36.000	7038
39.125	7424
42.250	8126
45.375	8778
48.500	8644
51.625	8832
54.750	9067
57.875	9962
61.000	11451
64.125	12682
67.250	12357
70.375	13269
73.500	14962
76.625	16637
79.750	17615
82.875	19400
86.000	18621
89.125	20714
92.250	20998
95.375	22112

Table 37. Transient extensional viscosity growth of HPC EF at 210 °C and 0.064 s^{-1}

Time [S]	$\bar{\eta}_e^+$ [Pa*s]
0.0000	0
0.4332	1474
1.2664	3018
2.0995	3587
2.9326	4053
3.7657	4524
4.5988	4923
5.4320	5399
6.2651	5825
7.0982	6271
7.9314	6789
8.7645	7199
9.5976	7786
10.4307	8390
11.2639	9103
12.0970	9872
12.9301	10569
13.7632	11244
14.5964	11951
15.4295	12582
16.2626	13389
17.0957	13905
17.9289	14572
18.7620	15123
19.5951	15699
20.4282	16094
21.2614	16587
22.0945	16713
22.9276	16559
23.7607	15428

Table 38. Transient extensional viscosity growth of HPC EF at 210 °C and 0.168 s^{-1}

Time [S]	$\bar{\eta}_e^+$ [Pa*s]
0.0000	0
0.1625	1714
0.4750	3207
0.7875	3624
1.1000	4180
1.4125	4309
1.7250	4479
2.0375	4677
2.3500	4862
2.6625	4933
2.9750	5106
3.2875	5316
3.6000	5561
3.9125	5725
4.2250	6011
4.5375	6252
4.8500	6628
5.1625	6948
5.4750	7307
5.7875	7735
6.1000	8138
6.4125	8530
6.7250	9047
7.0375	9532
7.3500	10183
7.6625	10768
7.9750	11381
8.2875	12063
8.6000	12745
8.9125	13455
9.2250	14182
9.5375	14766
9.8500	15514
10.1625	16048
10.4750	16511
10.7875	16865
11.1000	17186
11.4125	17449
11.7250	17625
12.0375	17494

Table 39. Transient extensional viscosity growth of HPC EF at 210 °C and 0.51 s^{-1}

Time [S]	$\bar{\eta}_e^+$ [Pa*s]
0.0000	0.0
0.0656	996.3
0.1906	2635.5
0.3156	3165.9
0.4406	3588.7
0.5656	3898.7
0.6906	4086.2
0.8156	4246.5
0.9406	4263.2
1.0656	4302.7
1.1906	4499.2
1.3156	4632.3
1.4406	4898.8
1.5656	5100.6
1.6906	5330.1
1.8156	5417.5
1.9406	5432.1
2.0656	5554.0
2.1906	5917.2
2.3156	6173.8
2.4406	6478.0
2.5656	6630.2
2.6906	6530.2

Table 40. Transient extensional viscosity growth of HPC G at 200 °C and 0.0078 s^{-1}

Time [S]	$\bar{\eta}_e^+$ [Pa*s]
0.000	0
2.167	205992
6.333	525324
10.500	720968
14.666	909817
18.833	1099099
22.999	1293136
27.166	1431977
31.332	1584823
35.499	1778575
39.666	1949441
43.832	2048761
47.999	2159473
52.165	2299707
56.332	2504725
60.498	2713708
64.665	2847050
68.831	2940416
72.998	3087015
77.165	3232974
81.331	3334651
85.498	3445318
89.664	3552234
93.831	3686456
97.997	3847741
102.164	3984980
106.330	4050692
110.497	4177375
114.663	4269971
118.830	4306616
122.997	4412161
127.163	4516480
131.330	4590751
135.496	4601311
139.663	4610668

Table 41. Transient extensional viscosity growth of HPC G at 200 °C and 0.0158 s^{-1}

Time [S]	$\bar{\eta}_e^+$ [Pa*s]
0.00	0
1.30	116990
3.80	323085
6.30	494464
8.80	632900
11.30	759917
13.80	879758
16.30	992105
18.80	1103969
21.30	1224824
23.80	1342356
26.30	1454294
28.80	1552765
31.30	1653003
33.80	1737888
36.30	1827243
38.80	1927861
41.30	2028435
43.80	2118245
46.30	2208152
48.80	2281682
51.30	2348777
53.80	2416862
56.30	2470094
58.80	2513011
61.30	2553107
63.80	2571327
66.30	2624434

Table 42. Transient extensional viscosity growth of HPC G at 200 °C and 0.142 s^{-1}

Time [S]	$\bar{\eta}_e^+$ [Pa*s]
0.0000	0
0.1625	29599
0.4750	84253
0.7875	127625
1.1000	165849
1.4125	201703
1.7250	235044
2.0375	267050
2.3500	299467
2.6625	329717
2.9750	359507
3.2875	387873
3.6000	413451
3.9125	437326
4.2250	459793
4.5375	480217
4.8500	497403
5.1625	510681
5.4750	519061
5.7875	529712
6.1000	535276
6.4125	533701

Table 43. Transient extensional viscosity growth of HPC G at 240 °C and 0.0085 s^{-1}

Time [s]	$\bar{\eta}_e^+$ [Pa*s]	Time [s]	$\bar{\eta}_e^+$ [Pa*s]
0.000	0	164.666	3594532
2.167	109495	168.833	3573646
6.333	311554	172.999	3696666
10.500	442146	177.166	3896095
14.667	556031	181.333	4043903
18.833	623938	185.499	4068471
23.000	685160	189.666	4005687
27.167	764087	193.833	4051119
31.333	909180	197.999	4155582
35.500	977844	202.166	4166725
39.667	1046037	206.333	4210224
43.833	1130030	210.499	4336852
48.000	1186150	214.666	4386127
52.166	1230113	218.833	4742080
56.333	1322595		
60.500	1433620		
64.666	1428966		
68.833	1473113		
73.000	1563865		
77.166	1637474		
81.333	1771009		
85.500	1891782		
89.666	1973566		
93.833	1990455		
98.000	2063098		
102.166	2128940		
106.333	2188395		
110.500	2262101		
114.666	2323316		
118.833	2470870		
123.000	2572090		
127.166	2647635		
131.333	2736896		
135.500	2765617		
139.666	2869123		
143.833	3033512		
147.999	3199243		
152.166	3236412		
156.333	3282304		
160.499	3461230		

Table 44. Transient extensional viscosity growth of HPC G at 240 °C and 0.017 s^{-1}

Time [s]	$\bar{\eta}_e^+$ [Pa*s]	Time [s]	$\bar{\eta}_e^+$ [Pa*s]
0	0	98.8	2556036
1.3	64481	101.3	2631585
3.8	178638	103.8	2685942
6.3	274066	106.3	2689236
8.8	348592	108.8	2723072
11.3	425126	111.3	2865706
13.8	511257	113.8	2900024
16.3	555251	116.3	2857341
18.8	606987	118.8	2853179
21.3	664787	121.3	2840309
23.8	736720	123.8	2886710
26.3	782256		
28.8	830959		
31.3	877386		
33.8	929034		
36.3	986130		
38.8	1044329		
41.3	1114511		
43.8	1176283		
46.3	1256941		
48.8	1338826		
51.3	1396366		
53.8	1457907		
56.3	1511953		
58.8	1590712		
61.3	1653710		
63.8	1718211		
66.3	1778811		
68.8	1807862		
71.3	1873206		
73.8	1949193		
76.3	1992664		
78.8	2045904		
81.3	2115000		
83.8	2201425		
86.3	2278271		
88.8	2325877		
91.3	2425108		
93.8	2502925		
96.3	2530035		

Table 45. Transient extensional viscosity growth of HPC G at 240 °C and 0.164 s^{-1}

Time [S]	$\bar{\eta}_e^+$ [Pa*s]
0.0000	0
0.1625	21123
0.4750	53314
0.7875	76260
1.1000	96840
1.4125	116814
1.7250	135814
2.0375	154394
2.3500	172121
2.6625	186813
2.9750	206391
3.2875	225043
3.6000	243106
3.9125	260981
4.2250	278801
4.5375	296954
4.8500	315169
5.1625	333758
5.4750	352109
5.7875	371220
6.1000	391224
6.4125	412032
6.7250	432311
7.0375	452412
7.3500	472442
7.6625	492650
7.9750	513445
8.2875	534497
8.6000	554626
8.9125	573679
9.2250	590447
9.5375	606694
9.8500	620183
10.1625	632384
10.4750	638727

Table 46. Transient extensional viscosity growth of Vectra A900 at 301 °C and 0.0290 s^{-1}

Time [s]	$\bar{\eta}_e^+$ [Pa*s]	Time [s]	$\bar{\eta}_e^+$ [Pa*s]
0.000	0	32.925	7740
0.433	1348	33.758	7657
1.266	2152	34.591	7455
2.099	2698	35.424	7447
2.933	3140	36.258	7652
3.766	3397	37.091	7505
4.599	3796	37.924	6979
5.432	4169	38.757	6713
6.265	4520		
7.098	4940		
7.931	5287		
8.764	5678		
9.598	6000		
10.431	6176		
11.264	6540		
12.097	6887		
12.930	7387		
13.763	7823		
14.596	8185		
15.429	8351		
16.263	8656		
17.096	8972		
17.929	9248		
18.762	9461		
19.595	9510		
20.428	9539		
21.261	9422		
22.094	9426		
22.928	9252		
23.761	9164		
24.594	9029		
25.427	9103		
26.260	8992		
27.093	8917		
27.926	8836		
28.759	8556		
29.593	8244		
30.426	8077		
31.259	8011		
32.092	7896		

Table 47. Transient extensional viscosity growth of Vectra A900 at 301 °C and 0.0840 s^{-1}

Time [S]	$\bar{\eta}_e^+$ [Pa*s]
0.000	0
0.325	821
0.950	1466
1.575	1787
2.200	2060
2.825	2377
3.450	2717
4.075	3076
4.700	3395
5.325	3786
5.950	4199
6.575	4633
7.200	5058
7.825	5441
8.450	5786
9.075	6228
9.700	6633
10.325	7107
10.950	7754
11.575	7511
12.200	6905

Table 48. Transient extensional viscosity growth of Vectra A900 at 301 °C and 0.151 s^{-1}

Time [s]	$\bar{\eta}_e^+$ [Pa*s]	Time [s]	$\bar{\eta}_e^+$ [Pa*s]
0.0000	0.0	12.3500	7267.8
0.1625	701.7	12.6625	7308.6
0.4750	1102.2	12.9750	7307.5
0.7875	1306.3	13.2875	7155.8
1.1000	1527.1		
1.4125	1753.7		
1.7250	2004.3		
2.0375	2249.9		
2.3500	2486.5		
2.6625	2694.4		
2.9750	2974.8		
3.2875	3244.4		
3.6000	3482.7		
3.9125	3809.6		
4.2250	4136.5		
4.5375	4427.1		
4.8500	4684.2		
5.1625	4981.3		
5.4750	5269.3		
5.7875	5482.3		
6.1000	5780.2		
6.4125	6095.3		
6.7250	6176.3		
7.0375	6214.0		
7.3500	6362.8		
7.6625	6429.5		
7.9750	6615.4		
8.2875	6886.1		
8.6000	7113.8		
8.9125	7265.0		
9.2250	7359.5		
9.5375	7365.7		
9.8500	7412.0		
10.1625	7538.2		
10.4750	7438.2		
10.7875	7387.7		
11.1000	7357.2		
11.4125	7085.0		
11.7250	7246.4		
12.0375	7420.4		

Table 49. Transient extensional viscosity growth of Vectra A900 at 301 °C and 0.482 s^{-1}

Time [S]	$\bar{\eta}_e^+$ [Pa*s]
0.0000	0.0
0.0813	397.4
0.2375	819.8
0.3938	1019.5
0.5500	1138.6
0.7063	1357.9
0.8625	1634.0
1.0188	1921.6
1.1750	2217.2
1.3313	2523.2
1.4875	2840.0
1.6438	3078.0
1.8000	3244.5
1.9563	3557.9
2.1125	3941.8
2.2688	4275.4
2.4250	4520.9
2.5813	4778.0
2.7375	4997.1
2.8938	5168.6
3.0500	5353.7
3.2063	5160.5

Table 50. Transient extensional viscosity growth of Vectra A900 at 320 °C and 0.054 s^{-1}

Time [s]	$\bar{\eta}_e^+$ [Pa*s]	Time [s]	$\bar{\eta}_e^+$ [Pa*s]
0.000	0.0	26.343	10190.0
0.350	925.1	27.010	10467.3
1.016	1643.0	27.676	10642.2
1.683	1894.2	28.343	10874.1
2.349	2138.0		
3.016	2457.6		
3.682	2886.1		
4.349	3244.2		
5.015	3577.1		
5.682	3845.7		
6.348	4135.1		
7.015	4476.6		
7.681	4704.5		
8.348	4878.2		
9.014	5080.5		
9.681	5317.8		
10.347	5477.0		
11.014	5634.6		
11.680	5922.7		
12.347	6068.1		
13.013	6204.3		
13.680	6387.2		
14.346	6638.4		
15.013	6790.8		
15.679	6975.3		
16.346	7238.9		
17.012	7527.8		
17.679	7792.8		
18.345	8081.4		
19.012	8291.3		
19.678	8428.5		
20.345	8557.5		
21.011	8783.5		
21.678	8980.2		
22.344	9158.7		
23.011	9352.7		
23.677	9718.7		
24.344	9883.5		
25.010	9977.4		
25.677	10040.5		

Table 51. Transient extensional viscosity growth of Vectra A900 at 320 °C and 0.173 s^{-1}

Time [S]	$\bar{\eta}_e^+$ [Pa*s]
0.0000	0.0
0.1313	565.2
0.3813	975.2
0.6313	1140.0
0.8813	1271.3
1.1313	1389.6
1.3813	1563.2
1.6313	1736.7
1.8813	1898.4
2.1313	2071.3
2.3813	2228.1
2.6313	2398.8
2.8813	2586.3
3.1313	2797.9
3.3813	2988.4
3.6313	3157.2
3.8813	3329.0
4.1313	3517.7
4.3813	3743.6
4.6313	3925.4
4.8813	4106.9
5.1313	4315.7
5.3813	4643.7
5.6313	4771.0
5.8813	4978.1
6.1313	5006.0
6.3813	4995.4
6.6313	5080.6
6.8813	5237.7
7.1313	5014.6

Table 52. Transient extensional viscosity growth of Vectra A900 at 320 °C and 0.450 s^{-1}

Time [S]	$\bar{\eta}_e^+$ [Pa*s]
0.0000	0.0
0.0500	480.3
0.1438	859.5
0.2375	990.2
0.3313	1146.7
0.4250	1266.1
0.5188	1343.3
0.6125	1438.0
0.7063	1541.9
0.8000	1684.6
0.8938	1825.5
0.9875	1952.2
1.0813	2100.9
1.1750	2253.5
1.2688	2393.2
1.3625	2544.6
1.4563	2671.0
1.5500	2792.5
1.6438	2897.5
1.7375	2959.2

Vita

Thomas S. Wilson was born in Livonia, Michigan on October 2, 1962. At the age of three, his family moved to Green Bay, Wisconsin, where he grew up, graduating from Preble High School. Desiring to know more about the physical makeup of the world around him, he studied chemical engineering at the University of Wisconsin-Madison, receiving his B.S in December, 1985.

Almost immediately after receiving his BS Tom began graduate school at Virginia Tech in pursuit of a PhD under the wing of Prof. Don Baird in the area of polymer rheology and processing. The fact that this is being read indicates he finally succeeded in his quest.

Outside of academics, Tom has actively participated in such activities as racquetball, fishing, juggling, tennis, golf, home computing, beer-making and swimming, but at the moment spends much of his time looking toward the west.